AN ABSTRACT OF A DISSERTATION

MODELING, SIMULATION, AND APPLICATION OF A DOUBLY-FED RELUCTANCE
ELECTRICAL MACHINE

Zhiqing Wu

Doctor of Philosophy in Engineering

Brushless doubly-fed (dual-winding, mixed-pole) machines have received renewed attention in the last few years for use in adjustable-speed drives and variable speed generator systems. This class of machine has two three-phase stator windings wound for different pole numbers and a cage or a reluctance rotor. It appears to be highly attractive due to its structural simplicity, high efficiency, lower manufacturing cost, and its ability to operate in induction and synchronous machine modes with the possibility of sub- and super-synchronous speeds operations.

This dissertation presents an accurate model of the doubly-fed reluctance machine, which considers the core-loss of the machine. The q-d equivalent circuits with series core-loss resistances or shunt core-loss resistances are given. The analysis and performance characterizations of a few systems with this machine are set forth. These systems are:

(1) Stand-alone doubly-fed reluctance generator system with capacitive excitation in both the power and control windings.
(2) Doubly-fed synchronous generator system with DC current excitation in control windings and three-phase impedance load or a loaded three-phase diode rectifier in power windings.
(3) Doubly-fed synchronous reluctance generator systems with controlled DC output voltage. DC-DC buck converter or boost converter is used as DC voltage regulator.
(4) Field-orientation doubly-fed motor control system that can run in a wide speed range. IP controller, Input-output linearization controller, voltage-controlled voltage source PWM inverter, and current-controlled voltage source PWM inverter are used in two control schemes.

Dynamic simulation, steady-state calculation, and experimental measurement are used to reveal its potential application.

VITA

Mr. Zhiqing Wu was born in Guangdong, People's Republic of China, on December 14, 1964. He attended Zhengzhou Light Industrial Institute of Technology and received a degree of Bachelor of Science in Electrical Engineering in July 1985. He entered the graduate school of Guangdong University of Technology in September 1987 and received a Master of Science degree in Electrical Engineering in July 1989. He started his Ph.D. program at Tennessee Technological University in January 1994 and received a Doctor of Philosophy Degree in Engineering in December 1998.

From 1985-1987, he worked as an electrical engineer in New Star Industry Company, GuangZhou, China. From 1989-1993, he joined Guangdong Province Technology Exchange Center as a project engineer in GuangZhou, China. He worked as a Research Assistant while he was a graduate student at Tennessee Technological University.

MODELING, SIMULATION, AND APPLICATION OF A DOUBLY-FED RELUCTANCE ELECTRICAL MACHINE

A Dissertation

Presented to

the Faculty of the Graduate School

Tennessee Technological University

by

Zhiqing Wu

In Partial Fulfillment

of the Requirements for the Degree

DOCTOR OF PHILOSOPHY

Engineering

December 1998

CERTIFICATE OF APPROVAL OF DISSERTATION

MODELING, SIMULATION, AND APPLICATION OF A DOUBLY-FED RELUCTANCE ELECTRICAL MACHINE

by

Zhiqing Wu

Graduate Advisory Committee:

________________________ ________
Chairperson date

________________________ ________
Member date

________________________ ________
Member date

________________________ ________
Member date

________________________ ________
Member date

________________________ ________
Member date

________________________ ________
Member date

Approved for the Faculty:

____
Dean of Graduate Studies

____
Date

DEDICATION

This dissertation is dedicated to my parents
and sisters

ACKNOWLEDGMENTS

I would like to express my appreciation to Dr. Olorunfemi Ojo, my major professor and chairman of the advisory committee, for his valuable direction and assistance. I would also like to thank Dr. Marie B. Ventrice a member of my advisor committee for her encouragement and assistance during this work. I also want to thank my other advisory committee members: Dr. A. Chandrasekaran, Dr. Brian M. O'Connor, Dr. Ahmad Smaili, Dr. Charles E. Hickman, and Dr. Ghadir Radman for their assistance.

I express my gratitude to Dr. P. K. Rajan and Dr. Ken Purdy for their assistance. I am grateful to Obasohan I. Omozusi, John Cox, Sandy Garrison, Helen Knott, and Keith Jones for their support. I acknowledge the financial support of the Center for Electric Power at Tennessee Technological University for this research.

TABLE OF CONTENTS

Page

LIST OF SYMBOLS

p_1, q = Pole pair number of the power and control windings, respectively

P_r = Pole pair number of the salient rotor structure

r_p, r_s = Per-phase winding resistance of the power and control windings, respectively

I_{Ap}, I_{as} = Power winding phase ‘A’ current and control winding phase ‘a’ current, respectively

I_{Ao} = Phase ‘A’ load current

I_{Ar}, I_{Br}, I_{Cr} = Phase currents flowing into the three-phase diode rectifier

S_{av}, S_{bv}, S_{cv} = Voltage switching functions of the three legs of the rectifier

S_{aI}, S_{bI}, S_{cI} = Current switching function of the rectifier

I_d = Filter inductor current

V_{Ap}, V_{as} = Power winding phase ‘A’ voltage and control winding phase ‘a’ voltage, respectively

λ_{Ap}, λ_{as} = Power winding phase ‘A’ flux linkage and control winding phase ‘a’ flux linkage, respectively

R_{mp}, R'_{ms} = Per-phase core-loss resistances for the power winding and control windings, respectively

V_{qp}, V_{dp} = Power winding terminal voltage magnitudes in the q-d reference frame

V_{qs}, V_{ds} = Control winding terminal magnitudes in the q-d reference frame

V'_{qs}, V'_{ds} = Referred control winding q-d terminal voltage

V_{qdp}, V_{qds} = Q-d complex form terminal voltage magnitudes of the power and control winding, respectively

V'_{qds} = Referred q-d complex form control winding voltage

ω_p, ω_s = Angular frequency of the power and control winding supply voltages, respectively

ω_r, ω_{rm} = Electrical and mechanical angular rotor speed

$\theta_p = \omega_p t$, $\theta_s = \omega_s t$, $\theta_r = \omega_r t$

N_p, N_s = Effective turns per-pole, per-phase for the power and control windings, respectively

r, l = Radius of the rotor and the effective length of the machine, respectively

α = Rotor pitch factor

I_{qp}, I_{dp} = Q and d power winding currents, respectively

I_{qs}, I_{ds} = Q and d control winding currents, respectively

I'_{qs}, I'_{ds} = Referred q and d control winding currents, respectively

I_{qo}, I_{do} = Q and d load currents, respectively

I_{qdp}, I_{qds} = Q-d complex form power and control winding current, respectively

I'_{qds} = Referred q-d complex form control winding current

I_{qdo} = Complex form load current

I_o = Load current of the rectifier circuit

λ_{qp}, λ_{dp} = Q and d power winding flux linkage, respectively

λ_{qs}, λ_{ds} = Q and d control winding flux linkage, respectively

λ'_{qs}, λ'_{ds} = Referred q and d control winding flux linkage, respectively

λ_{qm}, λ_{dm} = Q and d magnetizing flux linkage, respectively

λ_m = Magnitude of the magnetizing flux linkage

C_p, C_q = Per-phase shunt capacitor connected across the power and control winding terminals

C'_q = Referred per-phase shunt capacitor connected to the control windings

L_{AA}, L_{aa} = Self-inductance of the power and control windings, respectively

L_{BC}, L_{AB}, L_{AC} = Mutual inductances between phases of the power windings

L_{bc}, L_{ab}, L_{ac} = Mutual inductnces between phases of the control windings

$L_{j,k}$, j = a, b, c; k = A, B, C, = Mutual inductances between the power and control winding phases

L_1, L_2 = Per-phase leakage inductance of the power and control winding, respectively

L_p, L_s = Self-inductance of the power and control winding, respectively

L_{m12} = Mutual inductance between the power and control windings

L'_s, L_m = Referred control winding self-inductance and mutual inductance, between power and control winding, respectively

L_{lp} = L_p – L_m = Per-phase effective leakage inductance of the control winding

L'_{ls} = L'_s – L_m = Per-phase effectively referred leakage inductance of the control windings

R_o, L_o = Load resistance and inductance, respectively

V_{cd} = Rectifier filter capacitor voltage

I_d = Rectifier inductor current

Cd, Ld = Rectifier filter capacitor and inductance, respectively

p = d/dt

D = duty ratio

LIST OF TABLES

LIST OF FIGURES

Figure Page

Figure Page

CHAPTER 1
RESEARCH BACKGROUND

1.1 Introduction

Brushless doubly-fed (dual-winding, mixed-pole) machines have received renewed attention in the last few years for use in adjustable-speed drives where efficiency optimization and energy conservation are desirable. This class of machine has two three-phase stator windings wound for different pole numbers and a cage or a reluctance rotor. The three-phase stator windings that carry the load are called the power windings, while other three-phase windings usually used for speed and power flow control are called the control windings. The stator windings of the doubly fed machines are shown in Figure 1.1. Two sets of stator windings can be connected together or physically separated. In Figure 1.1(a), by following special rule of winding connection, the resulting windings can be divided into two sets of stator windings with different pole numbers when viewed from two sets of leads, A-B-C and a-b-c. When these two sets of leads are powered simultaneously from two independent sources, the terminal currents will not affect each other due to the symmetric nature of the winding. In Figure 1.1(b), two stator windings are separated from each other. Separate stator windings are generally undesirable except added flexibility of design or operation is necessary.

In general, brushless doubly-fed induction machine has a special cage construction to support the two air-gap fields produced by the two sets of stator windings.

The double-fed reluctance machine, on the other hand, has either a simple salient laminated pole (shown in Figure 1.1(c)) or axially laminated rotor structure with no cage windings (shown in Figure 1.1(d)).

The concept of a single machine with two sets of polyphase stator windings, which do not couple directly but interact via a specially formed rotor, originated one of those ingenious techniques developed to overcome fixed speed limitation of the induction motor before the frequency conversion was developed using power electronics. The first machine to use this concept, called Hunt motor [1], resulted from the incorporation of two effective machines in a single magnetic circuit. Based on the ideas of the Hunt

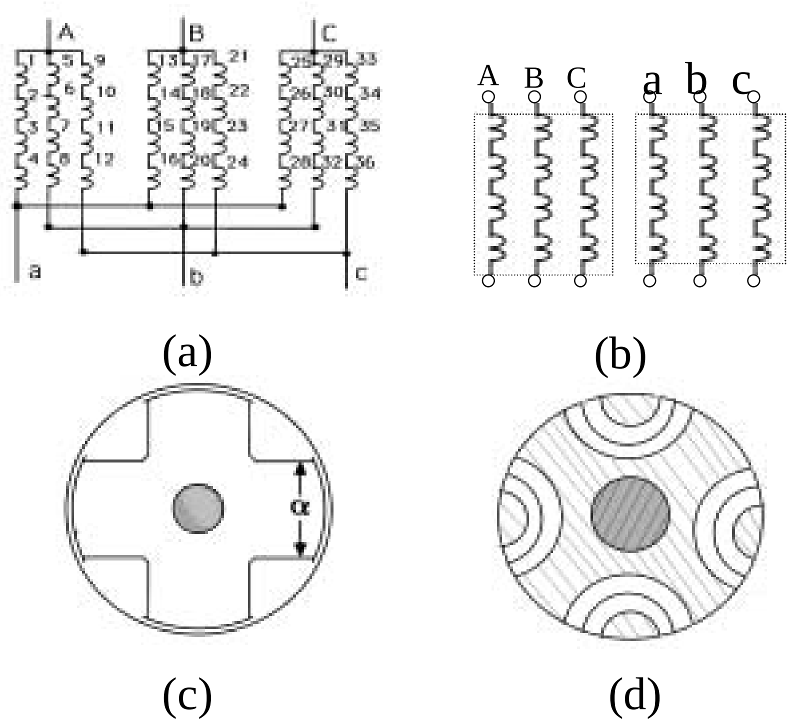

Figure 1.1. Doubly-fed reluctance machines. (a) The same group stator windings, (b) The separate group stator windings, (c) Salient-pole rotor, (d) Axially-laminated rotor.

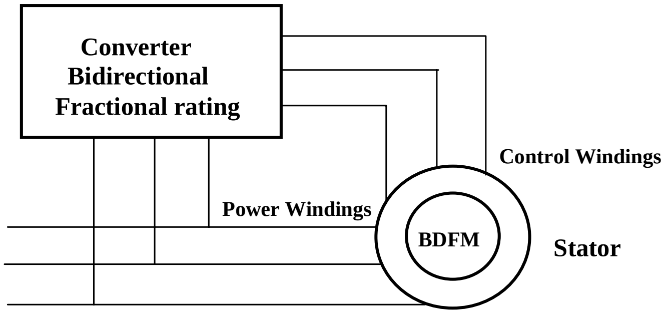

Figure 1.2. Schematic of BDFM ASD.

motor, the so-called self-cascaded induction machine [2] was made by overcoming the structural problems in design. Because the speed of the self-cascaded machine can be controllable without brush-gear by adjustable resistance, some significant industrial use has been found over several years [3]. Broadway and his associates [4-11] had extensively investigated this type of machine two decades ago. The advent of power electronics converters capable of adjustable-frequency, adjustable-voltage, bi-directional power flow has revived interest in the self-cascaded induction machine [12-13]. This interest is promoted by the demonstrated adjustable speed drive (ASD) capability in which one of the stator windings is supplied by a converter of a rating significantly smaller than that of the machine. This configuration, shown schematically in Figure 1.2, is now referred to as a brushless doubly fed machine (BDFM). Its basic adjustable speed principle is based on this equation: $\omega_r = (\omega_1 + \omega_2)/P_r$. Where ω_1 is the angular frequency of the power winding currents, while ω_2 is the angular frequency of the control winding currents. If P_r, rotor pole-pair number, and ω_1 are fixed, the rotor speed ω_r will be adjustable by increasing or decreasing the current frequency of the control windings.

1.2 Literature Survey

To explore the potential of brushless doubly-fed machine and improve its design to sufficiently obtain its expected advantages, intensive investigations have been undertaken. The research can be divided into four areas:

(a) The development of dynamic and steady state models for performance evaluation and design of doubly-fed machines [15-26].

(b) The investigation of doubly-fed machine as a motor in adjustable speed drives systems (ASD) [27-32].

(c) The investigation of doubly-fed machine as a generator in variable speed, constant-frequency powers generation and in stand-alone application [33-41].

(d) The design and analysis of the rotor structure of brushless doubly-fed machines with cage-rotor and reluctance rotor [42-45].

1.2.1 Modeling and Analysis of Doubly-Fed Reluctance Machines

An accurate model is very important for design and application engineers. The model can be used to investigate the performance of machines and show the effects of certain trends in machine design. The simulation, by using an accurate model, will provide adequate representation of full performance for control and stability. Recent research has developed a few models of brushless doubly-fed machine with cage and reluctance rotors.

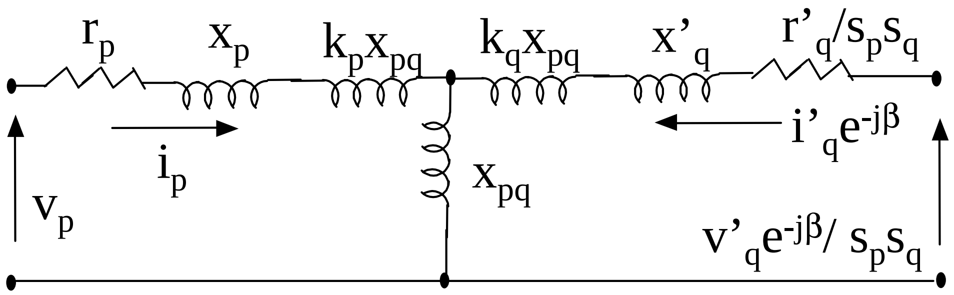

Figure 1.3. Steady-state equivalent circuit.

In early research [4,8-11], a steady state equivalent circuit is given to predict machine's performance in the synchronous mode of operation and to investigate the characteristics of the drive system in steady state conditions. The steady-state equivalent circuit was shown in Figure 1.3 [5].

This circuit is similar to that of a conventional induction machine, except for the extra series impedance $K_p X_{pq}$ and $K_q X_{pd}$ in the primary and secondary circuits, respectively. The constants K_p and K_q are dependent on the magnetic properties of the rotor. S_q and S_d are slip values of primary and secondary windings. X_{pq} is a referred value of mutual reactance between the 2p-pole and 2q-pole component windings. β is the relative displacement between the 2q-pole component winding and the rotor at a zero instant in time. X_p and X_q represent the self-reactances of 2p-pole and 2q-pole component windings. V_p, V_q, i_p, and i_q are the voltages and currents of the 2p-pole and 2q-pole component windings.

To investigate the characteristics of doubly-fed machines based on the steady state model, a common feature of all the above analytical work is the assumption that the machine is equivalent to two magnetically separate wound rotor motors, and different pole numbers of the rotors which are connected electrically and mounted on a common shaft. Although this approach is appropriate for conceptual understanding, it is not adequate for detailed machine and drive system design.

Recently, a detailed, dynamic model has appeared in the literature [19]. This model was developed for the brushless doubly-fed induction machine with the cage-rotor. To reduce the complexity of the detailed model so that it is suitable for BDFM drive system dynamic studies, the two-axis model [20] was developed from the detailed model. It only considers the fundamental mutual inductance and transforms the equations to a two-axis rotor reference frame. The two-axis model and the detailed model have been successfully used to predict the effects of certain trend in machine design [17,18] and to develop closed speed control systems [21]. However, these models do not include the expressions of the machine parameters so that the application of the models to predict different running modes and configurations were limited.

The two-axis model equivalent circuit of brushless doubly-fed machine with cage-rotor was shown in Figure 1.4[20] where V_{q6}, V_{d6}, i_{q6}, and i_{d6} represent 6-pole stator winding q-d voltages and currents, while V_{q2}, V_{d2}, i_{q2}, and i_{d2} represent 2-pole stator winding q-d voltages and currents. V_{qr}, V_{dr}, i_{qr}, and i_{dr} are rotor winding q-d voltages and currents. The q-d flux linkages of stator windings with 6-pole and 2-pole are $\lambda_{q6,}$ $\lambda_{d6,}$ λ_{q2}, and λ_{d2}. L_{m6}, L_{m2}, and L_{rm} represent the magnetizing inductances of stator windings (6-pole, 2-pole) and rotor winding, respectively. L_{l6} and L_{l2} are the leakage inductances of 6-pole and 2-pole stator windings. L_{lr} is leakage inductance of rotor winding. M_6 and M_2 are mutual inductances between stator windings (6-pole, 2-pole) and rotor winding. r_6, $r_{2,}$ and r_r represent the resistances of stator windings and rotor winding.

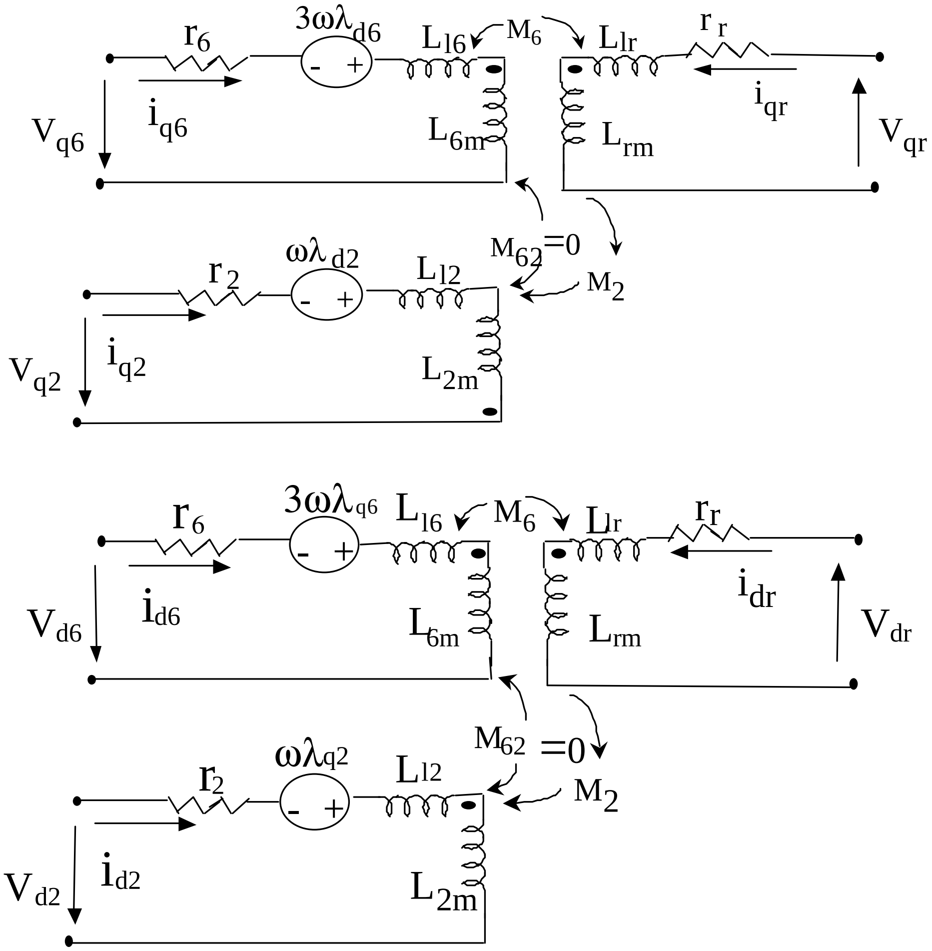

Figure 1.4. Two-axis dynamic model for the cage rotor machine.

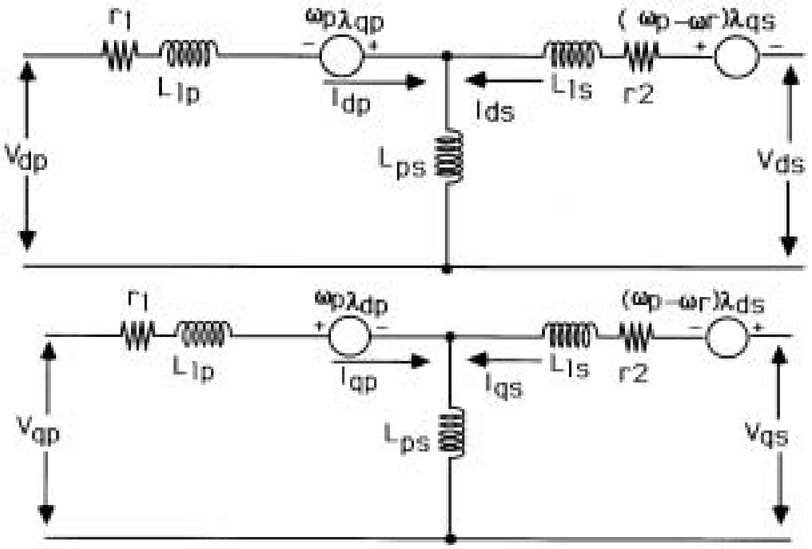

Figure 1.5. Q-d equivalent circuit of salient rotor machine.

Recent work has led to more progress. One has presented rigorous analytical model [22, 23] based on generalized harmonic theory [46]; another [24] described a time-stepping finite-element model, which can readily represent the effect of saturation in cage-rotor machine.

For the brushless doubly-fed reluctance machine having either salient or axially laminated rotor structure, a transient model is presented in [25, 26]. It is developed from the concept of winding functions and the principles of d-q arbitrary reference frame transformation.

The q-d equivalent circuit of this machine is shown in Figure 1.5[26]. This model ignores the influence of magnetic saturation and core loss, which are dominant in the operation of doubly-fed reluctance machines.

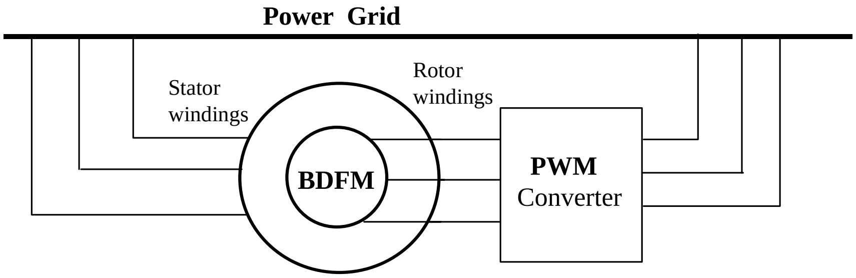

Figure 1.6. Conventional slip power recovery system.

1.2.2 The Application of Brushless Doubly-Fed Machines as Motors and Generators

The conventional slip power recovery system employing wound-field induction machines (shown in Figure 1.6), has reduced the required converter rating, but high cost and bulky size of wound-field induction machines and the maintenance required for the slip-rings, have unfortunately limited their applications.

To avoid the disadvantages of the system, slip power recovery system with brushless reluctance machine has drawn much attention recently. It has the same advantage of substantially reducing the inverter power rating. Furthermore, since brushless doubly-fed reluctance machines have both field and armature windings on the stator and reluctance rotor does not carry currents, brushes and rotor copper loss are completely eliminated. Therefore the system has a simpler and more reliable structure, less maintenance cost and higher efficiency than the conventional system. Besides, recent research have explored the potential of applying the brushless doubly-fed machine to variable speed generating systems, such as wind power generation.

In papers [28-31], the concept and implementation of field orientation control of brushless doubly-fed reluctance machine for variable speed drive and generating system are presented. The stator flux orientation is employed to achieve decoupled control of torque and active/reactive power through the secondary currents, so variable speed drive and generator operation with decoupled active/reactive power control can be achieved.

To apply this system to restricted applications where accessibility to the rotor shaft is prohibited, the literature [30] presents a sensorless control scheme. It will further enhance the reliability and reduce the cost of the drive.

1.3 Research Motivation

The brushless doubly fed reluctance machine with simple saliency on the rotor is considered. It appears to be highly attractive due to its structural simplicity, high efficiency, lower manufacturing cost, and compatibility with existent production line [14].

Some expected advantages of ASD or VSG system with this machine are listed below:

(1) Its ability to operate in induction and synchronous machine modes with the possibility of sub- and super-synchronous speeds operations.

(2) With a rotor structure optimized for minimum core loss, a double-fed reluctance machine may have better efficiency than an induction machine of the same rating.

(3) Controllable power-factor and low harmonic distortion of the utility supply.

(4) Robust machine construction.

(5) Operation as an induction motor in the event of converter failure.

Literature survey yields some important information of this machine:

(a) In recent years various efforts have been made to establish proper dynamic model and explore the design variations of the doubly-fed brushless machine with both cage-rotor and reluctance rotor. When the voltage, applied to one or both stator windings, is increased, the machine will naturally saturate. The performance analysis is less accurate if the model neglects the effects of iron loss and saturation. To solve this problem, a model [24] considering the effect of saturation has been presented for the application of the cage-rotor structure. The reluctance machine with saliency rotor has more iron loss and higher saturation than cage-rotor machine, so it is necessary to develop a model including the effect of iron loss and saturation. At present, the dynamic model developed for saliency rotor machine ignores these effects. Hence we need to look for a new model whose equations consider the general case which includes the influence of sequences of the stator windings and the saturation of the air-gap flux linkage on self and mutual inductance. We hope that this generalization can provide a more accurate insight into the machine design and performance analysis.

(b) While a lot of work is being done on the analysis and control of doubly-fed reluctance machines used in adjustable-speed drive application, relatively little attention has been paid to their use as stand-alone generators. The idea of using doubly-fed reluctance machines as generators was inspired by the fact that these machines can run at high speeds where the efficiencies of prime-movers (turbines) are relatively high. Also, since the reluctance generator is run with a prime mover, there is no need for special starting arrangement. These advantages look very attractive for some applications such as aeroplane power systems, marine generators for gas-turbine drives and electrical vehicle generator systems. Hence, it is significant to explore the potential of this machine as stand alone generator and use it to develop new DC power generation schemes.

One important characteristic of doubly-fed reluctance machine is its capability of operating in synchronous mode with one set of stator windings connected to a DC source. Little attention has been paid to its synchronous drive performance. The field orientation control strategy is now used in induction motors for achieving precise and fast dynamic speed and/or torque responses. Doubly-fed reluctance machine has been shown to be effective in variable-speed drive and generating system with the two sets of windings connected to AC sources. We hope the field orientation control of the doubly-fed reluctance machine in the synchronous mode can also achieve the same performance level as the induction machine.

The motivation for this work was inspired from the above discussion. With the use of PWM converter and digital signal processor, we hope that the proposed research will promote the doubly-fed reluctance machines to find more applications in industry, military and power system due to its low cost, high reliability and flexible control methods.

CHAPTER 2

PROPOSED RESEARCH

The research work will include these topics:

1. Modeling of a doubly-fed reluctance machine

This topic will deal with the modeling and analysis of the doubly-fed reluctance machines with simple salient or laminated rotor structure having $2P_r$ poles and two stator windings with pole numbers given as $2p_1$ and $2q$, respectively.

An experiment machine, supplied by the Advanced Motor Development Center of Emerson Motor Co. will be used for this research. Its stator winding arrangement and rotor structure are shown in Figure 1.1(a) and (c). The stator windings are distributed in 36 slots. When viewed from one set of terminals (a, b, c), it is a 6-pole winding construction and a two pole, three-phase winding construction from the other set of terminals (A, B, C).

The concept of the q-d harmonic balance is used to determine voltage equations. The electromagnetic torque and the contributions of the control and power windings to the mechanical output power is determined using the Manley-Rowe power-frequency relationships. The influence of the sequences of stator currents and machine windings are included in the analysis permitting the elucidation of the different possible modes of operations. The resulting model includes saturation effects and core losses, which is shown in Figure 2.1. In this equivalent circuit, R_{cp} and R_{cs} represent the core loss resistances of power windings and control windings, respectively. The inductance parameter, L_p, L_s, and L_m change with the air-gap flux linkage. Based on this model, the parameters of the experimental machine will be measured.

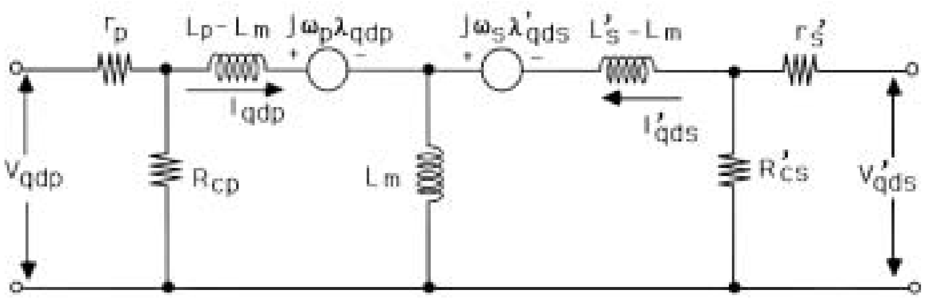

Figure 2.1. Q-d complex equivalent circuit of doubly fed reluctance machine.

To validate the modeling approach, the results of steady-state calculation and dynamic simulation will be compared with the experimental results from this machine.

2. The performance characteristics of a doubly-fed self-excited reluctance generator

Proposed self-excited generators are shown in Figure 2.2. A three phase capacitor banks will be connected to 6-pole winding, called control winding, and the load (impedance or rectifier) are connected to 2-pole winding, called power winding. A q-d equivalent circuit model accounting for saturation of the magnetic paths and saturation-dependent core and harmonic loss resistance will be used to predict experimental results. The experimental measurement and computer simulation will show the steady state and dynamic performance characteristics of this generator system.

3. Synchronous operation of a doubly-fed reluctance generator

Proposed synchronous generator system is shown in Figure 1.3. For this generator system, control winding (6-pole) will be fed with direct current source, while the power winding (2-pole) will be connected with impedance load and rectifier load.

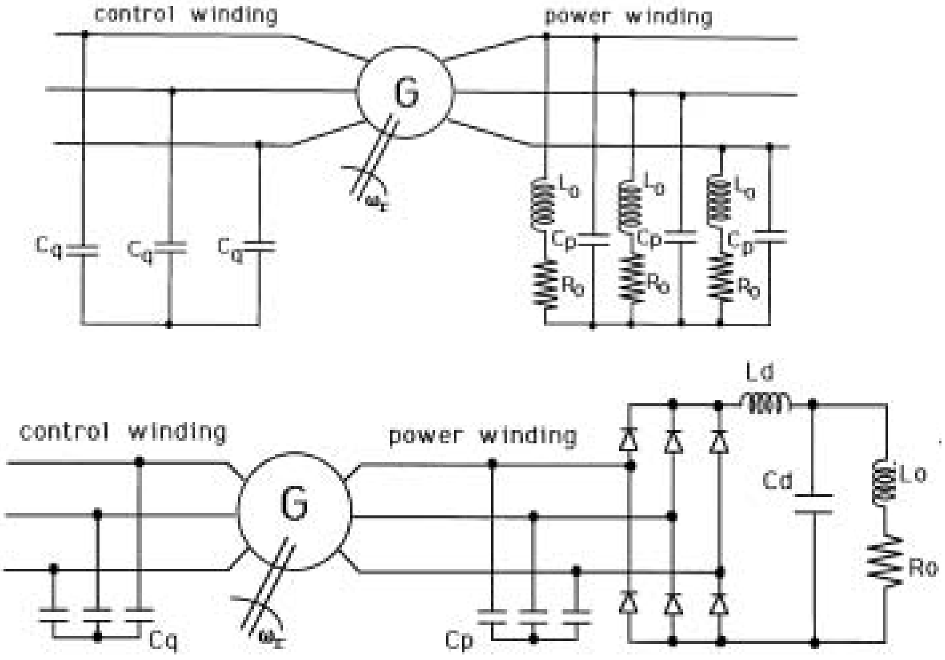

Figure 2.2. Self-excited doubly-fed reluctance generator systems**.**

Saturation effects, core, and harmonic losses will be included in the dynamic and steady state models of generator system. Its performance characteristics will be investigated by experimental measurement and computer simulation.

The operation performance of the doubly-fed synchronous reluctance generator as a controllable power source for DC loads will be investigated. System schematic diagram of feeding an impedance load and feeding a battery was shown in Figure 2.3. The system consists of a doubly fed reluctance machine, a DC-DC buck converter, a three-phase rectifier and a three-phase capacitor bank. Figure 2.3(a) shows the generator run by a source of mechanical power and feeding an impedance load, where a battery is used as

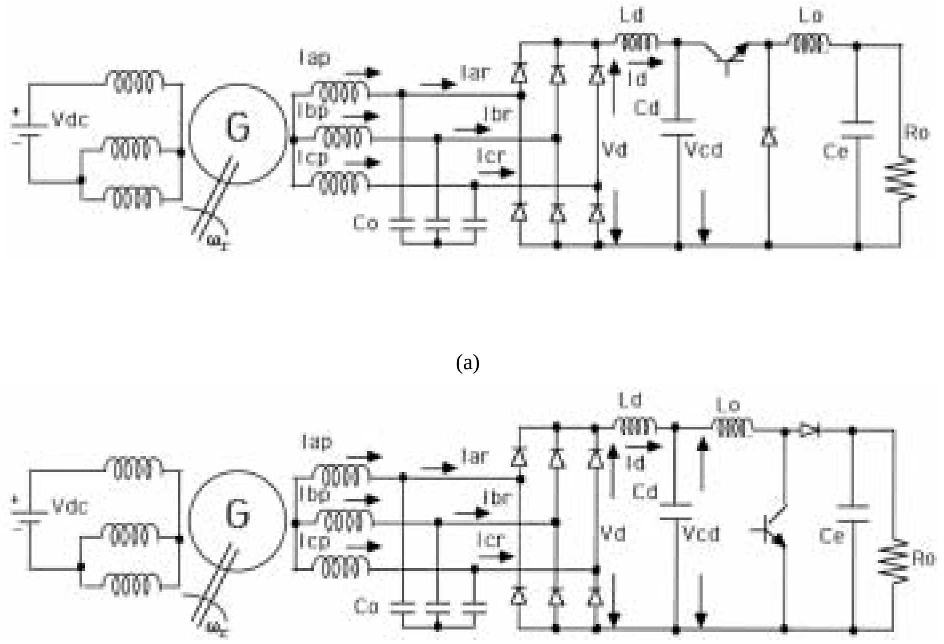

(a)

(b)

Figure 2.3. Doubly-fed reluctant synchronous generator systems. (a) With DC-DC buck converter,(b) with boost converter.

starting source. The generator scheme for battery charging is shown in Figure 2.3(b). The power winding will deliver the dc power to the load, with the control windings acting as the vehicle for excitation. The excitation process will be established by connecting the generated dc voltage to the machine's control windings through the buck converter. This generator scheme is envisaged for stand-alone applications requiring regulated dc voltage or current and in charging battery in electrical automotive applications. The dynamic and steady state models of generator topologies will be set forth and used to calculate steady state performance characteristics. Its performance characteristics including steady-state

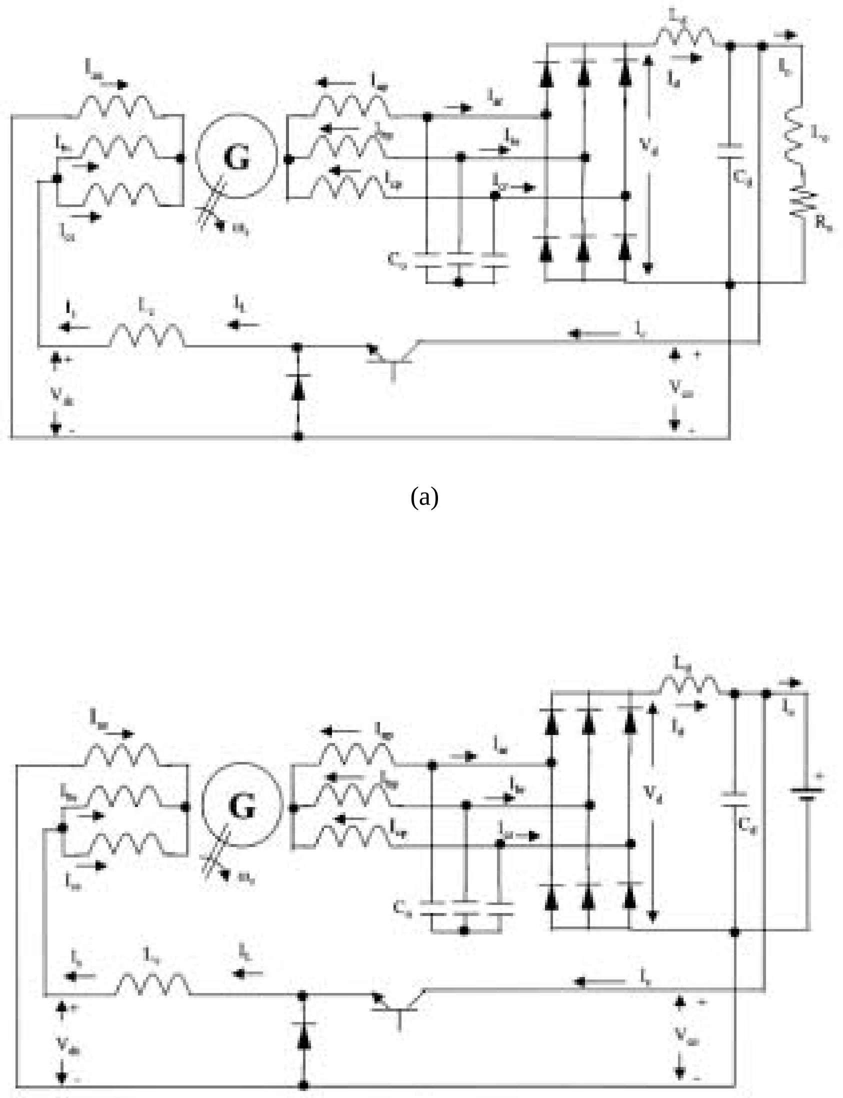

(a)

(b)

Figure 2.4. Regulated DC power generation systems using doubly-fed synchronous reluctant machine. (a) Feeding an impedance, (b) feeding battery.

and dynamic will be shown through the computer simulation and experimental measurement.

4. Field orientation control of a doubly-fed reluctance machine in the synchronous mode

The dynamic equations of the doubly-fed synchronous reluctance machine in the rotor reference frame are:

$$V_{qp} = r_p I_{qp} + p \lambda_{qp} + \omega_r \lambda_{dp} \tag{2.1}$$

$$V_{dp} = r_p I_{dp} + p \lambda_{dp} - \omega_r \lambda_{qp} \tag{2.2}$$

$$V_{qs} = r_s I_{qs} + p \lambda_{qs} \tag{2.3}$$

$$V_{ds} = r_s I_{ds} + p \lambda_{ds} \tag{2.4}$$

$$T_e = 1.5 (p_1 + q) L_m [I_{dp} I_{qs} - I_{qp} I_{ds}] \tag{2.5}$$

where voltage equations of power winding and control winding are (2.1) to (2.4), and torque equation is (2.5). I_{qs} and I_{ds} are the q-d control winding currents while I_{qp} and I_{dp} are q-d power winding current. L_m is mutual inductance. By connecting the control winding to a DC current source I_s, the following equations are obtained:

$$V_{qs} = (2/3)V_{dc}, \quad V_{ds} = 0$$

$$I_{qs} = I_s , \quad I_{ds} = 0 \quad .$$

Because of $I_{ds} = 0$, torque equation can be expressed as

$$T_e = 1.5 (p_1 + q) L_m I_{dp} I_{qs}. \quad .$$

The air-gap flux is regulated using I_{qs} while I_{dp} controls the instantaneous torque of doubly-fed synchronous reluctance motor.

The field orientation principle defines conditions, which has been yielded from the derivation above, for decoupling the field control from the torque control. A field-oriented doubly-fed synchronous reluctance machine will emulate a separately-excited dc motor. To investigate the performance of this machine running in a wide speed range, constant torque will be hold below the base speed while the field-weakening operation conditions must be used to achieve constant power output above the base speed.

Below the base speed, the voltages of the primary winding rise linearly with speed, I_{qs} will be kept constant to maintain the constant magnetizing flux while I_{dp} will be used to control the instantaneous torque with setting $I_{qp} = 0$.

Above the base speed, the voltages of power winding are kept at rated value while the control winding current, I_{qs}, is equal to rated value. To maintain the constant output power and maximize the output torque, I_{qp} and I_{dp} need to be regulated at the same time. This is called constant-power, field-weakening operation.

Figure 2.5 shows the block diagram of two control systems. The space vector pulse width modulation (SV-PWM) technique and hysterestic current control technique will be used to control voltage source inverter, which will provide an adjustable frequency voltage source for the power windings. The control windings will be supplied by a DC current source. In control scheme I, a novel nonlinear controller is used and its principle as well as design procedure will be described. IP controller with no-overshoot performance is used in control scheme II, its design procedure will also be given. Its steady state characteristics will be calculated and dynamic performance will be demonstrated using computer simulation program.

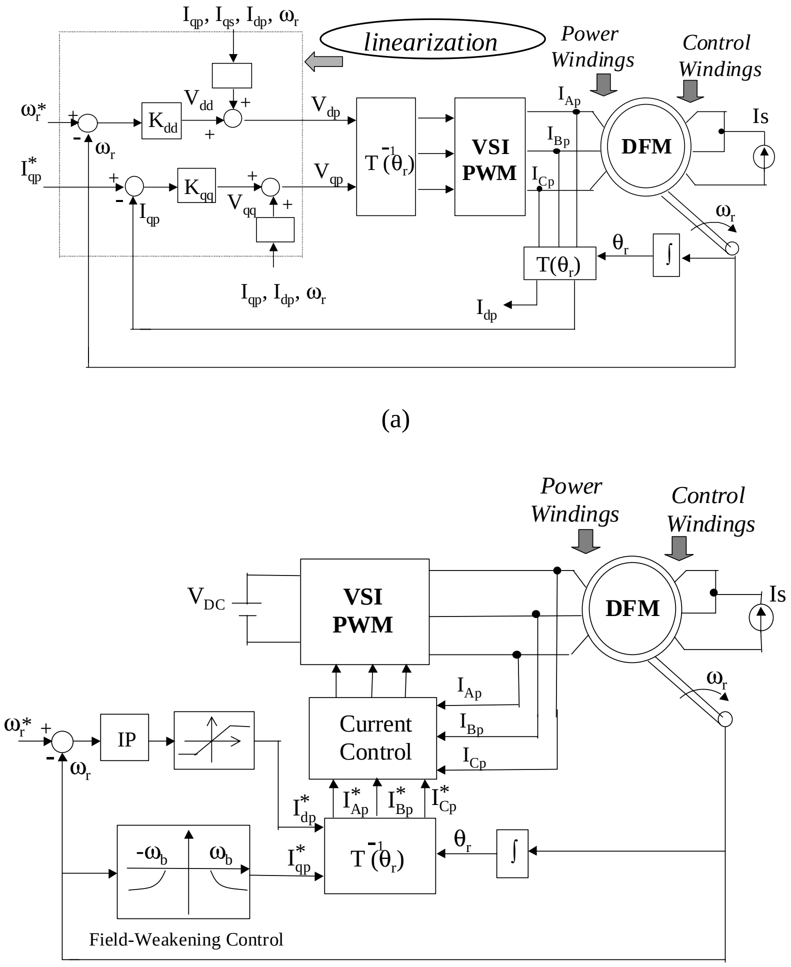

(a)

(b)

Figure 2.5. Field orientation control systems for a doubly-fed synchronous reluctance machine. (a) Control scheme I, (b) control scheme II.

The research work will make contribution in these areas:

(1) A dynamic model of doubly-fed reluctance machine considering the effects of core loss and saturation will be presented. It will provide a more accurate model for the performance evaluation and the design of doubly fed reluctance machine.

(2) The performance characteristics of doubly-fed self-excited reluctance generator and doubly-fed synchronous reluctance generator will be investigated and analysis methods will be presented. An innovative DC power generator scheme using doubly fed reluctance machine with salient rotor structure will be investigated. It has potential for use in stand-alone applications and in electric automobiles.

(3) Two field orientation control schemes for a doubly-fed synchronous reluctance machine will be investigated for high-performance operation both in the constant torque and constant power region. The simulation results will supply valuable information for realization and application of the control systems.

CHAPTER 3
MODELING OF A DOUBLY-FED RELUCTANCE MACHINE

3.1 Introduction

This chapter mainly deals with the modeling and analysis of the doubly-fed reluctance machine. First, the concept of winding functions is used to derive the machine inductances. The influence of the sequences of stator currents and machine windings are included in the analysis permitting the elucidation of the different possible modes of operations. Conditions for the development of average electromagnetic torque are developed which also give insight into the machine design criteria. The electromagnetic torque and the contributions of the control and power windings to the mechanical output power are determined using the Manley-Rowe power-frequency relationships. The resulting model, including saturation effects and core losses, is used to unveil the inherent oscillatory instability of the machine and to predict the steady-state performance and dynamic characteristics for its motor or generator systems in the following chapters.

3.2 Stator and Rotor Structure of the Experimental Machine

The model set forth in this chapter applies to doubly-fed reluctance machines with simple salient laminated rotor having 2Pr poles and two stator windings with pole numbers given as $2p_1$ and 2q, respectively. p_1, q, and Pr, respectively, represent the pole-pair number of the power windings, control windings, and rotor. The experimental machine used for this research has stator winding arrangement and rotor structure shown in Figure 3.1. Figure 3.1(a) shows the stator winding connection diagram of the machine distributed in 36 slots which when viewed from one set of terminals (a, b, and c), is a three-phase, 6-pole winding construction. From the other set of terminals (A, B, and C), a non-triplen two-pole, three-phase winding construction is observed. For any three-phase balance ac power supply, these two symmetrical sets of three-phase windings are electrically independent of each other.

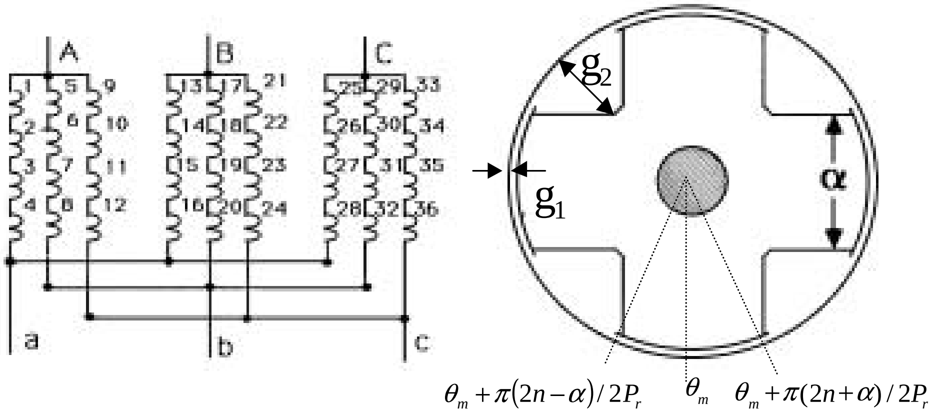

(a)

(b)

Figure 3.1. Stator and rotor structure of the experimental machine.

(a) Stator windings.

(b) Rotor structure.

3.3 Machine Model

In the analysis that follows, classical assumptions are made in order to obtain closed-form equations for machine inductances. The permeabilities of the stator and rotor iron parts are assumed to be infinite; the stator winding distributions are approximated by their fundamental components; and the air-gap length is assumed to take a constant value g_1 over the rotor arc and g_2 elsewhere as shown in Figure 3.1(b). Saturation effects will be included in section 3.7.

The stator windings are supplied with three-phase voltage vectors V_{ABC} and V_{abc}. Since the frequencies of the supply voltages can be positive or negative (positive or negative current sequence), they are defined as $k_3\omega_p$, $k_4\omega_s$, respectively, for the $2p_1$ and 2q windings where K_3 and K_4 are either +1 or -1. The stator voltage differential equations expressed in terms of the phase currents and flux linkages are, therefore, expressed as [27]

$$V_{ABC} = r_p I_{ABC} + p\lambda_{ABC} \tag{3.1}$$

$$V_{abc} = r_s I_{abc} + p\lambda_{abc} \tag{3.2}$$

where

$$\lambda_{ABC} = L_{ABC} I_{ABC} + L_{ABCabc} I_{abc} \tag{3.3}$$

$$\lambda_{abc} = L_{abc} I_{abc} + L_{abcABC} I_{ABC} \tag{3.4}$$

$$V_{ABC}^T = [V_A \, V_B \, V_C] \tag{3.5}$$

$$I_{ABC}^T = [I_A \, I_B \, I_C] \tag{3.6}$$

$$V_{abc}^T = [V_a \, V_b \, V_c] \tag{3.7}$$

$$\mathrm{I}_{\mathrm{abc}}^{\mathrm{T}} = [I_a \; I_b \; I_c] \tag{3.8}$$

$$L_{ABC} = \begin{bmatrix} L_{AA} & L_{AB} & L_{AC} \\ L_{BA} & L_{BB} & L_{BC} \\ L_{CA} & L_{CB} & L_{CC} \end{bmatrix} \tag{3.9}$$

$$L_{abc} = \begin{bmatrix} L_{aa} & L_{ab} & L_{ac} \\ L_{ba} & L_{bb} & L_{bc} \\ L_{ca} & L_{cb} & L_{cc} \end{bmatrix} \tag{3.10}$$

$$\mathrm{L}_{\mathrm{ABCabc}} = L_{abcABC}^{T} = \begin{bmatrix} L_{Aa} & L_{Ab} & L_{Ac} \\ L_{Ba} & L_{Bb} & L_{Bc} \\ L_{Ca} & L_{Cb} & L_{Cc} \end{bmatrix}. \tag{3.11}$$

The per-phase resistances of the stator windings are r_p and r_s, respectively, and the derivative d/dt is given as *p*. The phase voltages, currents, and flux linkages of each set of three-phase stator windings are transformed to their respective q-d-n synchronous reference frame equations using the matrix transformation $T(\theta_p)$ and $T(\theta_s)$, which are defined as follows:

$$V_{qdnp} = T(\theta_p)V_{ABC} \tag{3.12}$$

$$V_{qdns} = T(\theta_s)V_{abc} \tag{3.13}$$

$$I_{qdnp} = T(\theta_p)I_{ABC} \tag{3.14}$$

$$I_{qdns} = T(\theta_s)I_{abc} \tag{3.15}$$

$$\lambda_{qdnp} = T(\theta_p)\lambda_{ABC} \tag{3.16}$$

$$\lambda_{qdns} = T(\theta_s)\lambda_{abc} \tag{3.17}$$

and

$$T(\theta_p) = \frac{2}{3}\begin{bmatrix} \cos\theta_p & \cos(\theta_p - \frac{2\pi}{3}) & \cos(\theta_p + \frac{2\pi}{3}) \\ \sin\theta_p & \sin(\theta_p - \frac{2\pi}{3}) & \sin(\theta_p + \frac{2\pi}{3}) \\ \frac{1}{2} & \frac{1}{2} & \frac{1}{2} \end{bmatrix} \tag{3.18}$$

$$\theta_p = \int K_3\omega_p dt + \theta_{po} \tag{3.19}$$

$$T(\theta_s) = \frac{2}{3}\begin{bmatrix} \cos\theta_s & \cos(\theta_s - \frac{2\pi}{3}) & \cos(\theta_s + \frac{2\pi}{3}) \\ \sin\theta_s & \sin(\theta_s - \frac{2\pi}{3}) & \sin(\theta_s + \frac{2\pi}{3}) \\ \frac{1}{2} & \frac{1}{2} & \frac{1}{2} \end{bmatrix} \tag{3.20}$$

$$\theta_s = \int K_4\omega_s dt + \theta_{so} \tag{3.21}$$

where θ_{po} and θ_{so} are initial angles of the synchronous reference frames. Substituting Equations (3.18-3.21) into Equations (3.12-3.17), the resulting q-d-n voltage and flux linkage equations are given as

$$V_{qdnp} = r_p I_{qdnp} + p\lambda_{qdnp} + K_3\,\varpi_p\lambda_{qdnp} \tag{3.22}$$

$$V_{qdns} = r_p I_{qdns} + p\lambda_{qdns} + K_4\,\varpi_s\lambda_{qdns} \tag{3.23}$$

$$\lambda_{qdnp} = L_{pp} I_{qdnp} + L_{ps} I_{qdns} \tag{3.24}$$

$$\lambda_{qdns} = L_{ss} I_{qdn} + L_{sp} I_{qdnp} \tag{3.25}$$

where

$$\varpi_p = \omega_p\begin{bmatrix} 0 & 1 & 0 \\ -1 & 0 & 0 \\ 0 & 0 & 0 \end{bmatrix}, \quad \varpi_s = \omega_s\begin{bmatrix} 0 & 1 & 0 \\ -1 & 0 & 0 \\ 0 & 0 & 0 \end{bmatrix} \tag{3.26}$$

$$L_{pp} = T(\theta_p)L_{ABC}T(\theta_p)^{-1} = \begin{bmatrix} L_{qqp} & L_{qdp} & L_{qnp} \\ L_{dqp} & L_{ddp} & L_{dnp} \\ L_{nqp} & L_{ndp} & L_{nnp} \end{bmatrix} \tag{3.27}$$

$$L_{sp} = L_{ps}^{T} = T(\theta_p)L_{ABCabc}T(\theta_s)^{-1} = \begin{bmatrix} L_{mqq} & L_{mqd} & L_{mqn} \\ L_{mdq} & L_{mdd} & L_{mdn} \\ L_{mnq} & L_{mnd} & L_{mnn} \end{bmatrix} \tag{3.28}$$

$$L_{ss} = T(\theta_s)L_{abc}T(\theta_s)^{-1} = \begin{bmatrix} L_{qqs} & L_{qds} & L_{qns} \\ L_{dqs} & L_{dds} & L_{dns} \\ L_{nqs} & L_{nds} & L_{nns} \end{bmatrix} \ . \tag{3.29}$$

3.4 Calculation of Inductance Using Winding Function Theory

The q-d-n machine inductance matrices L_{pp}, L_{sp} and L_{ss} are calculated using the winding function approach [48,49]. According to this method, the mutual inductance between and winding "i" and "j" in any machine (mean airgap radius is constant) is calculated by

$$L_{ij} = \mu_0 rl \int_0^{2\pi} g^{-1}(\phi,\theta_{rm})N_j(\phi,\theta_j)N_i(\phi,\theta_i)d\phi \ .$$

The average air-gap radius is r, motor stack length is l, and the inverse gap-length is represented by $g^{-1}(\phi,\theta_{rm})$. The angle, ϕ, defines the angular position along the stator inner diameter while the angular position of the rotor with respect to the stator reference is θ_{rm}. The winding functions of winding "i" and "j" are given, respectively, as $N_i(\phi, \theta_{rm})$ and $N_j(\phi, \theta_{rm})$. The term $N_i(\phi, \theta_{rm})$ or $N_j(\phi, \theta_{rm})$ is called the winding function and represents, in effect, the MMF distribution along the air-gap for an unit current in winding "i" or "j". If this winding is located on the stator, the winding is only a function of the stator peripheral angle ϕ while if the winding is located on the rotor the winding must be expressed as a function of both ϕ and the mechanical position of the rotor θ_{rm}.

Winding functions representing the six and two pole windings are drawn in Figures 3.2 and 3.3, respectively. Although the winding functions for the mixed-pole machine have substantial space harmonic contents as shown in [14,50], they are represented here by their fundamental components since only these components, as shown in Figure 3.4, have the greatest effect on energy conversion.

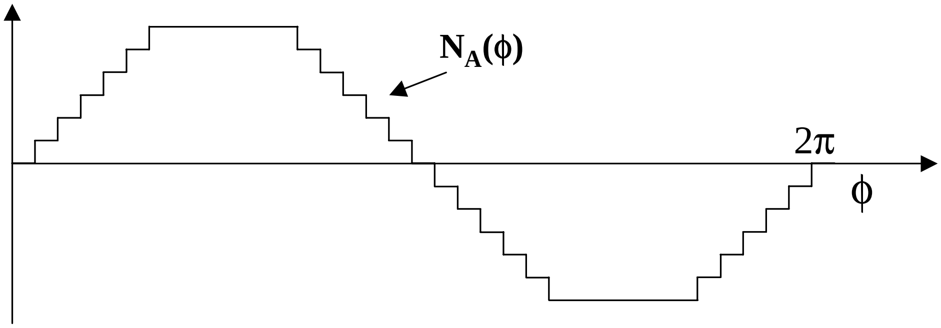

Figure 3.2. Winding function for 6-pole phase A.

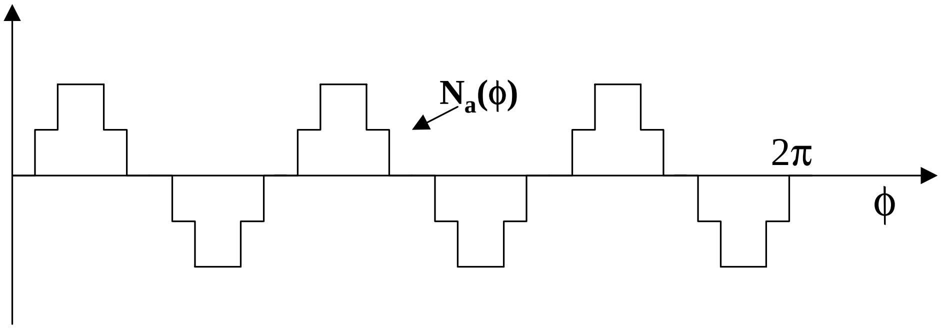

Figure 3.3. Winding function for 2-pole phase a.

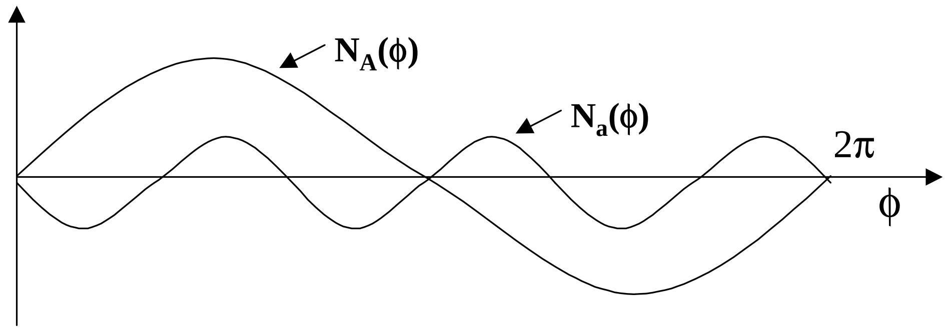

Figure 3.4. Fundamental components of the winding functions.

These components of the phase windings accounting for the winding sequences are expressed as

$$N_A = N_p \cos(p(\phi - \phi_p)) \tag{3.30}$$

$$N_B = N_p \cos(p(\phi - \phi_p) - K_1 \frac{2\pi}{3}) \tag{3.31}$$

$$N_C = N_p \cos(p(\phi - \phi_p) + K_1 \frac{2\pi}{3}) \tag{3.32}$$

$$N_a = N_s \cos(q(\phi - \phi_q)) \tag{3.33}$$

$$N_b = N_s \cos(q(\phi - \phi_q) - K_2 \frac{2\pi}{3}) \tag{3.34}$$

$$N_c = N_s \cos(q(\phi - \phi_q) + K_2 \frac{2\pi}{3}) \ . \tag{3.35}$$

By using the synchronous reference frame $T(\theta_p)$, the q-d components of phase winding function N_A, N_B and N_C are expressed as

$$N_{qp} = N_p \cos(p(\phi - K_1 \phi_p)) \tag{3.36}$$

$$N_{dp} = N_p \sin(p(\phi - K_1 \phi_p)) \ . \tag{3.37}$$

By using the synchronous reference frame $T(\theta_s)$, the q-d components of phase winding function N_a, N_b and N_c are expressed as

$$N_{qs} = N_s \cos(q(\phi - K_2\phi_q)) \tag{3.38}$$

$$N_{ds} = N_s \sin(q(\phi - K_2\phi_q)) \ . \tag{3.39}$$

K_1 and K_2, the signs of the winding sequence, as well as N_p and N_s are defined as

$$K_1, K_2 = \begin{cases} -1 & \text{clockwise} \\ 1 & \text{counterclockwise} \end{cases} \tag{3.40}$$

$$N_p = \frac{4}{C_p \pi p} N_1 K_{\omega p}, \quad N_s = \frac{4}{C_q \pi q} N_2 K_{\omega q} \ . \tag{3.41}$$

In Equation (3.41), N_1 and N_2 are the numbers of series connected turns per-phase of C_p and C_q circuits for the power and control windings, respectively. The fundamental winding distribution factors are defined as $K_{\omega p}$ and $K_{\omega q}$, respectively. The initial angular displacements between the fundamental components of the winding functions and the stator reference are ϕ_p and ϕ_q.

The air-gap function from Figure 3.1(b) is expressed as

$$g(\phi, \theta_m) = \begin{cases} g_1 & \theta_{\mathrm{rm}} + \frac{\pi}{2P_r}(2n - \alpha) \le \phi \le \theta_{\mathrm{rm}} + \frac{\pi}{2P_r}(2n + \alpha) \\ g_2 & \theta_{\mathrm{rm}} + \frac{\pi}{2P_r}(2n + \alpha) \le \phi \le \theta_{\mathrm{rm}} + \frac{\pi}{2P_r}(2n + 2 - \alpha) \end{cases} \tag{3.42}$$

where n = 0, 1, 2, 3, 4...$2P_r$-1 and the rotor pole pitch is α. With Equations (3.30-3.42) substituted in Equations (3.27-3.29), expressions for inductances comprising L_{pp}, L_{ss}, and L_{ps} are obtained. They are expressed as

$$L_{qqp} = \left(\frac{3}{2}\right) \mu_0 r \ell \int_0^{2\pi} g^{-1}(\phi, \theta_{rm}) \, N_{qp}^2 \, d\phi \tag{3.43}$$

$$L_{ddp} = \left(\frac{3}{2}\right)\mu_0 r\ell \int_0^{2\pi} g^{-1}(\phi, \theta_{rm})\, N_{dp}^2 \, d\phi \tag{3.44}$$

$$L_{qdp} = L_{dqp} = \left(\frac{3}{2}\right)\mu_0 r\ell \int_0^{2\pi} g^{-1}(\phi, \theta_{rm})\, N_{qp} N_{dp} \, d\phi \tag{3.45}$$

$$L_{qnp} = L_{nqp} = L_{dnp} = L_{ndp} = L_{nnp} = 0 \tag{3.46}$$

$$L_{qqs} = \left(\frac{3}{2}\right)\mu_0 r\ell \int_0^{2\pi} g^{-1}(\phi, \theta_{rm})\, N_{qs}^2 \, d\phi \tag{3.47}$$

$$L_{dds} = \left(\frac{3}{2}\right)\mu_0 rl \int_0^{2\pi} g^{-1}(\phi, \theta_{rm})\, N_{ds}^2 \, d\phi \tag{3.48}$$

$$L_{qds} = L_{dqs} = \left(\frac{3}{2}\right)\mu_0 r\ell \int_0^{2\pi} g^{-1}(\phi, \theta_{rm})\, N_{qs} N_{ds} \, d\phi \tag{3.49}$$

$$L_{qns} = L_{nqs} = L_{dns} = L_{nds} = L_{nns} = 0 \tag{3.50}$$

$$L_{qqm} = \left(\frac{3}{2}\right)\mu_0 r\ell \int_0^{2\pi} g^{-1}(\phi, \theta_{rm})\, N_{qp} N_{qs} \, d\phi \tag{3.51}$$

$$L_{ddm} = \left(\frac{3}{2}\right)\mu_0 r\ell \int_0^{2\pi} g^{-1}(\phi, \theta_{rm})\, N_{dp} N_{ds} \, d\phi \tag{3.52}$$

$$L_{qdm} = \left(\frac{3}{2}\right)\mu_0 r\ell \int_0^{2\pi} g^{-1}(\phi, \theta_{rm})\, N_{qp} N_{ds} \, d\phi \tag{3.53}$$

$$L_{dqm} = \left(\frac{3}{2}\right)\mu_0 r\ell \int_0^{2\pi} g^{-1}(\phi, \theta_{rm})\, N_{dp} N_{qs} \, d\phi \tag{3.54}$$

$$L_{qnm} = L_{nqm} = L_{dnm} = L_{ndm} = L_{nnm} = 0\ . \tag{3.55}$$

The expressions for these inductances are given in Appendix 3A. All inductances of the zero-sequence winding components are zero.

To realize the electric-mechanical energy conversion, the frequency of the speed voltage in a given phase must be the same as the frequency of the current flowing in the same phase. To reduce the pulsating torque, the self-induced voltages must also have the same frequency as those of the currents. By checking q-d component expressions of inductance L_p, L_s, and L_{ps} in Appendix 3A, we can see that all q-d components are equal to constant, if the combination of the pole-pair numbers: p_1, q, and P_r, and the relationship of frequencies among ω_p, ω_s, and ω_{rm} , are satisfied as expressed in Condition I and Condition II. The constant q-d inductance components make sure that the requirements of the electric-mechanical energy conversion and reducing the pulsating torque are satisfied.

Condition I

$$(K_1 p_1 + K_2 q)\omega_{rm} = K_3\omega_p + K_4\omega_s$$

$$\frac{K_1 p_1 + K_2 q}{P_r} = even = 2m, \quad \frac{K_1 p_1 - K_2 q}{P_r} = odd = 2n+1$$

$$\frac{2K_1 p_1}{P_r} = odd = 2k+1, \quad \frac{2K_2 q}{P_r} = odd = 2z+1$$

$$L_{ddp} = L_{qqp} = \frac{3\mu_0 rl}{2} N_p^2 \pi\alpha \left(\frac{1}{g_1} + \frac{1}{g_2}\right)$$

$$L_{qqs} = L_{dds} = \frac{3\mu_0 rl}{2} N_s^2 \pi\alpha \left(\frac{1}{g_1} + \frac{1}{g_2}\right)$$

$$L_{mqq} = -L_{mdd} = \frac{3\mu_0 rl p_r N_s N_p}{(K_1 p_1 + K_2 q)}\left(\frac{1}{g_1} - \frac{1}{g_2}\right)\cdot \sin\left[\frac{(K_1 p_1 - K_2 q)\pi\alpha}{2P_r}\right]$$

Condition II

$$(K_1 p_1 - K_2 q)\omega_{rm} = K_3\omega_p - K_4\omega_s$$

$$\frac{K_1 p_1 + K_2 q}{P_r} = odd = 2n+1, \quad \frac{K_1 p_1 - K_2 q}{P_r} = even = 2m$$

$$\frac{2K_1 p_1}{P_r} = odd = 2k+1, \quad \frac{2K_2 q}{P_r} = odd = 2z+1$$

$$L_{ddp} = L_{qqp} = \frac{3\mu_0 rl}{2} N_p^2 \pi\alpha \left(\frac{1}{g_1} + \frac{1}{g_2} \right)$$

$$L_{qqs} = L_{dds} = \frac{3\mu_0 rl}{2} N_s^2 \pi\alpha \left(\frac{1}{g_1} + \frac{1}{g_2} \right)$$

$$L_{mqq} = L_{mdd} = \frac{3\mu_0 rlP_r N_s N_p}{(K_1 p_1 + K_2 q)} \left(\frac{1}{g_1} - \frac{1}{g_2} \right) \cdot \sin\left[\frac{(K_1 p_1 - K_2 q)\pi\alpha}{2P_r} \right]$$

where m and n are positive or negative integers. Different operating modes are established from Condition I and Condition II for possible values of p_1, q, P_r by considering different combinations of values of K_1, K_2, K_3 and K_4. In general, it is found that the rotor speed is given as

$$(p_1 \pm q)\, \omega_{rm} = \omega_p \pm \omega_s.$$

By substituting the constraint condition, Condition I or Condition II, into the expressions of q-d inductance elements in Appendix 3A, we can prove that all of them are constants.

3.5 Calculation of Electromagnetic Torque

The mechanical equation of motion for the machine is expressed as

$$Jp\theta_{rm} = T_e - T_L \qquad (3.56)$$

where the load torque is T_L, the moment of inertia of the rotor and connected load is J and T_e is the developed electromagnetic torque. The electromagnetic torque is calculated from the magnetic co-energy ω_{co} as

$$T_e = \left[\frac{d\omega_{co}}{d\theta_{rm}}\right] . \tag{3.57}$$

If linearity is assumed (infinite permeability), the co-energy is equal to the stored magnetic energy given as

$$\begin{aligned}\omega_{co} &= \frac{1}{2}[I_{ABC}]^T[L_{ABC}][I_{ABC}] + \frac{1}{2}[I_{abc}]^T[L_{abc}][I_{abc}] \\ &\quad + [I_{ABC}]^T[L_{ABCabc}][I_{abc}] .\end{aligned} \tag{3.58}$$

Equation (3.58) is further expressed in terms of q-d-n quantities using Equations (3.12-3.15) and relationships between q-d inductance elements and a-b-c inductance elements expressed as follows

$$L_{ABC} = \begin{bmatrix} L_{AA} & L_{AB} & L_{AC} \\ L_{BA} & L_{BB} & L_{BC} \\ L_{CA} & L_{CB} & L_{CC} \end{bmatrix} = T(\theta_p)^{-1}\begin{bmatrix} L_{qqp} & L_{qdp} & L_{qnp} \\ L_{dqp} & L_{ddp} & L_{dnp} \\ L_{nqp} & L_{ndp} & L_{nnp} \end{bmatrix} T(\theta_p)$$

$$\mathrm{L}_{\mathrm{ABCabc}} = \begin{bmatrix} \mathrm{L}_{\mathrm{Aa}} & \mathrm{L}_{\mathrm{Ab}} & \mathrm{L}_{\mathrm{Ac}} \\ \mathrm{L}_{\mathrm{Ba}} & \mathrm{L}_{\mathrm{Bb}} & \mathrm{L}_{\mathrm{Bc}} \\ \mathrm{L}_{\mathrm{Ca}} & \mathrm{L}_{\mathrm{Cb}} & \mathrm{L}_{\mathrm{Cc}} \end{bmatrix} = \mathrm{T}(\theta_{\mathrm{p}})^{-1}\begin{bmatrix} \mathrm{L}_{\mathrm{mqq}} & \mathrm{L}_{\mathrm{mqd}} & \mathrm{L}_{\mathrm{mqn}} \\ \mathrm{L}_{\mathrm{mdq}} & \mathrm{L}_{\mathrm{mdd}} & \mathrm{L}_{\mathrm{mdn}} \\ \mathrm{L}_{\mathrm{mnq}} & \mathrm{L}_{\mathrm{mnd}} & \mathrm{L}_{\mathrm{mnn}} \end{bmatrix}\mathrm{T}(\theta_{\mathrm{s}})$$

$$\mathrm{L}_{\mathrm{abc}} = \begin{bmatrix} \mathrm{L}_{\mathrm{aa}} & \mathrm{L}_{\mathrm{ab}} & \mathrm{L}_{\mathrm{ac}} \\ \mathrm{L}_{\mathrm{ba}} & \mathrm{L}_{\mathrm{bb}} & \mathrm{L}_{\mathrm{bc}} \\ \mathrm{L}_{\mathrm{ca}} & \mathrm{L}_{\mathrm{cb}} & \mathrm{L}_{\mathrm{cc}} \end{bmatrix} = \mathrm{T}(\theta_{\mathrm{s}})^{-1}\begin{bmatrix} \mathrm{L}_{\mathrm{qqs}} & \mathrm{L}_{\mathrm{qds}} & \mathrm{L}_{\mathrm{qns}} \\ \mathrm{L}_{\mathrm{dqs}} & \mathrm{L}_{\mathrm{dds}} & \mathrm{L}_{\mathrm{dns}} \\ \mathrm{L}_{\mathrm{nqs}} & \mathrm{L}_{\mathrm{nds}} & \mathrm{L}_{\mathrm{nns}} \end{bmatrix}\mathrm{T}(\theta_{\mathrm{s}}) \ .$$

The developed electromagnetic torque becomes

$$\begin{aligned}T_e &= \frac{1}{2}[I_{qdnp}]^T \frac{d}{d\theta_{rm}}[L_{pp}][I_{qdnp}] + \frac{1}{2}[I_{qdns}]^T \frac{d}{d\theta_{rm}}[L_{ss}][I_{qdns}] \\ &\quad + [I_{qdnp}]^T \frac{d}{d\theta_{rm}}[L_{ps}][I_{qdns}]\end{aligned} \tag{3.59}$$

where

$$\frac{d}{d\theta_{rm}}[L_{pp}] = [L_{pp}]' = \begin{bmatrix} L'_{qqp} & L'_{qdp} & L'_{qnp} \\ L'_{dqp} & L'_{ddp} & L'_{dnp} \\ L'_{nqp} & L'_{ndp} & L'_{nnp} \end{bmatrix}$$

$$\frac{d}{d\theta_{rm}}[L_{ss}] = [L_{ss}]' = \begin{bmatrix} L'_{qqs} & L'_{qds} & L'_{qns} \\ L'_{dqs} & L'_{dds} & L'_{dns} \\ L'_{nqs} & L'_{nds} & L'_{nns} \end{bmatrix}$$

$$\frac{d}{d\theta_{rm}}[L_{ps}] = [L_{ps}]' = \begin{bmatrix} L'_{qqm} & L'_{qdm} & L'_{qnm} \\ L'_{dqm} & L'_{ddm} & L'_{dnm} \\ L'_{nqm} & L'_{ndm} & L'_{nnm} \end{bmatrix} \quad .$$

All the derivative components of inductance [L_{pp}], [L_{ss}], and [L_{ps}] are listed in Appendix 3B.

The torque is time varying in general since the inductances are time varying and $I_{qdns,}$ I_{qdnp} are constant quantities during steady-state operation conditions. By substituting the constraint conditions under Condition I or Condition II into the expressions in the Appendix 3B, the q-d-n components of inductance [L_{pp}]', [L_{ss}]' and [L_{ps}]' can be obtained. The results are

$$\frac{d}{d\theta_{rm}}[L_{pp}] = [L_{pp}]' = [0]$$

$$\frac{d}{d\theta_{rm}}[L_{ss}] = [L_{ss}]' = [0]$$

$$\frac{d}{d\theta_{rm}}[L_{ps}] = [L_{ps}]' = \begin{bmatrix} 0 & L'_{qdm} & 0 \\ L'_{dqm} & 0 & 0 \\ 0 & 0 & 0 \end{bmatrix}$$

where

$$L'_{qdm} = L'_{dqm} = -\frac{2}{3}L_{qqm}(K_1 p_1 + K_2 q) = \frac{2}{3}L_{ddm}(K_1 p_1 + K_2 q) \qquad \text{under Condition I}$$

and

$$L'_{qdm} = -L'_{dqm} = \frac{2}{3}L_{qqm}(K_1 p_1 - K_2 q) = \frac{2}{3}L_{ddm}(K_1 p_1 - K_2 q) \qquad \text{under Condition II .}$$

Under the Condition I or Condition II, Equation (3.59) will become

$$T_e = [I_{qp} \ \ \mathrm{I_{dp}} \ \ 0]\left(\frac{2}{3}\right)\left(\mathrm{K}_1 p_1 + K_2 q\right)\begin{bmatrix} 0 & L_{ddm} & 0 \\ -L_{qqm} & 0 & 0 \\ 0 & 0 & 0 \end{bmatrix}\begin{bmatrix} I_{qs} \\ I_{ds} \\ 0 \end{bmatrix}$$

$$= \left(\frac{2}{3}\right)\left(\mathrm{K}_1 p_1 + K_2 q\right)\left(I_{qp}L_{ddm}I_{ds} - I_{qs}L_{qqm}I_{dp}\right)$$

or

$$T_e = [I_{qp} \ \ \mathrm{I_{dp}} \ \ 0]\left(\frac{2}{3}\right)\left(\mathrm{K}_1 p_1 - K_2 q\right)\begin{bmatrix} 0 & L_{ddm} & 0 \\ -L_{qqm} & 0 & 0 \\ 0 & 0 & 0 \end{bmatrix}\begin{bmatrix} I_{qs} \\ I_{ds} \\ 0 \end{bmatrix}$$

$$= \left(\frac{2}{3}\right)\left(\mathrm{K}_1 p_1 - K_2 q\right)\left(I_{qp}L_{ddm}I_{ds} - I_{qs}L_{qqm}I_{dp}\right) \quad .$$

The power winding q-axis and d-axis flux linkage are expressed as

$$\lambda_{qp} = L_{qqm}I_{qp} + L_{qdm}I_{qs}$$

$$\lambda_{dp} = L_{ddm}I_{dp} + L_{qdm}I_{ds} \quad ,$$

By using these two equations and considering the equality of $I_{qqm} = I_{ddm}$, which can be proven using their expressions and constraint conditions in Appendix 3B, finally an average torque under Condition I and condition II are given respectively as

Under Condition I

$$T_e = \frac{3}{2}\left(K_1 p_1 + K_2 q\right)\left[\lambda_{dp}I_{qp} - \lambda_{qp}I_{dp}\right] \tag{3.60}$$

Under Condition II

$$T_e = \frac{3}{2}(K_1 p_1 - K_2 q)\left[\lambda_{dp} I_{qp} - \lambda_{qp} I_{dp}\right] . \tag{3.61}$$

It is usual in electric machine analysis to refer all state variables to one set of windings. If we refer the state variables of the control windings to the power windings, Equations (3.22-3.25) become

$$V_{qdnp} = r_p I_{qdnp} + p\lambda_{qdnp} + K_3 \varpi_p \lambda_{qdnp} \tag{3.62}$$

$$V'_{qdns} = r'_s I'_{qdns} + p\lambda'_{qdns} + K_4 \varpi_s \lambda'_{qdns} \tag{3.63}$$

$$\lambda_{qdnp} = L_{pp} I_{qdnp} + L'_{ps} I'_{qdns} \tag{3.64}$$

$$\lambda'_{qdns} = L'_{ss} I'_{qdns} + L'_{ps} I_{qdnp} \tag{3.65}$$

where

$$r'_s = \left(\frac{N_s}{N_p}\right)^2 r_s$$

$$\left[L'_{ss}\right] = \left(\frac{N_s}{N_p}\right)^2 \left[L_{ss}\right]$$

$$V'_{qds} = \left(\frac{N_s}{N_p}\right) V_{qds}$$

$$I'_{qds} = \left(\frac{N_p}{N_s}\right) I_{qds}$$

$$\left[L'_{ps}\right] = \left(\frac{N_s}{N_p}\right)\left[L_{ps}\right].$$

3.6 Some Design Aspects

Here certain design criteria arising from the derived model equations are briefly discussed. The selection of the number of poles for the stator windings and the rotor is based on constraint conditions in Condition I and Condition II. Simplification of these equations result in Equations (3.66-3.69) which explicitly calculate the two stator pole numbers given the number of rotor poles:

Condition I

$$K_1 p_1 = \frac{(2m+2n+1)P_r}{2} \tag{3.66}$$

$$K_2 q = \frac{(2m-2n-1)P_r}{2} \tag{3.67}$$

Condition II

$$K_1 p_1 = \frac{(2m+2n+1)P_r}{2} \tag{3.68}$$

$$K_2 q = \frac{(2n-2m+1)P_r}{2} \tag{3.69}$$

It can be easily verified that the pole numbers of our test machine with Pr = 2, $p_1 = 1$, q = 3 are generated from Equations (3.66-3.67) when n = -1 and m = 1.

The "effective" leakage inductances of two stator windings are the differences between the self-inductances and the magnetizing inductances. Figure 3.6 shows the graphs of the "effective" leakage factors K_p and K_s defined as

$$K_p \approx \frac{L_{qqp} - L_{qqm}}{L_{qqm}} = \frac{\pi\alpha m}{\sin(\pi\alpha m)} N_{ps} - 1$$

$$K_s \approx \frac{L_{qqs} - L_{qqm}}{L_{qqm}} = \frac{\pi\alpha m}{\sin(\pi\alpha m)} N_{sp} - 1$$

where $N_{ps} = \frac{N_p}{N_s}$, $N_{sp} = \frac{N_s}{N_p}$.

It is observed from Figure 3.5 that the leakage factors are small when the turn number per pole of the two stator windings are equal with αm less than 0.5. Ultimately, the pole arc factor selected for any design must take into consideration the saturation effect, the effect of the space harmonic components of the stator windings and the curvature of the rotor pole.

The leakage inductances of the power and control windings of the experimental machine are relatively high, this is partly because the machine design was not optimized and moreover, the magnetizing inductance of this salient-pole structure is theoretically limited by the practical feasible pole-arc of the rotor that ensures that the rotor and stator teeth under normal operating conditions are not in deep saturation. However, it is expected that a doubly fed reluctance machine with an axially laminated or multiple flux barrier rotor structure have potentially smaller “leakage” inductances similar to those of

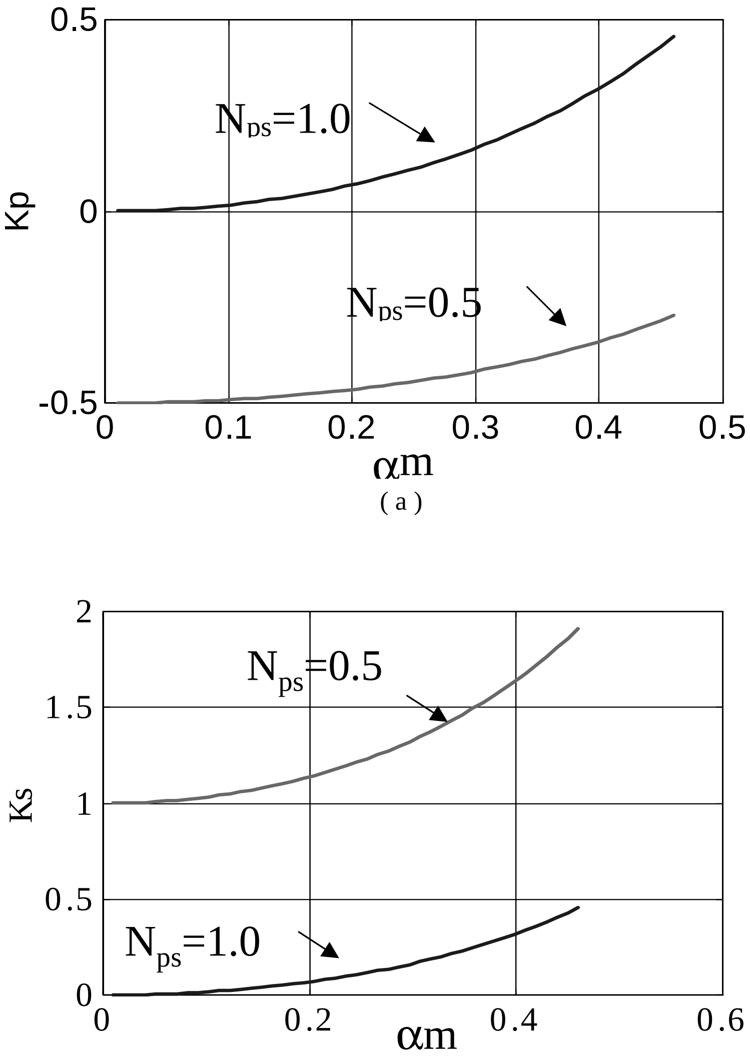

(a)

(b)

Figure 3.5. Effective leakage factors for values of αm and ratio of effective turns per pole of the power winding, $N_{ps} = N_p/N_s$. (a) Power windings, (b) Control windings.

three-phase synchronous or three-phase induction machine. How to optimize the design of this kind of machines for achieving best performance still have a lot of work to do.

3.7 Including Saturation Effects

Experimental waveforms of winding currents and air-gap flux linkage show that the machine has significant space-harmonic current components and is highly saturated at moderate supply voltage levels. No-load test also reveals that the core loss is significant.

Traditionally, core loss [53,54] has been divided into two components: hysteresis loss and eddy current loss. Within the iron of the machine, there are many small regions called domains. In each domain, all the atoms are aligned with their magnetic fields pointing in the same direction. Once the domains are aligned, some of them will remain aligned until a source of external energy is supplied to change them. The fact that turning domains in the iron requires energy leads to a common type of energy loss. So the hysteresis loss in an iron core of the machine is the energy required to accomplishing the reorientation of domains during each cycle of the ac current applied to the core. Eddy current losses are caused by induced electrical currents called eddy currents, since they tend to flow in closed paths within the core of the machine. Eddy current is proportional to the size of the paths they follow within the core. Using lamination stator and insulating resin between each lamination are the effect way to limit the eddy current and its loss.

It is clear that these significant effects must be included in the model to give accurate performance predictions. There are two ways to represent this part of losses, using shunt loss resistances or series loss resistances. These are shown in the equivalent circuit given

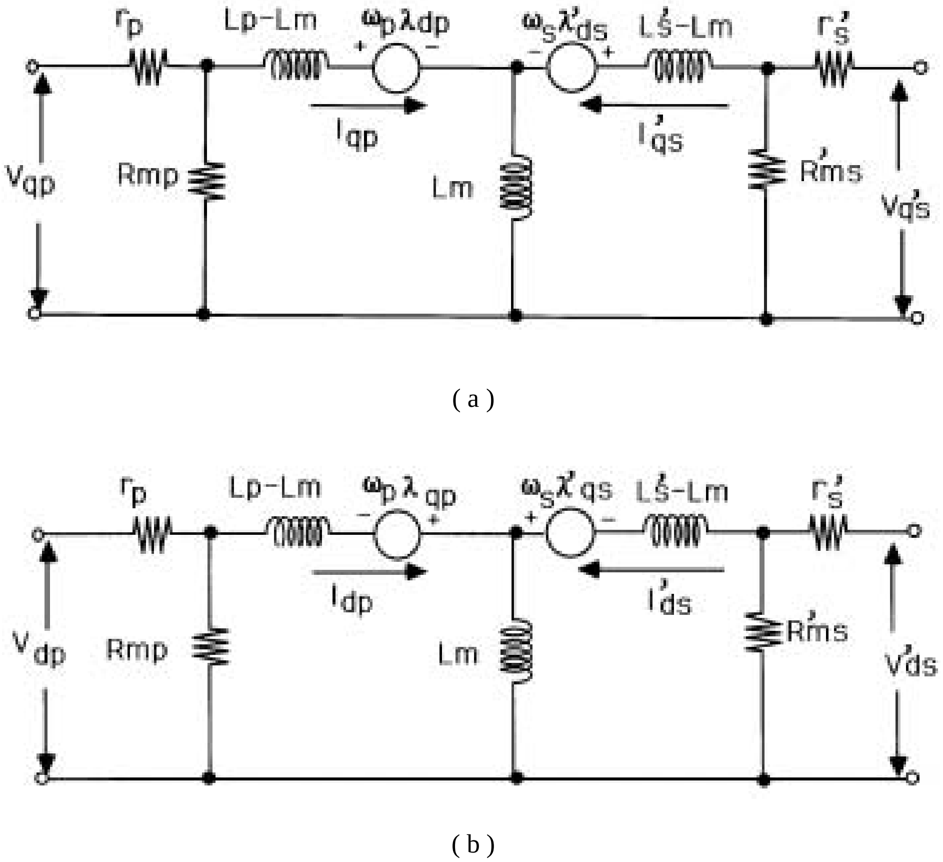

Figure 3.6. Q-d equivalent circuit with shunt core-loss resistances. (a) q-axis equivalent circuit, (b) d-axis equivalent circuit.

in Figures 3.6 and 3.7. In Figure 3.6, the resulting voltage equations including the shunt core loss resistances are expressed as

$$V_{qp} T_p = r_p T_p I_{qp} + p\lambda_{qp} - \omega_p \lambda_{dp}$$

$$V_{dp} T_p = r_p T_p I_{dp} + p\lambda_{dp} + \omega_p \lambda_{qp}$$

$$V'_{qs} T_s = r'_s T_s I'_{qs} + p\lambda'_{qs} - \omega_s \lambda'_{ds}$$

$$V'_{ds}T_s = r'_sT_sI'_{ds} + p\lambda'_{ds} + \omega_s\lambda'_{qs}$$

where

$$\lambda_{qp} = L_pI_{qp} + L_mI'_{qs}$$

$$\lambda_{dp} = L_pI_{dp} + L_mI'_{ds}$$

$$\lambda'_{qs} = L'_sI'_{qs} + L_mI_{qp}$$

$$\lambda'_{ds} = L'_sI'_{ds} + L_mI_{dp}$$

$$T_p = \frac{R_{mp}}{r_p + R_{mp}} \ , \ T_s = \frac{R'_{ms}}{r'_s + R'_{ms}}$$

$$r'_s = \left(\frac{N_p}{N_s}\right)^2 r_s \ , \ L'_s = \left(\frac{N_p}{N_s}\right)^2 L_s$$

$$V'_{qs} = V_{qs}\frac{N_p}{N_s} \ , \ V'_{ds} = V_{ds}\frac{N_p}{N_s}$$

$$I'_{qs} = I_{qs}\frac{N_p}{N_s} \ , \ I'_{ds} = I_{ds}\frac{N_p}{N_s}$$

$$L_m = \frac{3}{2}\frac{N_p}{N_s}L_{m12} \ .$$

In Figure 3.7, the resulting voltage equations including the series core loss resistances are expressed as

$$V_{qp} = (r_p + R_{mp})\, I_{qp} + p\lambda_{qp} - \omega_p\lambda_{dp}$$

$$V_{dp} = (r_p + R_{mp})\, I_{dp} + p\lambda_{dp} + \omega_p\lambda_{qp}$$

$$V'_{qs} = (r'_s + R'_{ms})\, I'_{qs} + p\lambda'_{qs} - \omega_s\lambda'_{ds}$$

$$V'_{ds} = (r'_s + R'_{ms})\, I'_{ds} + p\lambda'_{ds} + \omega_s\lambda'_{qs}$$

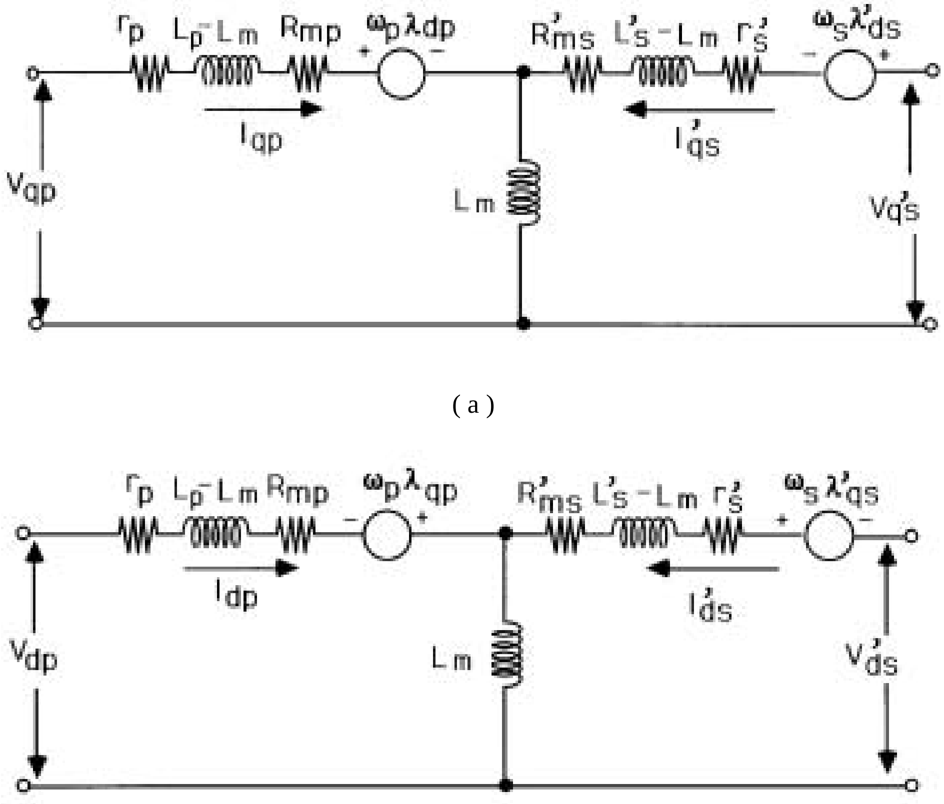

(a)

(b)

Figure 3.7. Q-d equivalent circuits with series core-loss resistances. (a) q-axis equivalent circuit, (b) d-axis equivalent circuit.

Where

$$\lambda_{qp} = L_p I_{qp} + L_m I'_{qs}$$

$$\lambda_{dp} = L_p I_{dp} + L_m I'_{ds}$$

$$\lambda'_{qs} = L'_s I'_{qs} + L_m I_{qp}$$

$$\lambda'_{ds} = L'_s I'_{ds} + L_m I_{dp}$$

$$r'_s = \left(\frac{N_p}{N_s}\right)^2 r_s \ , \quad L'_s = \left(\frac{N_p}{N_s}\right)^2 L_s$$

$$V'_{qs} = V_{qs} \frac{N_p}{N_s} \ , \quad V'_{ds} = V_{ds} \frac{N_p}{N_s}$$

$$I'_{qs} = I_{qs} \frac{N_p}{N_s} \ , \quad I'_{ds} = I_{ds} \frac{N_p}{N_s}$$

$$L_m = \frac{3}{2} \frac{N_p}{N_s} L_{m12} \ .$$

These two equivalent circuits are interchangeably used in the steady-state calculation and dynamic simulation, the same results are obtained using any one of them. By comparing two equivalent circuits, we find that the equivalent circuit in Figure 3.6 is more complicated and need accompanying computational burden, but the physical meaning is more clear, while Figure 3.7 is simpler for the equation derivation and parameter calculation.

3.8 Steady-State Equivalent Circuits

The complex form equations for the q-d equivalent circuits in Figure 3.7, can be expressed as

$$V_{qdp} = (r_p + R_{mp})\, I_{qdp} + p\lambda_{qdp} + j\omega_p \lambda_{qdp} \tag{3.70}$$

$$V'_{qds} = (r'_s + R'_{ms})\, I'_{qds} + p\lambda'_{qds} + j\omega_s \lambda'_{qds} \tag{3.71}$$

$$\lambda_{qdp} = L_p I_{qdp} + L_m I'_{qds} \tag{3.72}$$

$$\lambda'_{qds} = L_s I'_{qds} + L_m I_{qdp} \ . \tag{3.73}$$

Under the steady-state, the derivation items, $p\lambda_{qdp}$ and $p\lambda'_{qds}$, will equal to zero, substitute Equations (3.72-3.73) into (3.70-3.71), we can obtain the equations

$$V_{qdp} = (r_p + R_{mp}) I_{qdp} + j\omega_p (L_p - L_m) I_{qdp} + j\omega_p L_m (I_{qdp} + I'_{qds}) \tag{3.74}$$

$$\frac{V'_{qds}}{s} = \frac{(r'_s + R'_{ms})}{s} I'_{qds} + j\omega_p (L'_s - L_m) I'_{qds} + j\omega_p L_m (I_{qdp} + I'_{qds}) \tag{3.75}$$

where

$$s = \frac{\omega_s}{\omega_p}$$

$V_{qdp} = T(\theta_p) V_{ABC,}$ V_{ABC} power winding phase voltages

$I_{qdp} = T(\theta_p)\, I_{ABC,}$ I_{ABC} power winding phase currents

$V'_{qds} = T(\theta_s)\, I'_{abc}$, I_{abc} control winding phase voltages

$I'_{qds} = T(\theta_s)\, I'_{abc}$, I'_{abc} control winding phase currents .

Using the transformations of $T(\theta_s)$ and $T(\theta_p)$ and rewriting the Equations (3.74-3.75), the steady-state equations for phase A and a of the power winding and control winding are expressed as

$$V_A = (r_p + R_{mp}) I_A + j\omega_p (L_p - L_m) I_A + j\omega_p L_m (I_A + I'_a)$$

$$\frac{V'_a}{s} = \frac{(r'_s + R'_{ms})}{s} I'_a + j\omega_p (L'_s - L_m) I'_a + j\omega_p L_m (I_A + I'_a) \ .$$

According to these two equations, the steady-state equivalent circuit is shown in Figure 3.8. This is the situation considering the series core loss resistances.

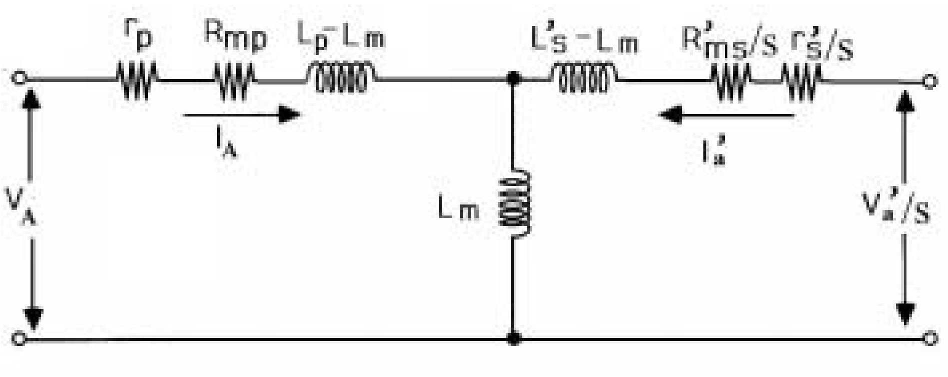

Figure 3.8. Steady-state equivalent circuit with series core-loss resistances.

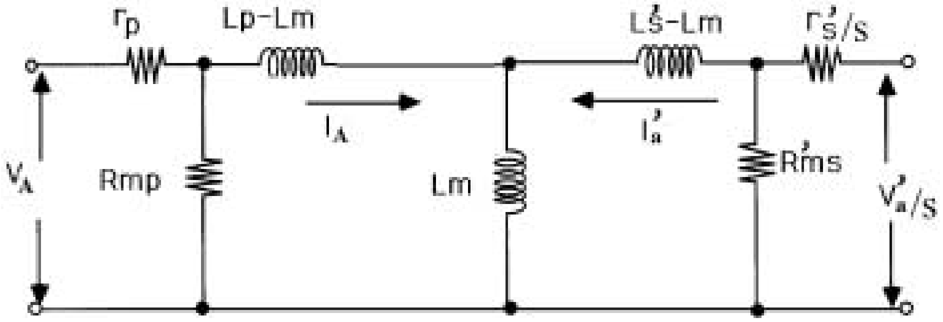

Figure 3.9. Steady-state equivalent circuit with shunt core-loss resistances.

Using the same way, we can derive the steady-state equations and equivalent circuit for the situation considering the shunt core-loss resistances. The steady-state equations are expressed as

$$T_p V_A = T_p I_A + j\omega_p (L_p - L_m) I_A + j\omega_p L_m (I_A + I_a^{'})$$

$$\frac{T_s V_a^{'}}{s} = \frac{T_s r_s^{'}}{s} I_a^{'} + j\omega_p (L_s^{'} - L_m) I_a^{'} + j\omega_p L_m (I_A + I_a^{'})$$

$$T_p = \frac{R_{mp}}{r_p + R_{mp}}, \quad T_s = \frac{R'_{ms}}{r'_s + R'_{ms}} \quad .$$

The steady-state equivalent circuit with shunt core-loss resistance is shown in Figure 3.9.

3.9 Calculation of Machine Parameters

The inductance and resistance values for the steady-state equivalent circuit can be found by a set of blocked rotor tests. For example, when the parameters of the power windings are tested, the rotor is clamped in the locked position, and an adjustable voltage source with 60Hz frequency is connected to the power winding and adjusted from 0 to the line-line rated voltage. Measurements are made of the voltage, current, and input power for power winding, and open circuit's voltage for control winding. The control winding has no connection with supply.

To test the parameters for the control winding, control winding is connected to adjustable voltage source while the power winding has no connection with any supply.

After collecting these test date, the parameters can be calculated for two kinds of steady-state equivalent circuits.

According to the angular frequency relationship among power winding, control winding and rotor

$\omega_p - \omega_s = \omega_r$,

and since rotor is blocked,

we can obtain

$$\omega_r = 0,\ \ \omega_p = \omega_s\ ,\ \ \text{and}\ \ s = \frac{\omega_s}{\omega_p} = 1\ .$$

Winding resistances, r_p and r_s, can be directly measured by using the multiple function meters.

The other parameters' calculation is based on the equivalent circuits with series core-loss resistance (Figure 3.8) or with shunt core-loss resistance (Figure 3.9).

A. Equivalent Circuit with Series Core-loss Resistances (considering turn ratio)

1.Open-circuit control winding, $I_a = 0$

For the given input power, voltage, and current for power windings, and open-circuit voltage for control windings,

$$|Z_p| = \left|\frac{V_A}{I_A}\right| = \sqrt{(r_p + R_{mp})^2 + (\omega_e L_p)^2}$$

$$Rp = \left|\frac{P_{3\phi}}{3I_A^2}\right| = r_p + R_{mp}$$

$$\omega_e L_m = \left|\frac{V_a'}{I_A}\right|\ .$$

We can obtain,

$$R_{mp} = R_p - r_p$$

$$L_p = \frac{1}{\omega_e}\sqrt{|Z_p|^2 - (r_p + R_{mp})^2}$$

$$L_m = \frac{1}{\omega_e}\left|\frac{V_a'}{I_A}\right|.$$

2. Open-circuit power windings, $I_A = 0$.

For the given input power, voltage, and current for control winding and open-circuit voltage for power winding,

$$|Z_s^{'}| = \left|\frac{V_a^{'}}{I_a^{'}}\right| = \sqrt{(r_s^{'} + R_{ms}^{'})^2 + (\omega_e L_s^{'})^2}$$

$$R_s^{'} = \left|\frac{P_{3\phi}}{3I_a^{'2}}\right| = r_s^{'} + R_{ms}^{'} \quad .$$

We can obtain

$$R_{ms}^{'} = R_s^{'} - r_s^{'}$$

$$L_s^{'} = \frac{1}{\omega_e}\sqrt{|Z_s^{'}|^2 - (r_s^{'} + R_{ms}^{'})^2} \quad .$$

By using these equations, the calculation results can be used to look for approximate polynomial equations relating the machine parameters to the air-gap flux linkage magnitude. These equations are given as

$$\begin{aligned}
\mathrm{L_m} &= -0.44\lambda_\mathrm{m}^2 + 0.085\lambda_\mathrm{m} + 0.0164 \\
\mathrm{L_p} &= -0.36\lambda_\mathrm{m}^2 + 0.0906\lambda_\mathrm{m} + 0.0373 \\
\mathrm{L_s^{'}} &= -0.55\lambda_\mathrm{m}^2 + 0.09\lambda_\mathrm{m} + 0.0385 \qquad (3.76) \\
R_{mp} &= -4.05\lambda_m^2 - 1.47\lambda_m + 1.217 \\
R_{ms}^{'} &= 7.24\lambda_m^2 - 4.25\lambda_m + 1.58 \quad .
\end{aligned}$$

The calculation results and approximate polynomial equations for these parameters are plotted in Figures 3.10(a)-(e).

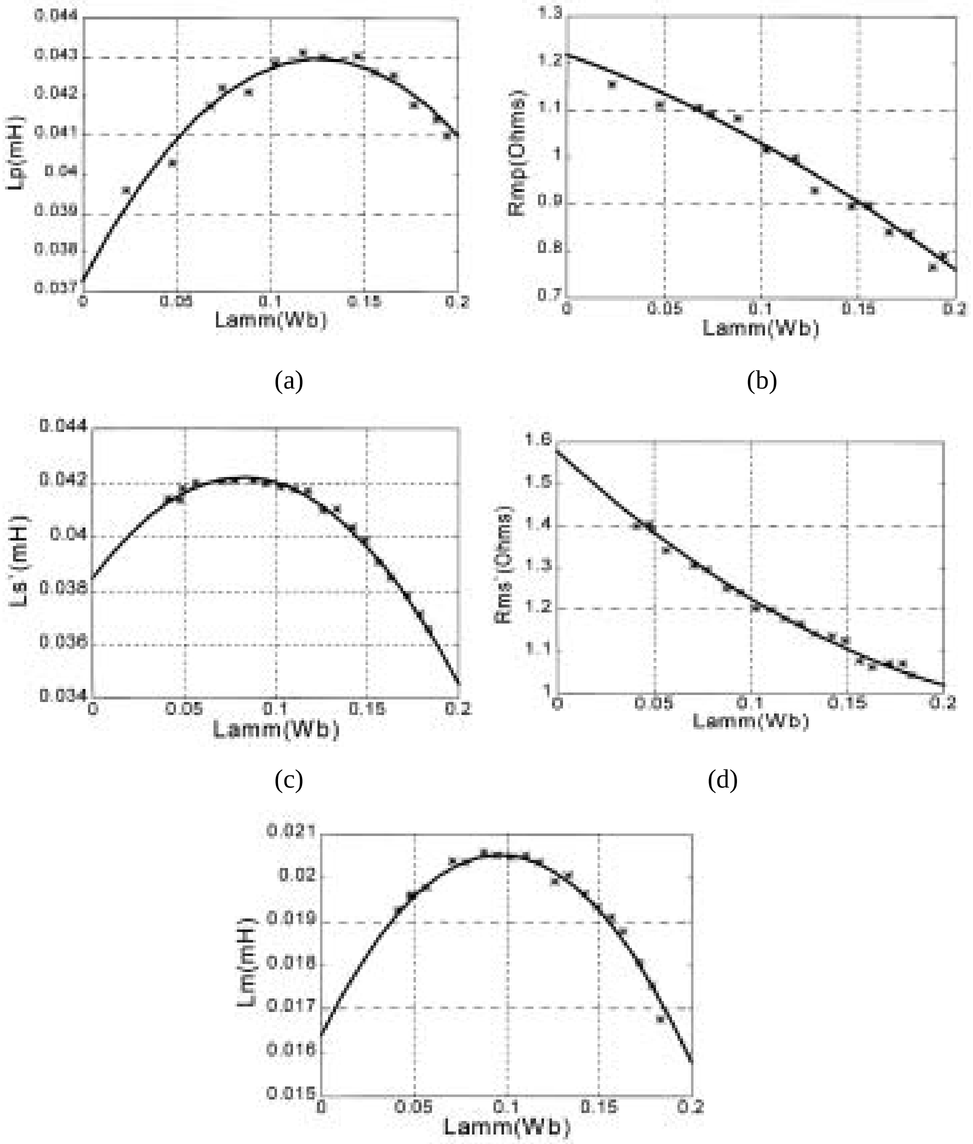

(a) (b)

(c) (d)

(e)

Figure 3.10. Machine parameters using steady-state equivalent circuits with series core-loss resistances. (a) Self-inductance of the power winding, (b) Series core-loss resistance of the power winding, (c) Self-inductance of the control winding, (d) Series core-loss resistance of the control winding, (e) Magnetizing inductance.

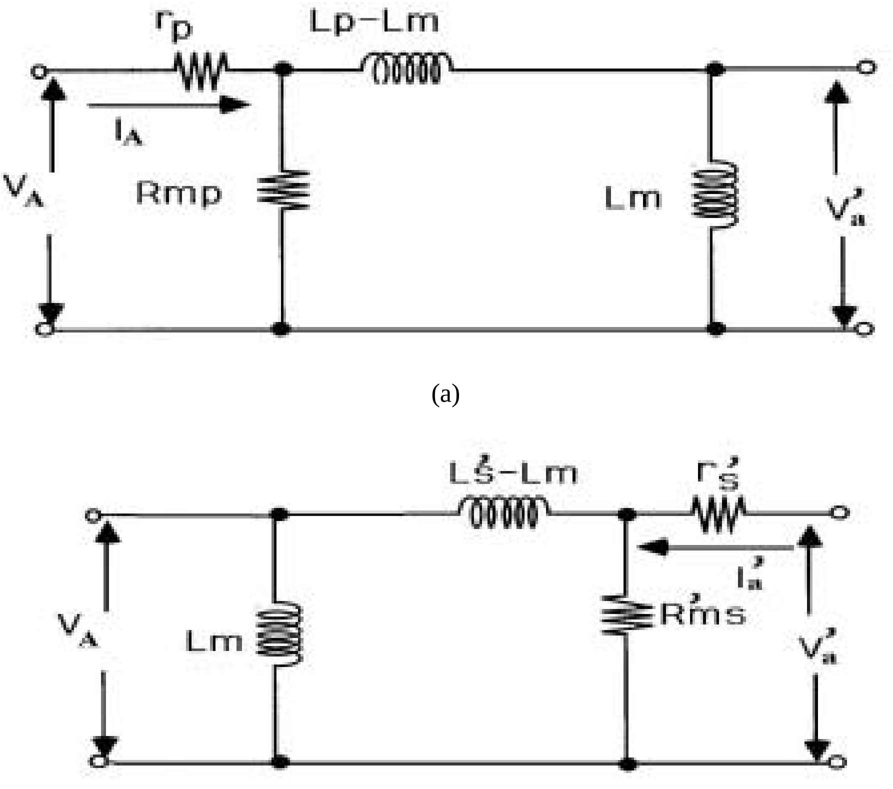

(a)

(b)

Figure 3.11. Approximate steady-state equivalent circuit for the parameter calculation. (a) For power windings, (b) for control windings.

B. Equivalent Circuit with Shunt Core-loss Resistances (considering turn ratio)

1.Open-circuit control winding, $I_a = 0$

To calculate parameters for the power winding, its input power $P_{3\phi}$, voltage V_A, and current I_A, and control winding open-circuit voltage V_a are measured. The approximated equivalent circuit, obtained from Figure 3.9 and shown in Figure 3.11(a), is used to derive the expressions of the parameters.

Input reactance of the power windings is

$$\left(\frac{V_a'}{I_a'}\right) = r_p + R_{mp} // \, \mathrm{jX_p}\,, \quad \mathrm{X_p} = \omega_e L_p$$

$$\left(\frac{V_a'}{I_a'}\right)^2 = \left(r_p + \frac{R_{mp} X_p^2}{R_{mp}^2 + X_p^2}\right) + j\,\frac{X_p R_{mp}^2}{R_{mp}^2 + X_p^2}$$

$$= \left(\mathrm{r_p} + \mathrm{R_{op}}\right) + \mathrm{jX_{oA}}$$

where

$$\mathrm{R_{op}} = \frac{\mathrm{R_{mp} X_p^2}}{\mathrm{R_{mp}^2 + X_p^2}}, \quad \mathrm{X_{oA}} = \frac{\mathrm{X_p R_{mp}^2}}{\mathrm{R_{mp}^2 + X_p^2}} \quad .$$

R_{op} and X_{oA} can be calculated by the equations

$$\mathrm{R_{op}} = \frac{\mathrm{P_{3\phi}}}{3\mathrm{I_A^2}} - \mathrm{r_p}$$

$$\mathrm{X_{oA}} = \sqrt{\left(\frac{\mathrm{V_A}}{\mathrm{I_A}}\right)^2 - \left(\frac{\mathrm{P_{3\phi}}}{3\mathrm{I_A^2}}\right)^2} \quad .$$

Open-circuit control winding voltage will be

$$\mathrm{V_a'} = \mathrm{I_A}\,\frac{\mathrm{R_{mp}\, jX_m}}{\mathrm{R_{mp} + jX_p}}, \text{ and } \mathrm{X_m} = \omega_e \mathrm{L_m}$$

hence,

$$\left|\frac{\mathrm{V_a'}}{\mathrm{I_A}}\right| = \frac{\mathrm{R_{mp} X_m}}{\sqrt{\mathrm{R_{mp}^2 + X_p^2}}}$$

core-loss resistance R_{mp}, self-inductance L_p, and magnetizing inductance L_m are expressed as

$$R_{mp} = \frac{X_{oA}^2 + R_{op}^2}{R_{op}}$$

$$L_p = \frac{R_{op}}{X_{oA}} \frac{R_{mp}}{\omega_e}$$

$$L_m = \frac{1}{\omega_e} \left| \frac{V_a^{'}}{I_A} \right| \sqrt{\frac{X_p}{X_{oA}}} \ .$$

2.Open-circuit power winding, $I_A = 0$

To calculate parameters for the control winding, its input power $P_{3\phi}$, voltage V_a, and current I_a, and power winding open-circuit voltage V_A are measured. The approximated equivalent circuit shown in Figure 3.11(b) is used to derive the expressions of the parameters.

Input reactance of the control winding is

$$\left(\frac{V_a^{'}}{I_a^{'}} \right) = r_s^{'} + R_{ms}^{'} // \ jX_s^{'}, \quad X_s^{'} = \omega_e L_s^{'}$$

$$\left(\frac{V_a^{'}}{I_a^{'}} \right)^2 = \left(r_s^{'} + \frac{R_{ms}^{'} X_s^{'2}}{R_{ms}^{'2} + X_s^{'2}} \right) + j \frac{X_s^{'} R_{ms}^{'2}}{R_{ms}^{'2} + X_s^{'2}}$$

$$= \left(r_s^{'} + R_{os}^{'} \right) + jX_{oa}^{'}$$

where

$$R_{os}^{'} = \frac{R_{ms}^{'} X_s^{'2}}{R_{ms}^{'2} + X_s^{'2}}, \quad X_{oa}^{'} = \frac{X_s^{'} R_{ms}^{'2}}{R_{ms}^{'2} + X_s^{'2}} \ .$$

$R_{os}^{'}$ and $X_{oa}^{'}$ can be calculated by the equations

$$R'_{os} = \frac{P_{3\phi}}{3I'^2_a} - r'_s$$

$$X'_{oa} = \sqrt{\left(\frac{V'_a}{I'_a}\right)^2 - \left(\frac{P_{3\phi}}{3I'^2_a}\right)^2}$$

open-circuit power winding voltage will be

$$V_A = I'_a \frac{R'_{ms} jX_m}{R'_{ms} + jX'_{ms}}, \text{ and } X_m = \omega_e L_m .$$

Hence,

$$\left|\frac{V_A}{I'_a}\right| = \frac{R'_{ms} X_m}{\sqrt{R'^2_{ms} + X'^2_s}}$$

core-loss resistance R'_{ms}, self-inductance L'_s, and magnetizing inductance L_m are expressed as

$$R'_{ms} = \frac{X'^2_{oa} + R'^2_{os}}{R'_{os}}$$

$$L'_s = \frac{R'_{os}}{X'_{oa}} \frac{R'_{ms}}{\omega_e}$$

$$L_m = \frac{1}{\omega_e} \left|\frac{V_A}{I'_a}\right| \sqrt{\frac{X'_s}{X'_{oa}}} .$$

By using these equations, the calculation results can be used to look for approximate polynomial equations relating the control winding's parameters to the air-gap flux linkage magnitude. These equations are given as

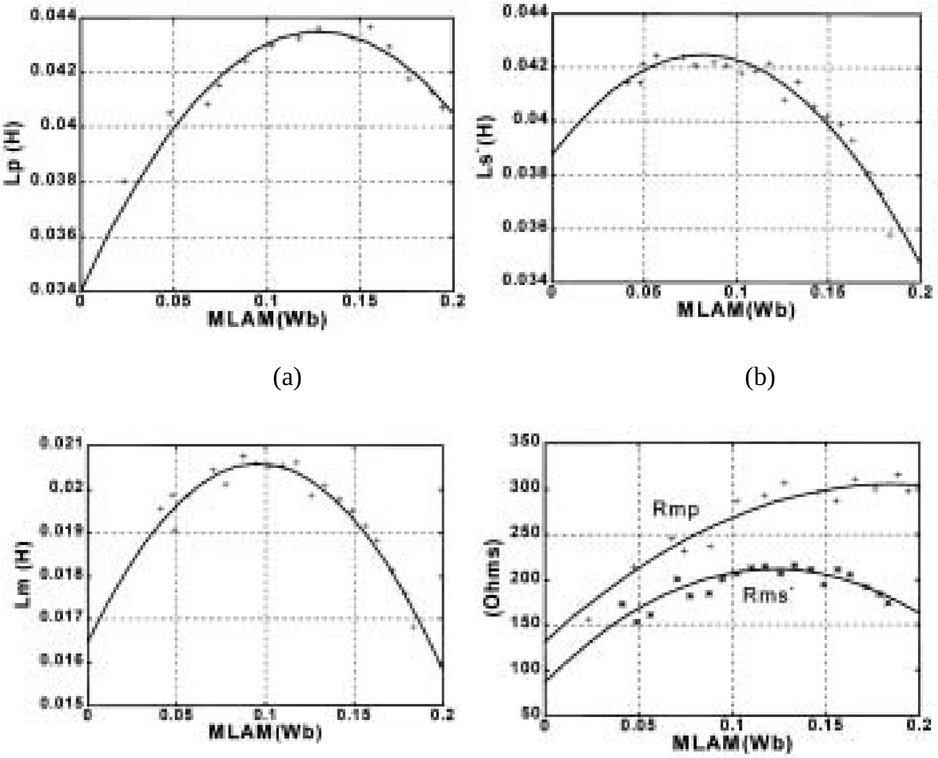

(a) (b)

(c) (d)

Figure 3.12. Machine parameters using steady-state equivalent circuit with shunt core-loss resistances. (a) Self-inductance of the power winding, (b) Self-inductance of the control winding, (c) The magnetizing inductance, (d) The shunt core-loss resistances for the power winding and control winding.

$$L_m = -0.44\lambda_m^2 + 0.085\lambda_m + 0.0164$$

$$L_p = -1.35\lambda_m^2 + 0.145\lambda_m + 0.0327$$

$$L'_s = -0.552\lambda_m^2 + 0.091\lambda_m + 0.0385 \qquad (3.77)$$

$$R_{mp} = -5022\lambda_m^2 + 1865\lambda_m + 132$$

$$R'_{ms} = -8218\lambda_m^2 + 2014.2\lambda_m + 88.2\ .$$

The calculation results and approximate polynomial equations for these parameters are plotted in Figures 3.12(a)-(d).

By comparing two groups of the machine parameters calculated from two different steady-state equivalent circuits, we can see that power winding self-inductance L_p, control winding self-inductance L'_s, and magnetizing inductance L_m are very close, but series core loss resistances (R'_{ms}, R_{mp}) are smaller than the shunt core loss resistances.

3.10 Manley-Rowe Relationships

The concept of power conservation at each frequency which governs the operation of a multi-frequency, dissipationless, linear, and time-invariant circuits is generally not applicable to circuits or systems with time-varying or nonlinear inductances (frequency converters). In such circuits, the powers delivered to or drawn from these nonlinear or time-varying inductances by the individual spectral frequency components of the operating signals are, in addition to the energy conservation law, governed by further principles which control the distribution of the energy exchanged between the nonlinear or time-varying inductances and the remaining part of the circuit or system.

Power relations for nonlinear resistive and storage elements excited by independent harmonic signals of different frequencies were published by Manley-Rowe [57] and Pantell [58]. These relations were applied to the first time by Penfield [59] and more recently by Russell and Pickup to elucidate the real power transfer mechanism from the stator circuit to the rotor circuit and the shaft [60].

The Manley-Rowe average real power/frequency relationships for a dissipationless circuit with nonlinear or time-varying inductances excited by two sources of independent angular frequencies (ω_1 and ω_2) are expressed as [57-60]

$$\sum_{m=0}^{\infty}\sum_{n=-\infty}^{\infty}\left[\frac{mP(m\omega_1+n\omega_2)}{m\omega_1+n\omega_2}\right]=0 \tag{3.78}$$

$$\sum_{m=-\infty}^{\infty}\sum_{n=0}^{\infty}\left[\frac{nP(m\omega_1+n\omega_2)}{m\omega_1+n\omega_2}\right]=0 \tag{3.79}$$

where $P(m\omega_1+n\omega_2)$ is the average real power flow due to a signal with an angular frequency of $(m\omega_1+n\omega_2)$. Equations (3.78-3.79) do not guarantee that the different frequencies they generate exist in the circuit under consideration and they give no information about the frequency components generated by the nonlinear or time-varying inductances (which are frequency converters) in the circuit.

The complex-variable d-q voltage equations of the doubly fed machine are given as

$$V_{qdp} = r_p I_{qdp} + p\lambda_{qdp} + j\omega_p\lambda_{qdp} \tag{3.80}$$

$$V_{qds} = r_s I_{qds} + p\lambda_{qds} + j\omega_s\lambda_{qds}\ . \tag{3.81}$$

The apparent input power equations for the power and control winding circuits are given as

$$\frac{3}{2}V_{qdp}I^*_{qdp} = \frac{3}{2}\left[r_p I_{qdp}I^*_{qdp} + p\lambda_{qdp}I^*_{qdp} + j\omega_p\lambda_{qdp}I^*_{qdp}\right] \tag{3.82}$$

$$\frac{3}{2}V_{qds}I^*_{qds} = \frac{3}{2}\left[r_s I_{qds} I^*_{qds} + p\lambda_{qds} I^*_{qds} + j\omega_s \lambda_{qds} I^*_{qds}\right] . \tag{3.83}$$

Also, the real powers sent by the power and control windings across the air-gap to the shaft at steady-state are from equations (3.82-3.83) and are expressed as

$$P(\omega_1) = \mathrm{Real}[\frac{3}{2} j\omega_1 \lambda_{qdp} I^*_{qdp}] \tag{3.84}$$

$$P(\omega_2) = \mathrm{Real}[\frac{3}{2} j\omega_2 \lambda_{qds} I^*_{qds}] \ . \tag{3.85}$$

The Manley-Rowe real power/frequency relationships are now applied to determine the active power distribution of the doubly fed reluctance machines. These relationships are only applicable to the input and output real powers (to and from the air-gap) of the time-varying mutual inductances between the power and control windings. The independent two angular frequency are ω_1 and $z\omega_2$ and the dependent angular frequency is $\omega_1 + z\omega_2$, which is the angular frequency of the air-gap power converted to the developed mechanical power. Assuming that power input into the time-varying inductances is positive and output power is negative, use of Equations (3.78-3.79) results in

$$\frac{P(\omega_1)}{\omega_1} + \frac{P(\omega_1 + z\omega_2)}{\omega_1 + z\omega_2} = 0 \tag{3.86}$$

$$\frac{P(z\omega_2)}{z\omega_2} + \frac{P(\omega_1 + z\omega_2)}{\omega_1 + z\omega_2} = 0 \tag{3.87}$$

where $P(\omega_1)$ is the real power contributed by the power winding circuit to the air-gap, the contribution of the control winding circuit is $P(z\omega_2)$ and $P(\omega_1+\omega_2)$ is the active power converted to mechanical power to produce the electromechanical torque. From Equations

(3.88-3.89) which are deduced from Equations (3.86-3.87), the following observations are deduced

$$\left|\frac{P(z\omega_2)}{P(\omega_1)}\right| = \frac{z\omega_2}{\omega_1} = \sigma \tag{3.88}$$

$$\left|\frac{P(\omega_1)}{P(\omega_1 + z\omega_2)}\right| = \frac{1}{1+\sigma}, \quad \left|\frac{P(z\omega_2)}{P(\omega_1 + z\omega_2)}\right| = \frac{\sigma}{1+\sigma} \,. \tag{3.89}$$

The ratio of the contributions of the control and power windings to the developed mechanical power is the same as the ratio of their source frequencies. Hence, if the control winding circuit is used to affect a small change of shaft speed around the synchronous speed of the power winding frequency in such applications as pumps and compressors, a relatively small rated inverter is required (compared to the power winding power requirement) confirming the experimental observation in [30]. However, in high-performance drive applications where extended speed range of operation is desirable, the

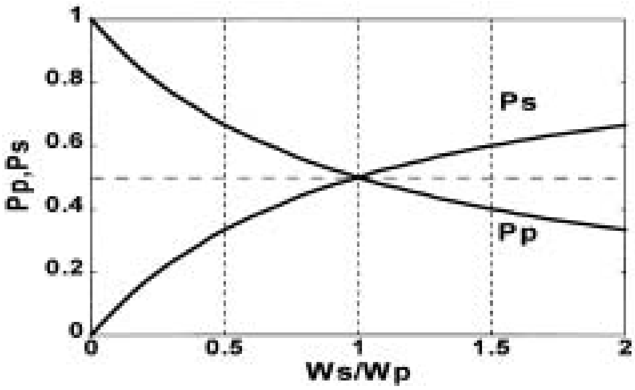

Figure 3.13. Air-gap power contribution of power (P_p) and control (P_s) windings normalized with developed mechanical power as a function of control winding frequency.

power requirement of the inverter feeding the control winding circuit may indeed exceed that of the power winding circuit when ω_2 is greater than $\omega_{1.}$

Figure 3.13 and Equation (3.89) show the contributions of the control and power winding circuits to the developed mechanical power. We can see that with increase of control winding frequency, the relative active power contribution of the power winding decreases to the point when it equals that of the control winding when $\omega_2 = \omega_1$ after which frequency the control winding active power contribution predominates. Hence, a doubly fed reluctance motor drive requiring a large-speed operation range is likely to be very expensive in view of the increase of inverter active power rating.

The electromagnetic torque of the machine is defined as the ratio of the developed mechanical power to the shaft speed, ω_{rm}. From Equations (3.86-3.87), we have

$$T_e = \frac{P(\omega_1 + z\omega_2)}{\omega_{rm}} = \frac{P(\omega_1)}{\omega_1}\frac{\omega_r}{\omega_{rm}} = \frac{P(\omega_1)}{\omega_1}(p_1 + q)$$

$$= \frac{P(z\omega_2)}{z\omega_2}\frac{\omega_r}{\omega_{rm}} = \frac{P(z\omega_2)}{z\omega_2}(p_1 + q) \quad . \tag{3.90}$$

Since power is invariant to reference frame transformations, the real power transferred from the power and control winding circuits across the airgap are given by equations (3.84-3.85). Hence, the electromagnetic torque is given as

$$T_e = \frac{3}{2}(p_1 + q)\,\mathrm{Re}al\left[j\lambda_{qdp} I^*_{qdp}\right] = \frac{3}{2}(p_1 + q)\,\mathrm{Re}al\left[j\lambda_{qds} I^*_{qds}\right] \quad . \tag{3.91}$$

3.11 Transient and Oscillatory Behavior

The starting transient, dynamic response, and waveforms of the machine operating as a motor can be simulated using Equations (3.92-3.102) with assumed power and control winding voltage sources.

$$\theta_p + \theta_s - \theta_r = 0 \tag{3.92}$$

$$\omega_p + \omega_s = \omega_r = (p_1 + q)\omega_{rm} \tag{3.93}$$

$$V_{qp} = r_p I_{qp} + \dot{\lambda}_{qp} - \omega_p \lambda_{dp} \tag{3.94}$$

$$V_{dp} = r_p I_{dp} + \dot{\lambda}_{dp} - \omega_p \lambda_{qp} \tag{3.95}$$

$$V'_{qs} = r'_s I_{qs} + \dot{\lambda}'_{qs} - \omega_s \lambda'_{ds} \tag{3.96}$$

$$V'_{ds} = r'_s I_{ds} + \dot{\lambda}'_{ds} + \omega_s \lambda'_{qs} \tag{3.97}$$

$$J\left(\frac{1}{p_1 + q}\right)\dot{\omega}_r = T_e - T_L \tag{3.98}$$

$$T_e = \frac{3}{2}\left(K_1 p_1 + K_2 q\right)\left[\lambda_{dp} I_{qp} - \lambda_{qp} I_{dp}\right] \tag{3.99}$$

$$\lambda_{qm} = \left[\frac{1}{L_{\ell p}} + \frac{1}{L'_{ls}} + \frac{1}{L_m}\right]^{-1}\left[\frac{\lambda'_{qs}}{L'_{ls}} + \frac{\lambda_{qp}}{L_{\ell p}}\right] \tag{3.100}$$

$$\lambda_{dm} = \left[\frac{1}{L_{\ell p}} + \frac{1}{L'_{ls}} + \frac{1}{L_m}\right]^{-1}\left[\frac{\lambda'_{qs}}{L'_{ls}} + \frac{\lambda_{dp}}{L_{\ell p}}\right] \tag{3.101}$$

$$\lambda_m^2 = \lambda_{qm}^2 + \lambda_{dm}^2 \tag{3.102}$$

To obtain Equations (3.100) and (3.101), flux linkage λ_{dm}, λ_{qm}, λ'_{ds}, λ_{dp}, λ'_{qs}, and λ_{qp} are defined as

$$\lambda_{dm} = L_m (I_{dp} + I'_{ds})$$

$$\lambda_{qm} = L_m (I_{qp} + I'_{qs})$$

$$\lambda_{qp} = L_p I_{qp} + L_m I'_{qs}$$

$$\lambda_{dp} = L_p I_{dp} + L_m I'_{ds}$$

$$\lambda'_{qs} = L'_s I'_{qs} + L_m I_{qp}$$

$$\lambda'_{ds} = L'_s I'_{ds} + L_m I_{dp} .$$

According these expressions, the current I_{dp}, I_{qp}, I'_{ds}, and I'_{qs} can be represented by the flux linkage and are expressed as follows

$$I_{qp} = \frac{\lambda_{qp} L'_s - L_m \lambda'_{qs}}{L_p L'_s - L_m^2}$$

$$I_{dp} = \frac{\lambda_{dp} L'_s - L_m \lambda'_{ds}}{L_p L'_s - L_m^2}$$

$$I'_{qs} = \frac{\lambda'_{qs} L_p - L_m \lambda_{qp}}{L_p L'_s - L_m^2}$$

$$I'_{ds} = \frac{\lambda'_{ds} L_p - L_m \lambda_{dp}}{L_p L'_s - L_m^2} \ .$$

We define the inductance leakage as

$$L_p - L_m = L_{lp}, \qquad L'_s - L_m = L'_{ls} \ .$$

Hence, $L_p L'_s - L_m^2$ can be transferred as

$$L_p L'_s - L_m^2 = L'_{ls} L_{lp} + L_m (L_{lp} + L'_{ls}) \ .$$

By substituting the expressions of I_{dp}, I_{qp}, I'_{ds}, and I'_{qs} into the expressions of λ_{dm} and λ_{qm}, we can obtain

$$\lambda_{qm} = \frac{L_m L'_{ls}}{L_{lp} L'_{ls} + L_m (L_{lp} + L'_{ls})} \lambda'_{qs} + \frac{L_m L_{lp}}{L_{lp} L'_{ls} + L_m (L_{lp} + L'_{ls})} \lambda_{qp}$$

$$= \frac{1}{\frac{1}{L_m}+\frac{1}{L_{lp}}+\frac{1}{L_{ls}^{'}}}\cdot\frac{1}{L_{ls}^{'}}\lambda_{qs}^{'} + \frac{1}{\frac{1}{L_m}+\frac{1}{L_{lp}}+\frac{1}{L_{ls}^{'}}}\cdot\frac{1}{L_{lp}}\lambda_{qp}$$

and

$$\lambda_{dm} = \frac{L_m L_{ls}^{'}}{L_{lp}L_{ls}^{'} + L_m(L_{lp}+L_{ls}^{'})}\lambda_{ds}^{'} + \frac{L_m L_{lp}}{L_{lp}L_{ls}^{'} + L_m(L_{lp}+L_{ls}^{'})}\lambda_{dp}$$

$$= \frac{1}{\frac{1}{L_m}+\frac{1}{L_{lp}}+\frac{1}{L_{ls}^{'}}}\cdot\frac{1}{L_{ls}^{'}}\lambda_{ds}^{'} + \frac{1}{\frac{1}{L_m}+\frac{1}{L_{lp}}+\frac{1}{L_{ls}^{'}}}\cdot\frac{1}{L_{lp}}\lambda_{dp}\ .$$

Finally, Equations (3-100) and (3-101) are obtained from above derivation.

However, it is required to determine either the reference frame angle of the control or power winding circuit and to properly account for saturation effect. These are achieved by the alignment of the air-gap flux linkage on the q-axis such that the d-axis air-gap flux linkage and its derivative are forced to be zero every time. When these constraints are applied to Equations (3.93, 3.95, 3.100-3.102), Equation (3.103) results from which ω_p can be determined

$$\omega_p = \frac{-(\omega_A + \omega_B)}{L_{\ell s}\lambda_{qp} + L_{\ell p}\lambda_{qs}} \tag{3.103}$$

where

$$\omega_A = V_{dp}L_{\ell s} + V_{ds}L_{\ell p} - L_{\ell p}\omega_r\lambda_{qs}$$

$$\omega_B = \lambda_{dp}(T_a - L_{\ell s}^2 T_b)$$

$$T_a = \frac{-L_{\ell s}^{'}}{D}[r_p L_s^{'} + r_s^{'} L_p] + \frac{L_{\ell p} r_s^{'} L_m}{D}$$

$$T_b = \frac{r_p L_m}{D L_{\ell p}}, \quad D = L_p L_s^{'} - L_m^2\ .$$

Figures 3.14 and 3.15 show the simulated no-load starting transient of the experimental machine in which the control winding circuit is supplied with a three-phase inverter with a constant Volts/Hz control scheme. During the initial starting period, the control windings are shorted after which the inverter connected to the control winding circuit has its frequency ramped linearly and levels off at 10Hz. It is significant to note that after reaching a steady-state operating condition, the rotor experiences a bounded oscillation around the average speed. However, when the frequency of the inverter is ramped to 15 Hz and kept constant at that frequency as shown in Figure 3.15 (showing only the steady-state waveform), the rotor speed oscillatory component is continuously increasing. After some time, a new operating speed is found with a lower average speed and a different frequency of rotor speed oscillation. A jump phenomenon has occurred. These simulation results have been confirmed in the laboratory. Figures 3.16(a) and 3.17(a) present experimental power winding current waveforms when inverter frequency is 10HZ and 15HZ. Figure 3.16(b) and Figure 3.17(b) show the significant power spectra of the power winding current confirming the presence of the side-band current components when the control winding frequency is 15Hz. The lower side-band current components of the control and power windings give rise to a negative damping torque leading to the machine oscillatory rotor motion.

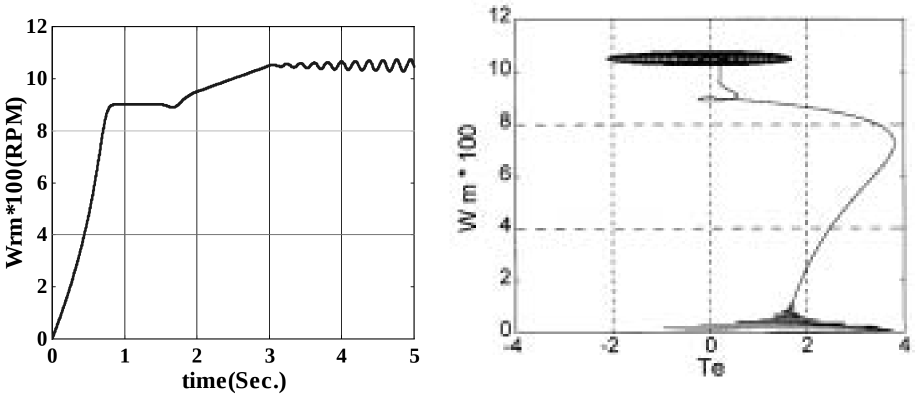

(a) (b)

Figure 3.14. No-load transient of rotor speed and torque when inverter frequency = 10 Hz. (a) The rotor speed of no-load, (b) The electromagnetic torque vs. rotor speed.

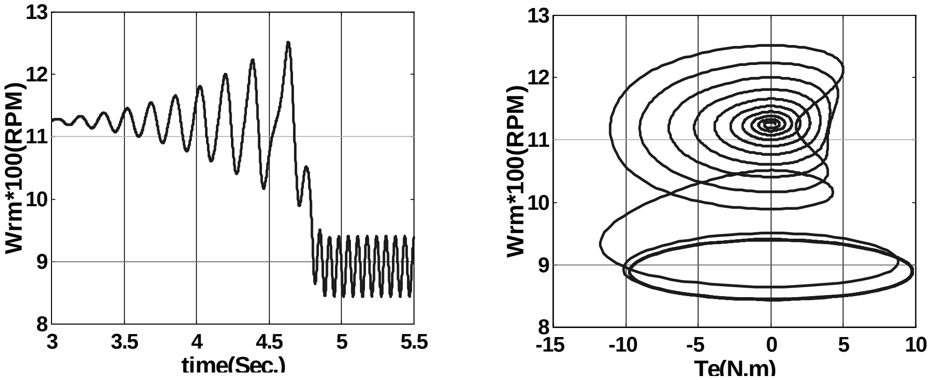

(a) (b)

Figure 3.15. No-load transient of rotor speed and torque when inverter frequency = 15 Hz. (a) The rotor speed, (b) Electromagnetic torque vs. rotor speed.

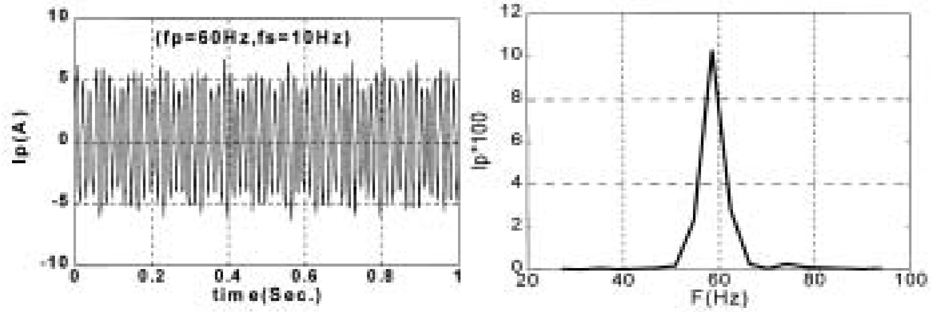

(a) (b)

Figure 3.16. Experimental waveforms showing machine oscillatory motion with inverter frequency=10Hz. (a) Phase 'a' power winding current, (b) Power spectra of the power winding current.

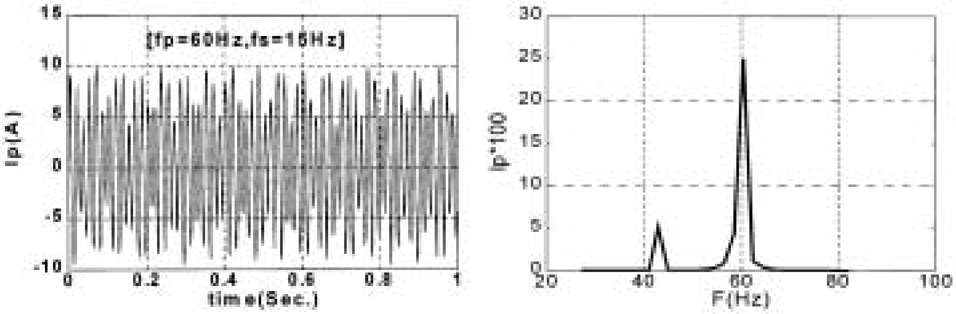

(a) (b)

Figure 3.17. Experimental waveforms showing machine oscillatory motion with inverter frequency=15Hz. (a) Phase 'a' power winding current, (b) Power spectra of the power winding current.

3.12 Synchronous Motor

With the power windings connected to a balanced three-phase voltage source having a frequency of ω_p and the control winding connected to a DC voltage source as shown in Figure 3.18, the doubly-fed reluctance machine is running in synchronous operation condition. The detailed information about the synchronous operation is referred to in Chapters 5 and 7.

The power winding and control winding q-d equations of the doubly-fed synchronous reluctance machine in the rotor reference frame are:

$$V_{qp} = R_p I_{qp} + p\lambda_{qp} + \omega_p \lambda_{dp} \tag{3.104}$$

$$V_{dp} = R_p I_{dp} + p\lambda_{dp} - \omega_p \lambda_{qp} \tag{3.105}$$

$$V_{qs}^{'} = R_s^{'} I_{qs}^{'} + p\lambda_{qs}^{'} \tag{3.106}$$

$$V_{ds}^{'} = R_s^{'} I_{ds}^{'} + p\lambda_{ds}^{'} \tag{3.107}$$

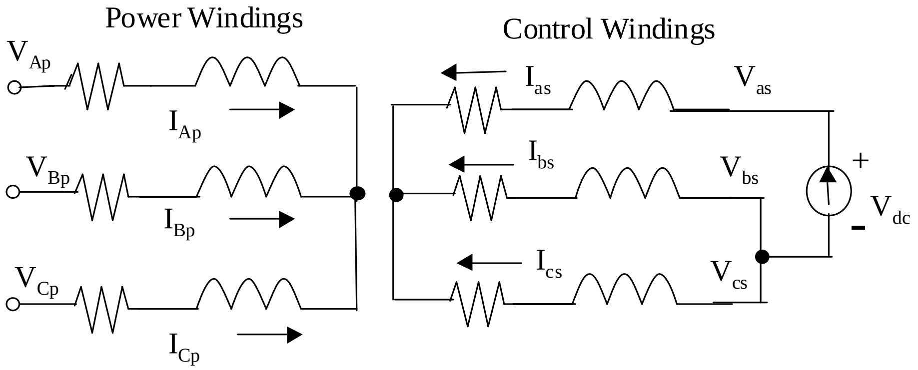

Figure 3.18. Schematic diagram of the doubly-fed synchronous reluctance motor with DC excitation.

where

$$\lambda_{qp} = L_p I_{qp} + L_m I'_{qs} \tag{3.108}$$

$$\lambda_{dp} = L_p I_{dp} + L_m I'_{ds} \tag{3.109}$$

$$\lambda'_{qs} = L'_s I'_{qs} + L_m I_{qp} \tag{3.110}$$

$$\lambda'_{ds} = L'_s I'_{ds} + L_m I_{dp} \ . \tag{3.111}$$

Torque equation is expressed as

$$T_e = \left(\frac{3}{2}\right)(p_1 + q) L_m (I_{dp} I'_{qs} - I_{qp} I'_{ds}) \tag{1.112}$$

Under the steady-state condition and considering the following conditions:

$$I'_{ds} = 0, \qquad I_s = \frac{N_s}{N_p} I'_{qs} = \frac{N_s}{N_p} I'_s$$

The following equations are obtained

$$I_{dp} = \left(\frac{2N_p}{3N_s}\right) \frac{T_e}{(p_1 + q) L_m I_s} \tag{3.113}$$

$$V_{qp} = R_p I_{qp} - \omega_p L_p I_{dp} \tag{3.114}$$

$$V_{dp} = R_p I_{dp} - \omega_p (L_p I_{qp} + L_m I'_s) \tag{3.115}$$

The peak value of power winding voltage is expressed as

$$V_m^2 = V_{qp}^2 + V_{dp}^2 \tag{3.116}$$

Substituting equation (3.114) and (3.115) into (3.116) yields

$$C_a \cdot I_{qp}^2 + C_b \cdot I_{qp} + C_c = 0 \tag{3.117}$$

Where

$$C_a = \omega_p^2 L_p^2 + R_p^2$$

$$C_b = 2\omega_p^2 L_m L_p I_s^{'}$$

$$C_c = (\omega_p L_p I_{dp})^2 + (R_p I_{dp} - \omega_p L_m I_s^{'})^2 - V_m^2$$

Then I_{qp} can be solved using equation (3.117) and expressed as

$$I_{qp} = \frac{-C_b + \sqrt{C_b^2 - 4C_a C_c}}{2C_a} \tag{3.118}$$

and

$$I_{qp} = \frac{-C_b - \sqrt{C_b^2 - 4C_a C_c}}{2C_a} \ . \tag{3.119}$$

Only Equation (3.118) is used in the calculation because the solution of Equation (3.119) leads to poorer power factor results.

The phase voltage and current of power windings are

$$I_{pa} = \frac{\sqrt{I_{dp}^2 + I_{qp}^2}}{\sqrt{2}}$$

$$V_{pa} = \frac{\sqrt{V_{dp}^2 + V_{qp}^2}}{\sqrt{2}} \ .$$

The active power and apparent power as well as power factor can be computed using following equations:

$$P_o = \frac{3}{2}(I_{qp}V_{qp} + I_{dp}V_{dp})$$

$$S_o = 3V_{pa}I_{pa}$$

$$pf = \frac{P_o}{S_o} \ .$$

By applying a given constant load to the shaft of the synchronous motor and varying the control winding current from underexcitation to overexcitation and recording the power winding current at each step, the curves of Figure 3.19(a) are obtained. The power winding phase current is plotted against the dc control winding current for 2 N.m, 4 N.m, and 8 N.m load torque values, respectively. As shown in Figure 3.19(b), the power factor is plotted against the dc control winding current for various given loads. Note that both sets of curves show that a slightly increased control winding current is required to produce unite power factor as the load is increased (points 1, 2, and 3). As load is applied, not only does the power winding current rise, but is also necessary to

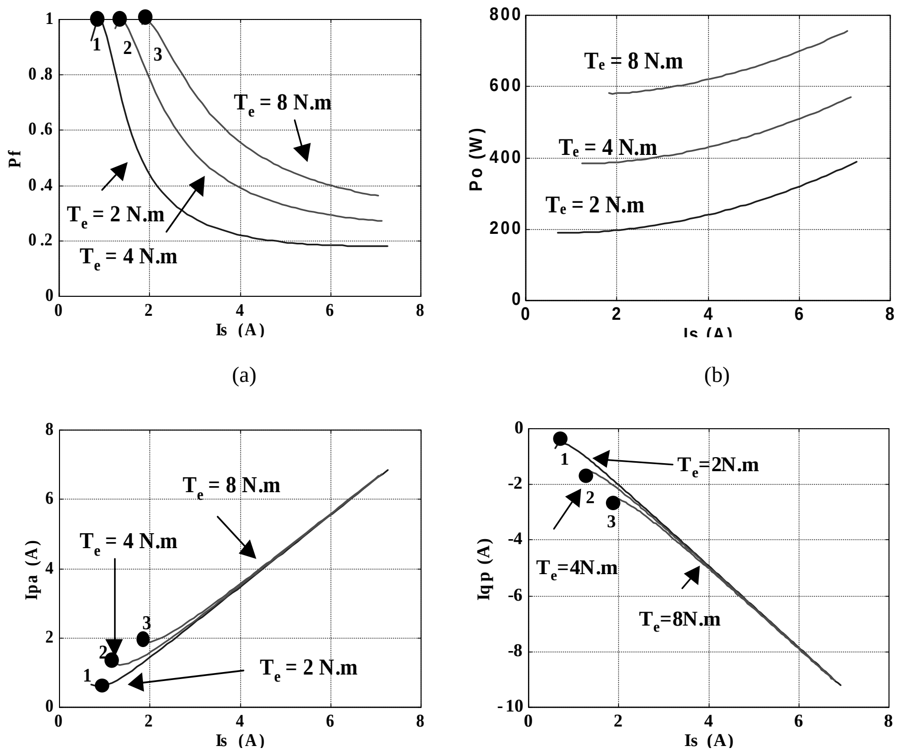

(a) (b)

(b) (d)

Figure 3.19. Doubly-fed synchronous reluctance motor characteristics. (a) Motor power factor vs. power winding current, (b) motor power vs. control winding current, (c) power winding current vs. control winding current, (d) q-axis current of power windings vs. control winding current.

increase the control winding current. Figure 3.19(c) show the curves of power winding input power against the control winding current. Note that slight input power increment for each load value is necessary to balance the losses of increment of control winding and power winding as increment. Figure 3.19(d) shows the cures of q-axis current of power windings against the control winding current, where we can see that the unity power factor is achieved when the maximum q-axis current of power windings is obtained. We also note that, the higher the load torque, the higher the magnitude of maximum q-axis current of power windings (see points 1, 2, and 3).

3.13 Conclusion

This chapter presents an accurate model of the doubly-fed reluctance machine, which consider the core-loss of the machine. The q-d equivalent circuits with series core-loss resistance or shunt core-loss resistance are given. The Manley-Rowe power-frequency relationships are used to determine the relative contribution of each stator winding circuit to the developed mechanical power. The machine inherent parameters are obtained by using the steady-state equivalent circuits and experimental test. These parameters and the model are successfully used to exposure the inherent oscillatory instability of the doubly fed reluctance machine in the motoring mode by computer simulation and experiment. They also will be used in the following chapters to investigate the steady-state characteristics and dynamic performance of some application systems with the doubly-fed reluctance machine.

CHAPTER 4

PERFORMANCE CHARACTERISTICS OF DOUBLY-FED RELUCTANCE GENERATOR

4.1 Introduction

The idea of using doubly-fed reluctance machines as generator was inspired by the fact [50, 40, 36]:

(1) These machines can run at high speeds where the efficiencies of prime-mover (turbines) are relatively high.

(2) As the reluctance generator is run with a prime-mover, there is no need for a special starting arrangement.

(3) In stand-alone generator applications with regulated turbine speed, an automatically regulated load frequency is achieved if two stator windings are connected in series.

(4) According to the frequency relationship ($\omega_p + \omega_s = \omega_r$) between the power winding and control winding, the frequency ω_p of the generated voltage in power winding can be controlled by regulating ω_s and active power (from battery source, solar system, for example) and reactive power provided to the load using a DC/AC PWM inverter in the secondary winding as the rotor speed ω_r varies. So the dual-winding reluctance generators have a better controllability than a squirrel-cage induction generator that required a rectifier-DC/AC-PWM inverter system to control the load voltage with no facility to augment the power provided by the shaft to meet excessive load demand.

(5) The dual-winding machine can be use as a generator for wind-power transfer. With

wind as the power source, the frequency and current in the control windings are manipulated using current-regulated voltage-source, pulsewidth-modulated (VSI-PWM) inverters to track the power speed profile of the wind turbine for maximum power capture.

This chapter explores the use of a dual-winding reluctance machine as an autonomous generator system in which reactive power is supplied to sustain the load. Two stand-alone generator systems considered in this chapter are shown schematically in Figure 4.1. In Figure 4.1a, the generator feeds balanced 3-phase load impedance. 3-capacitors are connected across the power and control windings to provide reactive power to the generator. In Figure 4.1b, power winding is connected to a rectifier that feeds an impedance load and control winding has the same connection as the system in Figure 4.1a. Section 4.2 and 4.3 give the derivation of the generator load model and the generator steady-state model. Calculated, measured generator steady-state characteristic curves and waveforms are included in Section 4.4 and 4.5. The dynamical simulation results of the self-excitation and de-excitation are given in Section 4.6. Conclusions are drawn in Section 4.7.

4.2 Model of Generator loads

The phase voltages and phase currents are balanced. The phase voltage and current for phase A of the power winding circuit are defined as

$$\begin{aligned} V_{Ap} &= V_p \cos(\theta_p + \alpha_{pv}) = \mathrm{Re}\,al[V_{qdp} e^{j\theta_p}] \\ I_{Ap} &= I_p \cos(\theta_p + \alpha_{pv}) = \mathrm{Re}\,al[I_{qdp} e^{j\theta_p}] \ . \end{aligned} \tag{4.1}$$

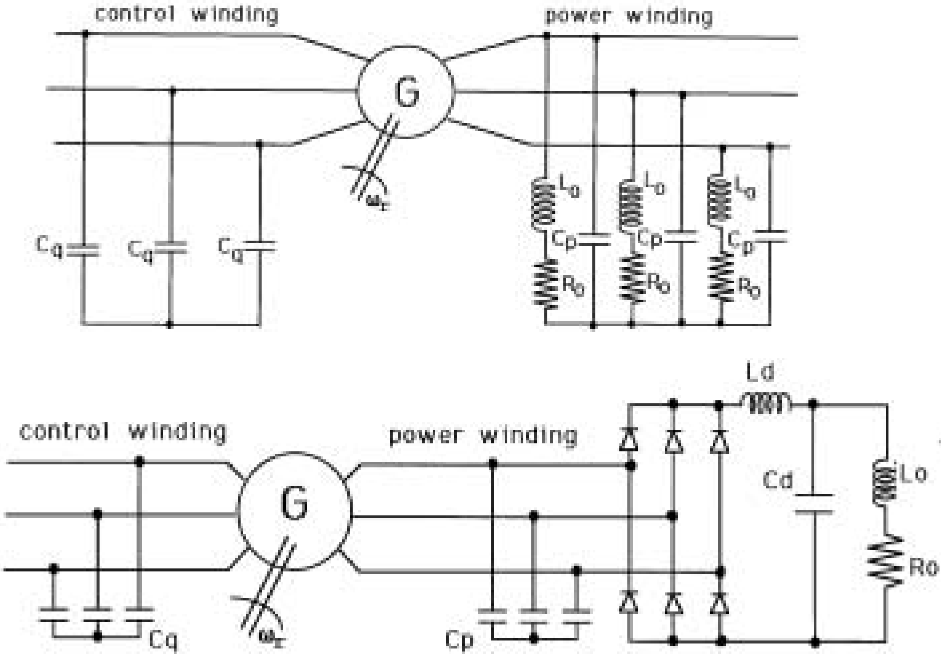

Figure 4.1. **Schematic diagram of stand-alone generator systems. (a)With impedance load (Top), (b) with a loaded 3-phase diode rectifier (Bottom).**

Similarly, the phase-a voltage and current of the control winding are giving as

$$\begin{aligned} V_{as} &= V_s \cos(\theta_s + \alpha_{sv}) = \mathrm{Re}\,al[V_{qds} e^{j\theta_s}] \\ I_{as} &= I_s \cos(\theta_s + \alpha_{sI}) = \mathrm{Re}\,al[I_{qds} e^{j\theta_s}] \ . \end{aligned} \tag{4.2}$$

The phase voltage equations of the load and capacitor circuits from Figure 4.1(a) are expressed as

$$pV_{as} = -\frac{I_{as}}{C_q} \tag{4.3}$$

$$pV_{AP} = -\frac{1}{C_P}(I_{AP} + I_{Ao}) \tag{4.4}$$

$$V_{AP} = L_o pI_{Ao} + R_o I_{Ao} \ . \tag{4.5}$$

Substituting Equations (4.1) and (4.2) into Equations (4.3)-(4.5) and using harmonic balance principles, the following complex-form equations are obtained:

$$pV_{qds}^{'} = -\frac{I_{qds}^{'}}{C_q^{'}} - j\omega_s V_{qds}^{'} \tag{4.6}$$

$$pV_{qdp} = \frac{1}{C_p} I_{qdp} - j\omega_p V_{qdp} \tag{4.7}$$

$$V_{qdp} = L_o pI_{qdp} + R_o I_{qdp} + j\omega_p I_{qdo} L_o \tag{4.8}$$

where

$$C_q^{'} = \left(\frac{N_s}{N_p}\right)^2 C_q, \quad V_{qds}^{'} = \left(\frac{N_p}{N_s}\right) V_{qdp}, \quad I_{qds}^{'} = \left(\frac{N_s}{N_p}\right) I_{qds} \ .$$

From Figure 4.1(b), the phase-A capacitor voltage, voltage and current equations of the rectifier and connected load are

$$pV_{AP} = -\frac{1}{C_q}(I_{AP} + I_{Ar}) \tag{4.9}$$

$$I_{Ar} = S_{aI} I_d, \ I_{Br} = S_{bI} I_d, \ I_{cr} = S_{cI} I_d \tag{4.10}$$

$$V_d = S_{av} V_{Ap} + S_{bv} V_{Bp} + S_{cv} V_{Vp} \tag{4.11}$$

$$pV_{cd} = \frac{1}{C_d}(I_d - I_o) \tag{4.12}$$

$$pI_o = \frac{1}{L_o}(V_{cd} - R_o I_o) \tag{4.13}$$

$$pI_d = \frac{1}{L_d}(V_d - V_{cd}) \ . \tag{4.14}$$

Assuming that the filter inductor current and filter capacitor voltage are DC quantities, the switching functions of the rectifier are approximated by their fundamental components and given as

$$S_{aI} = A\cos(\theta_p + \alpha_{sv}), \quad S_{av} = A\cos(\theta_p + \alpha_{pv}) \tag{4.15}$$

$$S_{bI} = A\cos(\theta_p - \beta + \alpha_{sv}), \quad S_{bv} = A\cos(\theta_p - \beta + \alpha_{pv}) \tag{4.16}$$

$$S_{cI} = A\cos(\theta_p + \beta + \alpha_{sv}), \quad S_{cv} = A\cos(\theta_p + \beta + \alpha_{pv}) \tag{4.17}$$

where

$$A = \frac{2\sqrt{3}}{\pi}, \qquad \beta = \frac{2\pi}{3} \ .$$

With Equations (4.1), (4.2), and (4.15)-(4.17) substituted in Equations (4.9)-(4.11) and applying harmonic balance technique, the following equations result:

$$pV_{qdp} = \frac{1}{C_p}(I_{qdp} - S_{qdI} I_d) + j\omega_p V_{qdp} \tag{4.18}$$

$$V_d = \mathrm{Re}\,al(V_{qdp} S_{qdv}) \tag{4.19}$$

where

$$S_{qdI} = Ae^{j\alpha_{sv}}, \quad S_{qdv} = Ae^{j\alpha_{pv}} \ . \tag{4.20}$$

We will show that the loaded rectifier (based on the fundamental component analysis) appears like a resistor (R_L) connected across the capacitor C_q (see Figure 4.2). The effective resistance is given as

$$R_L = \frac{\pi^2}{12} R_o \ . \tag{4.21}$$

The following equations are obtained from Equations (4.19) and (4.20):

$$S_{qI} = A\cos\alpha_{sv}, \quad S_{dI} = A\sin\alpha_{sv}$$

$$S_{qv} = A\cos\alpha_{pv,} \quad S_{dv} = A\sin\alpha_{pv}$$

$$I_{qr} = S_{qI} I_d, \qquad I_{dr} = S_{dI} I_d$$

$$V_d = S_{qv}V_{qp} + S_{dv}V_{dp} \ .$$

Under steady-state condition,

$$V_d = V_{cd}, \quad I_d = I_o, \quad V_{cd} = R_o I_o$$

$$V_{qp} = I_{qr}R_L = S_{qI} I_d R_L$$

$$V_{dv} = I_{dr}R_L = S_{dI} I_d R_L \ .$$

Hence,

$$V_d = S_{qv}V_{qp} + S_{dv}V_{dp} = R_L(S_{qv}S_{qI} + S_{dv}S_{dI})I_d$$

and

$$V_d = V_{cd} = R_o I_o = R_o I_L \ .$$

Now we can obtain

$$R_L = \frac{R_o}{S_{qv}S_{qI} + S_{dv}S_{dI}} \ .$$

Because α_{sv} are approximately equal to α_{pv} we can assume $S_{qv} = S_{qI}$ and $S_{dv} = S_{dI}$ to obtain:

$$S_{qv}S_{qI} + S_{dv}S_{dI} = A^2 = \frac{12}{\pi^2} \ .$$

Finally, the expression of the effective resistant R_L is obtained in Equation (4.21).

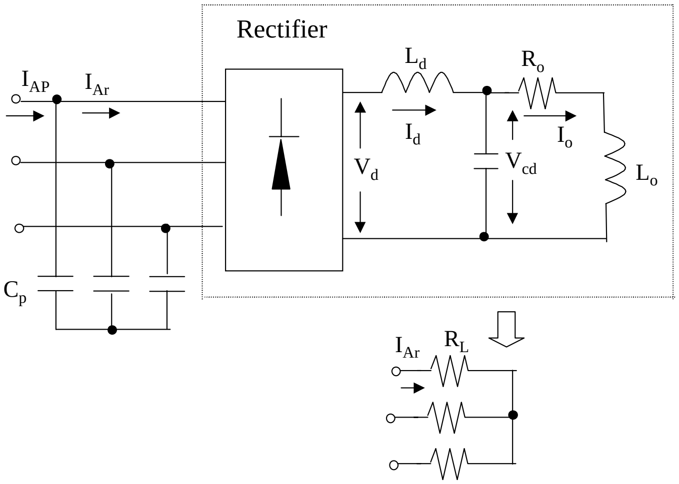

Figure 4.2. Effective resistance R_L.

4.3 Steady-State Generator Model

The generator system in Figures 4.1(a) and 4.1(b) can be described by following q-d equations:

$$V_{qp} = R_p I_{qp} + p\lambda_{qp} + \omega_p \lambda_{dp} \tag{4.22}$$

$$V_{dp} = R_p I_{dp} + p\lambda_{dp} - \omega_p \lambda_{qp} \tag{4.23}$$

$$V_{qs}^{'} = R_s^{'} I_{qs}^{'} + p\lambda_{qs}^{'} - \omega_s \lambda_{ds}^{'} \tag{4.24}$$

$$V_{ds}^{'} = R_s^{'} I_{ds}^{'} + p\lambda_{ds}^{'} + \omega_s \lambda_{qs}^{'} \tag{4.25}$$

$$pV_{qp} = \frac{1}{C_p}(-I_{qp} - I_{qo}) - \omega_p V_{dp} \tag{4.26}$$

$$pV_{dp} = \frac{1}{C_p}(-I_{dp} - I_{do}) + \omega_p V_{qp} \tag{4.27}$$

$$L_o pI_{qo} + R_o I_{qo} + \omega_p L_o I_{do} = V_{qp} \tag{4.28}$$

$$L_o pI_{do} + R_o I_{do} - \omega_p L_o I_{qo} = V_{dp} \tag{4.29}$$

$$pV_{qs}^{'} = -\frac{1}{C_q} I_{qs}^{'} + \omega_s V_{ds}^{'} \tag{4.30}$$

$$pV_{ds}^{'} = -\frac{1}{C_q} I_{ds}^{'} - \omega_s V_{qs}^{'} \tag{4.31}$$

where

$$\lambda_{qp} = L_p I_{qp} + L_m I_{qs}^{'} \tag{4.32}$$

$$\lambda_{ds} = L_p I_{ds} + L_m I_{ds}^{'} \tag{4.33}$$

$$\lambda_{qs}^{'} = L_s^{'} I_{qs}^{'} + L_m I_{qp} \tag{4.34}$$

$$\lambda_{ds}^{'} = L_s^{'} I_{ds}^{'} + L_m I_{dp} \tag{4.35}$$

$$R_p = r_p + R_{cp} \tag{4.36}$$

$$R_s^{'} = r_s^{'} + R_{cs}^{'} \,. \tag{4.37}$$

Since some parameters of machine are dependent on the airgap flux, the steady-state system equations are easily solved if the current state variables are replaced with flux linkages. By using Equations (4.34) and (4.35), the current states can be expressed with flux linkages as

$$I_{qp} = \frac{(\lambda_{qp} L_s^{'} - L_m \lambda_{qs}^{'})}{(L_p L_s^{'} - L_m^2)} \tag{4.38}$$

$$I_{dp} = \frac{(\lambda_{dp} L_s^{'} - L_m \lambda_{ds}^{'})}{(L_p L_s^{'} - L_m^2)} \tag{4.39}$$

$$I'_{qs} = \frac{(\lambda'_{qs} L_p - \lambda_{qp} L_m)}{(L_p L'_s - L_m^2)} \tag{4.40}$$

$$I'_{ds} = \frac{(\lambda'_{ds} L_p - \lambda_{dp} L_m)}{(L_p L'_s - L_m^2)} \quad . \tag{4.41}$$

Substituting Equations (4.38)-(4.41) into Equations (4.23)-(4.31), the following equations with flux linkages as state variables are obtained:

$$p\lambda_{qp} = V_{qp} - \omega_p \lambda_{dp} + T_{ss1}\lambda_{qp} + B_{ss1}\lambda'_{qs} \tag{4.42}$$

$$p\lambda_{dp} = V_{dp} + \omega_p \lambda_{qp} + T_{ss1}\lambda_{dp} + B_{ss1}\lambda'_{ds} \tag{4.43}$$

$$p\lambda'_{qs} = V'_{qs} + \omega_s \lambda'_{ds} + T_{ss2}\lambda'_{qs} + B_{ss2}\lambda_{qp} \tag{4.44}$$

$$p\lambda'_{ds} = V'_{ds} - \omega_s \lambda'_{qs} + T_{ss2}\lambda'_{ds} + B_{ss2}\lambda_{ds} \tag{4.45}$$

$$pV_{qp} = \frac{1}{C_p}(T_{s1}\lambda_{qp} + B_{s1}\lambda'_{qs} - I_{qo}) - \omega_p V_{dp} \tag{4.46}$$

$$pV_{dp} = \frac{1}{C_p}(T_{s1}\lambda_{dp} + B_{s1}\lambda'_{ds} - I_{do}) + \omega_p V_{qp} \tag{4.47}$$

$$pI_{qo} = \frac{V_{qp}}{L_o} - \frac{R_o I_{qo}}{L_o} - \omega_p I_{do} \tag{4.48}$$

$$pI_{do} = \frac{V_{dp}}{L_o} - \frac{R_o I_{do}}{L_o} - \omega_p I_{qo} \quad . \tag{4.49}$$

The complex form for Equations (4.42)-(4.49) are expressed as Equations (4.50)-(4.53):

$$p\lambda_{qdp} = V_{qdp} + j\omega_p \lambda_{qdp} + T_{ss1}\lambda_{qdp} + B_{ss1}\lambda'_{qds} \tag{4.50}$$

$$p\lambda'_{qds} = V'_{qds} - j\omega_s \lambda'_{qds} + T_{ss2}\lambda'_{qds} + B_{ss2}\lambda_{qdsp} \tag{4.51}$$

$$C_p pV_{qdp} = (T_{s1}\lambda_{qdp} + B_{s1}\lambda'_{qds} - I_{qdo}) + j\omega_p C_p V_{qdp} \tag{4.52}$$

$$L_o pI_{qdo} = (V_{qdp} - R_o I_{qdo}) + j\omega_p L_o I_{qdo} \tag{4.53}$$

$$C_q V_{qds}^{'} = (T_{s2}\lambda_{qds}^{'} + B_{s2}\lambda_{qdp}) - j\omega_s V_{qds}^{'} \,. \tag{4.54}$$

In the steady-state, all differential items of Equations (4.50)-(4.54) are equal to zero. The following equations are obtained and used to describe the steady-state performance of the generator system in Figure 4.1(a):

$$0 = V_{qdp} + j\omega_p \lambda_{qdp} + T_{ss1}\lambda_{qdp} + B_{ss1}\lambda_{qds}^{'} \tag{4.55}$$

$$0 = V_{qds}^{'} - j\omega_s \lambda_{qds}^{'} + T_{ss2}\lambda_{qds}^{'} + B_{ss2}\lambda_{qdsp} \tag{4.56}$$

$$0 = (T_{s1}\lambda_{qdp} + B_{s1}\lambda_{qds}^{'} - I_{qdo}) + j\omega_p C_p V_{qdp} \tag{4.57}$$

$$0 = (V_{qdp} - R_o I_{qdo}) + j\omega_p L_o I_{qdo} \tag{4.58}$$

$$0 = (T_{s2}\lambda_{qds}^{'} + B_{s2}\lambda_{qdp}) - j\omega_s V_{qds}^{'} \tag{4.59}$$

where

$$T_{s1} = -\frac{L_s^{'}}{L_p L_s^{'} - L_m^2}, \qquad \mathrm{B}_{\mathrm{s1}} = \frac{L_m}{L_p L_s^{'} - L_m^2}$$

$$T_{s2} = -\frac{L_p}{L_p L_s^{'} - L_m^2}, \qquad \mathrm{B}_{\mathrm{s2}} = \frac{L_m}{L_p L_s^{'} - L_m^2}$$

$$T_{ss1} = -\frac{R_p L_s^{'}}{L_p L_s^{'} - L_m^2}, \qquad \mathrm{B}_{\mathrm{ss1}} = \frac{R_p L_m}{L_p L_s^{'} - L_m^2}$$

$$T_{ss2} = -\frac{R_s^1 L_p}{L_p L_s^{'} - L_m^2}, \qquad \mathrm{B}_{\mathrm{ss1}} = \frac{R_s^{'} L_m}{L_p L_s^{'} - L_m^2} \,.$$

Equations (5.60)-(5.61) are obtained from Equations (4.58)-(4.59) and expressed as

$$I_{qdo} = \frac{V_{qdp}}{(R_o - j\omega_p L_o)} \tag{4.60}$$

$$V_{qds}^{'} = \frac{(T_{s2}\lambda_{qds}^{'} + B_{s2}\lambda_{qdp})}{j\omega_s C_q} \,. \tag{4.61}$$

Substituting Equations (4.60)-(4.61) into Equation (4.56) gives

$$0 = K_{11}\lambda_{qdp} + K_{12}\lambda'_{qds} \tag{4.62}$$

where

$$K_{11} = B_{ss2} + \frac{B_{s2}}{j\omega_s C_q}, \quad K_{12} = T_{ss2} - j\omega_s + \frac{T_{s2}}{j\omega_s C_q}.$$

Substituting Equation (4.60) into Equation (4.57) yields

$$V_{qdp} = A\lambda_{qdp} + B\lambda'_{qds} \tag{4.63}$$

where

$$A = \frac{T_{s1}(R_o - j\omega_p L_o)}{1 - j\omega_p C_p (R_o - j\omega_p L_o)}, \quad \mathrm{B} = \frac{\mathrm{B}_{s1}(R_o - j\omega_p L_o)}{1 - j\omega_p C_p (R_o - j\omega_p L_o)}$$

Replacing V_{qdp} with Equation (4.63) and I_{qdo} with Equation (4.60) in Equation (4.55) yields

$$0 = K_{21}\lambda_{qdp} + K_{22}\lambda'_{qds} \tag*{(4.64))}$$

where

$$K_{21} = A + j\omega_p + T_{ss1}, \quad K_{22} = B + B_{ss1}.$$

Now we obtain a complex-form equation system (Equations (4.65)-(4.66)) of the generator system in Figure 4.1(a):

$$0 = K_{11}\lambda_{qdp} + K_{12}\lambda'_{qds} \tag{4.65}$$

$$0 = K_{21}\lambda_{qdp} + K_{22}\lambda'_{qds}. \tag{4.66}$$

The matrix form of Equations (4.65)-(4.66) is

$$\begin{bmatrix} K_{11} & K_{12} \\ K_{21} & K_{22} \end{bmatrix} \begin{bmatrix} \lambda_{qdp} \\ {}'_{qds} \end{bmatrix} = \begin{bmatrix} 0 \\ 0 \end{bmatrix}. \tag{4.67}$$

As Equation (4.67) is singular, feasible solutions are obtained only when the determinant of K matrix is set equal to zero. That is

$$\Delta = K_{11}K_{22} - k_{12}K_{21} = 0\,. \tag{4.68}$$

By replacing $K_{11}, K_{22,} K_{12,}$ and K_{21} with corresponding expressions in Equation (4.68), a complex form equation is obtained and can be separated into real part and imaginary part

$$\Delta = \Delta_R + j\Delta_I = 0\,. \tag{4.69}$$

Δ_R and Δ_I, respectively, represent real part and imaginary part of Equation (4.68) and Appendix 4A gives the expressions of Δ_R and Δ_I.

To satisfy the condition of Equation (4.69), the Δ_R and Δ_I both must be equal to zero. That is

$$\Delta_R = 0\,,\ \ \Delta_I = 0\,.$$

By using the condition $\Delta_R = 0$, Equations (4.70)-(4.71) are obtained:

$$C_1\omega_p^9 + C_2\omega_p^8 + C_3\omega_p^7 + C_4\omega_p^6 + C_5\omega_p^5 + C_6\omega_p^4 + C_7\omega_p^3 + C_8\omega_p^2 + C_9\omega_p + C_{10} = 0 \tag{4.70}$$

$$R_o = \frac{s_a\omega_p^5 + t_a\omega_p^4 + u_a\omega_p^3 + v_a\omega_p^2 + x_a\omega_p + y_a}{l_a\omega_p^3 + m_a\omega_p^2 + n_a\omega_p + q_a}\,. \tag{4.71}$$

The quantities $s_a - y_a, l_a - q_a$, and $C_1 - C_{10}$ are determined by machine parameters and the values of the electrical components and rotor speed. The expressions of $s_a - y_a, l_a - q_a$, and $C_1 - C_{10}$ are listed in Appendix 4B.

The complex-form mutual airgap flux linkage is given as

$$\lambda_{qdm} = L_m(I_{qdp} + I_{qds}^{'})\,. \tag{4.72}$$

Combining Equations (4.38) and (4.39) into a complex-form gives

$$I_{qp} = \frac{(\lambda_{qdp} L_s^{'} - L_m \lambda_{qds}^{'})}{(L_p L_s^{'} - L_m^2)} \tag{4.73}$$

and the complex-form from Equations (4.40) and (4.41) is expressed as

$$I_{qds}^{'} = \frac{(\lambda_{qds}^{'} L_p - \lambda_{qdp} L_m)}{(L_p L_s^{'} - L_m^2)} . \tag{4.74}$$

Substituting Equations (4.73-4.74) into Equation (4.72) yields

$$\lambda_{qdm} = E\lambda_{qdp} + F\lambda_{qds} \tag{4.75}$$

where

$$E = (\frac{1}{L_m} + \frac{1}{L_{lp}} + \frac{1}{L_{ls}^{'}})^{-1}(L_{lp})^{-1}$$

$$F = (\frac{1}{L_m} + \frac{1}{L_{lp}} + \frac{1}{L_{ls}^{'}})^{-1}(L_{ls}^{'})^{-1} .$$

$L_{lp} = L_p - L_m$: The per-phase effective leakage inductance of the power winding.

$L_{ls}^{'} = L_s^{'} - L_m$: The per-phase effective leakage inductance of the control winding.

Using Equation (4.62) and Equation (4.75) to obtain a matrix equation (4.76):

$$\begin{bmatrix} E & F \\ K_{11} & K_{12} \end{bmatrix} \begin{bmatrix} \lambda_{qdp} \\ \lambda_{qds}^{'} \end{bmatrix} = \begin{bmatrix} \lambda_{\mathrm{qdm}} \\ 0 \end{bmatrix} . \tag{4.76}$$

Now we can obtain Equations (4.77) and (4.78) from Equation (4.76)

$$\lambda_{qdp} = \frac{K_{12}\lambda_{qdm}}{EK_{12} - FK_{11}} \tag{4.77}$$

$$\lambda_{qds}^{'} = \frac{-K_{11}\lambda_{qdm}}{EK_{12} - FK_{11}} . \tag{4.78}$$

With given values of ω_r, C_p, C_q, and varying the airgap flux linkage from zero to some reasonable values, the machine parameters are computed from their approximated equations and the quantities of $s_a - y_a, l_a - q_a,$ and $C_1 - C_{10}$ can also be determined. Then they are inserted in Equations (4.70) and (4.71) to determine corresponding load impedance (or load resistance) and the angular frequencies of the power and control winding currents. The state variables λ_{qdp}, λ'_{qds}, V_{qdp}, V'_{qds}, and I_{qdo} are then calculated using Equations (4.77), (4.78), (4.63), (4.61), and (4.58).

4.4 Steady-State Results

The mathematical derivation given in Sections 4.2 and 4.3 are used to obtain the steady-state results of the generator systems shown in Figure 4.1(a) and Figure 4.1(b). The results are verified experimentally by running the rotor of the generator at 750 and 825 rev./min corresponding to rotor angular electrical frequencies of 50Hz and 55Hz respectively. Cq = 90μF and Cp = 166μF are chosen. The Matlab program used to solve these nonlinear system equations is listed at appendix 4C. Figure 4.3 gives measured and calculated steady-state performance characteristics of the generator feeding an impedance load (generator system in Figure 4.1(a)). We can see from Figure 4.3(a) that output power is inversely proportional to the load resistor when the load resistor is bigger than some values; however the output power sharply decreases when the load resistor continuously reduces in the range, which has the values smaller than those values. Then the generator loses output power when the load resistor reaches its minimum limited value that is approximately equal to 12 ohms for this experimental generator system. Figure 4.3(b) shows that the higher the rotor speeds are, the larger the output power and load voltage. The maximum power points are clearly seen in this figure.

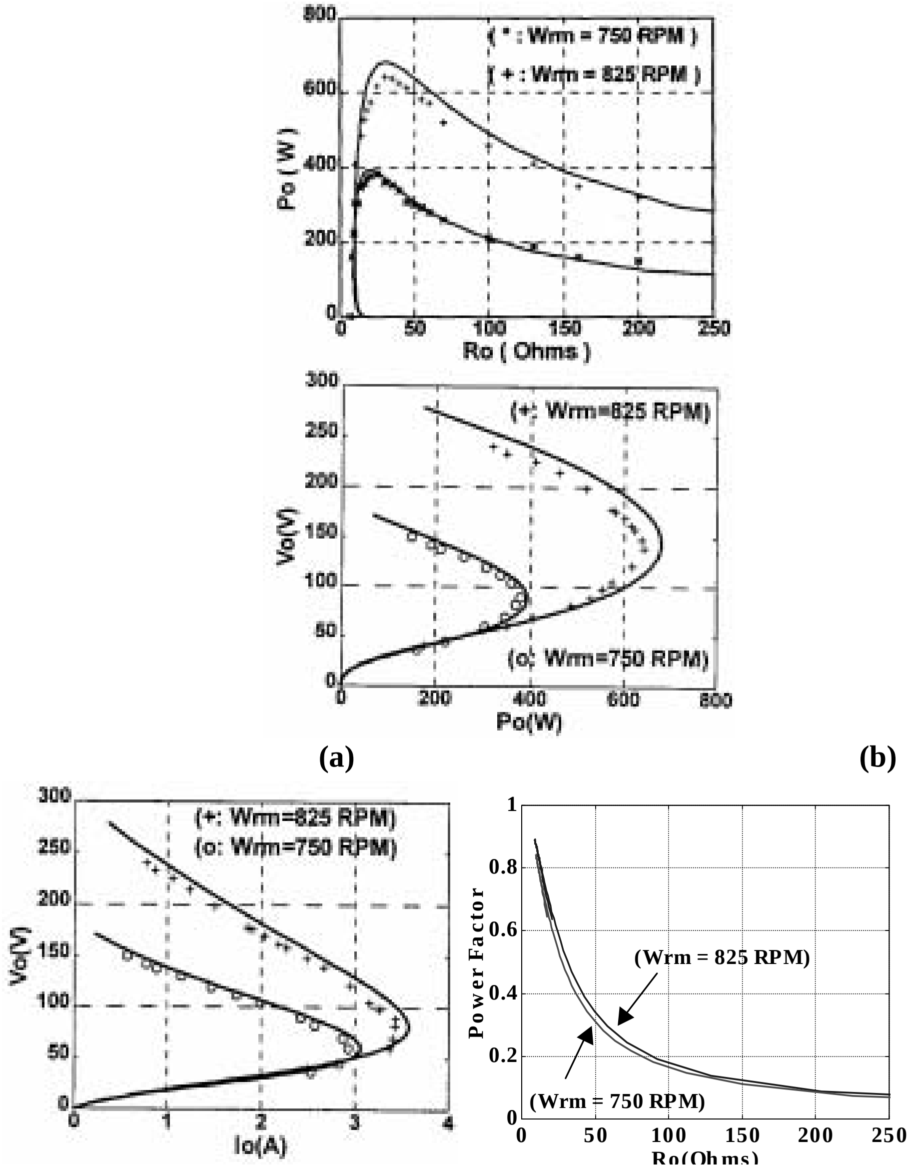

(a) **(b)**

(c) (d)

Figure 4.3. Measured and calculated results of doubly-fed reluctance generator system feeding impedance loads. (a) Output power against per-phase load resistance, (b) load

voltage against output power, (c) load voltage against load current, (d) power factor against load resistance.

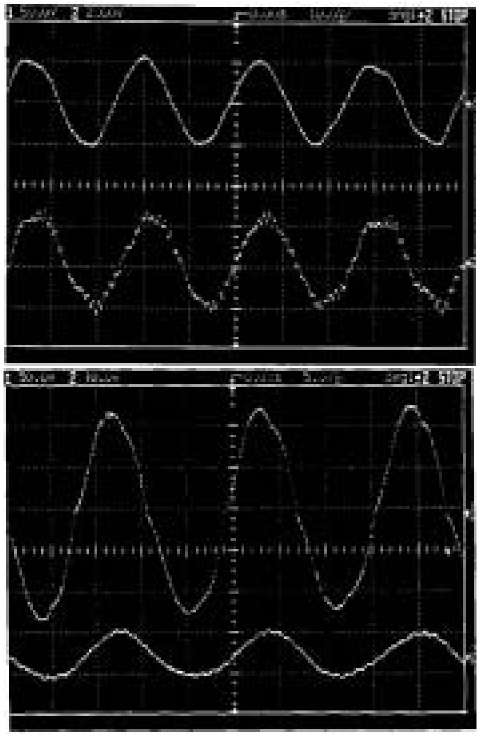

(a) (b)

Figure 4.4. Measured generator waveforms (rotor speed =850 rev/min, load resistance 20Ω) (10ms/div). (a) Generator line-line voltage (Top)(50V/div) and Generator phase current (Bottom)(2A/div), (b) control winding line-line voltage (Top)(50V/div) and Phase current in C_q (Bottom)(5A/div).

The relationships between the load voltages and currents are illustrated in Figure 4.3(c), in which the maximum load current points are easily obtained. It is observed from Figure 4.3(a)-(c) that there is good correlation between measurement and calculation results. The little discrepancies between measured and calculated results may be due to the high sensitivity of the machine performance to magnetic saturation and the presence of significant current space-harmonic components evidenced in the waveforms shown in Figure 4.4. In Figure 4.3(d), we can see that power factor will decrease with increasing load resistance and there is little affect with different rotor speeds.

Figure 4.5 shows the calculated generator characteristics of self-exciting generator system feeding an impedance load with three different inductance values. Increasing inductance value causes the increment of outout voltage, generator power factor, and

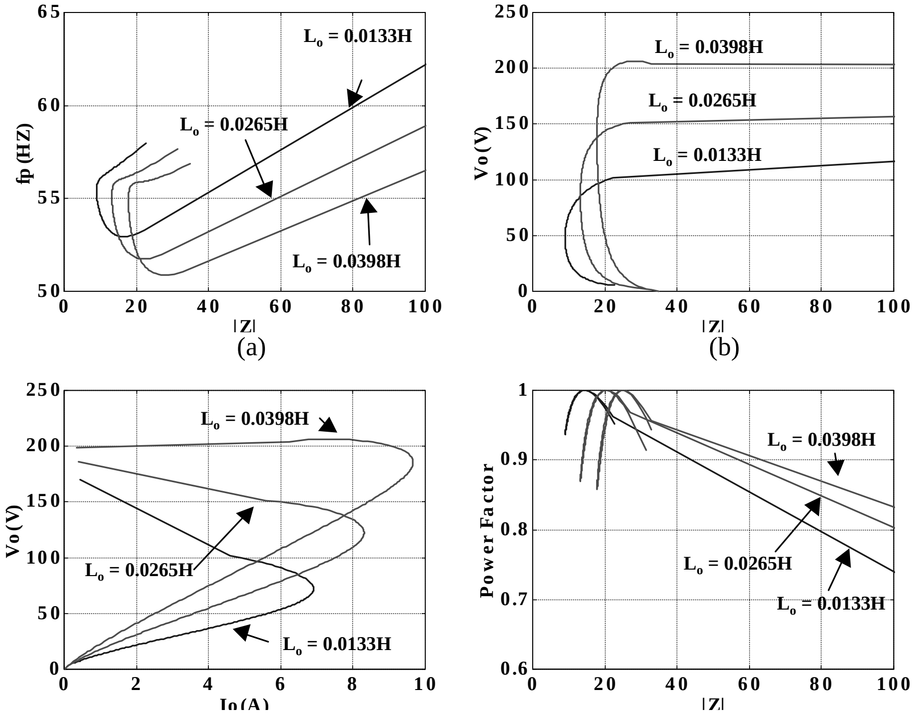

(a) (b)

(c) (d)

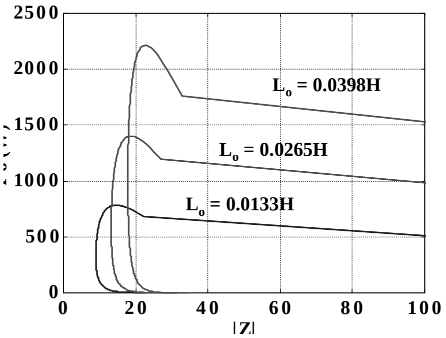

(e)

Figure 4.5. Calculated generator characteristics of self-exciting generator system feeding impedance load. (C_p=65uf, C_q =45uf, W_{rm} = 1800RPM) (a) Power winding frequency vs. load impedance, (b) load voltage vs. load impedance, (c) load voltage vs. load current, (d) generator power factor vs. load impedance, (e) output power vs. load impedance.

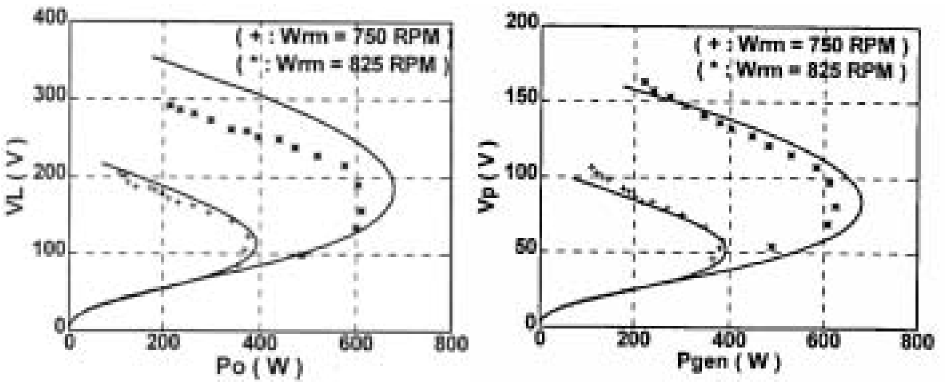

(a) (b)

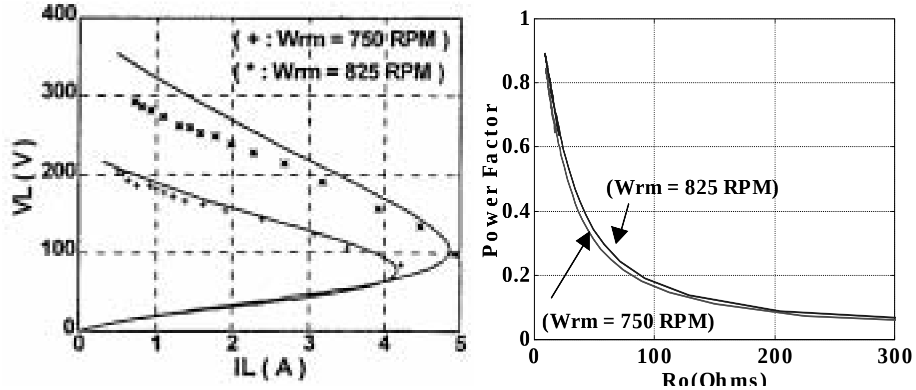

(c) (d)

Figure 4.6. Measured and calculated results of generator system feeding a loaded rectifier (ω_{rm} = 825 rev/min and ω_{rm} = 750 rev/min). (a) Load voltage against output power, (b) generator voltage against output power, (c) output voltage against load current, (d) power factor against load resistance.

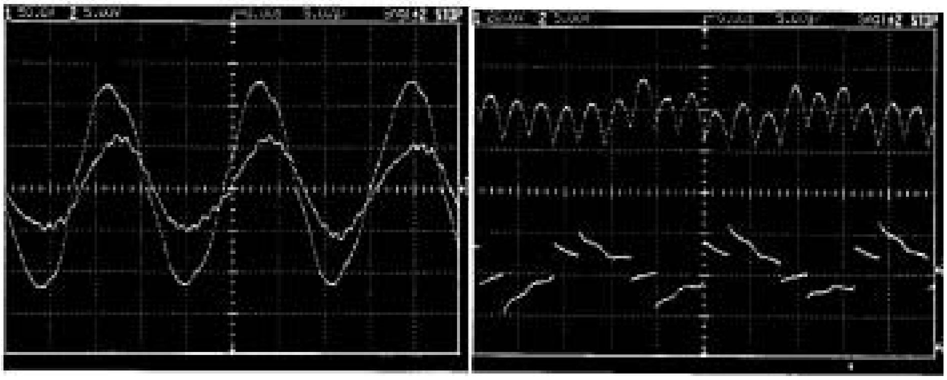

(a) (b)

Figure 4.7. Measured waveforms of generator system feeding a rectifier load.

(a) Generator line-line voltage (Top)(50V/div) and generator phase current (Bottom)(1A/div), (b) output rectifier voltage (Top)(50V/div) and Input rectifier current (bottom)(1A/div).

output power, as shown in Figures 4.5 (b), (d), and (e), respectively. The higher the load inductance, the higher the output maximun voltage, as shown in Figure 4.5(b). In Figure 4.5(a), we note that the frequency of power winding voltage and current increases with increasing the impedance value of load.

Figure 4.6 shows measured and calculated performance characteristics with the generator feeding a rectifier having a resistive load. Two rotor speeds: 725rev/min and 825rev/min, are choose for the steady-state calculation and experimental measurement.

The curves shown in Figures 4.6(a)-(d) are very similar to those in Figures 4.4(a)-(c), because a rectifier feeding a resistive load is equivalent to a resistive load on the fundamental component basis.

We can see that the higher the rotor speed is, the larger the output power, load voltage and load current. The maximum powers and load currents relating to two rotor speeds can be obtained in these figures. The correspondence experiment and calculation results are fairly good in view of the harmonics imposed on the generator voltages and currents due to the switching diodes shown in Figure 4.7.

4.5 Power Capability and Parametric Analysis

The active power supplied by the source of mechanical power to the generator systems in Figure 4.1(a) and Figure 4.1(b) are distributed to the power and control windings. The distributions of the active power across the airgaps determined by the Manley-Rowe power/frequency relationships are given as

$$\begin{gathered} \frac{P(\omega_p)}{\omega_p} + \frac{P(\omega_p + \omega_s)}{\omega_p + \omega_s} = 0 \\ \frac{P(\omega_s)}{\omega_s} + \frac{P(\omega_p + \omega_s)}{\omega_p + \omega_s} = 0 \quad . \end{gathered} \tag{4.79}$$

Note that P (ω_p +ω_s) is the power input to the airgap by a source with angular frequency given by ω_p +ω_s. It is evident from equation $\omega_{rm} = \omega r/(p_1+q)$ that P (ω_p +ω_s) is the input mechanical shaft power. Assuming that power input to airgap is positive and power received from the airgap is negative, the following relationships are derivable from Equation 4.79:

$$\frac{P(\omega_s)}{P(\omega_p)} = \frac{\omega_s}{\omega_p} = \sigma$$

$$\frac{P(\omega_p)}{P(\omega_p + \omega_s)} = \frac{\omega_p}{\omega_p + \omega_s} = \frac{1}{1+\sigma} \quad .$$

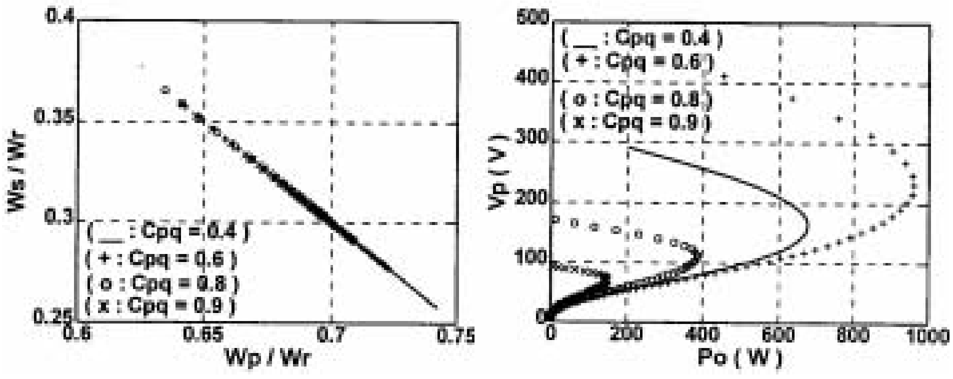

(a) (b)

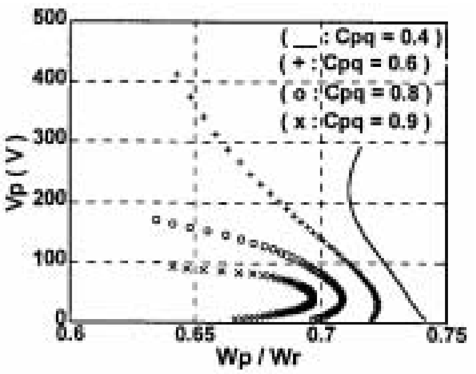

(c)

Figure 4.8. Parametric characteristics of generator feeding a resistive load rotor speed = 900 rev/min. (-: $C_{pq} = 0.4$; +: $C_{pq} = 0.6$; °: $C_{pq} = 0.8$; ×: $C_{pq} = 0.9$).

(a) Relative control winding frequency against load frequency, (b) load voltage against load power, (c) load voltage against relative load frequency.

Hence, the ratio of power transferred across the airgap to the power winding to meet load demand, power winding core and copper losses is directly proportional to the ratio of the power winding frequency and angular rotor speeds. Furthermore, it is inferred that smaller the angular frequency of the control winding, the higher the percentage of shaft power that can be utilized to meet load demand. In stand-alone generator applications operated by regulated turbines requiring regulated load frequency, capacitors C_q and C_p must be chosen to make ω_p to be slightly lower than the rotor angular speed. If an inverter is connected to the control winding, the frequency of the inverter source voltage must also be very low to ensure that most of the active power is sent to the power winding circuit. Figure 4.8 shows how the performance characteristics of the experimental machine are influenced by the selection of the capacitor C_p and C_q. The steady-state analysis chose C_q=90μF $(C_q^{'} = 360\mu F)$ and rotor speed ω_{rm}=900 rev/min, then different ratios $C_{pq} = C_p / C_q^{'}$, which are 0.4, 0.6, 0.8, and 0.9, are selected. Figure 4.8(a) shows that the ratios of capacity affect the regular range of power winding speed ω_p and control winding speed ω_s. Hence, the maximum frequency of the power winding current is different and directly relative to the capacitive ratios. The voltage and the output power does not increase monotonically with the capacitive ratios, which are shown in Figures 4.8(b) and 4.8(c). Figure 4.8(b) shows the relationship between output power and load voltage, where we can see that maximum output power curve is obtained when the capacitive ratio is 0.6. The relationship between load voltage and power winding frequency is shown in Figure 4.8(c). We also can see that the maximum load voltage curve is obtained when the capacitive ratio is 0.6.

4.6 Simulation of Self-Excitation Process

The electrical starting transient of the dual-winding reluctance generator system with an impedance load (shown in Figure 4.1(a)) is simulated. The system are described using following equations:

$$\omega_p + \omega_s = (p_1+q)\,\omega_{rm} \tag{4.80}$$

$$V_{qp} = R_{qp} I_{qp} + p\lambda_{qp} + \omega_p \lambda_{dp} \tag{4.81}$$

$$V_{dp} = R_{dp} I_{dp} + p\lambda_{dp} - \omega_p \lambda_{qp} \tag{4.82}$$

$$V_{qs}^{'} = R_{qs}^{'} I_{qs}^{'} + p\lambda_{qs}^{'} - \omega_{sp} \lambda_{ds}^{'} \tag{4.83}$$

$$V_{ds}^{'} = R_{ds}^{'} I_{ds}^{'} + p\lambda_{ds}^{'} + \omega_s \lambda_{qs}^{'} \tag{4.84}$$

$$pV_{qp} = \frac{1}{C_p}(-I_{qp} - I_{qo}) - \omega_p V_{dp} \tag{4.85}$$

$$pV_{dp} = \frac{1}{C_p}(-I_{dp} - I_{do}) + \omega_p V_{qp} \tag{4.86}$$

$$L_o pI_{qo} + R_o I_{qo} + \omega_p L_o I_{do} = V_{qp} \tag{4.87}$$

$$L_o pI_{do} + R_o I_{do} - \omega_p L_o I_{qo} = V_{dp} \tag{4.88}$$

$$pV_{qs}^{'} = -\frac{1}{C_q} I_{qs}^{'} + \omega_s V_{ds}^{'} \tag{4.89}$$

$$pV_{ds}^{'} = -\frac{1}{C_q} I_{ds}^{'} - \omega_s V_{qs}^{'} \tag{4.90}$$

where

$$\lambda_{qp} = L_{qp} I_{qp} + L_{qm} I_{qs}^{'} = L_{lpq} I_{qp} + L_{mq}(I_{qp} + I_{qs}^{'}) \tag{4.91}$$

$$\lambda_{dp} = L_{dp} I_{ds} + L_{dm} I_{ds}^{'} = L_{lpd} I_{dp} + L_{md}(I_{dp} + I_{ds}^{'}) \tag{4.92}$$

$$\lambda_{qs}^{'} = L_{qs}^{'} I_{qs}^{'} + L_{qm} I_{qp} = L_{lsq}^{'} I_{qs}^{'} + L_{mq}(I_{qp} + I_{qs}^{'}) \tag{4.93}$$

$$\lambda_{ds}^{'} = L_{ds}^{'} I_{ds}^{'} + L_{dm} I_{dp} = L_{lsd}^{'} I_{ds}^{'} + L_{md}(I_{dp} + I_{ds}^{'}) \tag{4.94}$$

$$L_{lpq} = L_{pq} - L_{mq} \tag{4.95}$$

$$L_{lpd} = L_{pd} - L_{md} \tag{4.96}$$

$$L_{lsq}^{'} = L_{sq}^{'} - L_{mq} \tag{4.97}$$

$$L_{lsd}^{'} = L_{sd}^{'} - L_{md} \tag{4.98}$$

$$\lambda_{qm} = L_{mmq}\left[\frac{\lambda_{qp}}{L_{lpq}} + \frac{\lambda_{qs}^{'}}{L_{lsq}^{'}}\right] \tag{4.99}$$

$$\lambda_{dm} = L_{mmd}\left[\frac{\lambda_{dp}}{L_{lpd}} + \frac{\lambda_{ds}^{'}}{L_{lsd}^{'}}\right] \tag{4.100}$$

$$R_{pq} = r_p + R_{mpq} \tag{4.101}$$

$$R_{pd} = r_p + R_{mpd} \tag{4.102}$$

$$R_{msq}^{'} = r_s^{'} + R_{msq}^{'} \tag{4.103}$$

$$R_{msd}^{'} = r_s^{'} + R_{msd}^{'} \tag{4.104}$$

$$R_{mpq} = -4.05\lambda_{mq}^2 - 1.47\lambda_{mq} + 1.217 \tag{4.105}$$

$$R_{msq}^{'} = 7.24\lambda_{mq}^2 - 4.25\lambda_{mq} + 1.58 \tag{4.106}$$

$$L_{mq} = -0.44\lambda_{mq}^2 + 0.085\lambda_{mq} + 0.0164 \tag{4.107}$$

$$L_{pq} = -0.36\lambda_{mq}^2 + 0.0906\lambda_{mq} + 0.0373 \tag{4.108}$$

$$L_{sq}^{'} = -0.55\lambda_{mq}^2 + 0.09\lambda_{mq} + 0.0385 \tag{4.109}$$

$$R_{mpd} = -4.05\lambda_{md}^2 - 1.47\lambda_{md} + 1.217 \tag{4.110}$$

$$R_{msd}^{'} = 7.24\lambda_{md}^2 - 4.25\lambda_{md} + 1.58 \tag{4.111}$$

$$L_{md} = -0.44\lambda_{md}^2 + 0.085\lambda_{md} + 0.0164 \tag{4.112}$$

$$L_{pd} = -0.36\lambda_{md}^2 + 0.0906\lambda_{md} + 0.0373 \tag{4.113}$$

$$L_{sd}^{'} = -0.55\lambda_{md}^2 + 0.09\lambda_{md} + 0.0385\,. \tag{4.114}$$

The effect of magnetizing flux-linkage saturation on the machine parameters must be accounted for and a means must be found to determine either ω_p or ω_s from Equation (4.80) given the rotor speed. If the magnetizing path is unsaturated, all the machine parameters are constant but vary with magnetizing flux linkage under saturated condition. The parameter variations are accounted for by choosing a reference frame speed for the power winding (ω_p), such that the total magnetizing flux linkage is aligned with q-axis. The d-axis magnetizing flux linkage and its derivative then become identically equal to zero. These conditions are expressed as

$$\lambda_{dm} = 0 \tag{4.115}$$

$$p\lambda_{dm} = 0\ . \tag{4.116}$$

When the condition (4.115) is enforced in Equations (4.81)-(4.94), all d-axis machine parameters become constant while all q-axis parameters are dependent on the q-axis magnetizing linkage.

When the conditions expressed in Equations (4.115)-(4.116) are used in Equation (4.100), the following Equations (4.117) and (4.118) are obtained

$$\lambda_{dp} = -\frac{L_{lpd}}{L^{'}_{lsd}} \lambda^{'}_{ds} \tag{4.117}$$

$$p\lambda_{dp} = -\frac{L_{lpd}}{L^{'}_{lsd}} p\lambda^{'}_{ds} \quad . \tag{4.118}$$

Because the machine parameters are dependent on the magnetizing flux linkage, it is necessary to use flux linkages as state variables in generator system equations. To realize this purpose, the following derivations are done.

The derivation from Equations (4.91)-(4.94) yield following equation:

$$-R_{pq} I_{qp} = T_{ppq}\lambda_{qp} + B_{ppq}\lambda^{'}_{qs} \tag{4.119}$$

$$-R_{pd} I_{dp} = T_{ppd}\lambda_{dp} + B_{ppd}\lambda^{'}_{ds} \tag{4.120}$$

where

$$T_{ssq1} = \frac{-R_{pq}L^{'}_{sq}}{L_{pq}L^{'}_{sq} - L^{2}_{mq}}, \qquad B_{ssq1} = \frac{R_{pq}L_{mq}}{L_{pq}L^{'}_{sq} - L^{2}_{mq}}$$

$$T_{ssd1} = \frac{-R_{pd}L^{'}_{sd}}{L_{pd}L^{'}_{sd} - L^{2}_{md}}, \qquad B_{ssd1} = \frac{R_{pd}L_{md}}{L_{pd}L^{'}_{sd} - L^{2}_{md}}$$

$$-R^{'}_{sq} I^{'[}_{qs} = T_{ssq}\lambda^{'}_{qs} + B_{ssq}\lambda_{qp} \tag{4.121}$$

$$-R^{'}_{sd} I_{ds} = T_{ssd}\lambda^{'}_{ds} + B_{ssd}\lambda_{dp} \tag{4.122}$$

where

$$T_{ssq2} = \frac{-R^{'}_{sq}L_{qp}}{L_{pq}L^{'}_{sq} - L^{2}_{mq}}, \qquad B_{ssq2} = \frac{R^{'}_{sq}L_{mq}}{L_{pq}L^{'}_{sq} - L^{2}_{mq}}$$

$$T_{ssd2} = \frac{-R^{'}_{sd}L_{sd}}{L_{pd}L^{'}_{sd} - L^{2}_{md}}, \qquad B_{ssd2} = \frac{R^{'}_{sd}L_{md}}{L_{pd}L^{'}_{sd} - L^{2}_{md}} \quad .$$

Substituting Equations (4.119)-(4.122) into Equations (4.80)-(4.90) yield

$$p\lambda_{qp} = V_{qp} + T_{ssq1}\lambda_{qp} - \omega_{p}\lambda_{dp} + B_{ssq1}\lambda^{'}_{qs} \tag{4.123}$$

$$p\lambda_{dp} = V_{dp} + T_{ssd1}\lambda_{dp} + \omega_{p}\lambda_{qp} + B_{ssd1}\lambda^{'}_{ds} \tag{4.124}$$

$$p\lambda^{'}_{qs} = V^{'}_{sq} + T_{ssq2}\lambda^{'}_{qs} - (\omega_{p} - \omega_{r})\lambda^{'}_{ds} + B_{ssq2}\lambda_{qp} \tag{4.125}$$

$$p\lambda^{'}_{ds} = V^{'}_{ds} + T_{ssd2}\lambda^{'}_{ds} + (\omega_{p} - \omega_{r})\lambda^{'}_{qs} + B_{ssd2}\lambda_{dp} \tag{4.126}$$

$$pV_{qp} = \gamma_{1}T_{sq1}\lambda_{qp} + B_{sq1}\gamma_{1}\lambda^{'}_{qs} - \omega_{p}V_{dp} - \gamma_{1}I_{qo} \tag{4.127}$$

$$pV_{dp} = \gamma_{1}T_{sd1}\lambda_{dp} + B_{sd1}\gamma_{1}\lambda^{'}_{ds} + \omega_{p}V_{qp} - \gamma_{1}I_{do} \tag{4.128}$$

$$pI_{qo} = \frac{1}{L_o} V_{qp} - \frac{R_o}{L_o} I_{qo} - \omega_p I_{do} \tag{4.129}$$

$$pI_{do} = \frac{1}{L_o} V_{dp} - \frac{R_o}{L_o} I_{do} + \omega_p I_{qo} \tag{4.130}$$

$$pV'_{qs} = \gamma_2 T_{sq2} \lambda'_{qs} + B_{sq2} \gamma_2 \lambda_{qp} - (\omega_p - \omega_r) V'_{ds} \tag{4.131}$$

$$pV'_{ds} = \gamma_2 T_{ds2} \lambda'_{ds} + B_{sd2} \gamma_2 \lambda_{dp} + (\omega_p - \omega_r) V'_{qs} \tag{4.132}$$

where

$$T_{sq1} = \frac{-L'_{sq}}{L_{pq} L'_{sq} - L_{mq}^2}, \qquad B_{sq1} = \frac{L_{mq}}{L_{pq} L'_{sq} - L_{mq}^2}$$

$$T_{sd1} = \frac{-L'_{sd}}{L_{pd} L'_{sd} - L_{md}^2}, \qquad B_{sd1} = \frac{L_{md}}{L_{pd} L'_{sd} - L_{md}^2}$$

$$T_{sq2} = \frac{-L_{qp}}{L_{pq} L'_{sq} - L_{mq}^2}, \qquad B_{sq2} = \frac{L_{mq}}{L_{pq} L'_{sq} - L_{mq}^2}$$

$$T_{sd2} = \frac{-L_{sd}}{L_{pd} L'_{sd} - L_{md}^2}, \qquad B_{sd2} = \frac{L_{md}}{L_{pd} L'_{sd} - L_{md}^2}$$

$$\gamma_1 = \frac{1}{C_p}, \qquad \gamma_2 = \frac{1}{C_q} \ .$$

Substituting Equations (4.124) and (4.126) into Equation (4.116) yields Equation (4.133), in which ω_p is expressed in terms of ω_r, flux linkages and machine parameters.

$$\omega_p = -\frac{(\omega_A + \omega_b)}{L'_{lsd} \lambda_{qp} + L_{lpd} \lambda'_{qs}} \tag{4.133}$$

where

$$\omega_A = (V_{dp} L'_{lsd} + V'_{ds} L_{lpd} - L_{lpd} \omega_r \lambda'_{qs})$$

$$\omega_B = \lambda_{dp} (T_{ssd1} L'_{lsd} + B_{ssd2} L_{lpd} - \frac{L'^2_{lsd}}{L_{lpd}} B_{ssd1} - L_{lpd} \omega_r \lambda'_{qs}) \ .$$

Equations (4.123)-(4.132) and Equation (4.133) are used for the simulation of the electrical starting transient of the dual-winding reluctance generator. The self-excitation process of the generator feeding an impedance load was simulated with values of C_p and C_q Selected as 168μF and 360μF, respectively, and a constant rotor speed of 1500 rev/min.

The simulation results given in Figure 4.9 display the growth of the generator terminal voltage and current as the magnetizing flux linkage builds up. Saturation effect limits the growth of the magnetizing flux linkage, which brings the generator to a stable 0perating condition. Figure 4.10 gives experimental results for the self-excitation process corresponding to the simulation results. The simulation results are similar to the

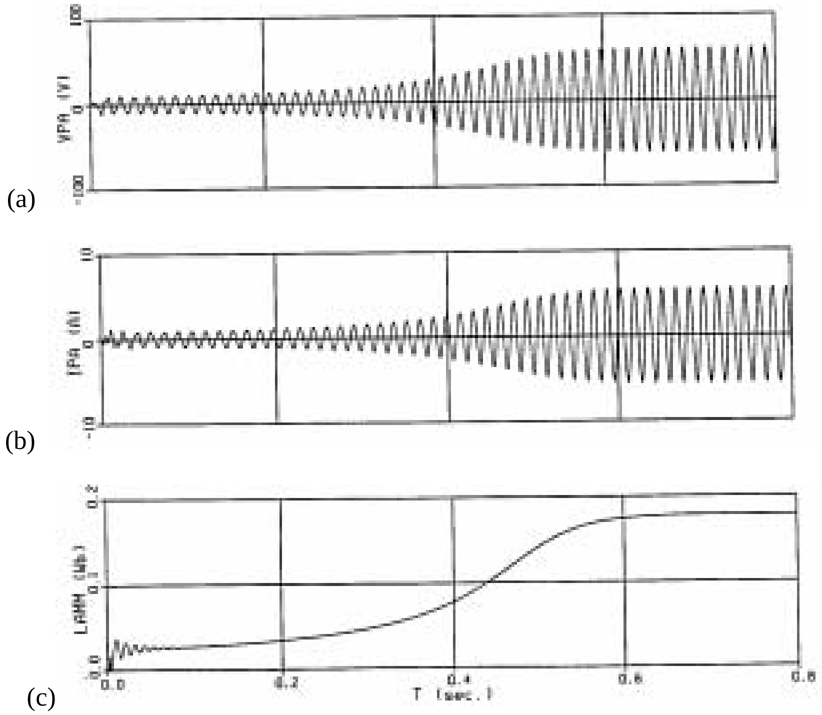

Figure 4.9. Self-excitation process of doubly-fed reluctance generator. (a)Power winding phase voltage, (b) power winding phase current, (c) magnetizing flux linkage magnitude.

experimental results, which proves that mathematical model used in the simulation program effectively reflects the true situation.

We also simulate the de-excitation phenomenon of the generator. When the generator is critically loaded such as when the load impedance is reduced beyond a certain threshold value, the load voltages collapse (de-excite) due to a rapidly reducing airgap flux linkage. This dynamic process is displayed in Figure 4.10. Figure 4.10(a) shows the dynamic process of airgap flux linkage when the load impedance is reduced

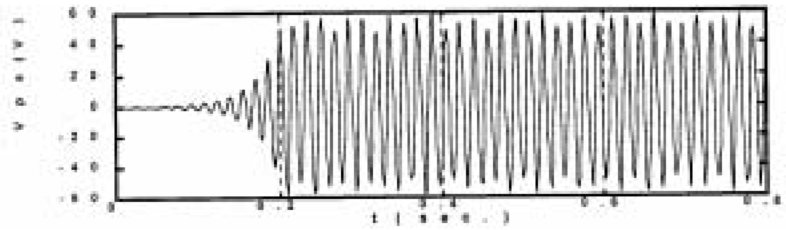

(a)

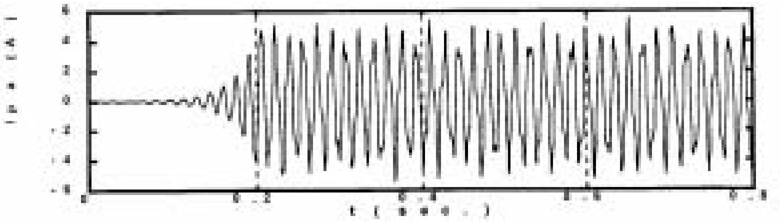

(b)

Figure 4.10. Experimental waveforms of self-excitation process.

(a) Power winding phase voltage, (b) power winding phase current.

beyond a certain threshold value. The collapse process of the voltage and current is shown in Figures 4.11(b) and (c). (The simulation program is listed in Appendix 4C)

Comment [GS1]:

4.7 Conclusions

This chapter sets forth the analysis and performance prediction of a stand-alone dual winding reluctance generator with capacitive excitation in both the power and control windings. A q-d model of the generator is proposed that accounts for the core and harmonic losses and the influence of magnetic path saturation on the machine self and mutual inductances. This should find utility in the accurate prediction of the dynamic and transient performance of the generator and in the design optimization of stand-alone

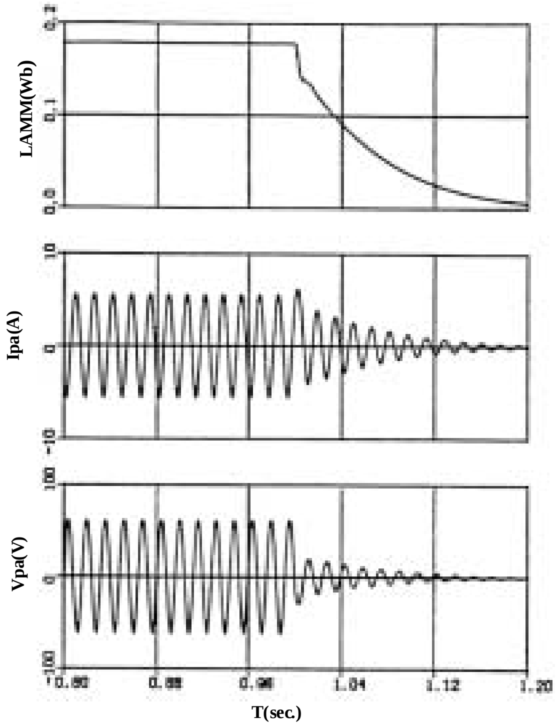

Figure 4.11. Voltage de-excitation phenomena in the generator feeding R-L load.

(a) Airgap flux linkage, (b) power winding phase current, (c) power winding phase voltage.

doubly-fed reluctance generators. Measured performance characteristics compare favorably with the analysis results.

CHAPTER 5

SYNCHRONOUS OPERATION OF A DOUBLY-FED RELUCTANCE GENERATOR

5.1 Introduction

A doubly-fed reluctance machine can realize its synchronous operation when its control windings are supplied by a direct current (DC) source. The machine can be working in the synchronous mode as generator or motor. The frequency of load voltage generated in power winding is directly dependent on the rotor speed in the generating mode. The rotor electrical angular frequency is proportional to AC supply angular frequency of the power windings in the motoring mode based on the angular frequency relationship $\omega_p = (p_1 + q)\omega_{rm}$.

Doubly-fed synchronous reluctance motors show potential in fan, pump, refrigeration and air-conditioning applications. It is anticipated that the machine will also find utility as a medium to high frequency generator in stand-alone applications such as in airplane power systems and marine generator for gas turbine drives [7,14]. The obvious advantages of this generator system include the absence of brushes, slip rings and possibility of operating the load at leading or unity power factor by controlling the excitation current.

In this chapter, the performance of doubly-fed synchronous generator is investigated when feeding an impedance load and a rectifier load. This chapter is

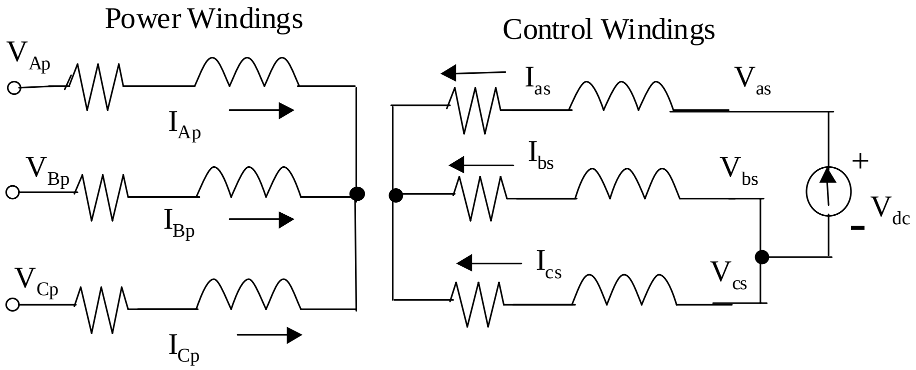

Figure 5.1. Schematic diagram of the doubly-fed reluctance machine with DC excitation.

organized as follow. Section 5.2 gives the derivation of the machine voltage and torque equations using the concept of q-d harmonic balance technique, including the effect of magnetic saturation, core and harmonic losses. The operation of the machine in stand-alone generator mode feeding an impedance load is set forth in Section 5.3. This section also contains comparison of experimental and simulation results. The generator connected to a three-phase rectifier feeding a load is analyzed in Section 5.4. Finally the concluding remarks are contained in Section 5.5.

5.2 Machine Model

With the power windings connected to a balanced three-phase voltage source having a frequency of ω_p and the control winding connected to a DC voltage source as shown in Figure 5.1, the voltage equations of the control windings are expressed as

$$V_{as} = R_s I_{as} + p\lambda_{as} \tag{5.1}$$

$$V_{bs} = R_s I_{bs} + p\lambda_{bs} \tag{5.2}$$

$$V_{cs} = R_s I_{cs} + p\lambda_{cs}\,. \tag{5.3}$$

The flux linkages of the control winding are also given as:

$$\lambda_{as} = L_{aa} I_{as} + L_{ab} I_{bs} + L_{ac} I_{cs} + L_{aA} I_{Ap} + L_{aB} I_{Bp} + I_{aC} I_{Cp} \tag{5.4}$$

$$\lambda_{bs} = L_{ba} I_{as} + L_{bb} I_{bs} + L_{bc} I_{cs} + L_{bA} I_{Ap} + L_{bB} I_{Bp} + I_{bC} I_{Cp} \tag{5.5}$$

$$\lambda_{as} = L_{ca} I_{as} + L_{cb} I_{bs} + L_{cc} I_{cs} + L_{cA} I_{Ap} + L_{cB} I_{Bp} + I_{cC} I_{Cp} \tag{5.6}$$

Where L_{aa}, L_{bb} , L_{cc} are the self-inductances of the control windings carrying currents I_{as} ,I_{bs} ,I_{cs} , respectively; L_{ab}, L_{ac} , L_{bc} are the mutual-inductances between the phase-windings of control windings. The mutual-inductances between the control windings and power windings are given by $L_{i,j}$ where $i = a, b, c$ *and* $j = A, B, C$. I_{ap}, I_{bp} and I_{cp} are the currents flowing in the power windings.

The inductances are given by the following expression [25]:

$$L_{aa} = L_{bb} = L_{cc} = L_{ls} + L_{ms}$$

$$L_{ab} = L_{ac} = L_{bc} = -L_{ms/} / 2$$

$$L_{AA} = L_{BB} = L_{CC} = L_{lp} + L_{mp}$$

$$L_{AB} = L_{AC} = L_{BC} = -L_{msp} / 2$$

$$L_{i,j} = L_{m12} \cos(\theta_r + k\beta), \beta = 2\pi / 3, k = 0,1,2 \tag{5.7}$$

$$k = 0 \text{ for } L_{Aa} = L_{Bc} = L_{Cb}$$

$$k = 1 \text{ for } L_{Ab} = L_{Ba} = L_{Cc}$$

$$k = 2 \text{ for } L_{Ac} = L_{Ca} = L_{Bb}$$

$$L_s = \frac{3}{2} L_{m12} + L_{ls}$$

$$L_p = \frac{3}{2} L_{m12} + L_{lp} \, .$$

L_{m12} is given by

$$L_{m12} = -2P_r \frac{\mu_0 r l N_A N_a}{g_1(q-p_1)} \sin[(p_1+q)\frac{\pi\alpha}{2p_r}]$$

where, p_1, q, and Pr are the pole pair number of power windings, control windings, and rotor, respectively. r is the radius of stator. l is the length of stator lamination. N_A and N_a are the winding functions of power windings and control windings (see Figures 3.3 and 3.4). g_1 is air-gap width and α is pole-arc width (see Figure 3.1). μ_0 is magnetic permeability.

Three real signals (f_a, f_b, f_c) which could be three-phase balanced voltages, currents, flux linkages, etc., can be transformed into a complex-form signal (f_{qd}) and zero sequence signal (f_n) using the following equations where θ is the reference frame angle:

$$\begin{aligned} f_{qd} &= \frac{2}{3} e^{-j\theta}[f_a + af_b + a^2 f_c] \\ f_n &= \frac{\sqrt{2}}{3}[f_a + f_b + f_c] \, . \end{aligned} \tag{5.8}$$

It can also be shown that the original signals can be recovered from the transformed quantities using the following expressions:

$$\begin{aligned} f_a &= \mathrm{Re}[f_{qd} e^{j\theta}] + \frac{1}{\sqrt{2}} f_n \\ f_b &= \mathrm{Re}[a^2 f_{qd} e^{j\theta}] + \frac{1}{\sqrt{2}} f_n \\ f_c &= \mathrm{Re}[af_{qd} e^{j\theta}] + \frac{1}{\sqrt{2}} f_n \\ a &= e^{j\frac{2\pi}{3}} \, . \end{aligned} \tag{5.9}$$

Using Equation (5.8) to transform the voltages and currents of the power windings with balanced three-phase voltage supply to a reference frame with an angular angle θ_p (or angular speed of ω_p), the zero sequence current (I_{np}) and voltage (V_{np}) are zero. The actual phase voltages and currents can be expressed in terms of the transformed complex-form current (I_{qdp}) by using Equation (5.9), which are given as

$$V_{Ap} = \mathrm{Re}[V_{qdp}e^{j\theta_p}], \quad V_{Bp} = \mathrm{Re}[a^2V_{qdp}e^{j\theta_p}], \quad V_{Cp} = \mathrm{Re}[aV_{qdp}e^{j\theta_p}] \tag{5.10}$$

$$I_{Ap} = \mathrm{Re}[I_{qdp}e^{j\theta_p}], \quad I_{Bp} = \mathrm{Re}[a^2I_{qdp}e^{j\theta_p}], \quad I_{Cp} = \mathrm{Re}[aI_{qdp}e^{j\theta_p}]. \tag{5.11}$$

From Figure 5.1, we can see

$$V_{dc} = V_{as} - V_{bs} \tag{5.12}$$

$$0 = V_{bs} - V_{cs} \tag{5.13}$$

$$I_{as} + I_{bs} + I_{cs} = 0 \ . \tag{5.14}$$

These phase voltages and currents are transformed into complex-form equations in the stationary reference frame, which are

$$V_{qds} = \frac{2}{3}V_{dc}, \qquad V_{ns} = \frac{2}{3}[V_{an} + V_{bn} + V_{cn}] \tag{5.15}$$

$$I_{qds} = \frac{2}{3}[\frac{3}{2}I_{as} + \frac{\sqrt{3}}{2}j(I_{bs} - I_{cs})], \quad I_{ns} = 0 \tag{5.16}$$

$$V_{as} = \mathrm{Re}[V_{qds}], \quad V_{bs} = \mathrm{Re}[a^2V_{qds}], \quad V_{cs} = \mathrm{Re}[aV_{qds}] \tag{5.17}$$

$$I_{as} = \mathrm{Re}[I_{qds}], \quad I_{bs} = \mathrm{Re}[a^2I_{qds}], \quad I_{cs} = \mathrm{Re}[aI_{qds}] \ . \tag{5.18}$$

Control Winding Mathematical Model

By substituting Equation (5.7) to Equations (5.1)-(5.3), the following derivation are done (detailed derivation is listed in Appendix 5A):

$$V_{as} = R_s I_{as} + p\lambda_{as}$$

$$= R_s I_{as} + p[L_{aa} I_{as} + L_{ab} I_{bs} + L_{ac} I_{cs} + L_{aA} I_{Ap} + L_{aB} I_{Bp} + I_{aC} I_{Cp}]$$

$$= R_s I_{as} + p\{(\frac{3}{2}L_{m12} + L_{ls})I_{as} + L_{m12}\cos[(p_1+q)\theta_{rm}]I_{As}$$

$$+\cos[(p_1+q)\theta_{rm} - \frac{2\pi}{3}]I_{Bs} + \cos[(p_1+q)\theta_{rm} + \frac{2\pi}{3}]I_{Cs}\}.$$

Defining $\beta = \frac{2\pi}{3}, \theta_x = (p_1+q)\theta_{rm}$ and using the following relationships:

$$\mathrm{Re}\,al(A)\cdot \mathrm{Re}\,al(B) = \frac{1}{2}[\mathrm{Re}\,al(A\cdot B) + \mathrm{Re}\,al(A\cdot B^*)] \tag{5.19}$$

$$1 + e^{j\beta} + e^{-j\beta} = 0 \tag{5.20}$$

the following expression of V_{as} is obtained

$$V_{as} = R_s I_{as} + p\{L_s I_{as} + \frac{3}{2}L_{m12}\,\mathrm{Re}(I_{dqp}^* e^{j(\theta_p - \theta_r)})\}\ . \tag{5.21}$$

Substituting equation (5.10)-(5.11) and (5.15)-(5.18) into equation (5.21) yields the q-d complex-form voltage equations (in the stationary reference frame) for the control windings given as

$$V_{qds} = \frac{2}{3}V_{dc} = R_s I_{qds} + p[L_s I_{qds} + \frac{3}{2}L_{m12} I_{qdp} e^{j(\theta_p - \theta_r)}]. \tag{5.22}$$

Extending equation (5.22) into q-axis and d-axis equations (in the synchronous reference frame) gives

$$\frac{2}{3}V_{dc} = R_s I_{qs} + p(L_s I_{qs} + \frac{3}{2}L_{m12} I_{qp}) \tag{5.23}$$

$$0 = R_s I_{ds} + p(L_s I_{ds} + \frac{3}{2}L_{m12} I_{dp}). \tag{5.24}$$

Power Winding Mathematical Model

The phase 'A' voltage of balanced three-phase power windings is also given as (The detailed derivation is obtained in Appendix 5B):

$$V_{Ap} = R_p I_{Ap} + p\lambda_{Ap} \tag{5.25}$$

where the flux linkage is given in Equation (5.26):

$$\lambda_{Ap} = L_{AA} I_{Ap} + L_{AB} I_{Bp} + L_{AC} I_{Cp} + L_{Aa} I_{as} + L_{Ab} I_{bs} + L_{Ac} I_{cs} \ . \tag{5.26}$$

Using Equation (5.7) to Equation (5.26) and then substituting Equation (5.26) into Equation (5.25) yield

$$\begin{aligned} V_{Ap} &= R_p I_{Ap} + p[L_{AA} I_{Ap} + L_{AB} I_{Bp} + L_{AC} I_{Cp} + L_{Aa} I_{as} + L_{Ab} I_{bs} + L_{Ac} I_{cs}] \\ &= (R_p I_{Ap} + L_p p I_{Ap}) + L_{m12} p\{\mathrm{Re}(e^{j\theta_x}) I_{as} + \mathrm{Re}(e^{j\theta_x} e^{-j\beta}) I_{bs} + \mathrm{Re}(e^{j\theta_x} e^{j\beta}) I_{cs}\} \ . \end{aligned} \tag{5.27}$$

Replacing the V_{Ap} and I_{Ap} with the expression (5.10)-(5.11) which are substituted in Equation (5.27) and using harmonic balance principle yield the d-q complex-form equation of the power windings given as

$$\begin{aligned} V_{qdp} &= R_p I_{qdp} + j\omega_p [L_p I_{qdp} + \frac{3}{2} L_{m12} I_{qds} e^{j(\theta_r - \theta_p)}] \\ &\quad + p[L_p I_{qdp} + \frac{3}{2} L_{m12} I_{qds} e^{j(\theta_r - \theta_p)}] \ . \end{aligned} \tag{5.28}$$

Its q-axis and d-axis form equations from Equation (5.28) are obtained (in the synchronous reference frame ω_p)

$$V_{qp} = R_p I_{qp} - \omega_p (L_p I_{dp} + \frac{3}{2} L_{m12} I_{ds}) + p(L_p I_{qp} + \frac{3}{2} L_{m12} I_{qs}) \tag{5.29}$$

$$V_{dp} = R_p I_{dp} + \omega_p (L_p I_{qp} + \frac{3}{2} L_{m12} I_{qs}) + p(L_p I_{qd} + \frac{3}{2} L_{m12} I_{ds}) \ . \tag{5.30}$$

To combine the mathematical models of control windings and power windings in the same system, we chose the power windings as reference windings. After control windings are referred to the power windings using the winding turns-ratio, the system Equations (5.31)-(5.34) are obtained as

$$V_{qp} = R_p I_{qp} - \omega_p (L_p I_{dp} + L_m I'_{ds}) + p(L_p I_{qp} + L_m I'_{qs}) \tag{5.31}$$

$$V_{dp} = R_p I_{dp} + \omega_p (L_p I_{qp} + L_m I'_{qs}) + p(L_p I_d + L_m I'_{ds}) \tag{5.32}$$

$$\frac{2}{3} V_{dc} = R'_s I'_{qs} + p(L'_s I'_{qs} + L_m I_{qp}) \tag{5.33}$$

$$0 = R'_s I'_{ds} + p(L'_s I'_{ds} + L_m I_{dp}) \quad . \tag{5.34}$$

The q-d complex-form equations of power windings and control windings in the synchronous reference frame are given as Equations (5.35) and (5.36)

$$V_{qdp} = R_p I_{qdp} + j\omega_p [L_p I_{qdp} + L_m I'_{qds}] + p[L_p I_{qdp} + L_m I'_{qds}] \tag{5.35}$$

$$V'_{qds} = R'_s I'_{qds} + p[L'_s I'_{qds} + L_m I_{qdp}] \ . \tag{5.36}$$

Torque Equation

The mechanical equation of motion is expressed as

$$J p^2 \theta_{rm} = T_e - T_L \tag{5.37}$$

where the load torque is T_L, the moment of inertia of the rotor and connected load is J, and T_e is the electromagnetic torque. The electromagnetic torque is calculated from the magnetic co-energy. It can be shown that the electromagnetic torque is given as (see Appendix 5C)

$$T_e = \frac{3}{2}(p_1 + q) L_{m12} \,\mathrm{Re}[\, j I^*_{qdp} I_{qds} e^{j(\theta_r - \theta_p)}] \quad . \tag{5.38}$$

Considering the turns ratio between the power windings and control windings and since $\theta_r = \theta_p$, the time-invariant electromagnetic torque equation is

$$
\begin{aligned}
T_e &= \frac{3}{2}(p_1 + q)L_m \operatorname{Re}[jI^*_{qdp}I'_{qds}] \\
&= \frac{3}{2}(p_1 + q)L_m (I_{dp}I'_{qs} - I_{qp}I'_{ds}) \quad .
\end{aligned}
\tag{5.39}
$$

Since the core losses in the machine are significant, we use magnetizing flux dependent series or shunt core-loss resistances: R_{mp} and R'_{ms} to represents these losses. Considering these factors and using the flux linkage variables, the complex-form Equations (5.22) and (5.28) of the power windings and control windings are expressed as

With shunt core-loss resistances

$$V_{qdp}T_p = r_pT_pI_{qdp} + j\omega_p\lambda_{qdp} + p\lambda_{qdp}$$

$$V'_{qds} = r'_sT_sI'_{qds} + p\lambda'_{qds}$$

$$\lambda_{qdp} = L_pI_{qdp} + L_mI'_{qds}$$

$$\lambda'_{qds} = L'_sI'_{qds} + L_mI_{qdp}$$

where

$$T_p = \frac{R_{mp}}{r_p + R_{mp}}, \quad T_s = \frac{R'_{ms}}{r'_s + R'_{ms}}$$

$$r'_s = \left(\frac{N_p}{N_s}\right)^2 r_s, \quad L'_s = \left(\frac{N_p}{N_s}\right)^2 L_s$$

$$L_m = \frac{3}{2}\frac{N_p}{N_s}L_{m12}, \quad R'_{ms} = \left(\frac{N_p}{N_s}\right)^2 R_{ms}$$

$$I_{qds}^{'} = \frac{N_s}{N_p} I_{qds}, \qquad V_{qds}^{'} = \frac{2}{3}\frac{N_p}{N_s} V_{dc}.$$

<u>With series core-loss resistances</u>

$$V_{qdp} = (r_p + R_{mp}) I_{qdp} + j\omega_p \lambda_{qdp} + p\lambda_{qdp}$$

$$V_{qds}^{'} = (r_s^{'} + R_{ms}^{'}) I_{qds}^{'} + p\lambda_{qds}^{'}$$

$$\lambda_{qdp} = L_p I_{qdp} + L_m I_{qds}^{'}$$

$$\lambda_{qds}^{'} = L_s^{'} I_{qds}^{'} + L_m I_{qdp}$$

where

$$r_s^{'} = \left(\frac{N_p}{N_s}\right)^2 r_s, \quad L_s^{'} = \left(\frac{N_p}{N_s}\right)^2 L_s$$

$$L_m = \frac{3}{2}\frac{N_p}{N_s} L_{m12}, \qquad R_{ms}^{'} = \left(\frac{N_p}{N_s}\right)^2 R_{ms} \quad .$$

The corresponding complex-form equivalent circuits with shunt or series loss resistors are shown in Figure 5.2 and Figure 5.3.

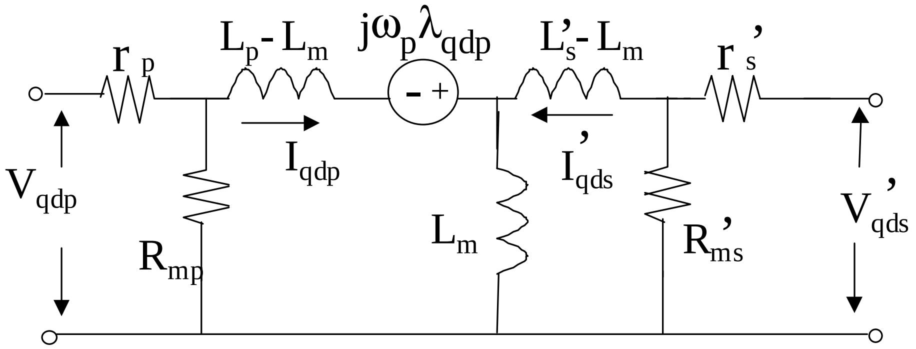

Figure 5.2. Complex-form equivalent circuit of doubly-fed synchronous reluctance machine with shunt core-loss resistances.

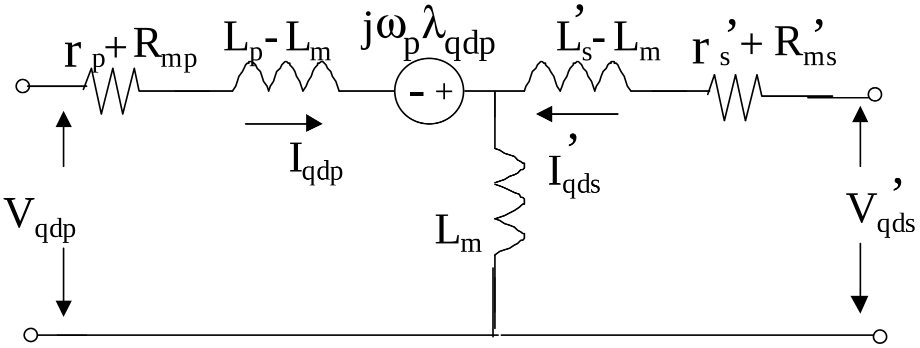

Figure 5.3 Complex-form equivalent circuit of doubly-fed synchronous reluctance machine with series core-loss resistances.

5.3 Generator with Impedance Load

Figure 5.4 shows the schematic diagram of the machine operating as a stand-alone generator feeding a three-phase impedance R-L load. A three-phase capacitor bank is connected in parallel to the power windings to provide generator reactive power to sustain the load.

The generator system with impedance load in Figure 5.4(a) can be described by the following q-d equations using the synchronous reference frame angle θ_p.

Load Model

$$pV_{qp} = -\frac{1}{C_p}(I_{qp} + I_{qo}) + \omega_p V_{dp}$$

$$pV_{dp} = -\frac{1}{C_p}(I_{dp} + I_{do}) - \omega_p V_{qp} \tag{5.40}$$

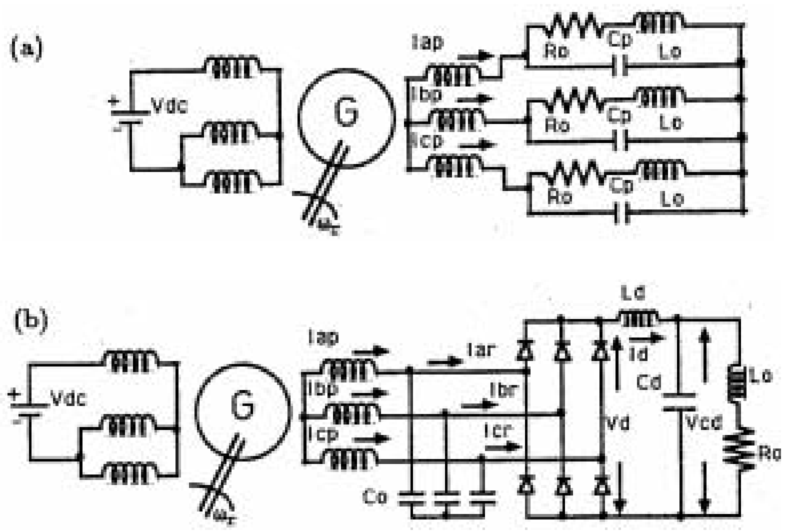

Figure 5.4. Doubly-fed synchronous generator systems. (a) With impedance, (b) with a loaded rectifier.

$$L_o \frac{dI_{qo}}{dt} + R_o I_{qo} + \omega_p L_o I_{do} = V_{qp}$$

$$L_o \frac{dI_{do}}{dt} + R_o I_{do} - \omega_p L_o I_{qo} = V_{dp} \qquad (5.41)$$

Machine Model with series core-loss resistances (Figure 5.3)

$$V_{qp} = R_p I_{qp} - \omega_p (L_p I_{dp} + L_m I'_{ds}) + p(L_p I_{qp} + L_m I'_{qs})$$

$$V_{dp} = R_p I_{dp} + \omega_p (L_p I_{qp} + L_m I'_{qs}) + p(L_p I_d + L_m I'_{ds}) \qquad (5.42)$$

$$\frac{2}{3} V'_{dc} = R'_s I'_{qs} + p(L'_s I'_{qs} + L_m I_{qp})$$

$$0 = R'_{ds} I'_{ds} + p(L'_s I'_{ds} + L_m I_{dp}) \qquad (5.43)$$

where

$$R_p = r_p + R_{cp}, \quad R'_s = r'_s + R'_{cs}$$

$$\lambda_{qp} = L_p I_{qp} + L_m I'_{qs}$$

$$\lambda_{dp} = L_p I_{dp} + L_m I'_{ds} \tag{5.44}$$

$$\lambda'_{qs} = L'_s I'_{qs} + L_m I_{qp}$$

$$\lambda'_{ds} = L'_s I'_{ds} + L_m I_{dp} \quad . \tag{5.45}$$

Since the parameters of the machine are dependent on the airgap flux linkage, It is necessary to express Equations (5.40)-(5.43) in terms of flux linkages. From Equations (5.44) and (5.45), we can obtain

$$I_{qp} = \frac{L'_s \lambda_{qp} - L_m \lambda'_{qs}}{L_p L'_s - L_m^2}, \quad I_{dp} = \frac{L'_s \lambda_{dp} - L_m \lambda'_{ds}}{L_p L'_s - L_m^2}$$

$$I'_{qs} = \frac{L_p \lambda'_{qs} - L_m \lambda_{qp}}{L_p L'_s - L_m^2}, \quad I'_{ds} = \frac{L_p \lambda'_{ds} - L_m \lambda_{dp}}{L_p L'_s - L_m^2} \quad .$$

Substituting these expressions into Equations (5.40)-(5.43), we obtain the following equations.

$$pV_{qp} = \gamma_c T_{s1} \lambda_{qp} + \gamma_c B_{s1} \lambda'_{qs} - \gamma_c I_{qo} - \omega_p V_{pd}$$

$$pV_{dp} = \gamma_c T_{s1} \lambda_{dp} + \gamma_c B_{s1} \lambda'_{ds} - \gamma_c I_{do} + \omega_p V_{qp} \tag{5.46}$$

$$pI_{qo} = \gamma_L V_{qp} - \omega_p I_{do} - \gamma_L R_o I_{qo}$$

$$pI_{do} = \gamma_L V_{dp} + \omega_p I_{qo} - \gamma_L R_o I_{do} \tag{5.47}$$

$$p\lambda_{qp} = V_{qp} + \omega_p \lambda_{dp} + T_{ss1} \lambda_{qp} + B_{ss1} \lambda'_{qs}$$

$$p\lambda_{dp} = V_{dp} - \omega_p \lambda_{qp} + T_{ss1} \lambda_{dp} + B_{ss1} \lambda'_{ds} \tag{5.48}$$

$$\begin{aligned} p\lambda'_{qs} &= \frac{2}{3}V_{dc} + T_{ss2}\lambda'_{qs} + B_{ss2}\lambda_{qp} \\ p\lambda'_{ds} &= T_{ss2}\lambda'_{ds} + B_{ss2}\lambda_{dp} \end{aligned} \qquad (5.49)$$

where

$$T_{s1} = \frac{-L'_s}{L'_s L_p - L_m^2}, \qquad B_{s1} = \frac{L_m}{L'_s L_p - L_m^2}$$

$$T_{s2} = \frac{-L_p}{L'_s L_p - L_m^2}, \qquad B_{s2} = \frac{L_m}{L'_s L_p - L_m^2}$$

$$T_{ss1} = \frac{-r_p L'_s}{L'_s L_p - L_m^2}, \qquad B_{ss1} = \frac{r_p L_m}{L'_s L_p - L_m^2}$$

$$T_{ss2} = \frac{-r_s^1 L'_s}{L'_s L_p - L_m^2}, \qquad B_{ss2} = \frac{r_s^1 L_m}{L'_s L_p - L_m^2}$$

$$\gamma_c = \frac{1}{C_p}, \qquad \gamma_L = \frac{1}{L_o} \ .$$

The q-d complex-form equations of the generator system are expressed as

$$pV_{qdp} = \gamma_c T_{s1}\lambda_{qdp} + \gamma_c B_{s1}\lambda'_{qds} - \gamma_c I_{qdo} + j\omega_p V_{qdp} \qquad (5.50)$$

$$pI_{qdo} = \gamma_L V_{qdp} + j\omega_p I_{qdo} - \gamma_L R_o I_{qdo} \qquad (5.51)$$

$$p\lambda_{qdp} = V_{qdp} - j\omega_p \lambda_{qdp} + T_{ss1}\lambda_{qdp} + B_{ss1}\lambda'_{qds} \qquad (5.52)$$

$$p\lambda'_{qds} = \frac{2}{3}V_{dc} + T_{ss2}\lambda'_{qds} + B_{ss2}\lambda_{qdp} \ . \qquad (5.53)$$

Under the steady-state operation, the derivatives of the state variables are identically equal to zero leading to the following system equation:

$$\begin{bmatrix} \gamma_c T_{s1} & \gamma_c B_{s1} & -\gamma_c & j\omega_p \\ 0 & 0 & (j\omega_p - \gamma_L R_o) & \gamma_L \\ (T_{s1} - j\omega_p) & B_{ss1} & 0 & 1 \\ B_{ss2} & T_{ss2} & 0 & 0 \end{bmatrix} \begin{bmatrix} \lambda_{qdp} \\ \lambda'_{qds} \\ I_{qdo} \\ V_{qdp} \end{bmatrix} = \begin{bmatrix} 0 \\ 0 \\ 0 \\ -\frac{2}{3} V_{dc} \end{bmatrix} . \qquad (5.54)$$

This equation is nonlinear since the machine inductances and core loss resistances vary with the magnitude of the airgap flux linkage as shown in Figure 3.11.

The relationship between these parameters and airgap flux linkage magnitude are empirically determined as

$$L_m = -0.44\lambda_m^2 + 0.085\lambda_m + 0.0164$$

$$L_p = -0.36\lambda_m^2 + 0.0906\lambda_m + 0.0373$$

$$L'_s = -0.55\lambda_m^2 + 0.09\lambda_m + 0.0385 \qquad (5.55)$$

$$R_{mp} = -4.05\lambda_m^2 - 1.47\lambda_m + 1.217$$

$$R'_{ms} = 7.24\lambda_m^2 - 4.25\lambda_m + 1.58$$

where the airgap flux linkage is given as

$$\lambda_{qdm} = L_{mm}\left[\frac{\lambda_{qdp}}{L_{lp}} + \frac{\lambda'_{qds}}{L'_{ls}}\right], \quad L_{mm} = [\frac{1}{L_{lp}} + \frac{1}{L_m} + \frac{1}{L'_{ls}}]^{-1}, \quad \lambda_m = \left|\lambda_{qdm}\right| . \qquad (5.56)$$

If we use the machine model with the shunt loss resistor (see Figure 5.2), similar derivation is done and the complex-form equations of generator system in terms of flux linkage are given as

$$pV_{qdp} = \gamma_c T_o \lambda_{qdp} + \gamma_c B_o \lambda'_{qds} - \gamma_c I_{qdo} + (j\omega_p - T_c)V_{qdp} \qquad (5.57)$$

$$pI_{qdo} = \gamma_L V_{qdp} + j\omega_p I_{qdo} - \gamma_L R_o I_{qdo} \qquad (5.57)$$

$$p\lambda_{qdp} = T_p V_{qdp} - j\omega_p \lambda_{qdp} + T_{pp}\lambda_{qdp} + B_{pp}\lambda'_{qds} \qquad (5.58)$$

$$p\lambda'_{qds} = T_s V'_{qds} + T_{ss}\lambda'_{qds} + B_{ss}\lambda_{qdp} \ . \tag{5.59}$$

Under the steady-state operation, the following matrix equation is obtained

$$\begin{bmatrix} \gamma_c T_o & \gamma_c B_o & -\gamma_c & (j\omega_p - T_c) \\ 0 & 0 & (j\omega_p - \gamma_L R_o) & \gamma_L \\ (T_{pp} - j\omega_p) & B_{pp} & 0 & T_p \\ B_{ss} & T_{ss} & 0 & 0 \end{bmatrix} \begin{bmatrix} \lambda_{qdp} \\ \lambda'_{qds} \\ I_{qdo} \\ V_{qdp} \end{bmatrix} = \begin{bmatrix} 0 \\ 0 \\ 0 \\ -\frac{2}{3}V_{dc} \end{bmatrix} \tag{5.60}$$

where

$$T_{pp} = -\frac{r_p L'_s T_p}{\Delta}, B_{pp} = \frac{r_p L_m T_p}{\Delta}$$

$$T_{pp} = -\frac{r'_s L_p T_s}{\Delta}, B_{ss} = \frac{r'_s L_m T_s}{\Delta}$$

$$T_o = -\frac{L'_s T_p}{\Delta}, B_o = \frac{L_m T_p}{\Delta} \ .$$

For the machine model with the shunt loss resistor is used, the machine's parameters are determined as follows:

$$\mathrm{L_m} = -0.44\lambda_m^2 + 0.085\lambda_m + 0.0164$$

$$\mathrm{L_p} = -1.35\lambda_m^2 + 0.145\lambda_m + 0.0327$$

$$\mathrm{L'_s} = -0.552\lambda_m^2 + 0.091\lambda_m + 0.0385$$

$$\mathrm{r_{mp}} = -5022\lambda_m^2 + 1865\lambda_m + 132$$

$$\mathrm{r'_{ms}} = -8218\lambda_m^2 + 2014.2\lambda_m + 88.2 \ .$$

To investigate the steady-state performance characteristics of the machine, Equations (5.54)-(5.56) are numerically solved for fixed values of $C_p = 45\mu F$, various values of rotor speed, control winding dc current, and load impedance. Figure 5.5 gives the generator characteristics when fixed I_{dc} = 4.5A and choosing three different rotor speeds. In Figure 5.5(a), the curves show the steady-state relationship between the output power and load voltage while the steady-state relationship between the load voltage and load current is displayed in Figure 5.5(b). It is observed from these figures that the higher the rotor speeds, the higher the output power, load voltage and load current.

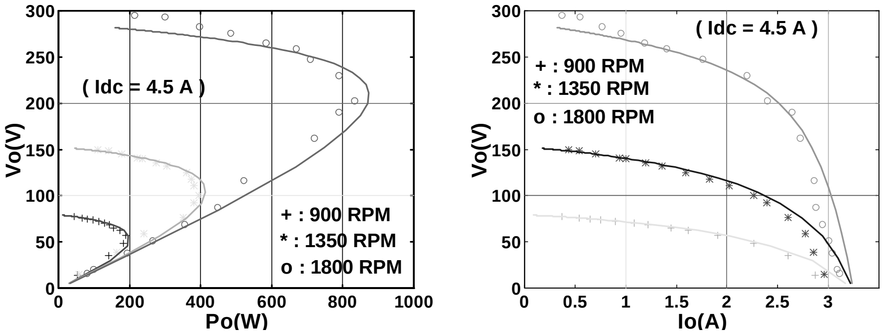

(a) (b)

Figure 5.5. Calculated and measured characteristics of synchronous generator system with impedance load for different rotor speeds. (a) Load voltage vs. output power, (b) load voltage vs. load current.

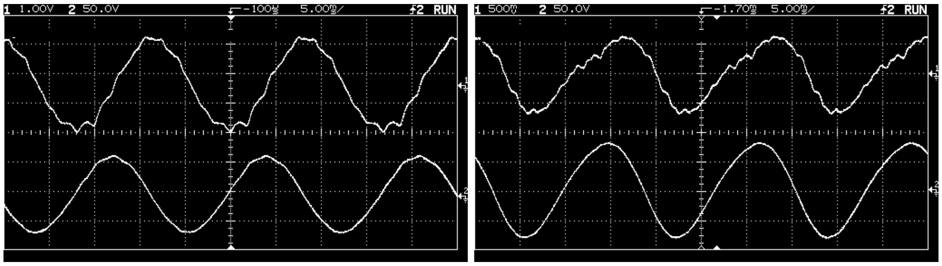

(a) $R_L = 21\Omega$

(b) $R_L = 400\Omega$

Figure 5.6. Measured waveforms of synchronous generator system with impedance load (5msec/div). (a) High output power.Top:generator current (1A/div); Bottom:generator voltage (50V/div), (b) Low output power. Top: generator current (0.5A/div); Bottom: generator voltage (50V/div).

Figure 5.6 shows the waveforms of the generator when the rotor speed is 900rpm and feeding a low resistive load (R_L = 20ohms) or a high resistive load (R_L = 400 ohms). In either case: a low resistive load or a high resistive load, the waveforms of voltage and current are not pure sinusoidal waveforms because of existing harmonic components. The influence of the dc excitation current on the voltage regulation of the generator is shown in Figure 5.7. Three different dc current values, 3A, 4.5A, and 6A, are chosen to do the experimental measurement and steady-state calculation. The curves in Figure 5.7(a) show the steady-state relationship between the load voltage and output power while the steady-state relationship between the load voltage and load current is displayed in Figure 5.7(b). It is observed in Figure 5.7 that increasing the excitation current increases the maximum attainable power and also the no-load generator voltage. These figures show that the measured and calculated generator characteristics correlate very well. The discrepancies between calculations and experimental results are due to the high sensitivity of the

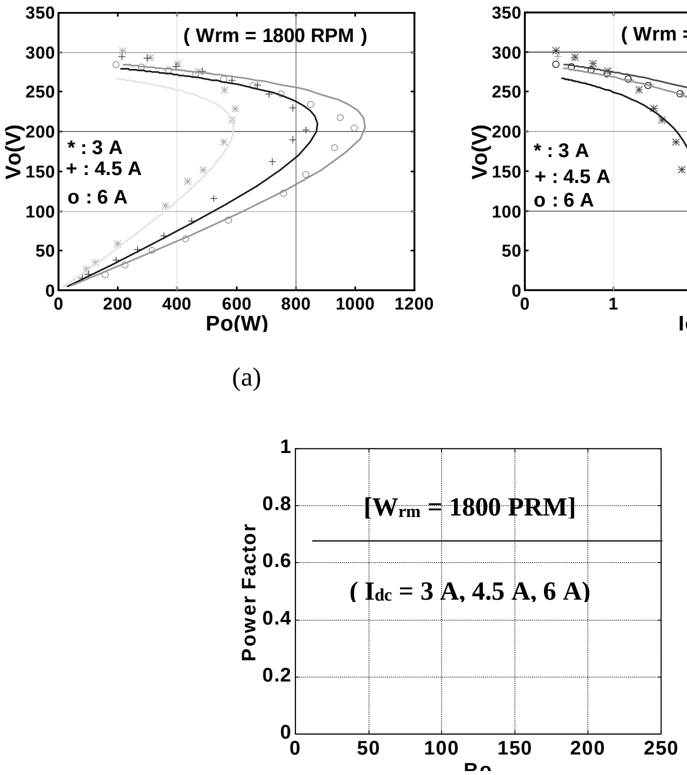

(a)

(b)

(c)

Figure 5.7. Calculated and measured characteristics of synchronous generator system with impedance load for a constant rotor speed and different control winding excitation currents. (a) Load voltage vs. output power, (b) phase load voltage vs. load current, (c) power factor vs. load resistance.

operating points to the airgap flux linkage and non-negligible generator harmonic currents seen in Figure 5.6. In Figure 5.7(c), we can see the power factor will not be affected by varying the load resistance or control winding current.

Figure 5.8 demonstrates calculated synchronous generator characteristics of generator system feeding an impedance load with three inductance volue. Increasing the load

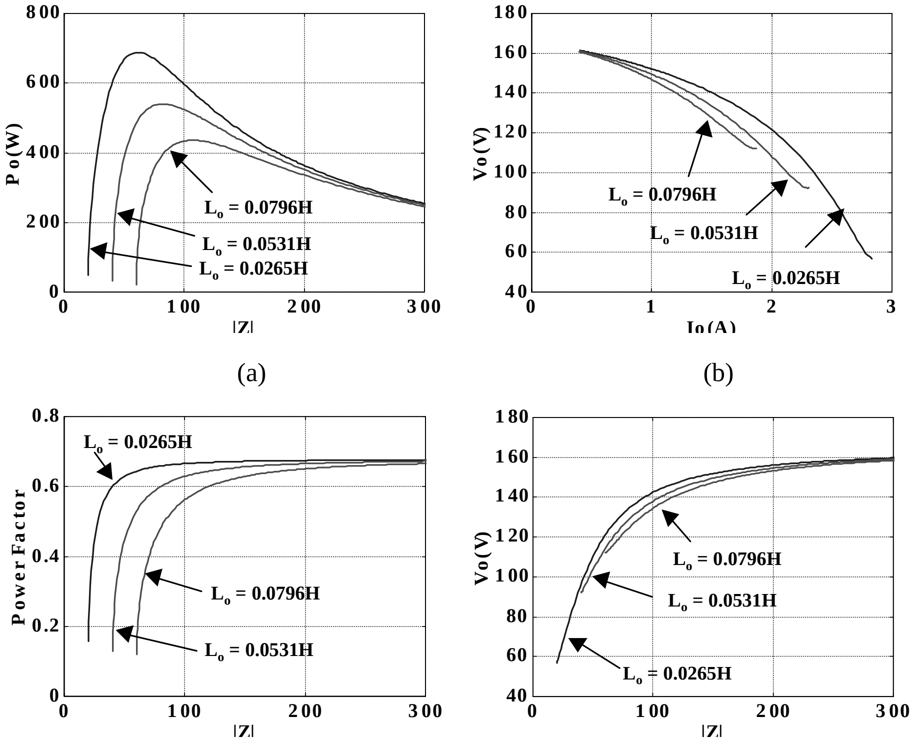

(a) (b)

(c) (d)

Figure 5.8. Calculated synchronous generator characteristics of generator system feeding impedance load. (W_{rm} = 1800RPM, I_{dc} = 4.5A). (a) Load power vs. load impedance, (b) load voltage vs. load current, (c) generator power factor vs. load impedance, (d) load voltage vs. impedance.

inductance value decreases the maximun output power, generator power factor, output current, and output voltage as shown in Figures 5.8(a)-(d). These reductions are obvious in lower impedance values, however, these reduction gradually disappear with increasing impedance load values.

The starting electrical transients of the generator system feeding an impedance load are simulated using Equations (5.50)-(5.53) or (5.57)-(5.59). Figure 5.9 displays the simulation results. The generator is fitted with an excitation capacitor bank with a per-phase value of 45μF and is driven at a constant speed of 1800rpm. Saturation effects are accounted for by updating the inductances and core loss resistances based on the instantaneous airgap flux linkage magnitude. There is a gradual growth of the load voltage and current magnitudes, which are respectively illustrated in Figures 5.9(a) and 5.9(b), as the airgap flux linkage is built up until they all reach a steady-state operating condition.

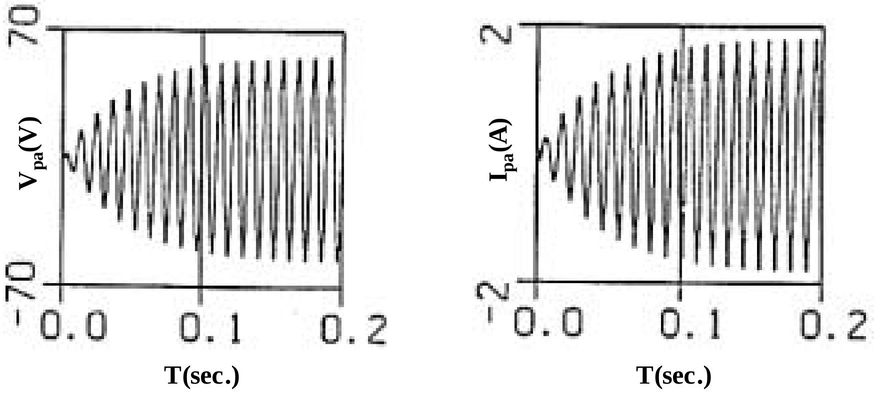

(a) (b)

Figure 5.9. Simulated starting transient of the synchronous doubly-fed reluctance generator system feeding an impedance load. (a) Phase ‘A’ terminal voltage, (b) phase ‘A’ generator current.

5.4 Generator with Rectifier Load

The model of the generator-rectifier system is shown in Figure 5.4(b). The model of the rectifier load connected to power winding of the generator has been derived in Section 4.2. This section also shows that a three-phase rectifier with an impedance load in steady-state behaves like a wye-connected three-phase resistive load (R_L) connected across the excitation capacitor. The relationship between R_L and R_o is expressed as

$$R_L = \frac{\pi^2}{12} R_o \ .$$

Consequently, the analytical approach used for the generator feeding impedance can be used for the generator with rectifier load.

The rectifier voltage V_d and current I_d can be found using the following equations

$$pV_{qdp} = \frac{1}{C_o}[I_{qdp} - S_{qdI} I_d] + j\omega_p V_{qdp}$$

$$V_d = \mathrm{Re}\, al[V_{qdp} S_{qdv}] \,.$$

Figure 5.11 gives the measured and calculated performance characteristics of the generator feeding a rectifier that has a high impedance load (R_L=400 ohms) or a low impedance load (R_L = 5 ohms). Three different dc current values, 3A, 4.5A, and 6A, are used in the steady-state calculation and the experimental measurement. The curves of load voltage vs. output power is shown in Figure 5.11(a), where we can see that increasing control winding dc current increases the maximum attainable power. The load voltage and load current also increase with increasing the control winding dc current, which is observed from the curves of load voltage vs. load current shown in Figure

5.11(b). Figure 5.11(c) shows us that the power factor will not be affected by varying the control winding current or rectifier resistance load. The difference between calculation and measured results are due to these factors: profound commutation overlap, waveform distortions and high value of stator leakage inductance. Figure 5.10 shows the measured voltage and current waveforms of the generator feeding a three-phase rectifier feeding a high impedance load or low impedance. In either case, waveform distortions are clearly seen in Figures 5.10(a) and 5.10(b). Profound commutation overlap is found in the waveform of the generator voltage as shown in Figure 5.10(b). Like the generator feeding an impedance load, there is a maximum output power corresponding to each rotor speed and control excitation current.

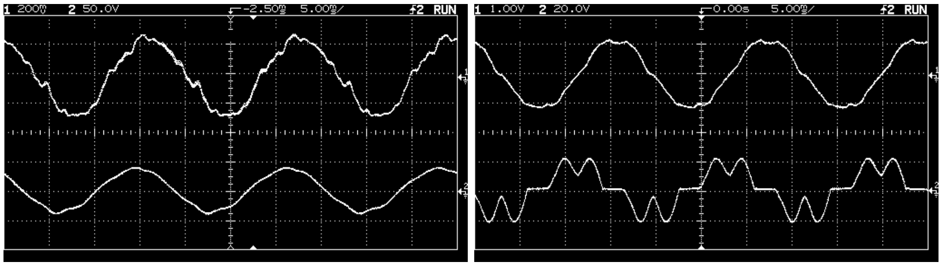

(a) $R_L = 400\Omega$ (b) $R_L = 5\Omega$

Figure 5.10. Measured waveforms of the synchronous generator system feeding a three-phase rectifier load (5msec/div). (a) High impedance load, Top: generator current (0.2A/div); Bottom: generator voltage (50V/div), (b) low impedance load, Top: generator current (1A/div); Bottom: generator voltage (20V/div).

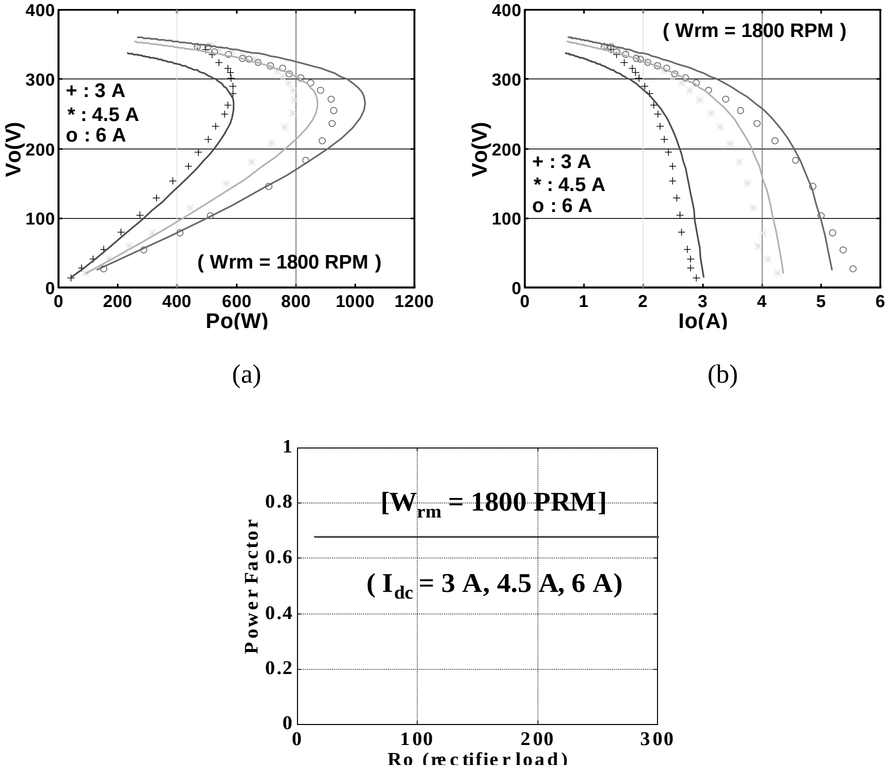

(a) (b)

(c)

Figure 5.11. Measured and calculated steady-state performance curves of synchronous generator system with a three-phase rectifier load. (a) Load voltage vs. output power, (b) Load voltage vs. load current, (c) power factor vs. rectifier load resistance.

5.5 Conclusion

In this chapter, we have presented the modeling and analysis of the doubly-fed synchronous reluctance generator with a dc control winding excitation. The generator operates essentially like a cylindrical rotor synchronous generator in which the frequency of the generated voltage is directly related to the rotor speed and the pole numbers of the windings. Hence this machine is suitable as a medium to high frequency generator. Steady-state calculation results compare fairly well with experimental results. The discrepancies between calculations and experimental results are due to the airgap flux linkage and the non-negligible generator harmonic currents. The severe commutation overlaps in the operation of the rectifier also contribute to the differences of calculation and experimental results. The model equations derived in this chapter can be used with profit to calculate the transient and steady-state performance of the doubly-fed synchronous reluctance motor fed with either a variable or constant frequency supply.

CHAPTER 6

THE PERFORMANCE OF A DOUBLY-FED SYNCHRONOUS RELUCTANCE GENERATOR WITH CONTROLLED DC OUTPUT VOLTAGE

6.1 Introduction

The attention in this chapter is focused on the operation of the doubly-fed synchronous reluctance generator as a controllable power source for DC loads and for use in battery charging. Using the generated DC voltage at the power winding to excite the control winding circuit brings these advantages of eliminating the need for an independent excitation arrangement and the absence of slip-rings and brushes. This kind of generator systems can be realized by connecting the generated DC voltage from the power windings to machine control windings through a DC-DC converter such as buck or boost converter.

In this chapter, the AC output power from the power windings of the doubly-fed synchronous reluctance generator is rectified with a three-phase rectifier and is further processed by either a DC-DC buck or boost converter for output power or load voltage regulation. Section 6.2 gives a description of the generator systems investigated, in addition to the derivation of the models of the machine, shunt capacitors, three-phase diode rectifier and buck and boost DC-DC converters. In Section 6.3, the steady-state calculation and experimental results are compared and discussed. The simulation of the excitation process for the generator system with exciting source from the power windings is discussed in Section 6.3. The simulation of the starting transients and steady-state waveforms of using this generator system for battery charging is also included in this section. Conclusions are contained in Section 6.4.

6.2 Description and Modeling of Generator Systems

Figures 6.1 and 6.2 show the schematic diagram of the synchronous reluctance generator systems considered in this chapter.

In Figure 6.1, the generator is connected to a three-phase diode rectifier. The output of that is further processed by either a DC-DC buck or boost converter. The three-

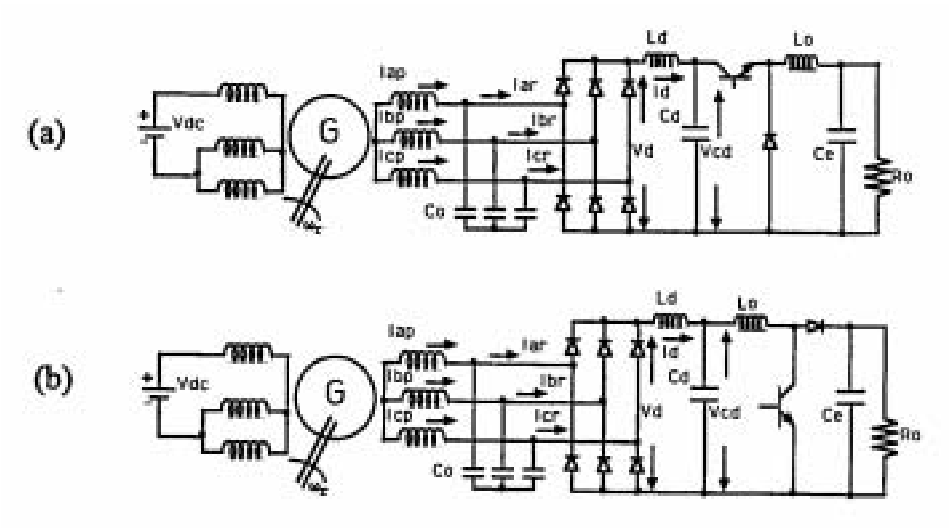

Figure 6.1. Schematic diagram of the doubly-fed synchronous generator systems. (a)With buck DC-DC converter, (b) with DC-DC boost converter.

phase control windings are connected to a controllable source of DC current or voltage source while the three-phase power windings are connected to a three-phase diode rectifier. Delta-connected capacitors are connected across the power winding terminals to provide reactive power and to enhance the generator real power output capability. Controllable DC voltage or power is obtained by connecting the filtered output of the

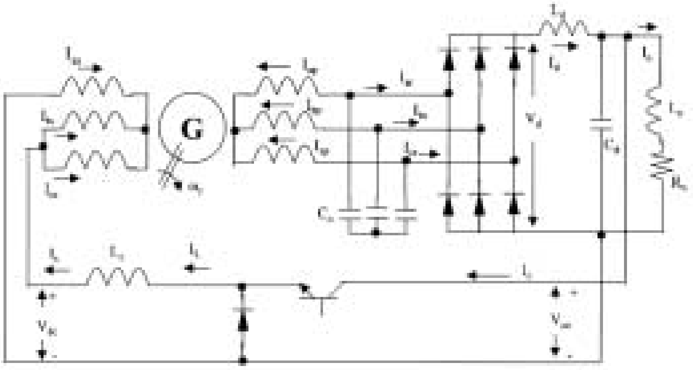

(a)

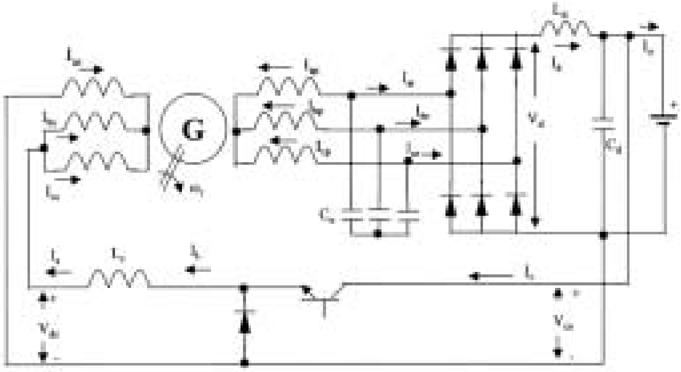

(b)

Figure 6.2. Schematic diagram of the doubly-fed synchronous generator system with dc-dc buck converter. (a) Feeding an impedance load, (b) feeding a battery.

rectifier to either a DC-DC buck or boost converter. The DC-DC converter controls the output power or voltage using a constant frequency, pulse-wide modulation control (PWM) scheme that varies the turn-on time (the duty ratio) of the transistor.

The generator systems shown in Figure 6.2 are further application of the generator system with DC-DC buck converter in Figure 6.1(a). In Figure 6.2(a), the generator is excited by feeding the control winding from a battery at first, then the generator generates output voltage whose filtered rectified dc voltage feeds the impedance load and at the same time activates the dc-dc buck converter. At last, the battery source is disconnected when a steady-state operating condition is obtained.

The generator scheme for battery charging is shown in Figure 6.2(b) in which the filtered dc voltage is directly connected to the battery. For this application, the battery, which also acts as the source to the DC-DC converter, excites the generator through the control windings. When DC output voltage is sufficiently built up, the generator sends charging current to the battery whose value is determined by the converter duty-ratio and battery open circuit voltage.

The model equations of the generator schemes shown in Figures 6.1 and 6.2 are presented in the following subsections.

Synchronous Reluctance Generator

If we use the complex-form equivalent circuit shown in Figure 5.2, which has the shunt core-loss resistances R_{mp} and R'_{ms}, the complex-form q-d equations of the generator in the synchronous reference frame rotating with angular speed ω_p (ω_p is the angular speed of the generated voltage) are given as

$$V_{qdp}T_p = r_pT_pI_{qdp} + j\omega_p\lambda_{qdp} + p\lambda_{qdp} \tag{6.1}$$

$$V'_{qds} = r'_sT_sI'_{qds} + p\lambda'_{qds} \tag{6.2}$$

$$\lambda_{qdp} = L_pI_{qdp} + L_mI'_{qds} \tag{6.3}$$

$$\lambda'_{qds} = L'_sI'_{qds} + L_mI_{qdp} \tag{6.4}$$

where

$$T_p = \frac{R_{mp}}{r_p + R_{mp}}, \quad T_s = \frac{R'_{ms}}{r'_s + R'_{ms}}$$

$$r'_s = \left(\frac{N_p}{N_s}\right)^2 r_s, \quad L'_s = \left(\frac{N_p}{N_s}\right)^2 L_s$$

$$L_m = \frac{3}{2}\frac{N_p}{N_s}L_{m12}, \quad R'_{ms} = \left(\frac{N_p}{N_s}\right)^2 R_{ms}$$

$$I'_{qds} = \frac{N_s}{N_p}I_{qds}, \quad V'_{qds} = \frac{2}{3}\frac{N_p}{N_s}V_{dc}$$

or the model equations of the generator can be described by the following equations if we use the complex-form equivalent circuit shown in Figure 5.3, which has the series loss resisters R_{mp} and $R_{ms}^{'}$.

$$V_{qdp} = (r_p + R_{mp})I_{qdp} + j\omega_p\lambda_{qdp} + p\lambda_{qdp} \tag{6.5}$$

$$V_{qds}^{'} = (r_s^{'} + R_{ms}^{'})I_{qds}^{'} + p\lambda_{qds}^{'} \tag{6.6}$$

$$\lambda_{qdp} = L_p I_{qdp} + L_m I_{qds}^{'} \tag{6.7}$$

$$\lambda_{qds}^{'} = L_s^{'} I_{qds}^{'} + L_m I_{qdp} \tag{6.8}$$

where

$$r_s^{'} = \left(\frac{N_p}{N_s}\right)^2 r_s, \quad L_s^{'} = \left(\frac{N_p}{N_s}\right)^2 L_s$$

$$L_m = \frac{3}{2}\frac{N_p}{N_s}L_{m12}, \quad R_{ms}^{'} = \left(\frac{N_p}{N_s}\right)^2 R_{ms}$$

$$I_{qds}^{'} = \frac{N_s}{N_p}I_{qds}, \quad V_{qds}^{'} = \frac{2}{3}\frac{N_p}{N_s}V_{dc}.$$

In these equations, $p=d/dt$, V_{qdp}, and I_{qdp} are the complex-form generator terminal voltage produced by the power windings and current flowing through them, respectively, the referred control winding complex-form current and flux linkage are $I_{qds}^{'}$ and $\lambda_{qds}^{'}$, respectively. The quantity Vs is the input voltage to the control winding while N_p and N_s are the effective per-phase, per pole turn numbers of the power and control windings, respectively. λ_{qdp} is the complex q-d flux linkage for the power windings. The measured self and magnetizing inductances of the windings and core-loss resistances of the machine used for this work are shown in Figure 3.11 (series loss resistors) or Figure 3.17

(shunt loss resistors). The relationship between these parameters and airgap flux linkage magnitude are empirically determined in equation (3.86) (series loss resistors) or equation (3.87) (shunt loss resistors).

Shunt Capacitor, Rectifier and Load

The complex-form q-d equations of the shunt capacitors (C_o) connected across the power windings is given as

$$pV_{qdp} = \frac{1}{C_o}(-I_{qdp} - S_{qdI} I_d) + j\omega_p V_{qdp} \quad . \tag{6.9}$$

Also, the equations describing the input-output voltages and currents of the rectifier, filter elements and the load are defined as

$$V_d = \mathrm{Re}\,al(V_{qdp} S^*_{qdv}) \tag{6.10}$$

$$pI_d = \frac{1}{L_d}(V_d - V_{co}) \tag{6.11}$$

$$pV_{co} = \frac{1}{C_d}(I_d - I_o - I_c) \tag{6.12}$$

$$pI_o = \frac{1}{L_o}(V_{co} - R_o I_o) \tag{6.13}$$

where

$$S_{qdI} = A_I e^{j(\sigma+\theta)}, \qquad S_{qdv} = A_v e^{j\sigma}$$

$$A_I = \frac{2\sqrt{3}}{\pi}\sin(\mu/2)/(\mu/2), \qquad A_V = \frac{2\sqrt{3}}{\pi}\cos(\frac{\mu}{2}) \ .$$

S_{qdv} and S_{qdI} are, respectively, the complex-form q-d voltage and current switching functions of the rectifier, μ is the commutation angle, V_d is the rectifier output voltage, I_o is the load current with the filter inductor current and filter capacitor voltage represented as I_d and V_{co}, respectively. The quantity C_d is the filter capacitor, L_d is the filter inductor with the impedance load represented as R_o and L_o. The initial angle between the power and control winding axes is σ and the power factor angle of the generator at the power winding terminals is θ. The conjugate is presented by *.

DC-DC Buck Converter

The model of the DC-DC buck converter feeding a resistive load or battery shown in Figure 6.1(a) and Figure 6.2 are derived in this subsection [81-82]. The output voltage and power are controlled by varying the turn-on time of the transistor d_1T that is regulated by changing the magnitude of the reference voltage compared to a constant frequency saw-tooth waveform. T is transistor's switching period. Figure 6.3 (a) gives a typical converter inductor current and converter switching functions corresponding to the three converter operational modes given in Figures 6.3 (b-d). The switching functions of transistor and diode are S_1 and S_2, respectively, which take values of unity when the devices are turned on and zero when they are turned off. The switching function when the transistor and diode are not conducting at the same time is S_3.

Mode I: Transistor is on: 0 #t #d_1T

The voltage equations are given as

$$L_o pI_L = V_{cd} - V_{co} \tag{6.14}$$

$$C_e pV_{co} = I_e \tag{6.15}$$

$$V_{co} - R_o I_L + R_o I_e = 0 \tag{6.16}$$

where I_L is the inductor current, V_{co} is the output filter capacitor voltage, the current through the output capacitor is I_e and the load resistance is R_o.

Mode II: Diode is on: d_1T # t # $(d_1+ d_2)T$

The voltage equations from figure 6.3 (c) are expressed as

$$L_o pI_L = -V_{co} \qquad (6.17)$$

$$C_e pV_{co} = I_e \qquad (6.18)$$

$$V_{co} - R_o I_L - R_o I_e = 0 \ . \qquad (6.19)$$

Mode III: Transistor and diode are off: $(d_1+ d_2)T$# t # $(d_1+ d_2+d_3)T$

The voltage equations from Figure 6.3(d) are given as

$$C_e pV_{co} = I_e \qquad (6.20)$$

$$V_{co} - R_o I_e = 0 \ . \qquad (6.21)$$

The equations of the three modes of operation are averaged using the switching functions and are given as

$$L_o pI_L (S_1 + S_2) = V_{cd} S_1 - V_{co}(S_1 + S_2) \qquad (6.22)$$

$$C_e pV_{co} = I_e \qquad (6.23)$$

$$V_{co} - R_o I_L (S_1 + S_2) - R_o I_e = 0 \ . \qquad (6.24)$$

Boost DC-DC Converter

The model of the DC-DC boost converter feeding a resistive load shown in Figure 6.1(b) is set forth in this subsection. Figure 6.4(a) shows the inductor current of the boost DC-DC converter with the switching functions and the three modes of operation of this converter are shown in Figure 6.4 (b-c). The voltage equations are derived below

Mode I: Transistor is on: 0 # t # d_1T

The voltage equations from Figure 6.4(a) are

$$L_o pI_L = V_{cd} \qquad (6.25)$$

$$C_e pV_{co} = I_e \qquad (6.26)$$

$$-V_{co} - R_o I_e = 0 \ . \qquad (6.27)$$

Mode II: Diode is on: d_1T # t # $(d_1+ d_2)T$

The voltage equations of this mode from Figure 6.4(c) are expressed as

$$L_o pI_L = V_{cd} - V_{co} \tag{6.28}$$

$$C_e pV_{co} = I_e \tag{6.29}$$

$$V_{co} - R_o I_L + R_o I_e = 0\ . \tag{6.30}$$

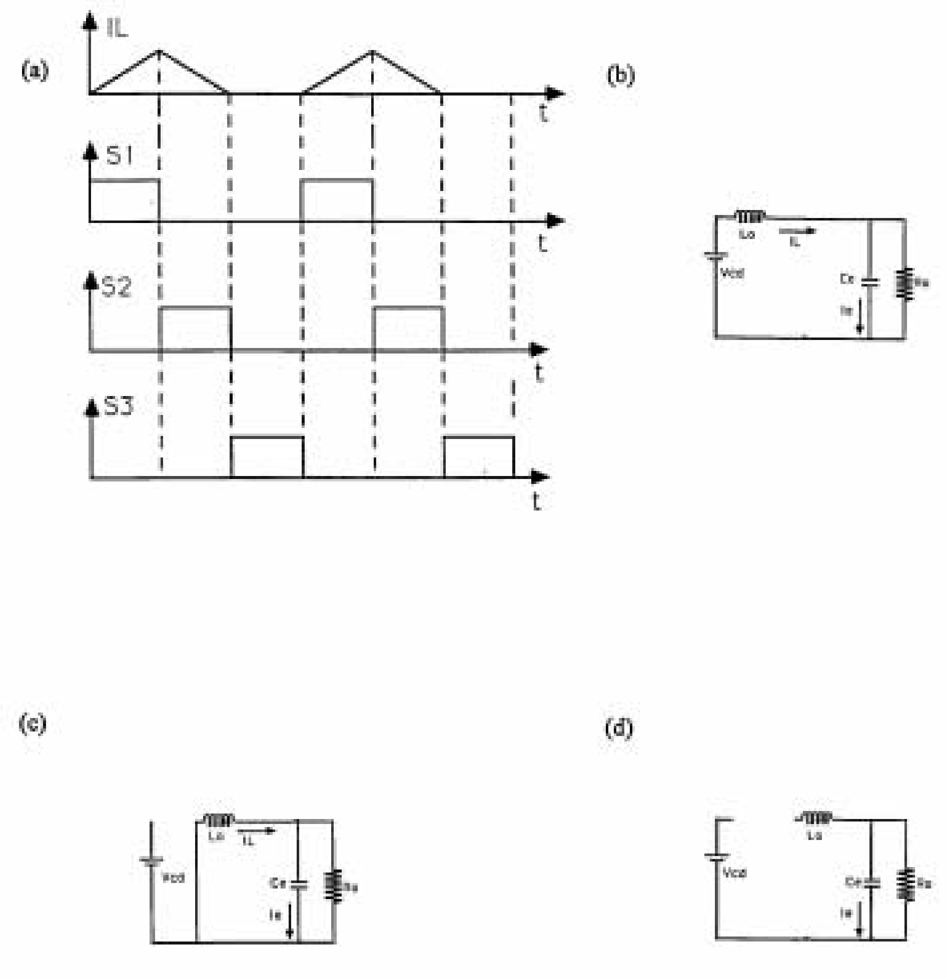

Figure 6.3. Buck DC-DC converter. (a) Converter inductor current and switching functions, (b) circuit when transistor is on, (c) circuit when the diode is on, (d) circuit when both transistor and diode are off.

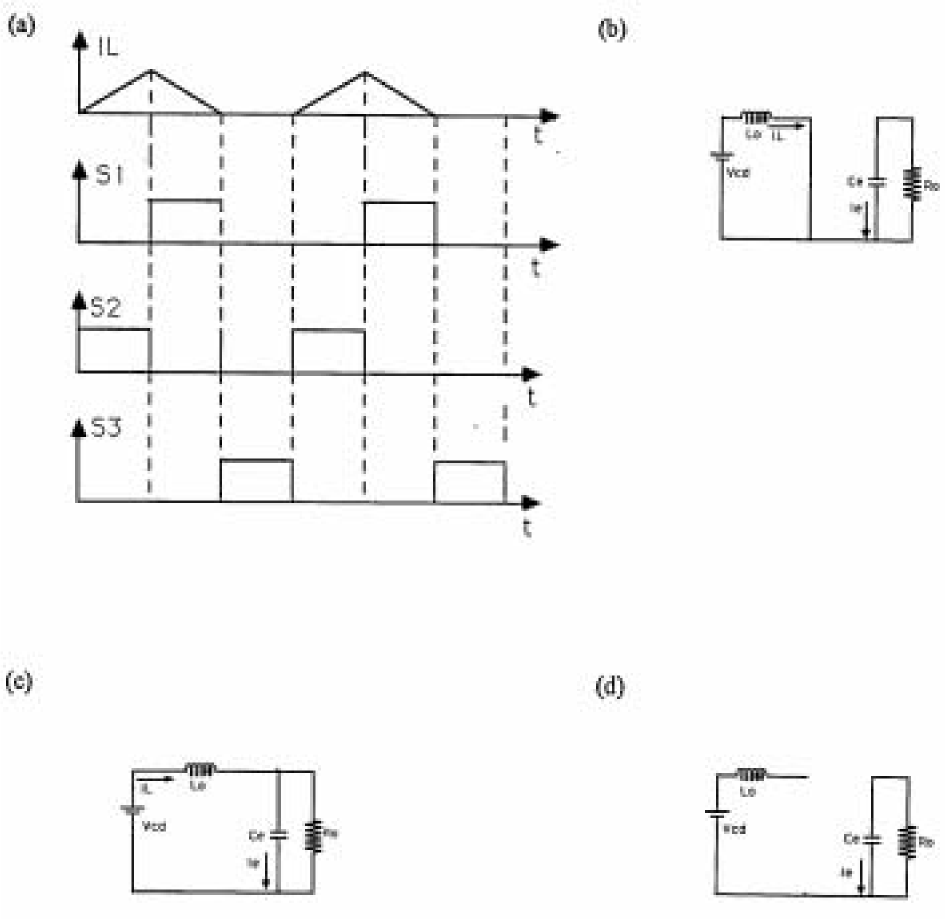

Figure 6.4. Boost DC-DC converter. (a) Converter inductor current and switching functions, (b) circuit when transistor is on, (b) circuit when diode is on, (c) circuit when both diode and transistor are off.

Mode III: Transistor and diode are off: $(d_1+ d_2)T$#t #$(d_1+ d_2+d_3)T$

The model equations from Figure 6.4(d) are expressed as

$$C_e pV_{co} = I_e \qquad (6.31)$$

$$V_{co} - R_o I_e = 0 \ . \qquad (6.32)$$

Finally, the equations for three modes are combined and are given as

$$L_o pI_L(S_1 + S_2) = -V_{co}S_2 + V_{cd}(S_1 + S_2) \qquad (6.33)$$

$$C_e pV_{co} = I_e \qquad (6.34)$$

$$V_{co} - R_o I_e(S_1 + S_2 + S_3) - R_o I_L S_2 = 0 \ . \qquad (6.35)$$

Lead-acid Battery

From [61] and Figure 6.5, the dynamic equations describing the lead-acid battery are given as

$$C_{b[} pV_{bp} = I_b - \frac{V_{bp}}{R_{bp}} \qquad (6.36)$$

$$C_{b1} pV_{b1} = I_b - \frac{V_{b1}}{R_{b1}} \qquad (6.37)$$

$$V_c = V_{bp} + V_{b1} + I_b(R_{bs} + R_{bt}) \ . \qquad (6.39)$$

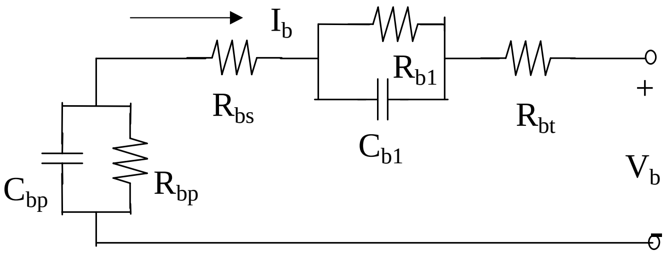

Figure 6.5. Equivalent circuit representation of a lead-acid battery

Appendix 6A contains the definitions of the different resistors and capacitors in Equations (6.18)-(6.19).

6.3 Steady-state Characteristics of the Generator Systems

During steady-state operation, the q-d state variables of the generator, shunt capacitor and rectifier equations are constant. Also, the average inductor voltages and capacitor currents in the rectifier output filter and the DC-DC converters are zero. Hence averaging the converter equations (6.22)-(6.24) and (6.33)-(6.35) and setting the derivatives of the generator, rectifier variables and shunt capacitors to zero, the models of the generator systems are obtained as following

The Model of the generator system with buck converter in Figure 6.1(a)

$$V_{qdp}T_p = r_p T_p I_{qdp} + j\omega_p \lambda_{qdp}$$

$$\frac{2}{3}V_{dc}T_s \frac{N_p}{N_s} = r_s^{'} T_s I_{qds}^{'}$$

$$S_{qdI} I_d = I_{qdp}$$

$$V_d = \mathrm{Re}\,al[V_{qdp} S_{qdv}] = V_{cd} \tag{6.40}$$

$$\hat{I}_L = I_d$$

$$V_{cd} d_1 - \hat{V}_{co}(d_1 + d_2) = 0$$

$$\hat{V}_{co} = R_o \hat{I}_L (d_1 + d_2) \ .$$

The Model of the generator system with boost converter in Figure 6.1(b)

$$V_{qdp}T_p = r_p T_p I_{qdp} + j\omega_p \lambda_{qdp}$$

$$\frac{2}{3}V_{dc}T_s \frac{N_p}{N_s} = r_s^{'} T_s I_{qds}^{'}$$

$$S_{qdI} I_d = I_{qdp}$$

$$V_d = \mathrm{Re}\,al[V_{qdp} S_{qdv}] = V_{cd} \tag{6.41}$$

$$V_{cd}(d_1 + d_2) - \hat{V}_{co} d_2 = 0$$

$$\hat{V}_{co} - R_o \hat{I}_L d_2 = 0 \ .$$

The Model of the generator system in Figure 6.2(a)

$$V_{qdp}T_p = r_p T_p I_{qdp} + j\omega_p \lambda_{qdp}$$

$$\frac{2}{3}\hat{V}_s T_s \frac{N_p}{N_s} = r_s^{'} T_s I_{qds}^{'}$$

$$S_{qdI} I_d = I_{qdp}$$

$$V_d = \mathrm{Re}\,al[V_{qdp} S_{qdv}] = V_{cd} \tag{6.42}$$

$$I_d = I_o + \hat{I}_c$$

$$V_{co} = R_o I_o$$

$$\hat{I}_c = d_1 \hat{I}_L$$

$$d_1 V_{co} = \hat{V}_s \quad .$$

The Model of the generator system in Figure 6.2(b)

$$V_{qdp} T_p = r_p T_p I_{qdp} + j\omega_p \lambda_{qdp}$$

$$\frac{2}{3} \hat{V}_s T_s \frac{N_p}{N_s} = r_s^{'} T_s I_{qds}^{'}$$

$$S_{qdI} I_d = I_{qdp}$$

$$V_d = \mathrm{Re}\,al[V_{qdp} S_{qdv}] = V_{cd} \tag{6.43}$$

$$I_d = I_o + \hat{I}_c$$

$$V_{co} = V_{bp} + V_{b1} - I_o (R_{bs} + R_{bt})$$

$$I_o = -\frac{V_{bp}}{R_{bp}}$$

$$I_o = -\frac{V_{b1}}{R_{b1}}$$

$$\hat{I}_c = d_1 \hat{I}_L$$

$$d_1 V_{co} = \hat{V}_s$$

where the average of the switching functions S_1, S_2, and S_3 are d_1, d_2, and d_3, respectively and are related by

$$d_1 + d_2 + d_3 = 1 \ . \tag{6.44}$$

$\hat{I}_L$ and $\hat{I}_c$ are, respectively, the averaged inductor current and input converter current. $\hat{V}_s$ is the averaged converter output voltage while $\hat{V}_{co}$ is the capacitor voltage. When the DC-DC converters operate in the continuous-current conduction mode (CCM), d_3 is equal to zero. Under steady-state operation, the state variables of the generator, rectifier, filter and the average of the states of the DC-DC converter are constant and their time derivatives become zero. With these constraints enforced on Equations (6.40-6.43), it can be easily derived that the effective resistance seen at the input of the loaded DC-DC buck converter and the phase resistance presented by the load at the output of the machine terminals are respectively given as [62,63]

Buck DC-DC Converter

$$R_{in} = \frac{R_o}{d_1^2} \frac{\pi^2}{12} \tag{6.45}$$

Boost DC-DC Converter

$$R_{in} = R_o (1 - d_1) \frac{\pi^2}{12} \ . \tag{6.46}$$

Hence, When the converter operates in (CCM) mode, Equations (6.40)-(6.44) can be numerically solved given the duty ratio d_1 and load to determine the characteristics of the generator system.

However, when the operation is in the discontinuous condition mode (DCM), d_3 needs to be determined from Figure 6.3(b-d) for the buck DC-DC converter. The average inductor current expressed in terms of the load, input and output voltages is given as [64]

$$\hat{I}_L = (V_{cd} - \hat{V}_{co}) d_1 T \frac{(d_1 + d_2)}{2L_o} \ . \tag{6.47}$$

Using Equation 6.40 or 6.42, the equation below from which d_3 can be determined is obtained:

$$d_3^2 + d_3(d_1 - 2) + \left(1 - d_1^2 - 2d_1 - \frac{2L_o}{TR_o}\right) = 0 \tag{6.48}$$

Similar analysis for the boost converter using Figures 6.4(b-d) and Equation 6.41 or 6.43, the equation for d_3 is given as

$$d_3 = 1 - d_1 - \sqrt{\frac{2L_o}{TR_o d_1}} \tag{6.49}$$

Using the same method of deriving Equations (6.45) and (6.46), the output load resistances referred to the input of the DC-DC converter using Equations (6.40-6.43) are given as

Buck DC-DC Converter

$$R_{in} = \frac{R_o(1 - d_3)^2}{d_1^2} \tag{6.50}$$

Boost DC-DC Converter

$$R_{in} = \frac{R_o(1 - d_1 - d_3)^2}{(1 - d_3)^2} \ . \tag{6.51}$$

These converter input resistances are further referred to the input side of the three-phase diode rectifier using equation (6.40)-(6.43) and are expressed as

Buck DC-DC Converter

$$R_{in} = \frac{R_o(1 - d_3)^2}{d_1^2} \frac{\pi^2}{12} \tag{6.52}$$

Boost DC-DC Converter

$$R_{in} = \frac{R_o(1 - d_1 - d_3)^2}{(1 - d_3)^2} \frac{\pi^2}{12} \ . \tag{6.53}$$

It is observed that the converter load appears as a duty-ratio dependent resistor. For a given load, converter switching frequency and other converter parameters, it is determined whether the converter operates in the CCM or DCM mode by using Equation 6.48 or 6.49. Then with known d_1, d_2 and d_3, the steady-state equations from any generator system model expressed by Equations (6.45-6.46, 6.52-6.53), are numerically solved with the empirical equations of the generator parameters given the control winding excitation voltage, rotor speed, and the load resistances of the DC-DC converter.

Figures 6.6 and 6.7 show both steady-state calculated and measured characteristics of the generator system with a DC-DC buck converter while corresponding results are displayed in Figures 6.8 and 6.9 for the system with DC-DC boost converter. Two control winding currents, 2A and 4A, are chosen in the experimental measurement and the calculation. The rotor speed is set at 1200 rev/min. These two converters operate in the continuous-conduction current mode of operation.

Figures 6.6(a) and 6.8(a) show the curves of load voltage vs. duty ratio. Load voltages of both have maximum values when the duty ratio is close to 0.5, and decrease when the duty ratio deviates that value. The load voltage of boost converter is much higher than that of the buck converter.

Figures 6.6(b) and 6.8(b) show the curves of effective input resistance of converter vs. duty ratio. Their effective input resistances are inverse-proportional to the duty ratio, the higher the duty ratio, the lower the effective input resistances.

Figures 6.6(c) and 6.8(c) show the curves of load power vs. duty ratio. The load powers of both have the maximum values when the duty ratio is close to 0.5, and then they decrease when the duty ratio leaves that value. They both have the same maximum output powers.

Figures 6.6(d) and 6.8(d) show the curves of converter input voltage vs. duty ratio. The converter input voltages of both are inverse-proportional to the duty-ratio. Boost converter input voltage is higher than one of buck input voltage.

The steady-state characteristics of the generator system with either DC-DC buck converter or DC-DC boost converter, which are displayed in Figure 6.7 and Figure 6.9, are similar each other. The curves of generator output power vs. duty ratio are shown in Figures 6.7(a) and 6.9(a)). Per-phase generator voltage vs. duty ratio are shown in Figure 6.7(b) and 6.9(b). Figures 6.7(c) and 6.9(c) show the curves of per-phase generator voltage vs. per-phase generator output power.

There is good agreement between measured and calculated steady-state performance curves. Since the rectifier output voltage also depends on the load impedance that in turn is influenced by the duty-ratio and the generator load performance, we can see the output voltage profiles of these two converters differ remarkable from those of the converters fed with a constant voltage source. Figures 6.10 and 6.11, respectively, for the buck and boost converters give measured waveforms of the converters operating in the continuous-current mode.

The steady-state performance of the generator system (shown in Figure 6.2(a)), that is special because of its excitation depending on the generated output DC voltage from the power windings, is shown in Figure 6.12. Two rotor speeds, 900rev/min and 1350rev/min, are used in the experimental measurement and the calculation.

Figure 6.12(a) and (b) show the curves of duty-ratio vs. generator per-phase terminal voltage or DC load voltage. Changing the duty-ratio during the range from zero to near 0.2 can regulate these voltages. Figure 6.12(c) shows the curves of per-phase terminal voltage vs. generator output power while the curves of duty-ratio vs. control winding DC current are shown in Figure 6.12(d). The higher the rotor speed, the higher the attainable maximum control winding DC currents and generator output powers.

It is observed from the Figure 6.12 that it is necessary to keep the duty ratio not less some values near 0.2 so that the generator system (shown in Figure 6.2(a)) avoids the collapse of the generator terminal voltage.

Overall, there are good agreements between measurement and calculation results. The little differences must be due to the presence of factors not accommodated in the derived models: significant harmonic components in the generator and input rectifier currents in addition to the non-negligible over-lap commutation of the rectifier diodes which can be seen in Figure 6.14.

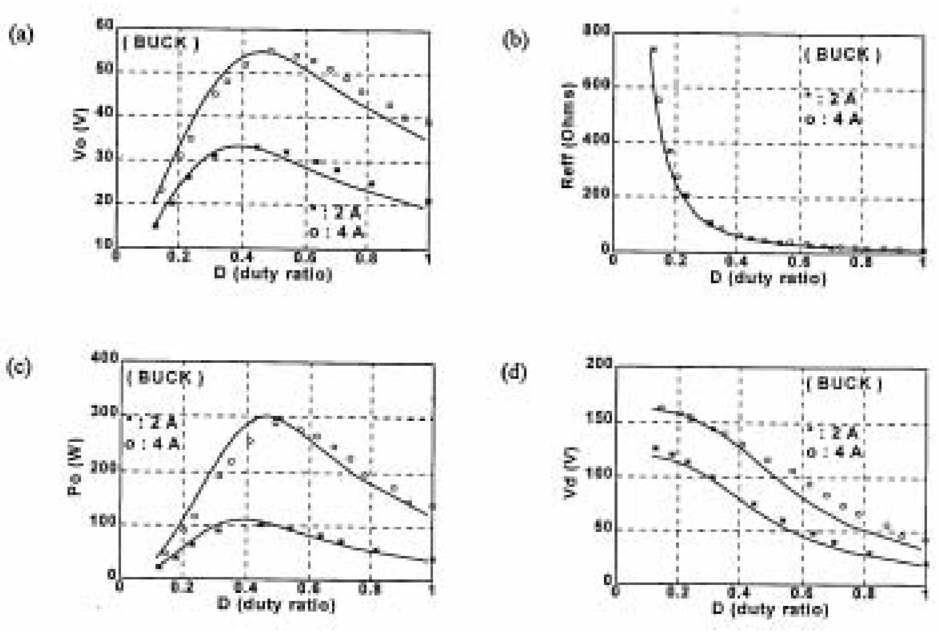

Figure 6.6. The steady-state characteristics of the generator system with DC-DC buck converter in the Figure 6.1(a). (Rotor speed = 1200 rpm). (a) Load voltage vs. duty ratio, (b) effective input resistance of converter vs. duty ratio, (c) load power vs. duty ratio, (d) converter input voltage vs. duty-ratio.

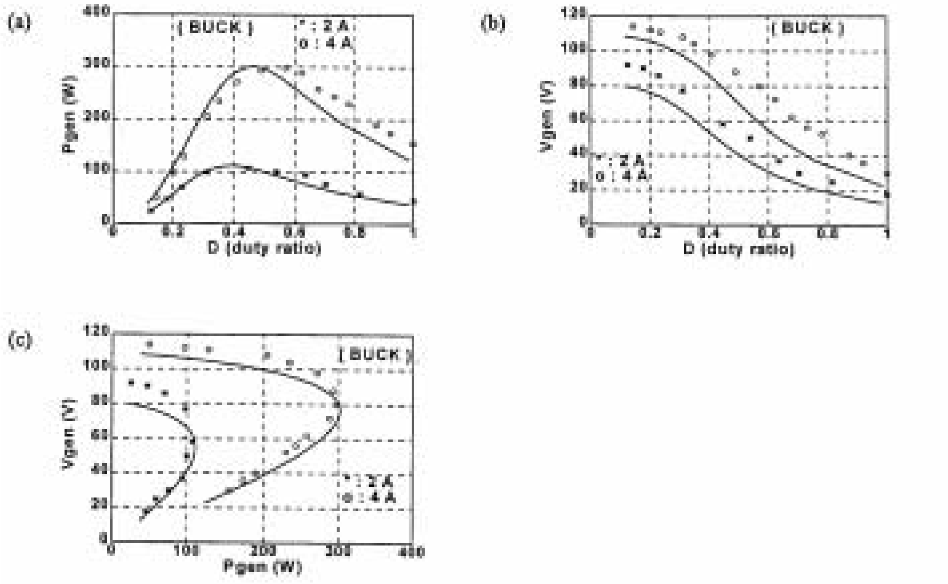

Figure 6.7. The steady-state characteristics of the generator system with DC-DC buck converter in the Figure 6.1(a) (Rotor speed = 1200 rpm). (a) Generator output power vs. duty ratio, (b) per-phase generator voltage vs. duty ratio, (c) per-phase generator voltage vs. generator output power.

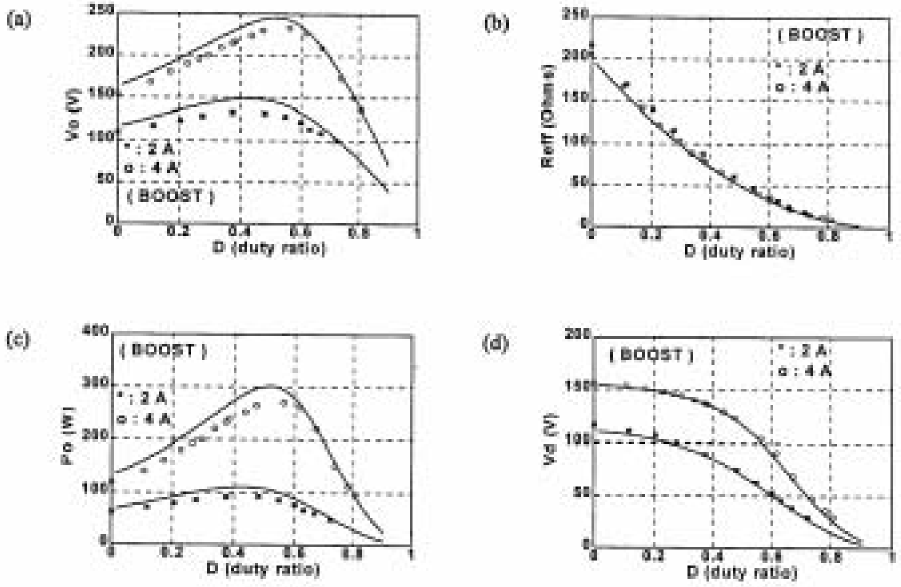

Figure 6.8. The steady-state characteristics of the generator system with DC-DC boost converter in the Figure 6.1(b) (Rotor speed = 1200 rpm). (a) Load voltage vs. duty ratio, (b) effective input resistance of converter vs. duty ratio, (c) load power vs. duty ratio, (d) converter input voltage vs. duty-ratio.

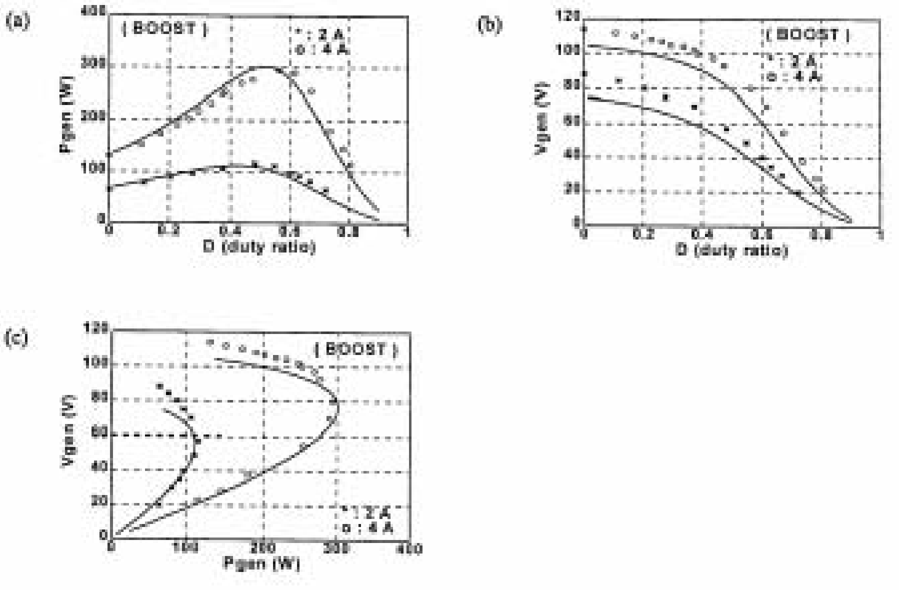

Figure 6.9. The steady-state characteristics of the generator system with DC-DC boost converter in the Figure 6.1(b) (Rotor speed = 1200 rpm). (a) Generator output power vs. duty ratio, (b) per-phase generator voltage vs. duty ratio, (c) per-phase generator voltage vs. generator output power.

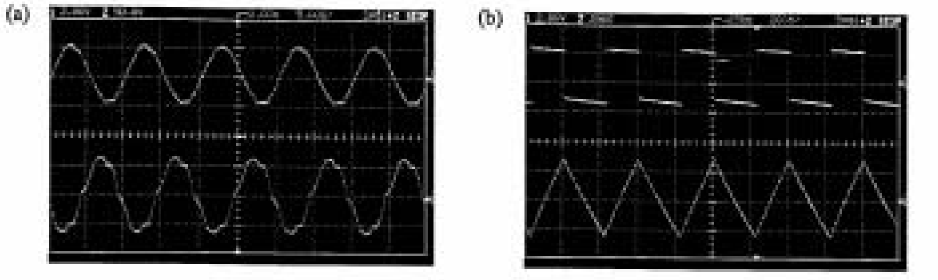

Figure 6.10. Measured waveform of the generator with DC-DC buck converter in the Figure 6.1(a). (Rotor speed = 1200 rpm, duty-ratio = 0.6)

(a) Top: Generator phase current. Bottom: Generator line-line voltage.

(b) Top: Input converter current. Bottom: Converter inductor current.

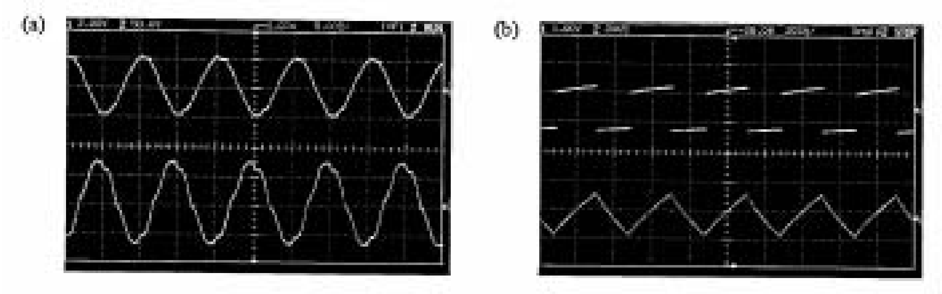

Figure 6.11. Measured waveform of the generator with DC-DC boost converter in the Figure 6.1(a). (Rotor speed = 1200 rpm, duty-ratio = 0.6)

(a) Top: Generator phase current. Bottom: Generator line-line voltage.

(b) Top: Input converter current. Bottom: Converter inductor current.

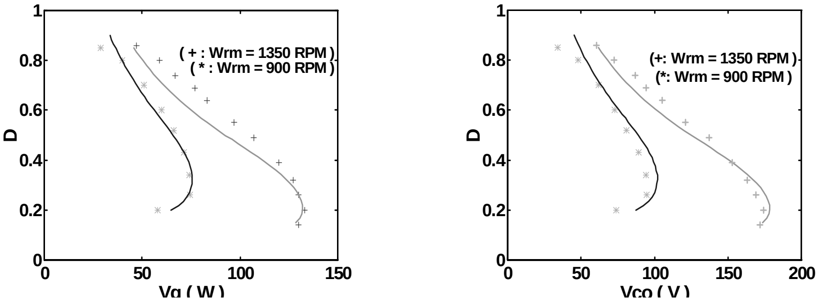

(a) (b)

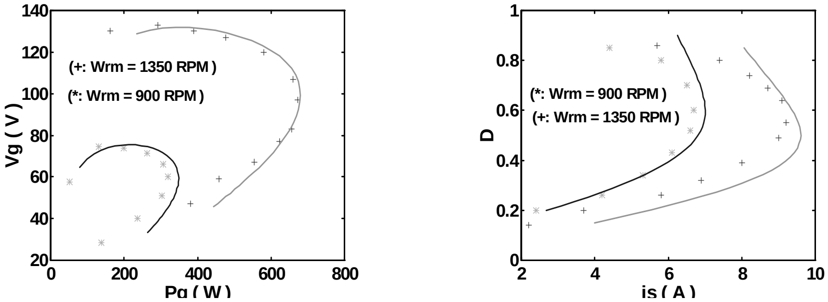

(c) (d)

Figure 6.12. Measured and calculated steady-state characteristics of the doubly-fed synchronous reluctance generator feeding an impedance load (RL=400Ω).(Figure 6.2(a))

(a) Duty-ratio vs. generator per-phase terminal voltage

(b) Per-phase terminal voltage vs. generator output power

(c) Duty-ratio vs. dc load voltage

(d) Duty ratio vs. control winding dc current.

6.4 Simulation of Generator System

For a complete understanding of the generator system in Figure 6.2, the starting transient of the generator system assuming that the root speed is constant is simulated and shown in Figure 6. 13. Three starting stages are: (1) a battery is connected to the control windings while the converter is turned off. (2) after 0.4 seconds, the converter is turned on with the battery still connected for another 0.4 seconds and (3) finally, the battery is disconnected with only the converter supplying the excitation current to the control windings. It is observed that the generator easily excites and the period taken to achieve steady-state operating condition depends on the battery voltage and the converter duty ratio. The simulated steady-state waveforms and corresponding experimental results are now displayed in Figure 6.14. Figure 6.15 gives the simulation results of the generator system when the converter duty ratio is reduced while operating at a stable steady-state point. In view of the low excitation current, the generator voltage collapses indicating that for a stable operation, a minimum converter duty ratio requirement for a given rotor speed and load must be met to sustain the generator operation.

The electrical excitation process of the generator charging a lead-acid battery shown in Figure 6.2(b) is simulated and the simulation results are shown in Figure 6.16. With the generator shaft running at a constant speed and the converter turned on, the generator excites, building up the generator DC output voltage. The battery initially provides an average current flowing into the converter and, after the generator voltage has sufficiently risen, an effective current flows into the battery to charge it. Figure

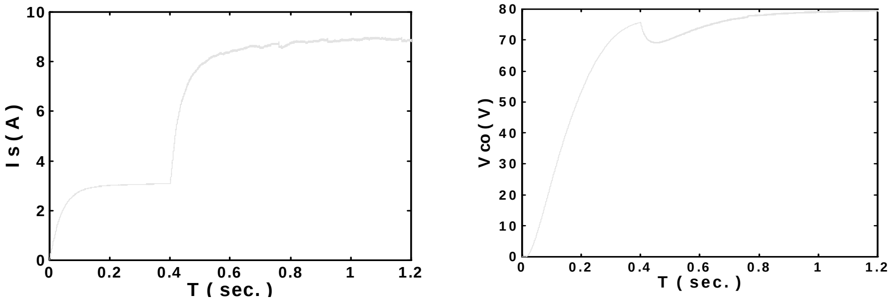

(a) (b)

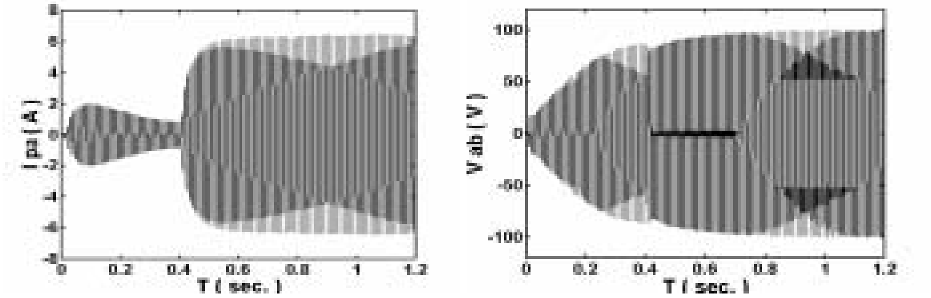

(c) (d)

Figure 6.13. Starting transient of the generator system shown in Figure 6.2(a). Rotor speed = 1350 rpm, duty ratio = 0.6, load resistance = 400 ohms. (a) Control winding current, (b) DC load voltage, (c) line-to-line generator voltage, (d) generator phase ‘a’ current.

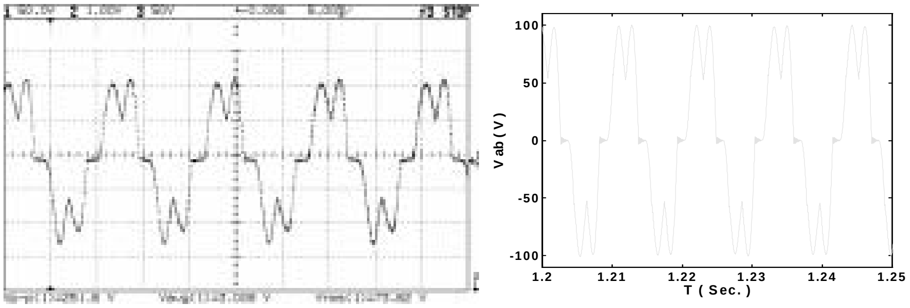

(a) (b)

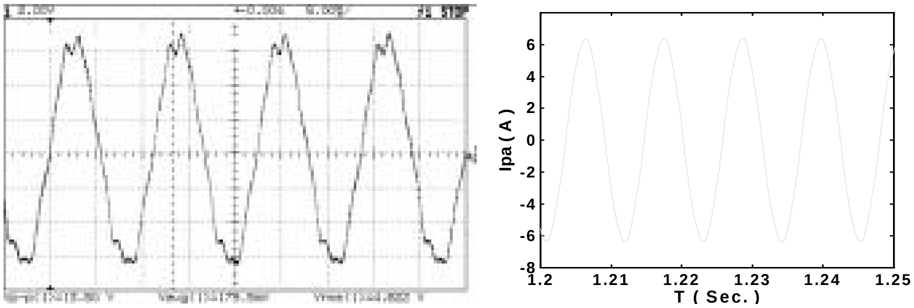

(c) (d)

Figure 6.14. Steady-state waveforms of the generator system feeding impedance load. Rotor speed = 1350 rpm, load resistance = 400 ohms, duty ratio of converter = 0.6.
(a) Generator line-to-line voltage, 50V/div, (b) phase ‘a’ generator current, 2A/div.

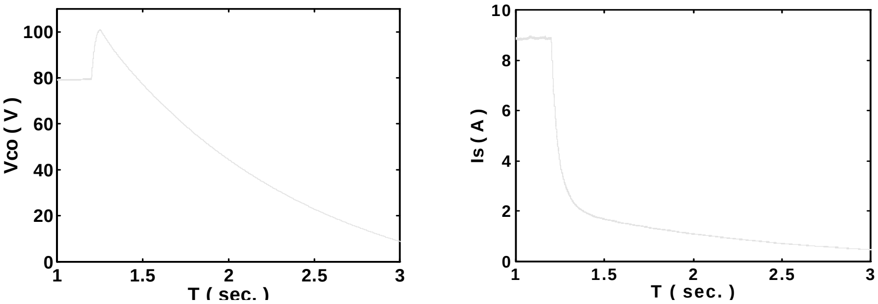

(a) (b)

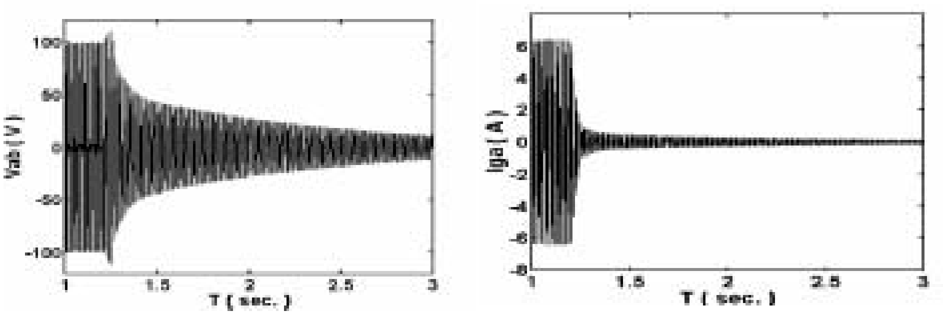

(c) (d)

Figure 6.15. Generator de-excitation due to reduced DC-DC converter duty ratio.

(a) DC load voltage, (b) control winding current, (c) generator loine-to-line voltage, (d) generator phase current.

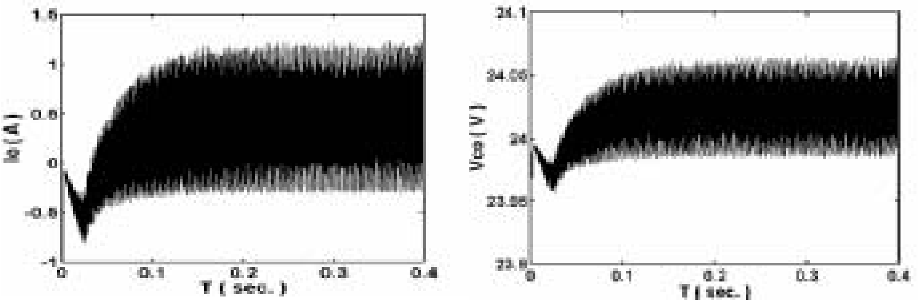

(a) (b)

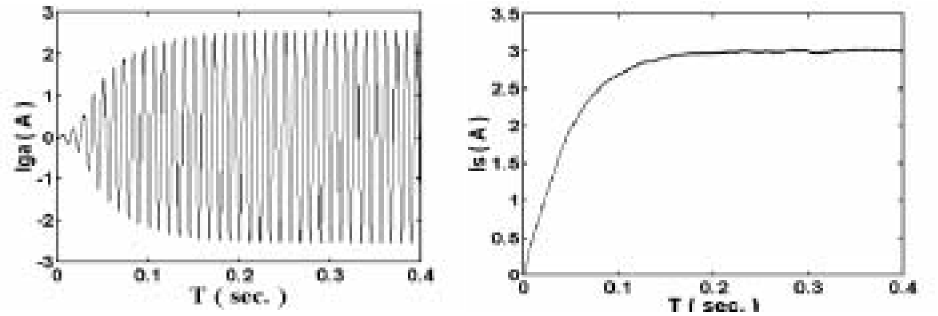

(c) (d)

Figure 6.16. Electrical excitation transient for the doubly-fed synchronous reluctance generator charging a lead-acid battery. (a) Current flowing into the battery, (b) generator DC voltage, (c) phase 'a' generator current, (d) control winding current.

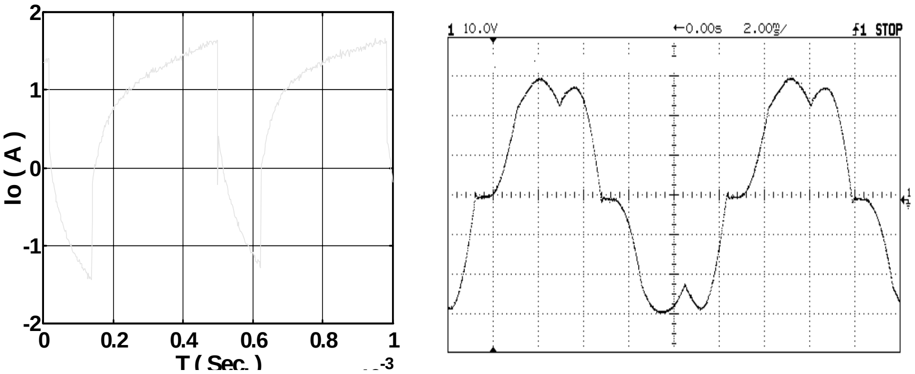

(a) (b)

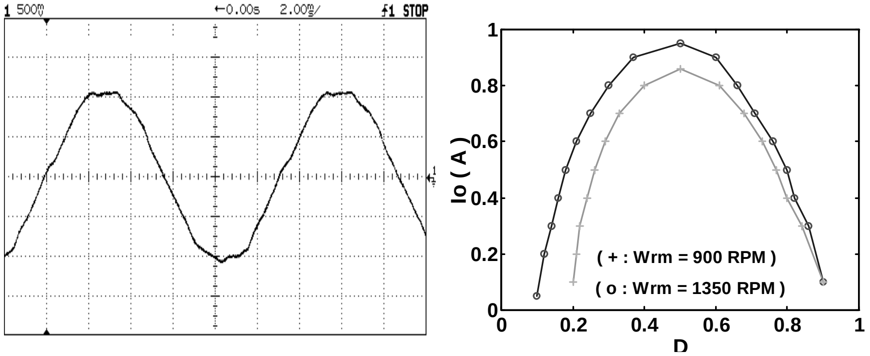

(c) (d)

Figure 6.17. Measured steady-state waveforms of the generator charging a 24V battery. Average charging current = 0.7A. (a) Battery current, (b) generator line-line voltage, 10V/div, (c) generator phasse current, 0.5A/div, (d) variation of charging curent with converter duty ratio for 900 rpm and 1350 rpm.

6.17(a)-(c) display measured steady-state waveforms of the generator charging a 24V battery when the rotor speed is 1350rpm and the duty ratio of the DC-DC converter is 0.25. The average charging battery current is fixed at 0.7A. Finally, Figure 6.17(d) shows the measured variation of the average charging current as a function of the duty ratio of the converter for two rotor speeds. From this graph, it is concluded that there is a maximum average charging current achievable below which there are two possible duty ratios that result in the same average charging current.

6.5 Conclusion

The modeling and analysis of the doubly-fed synchronous reluctance generator with a DC excitation , which can be an outside source or a self source from DC output of power windings, are presented. The generator systems successfully use buck or boost DC-DC converter connected to the power windings as the DC source regulators. The generator system characteristics are predicted based on the proposed models and the results of which compare favorably with measured results. The excitation process of the generator systems feeding an impedance load or charging a battery are simulated and discussed. The computer simulation results show that the excitation process is fast and reliable. These generator systems have a potential for use in stand-alone applications and in electric automotive applications.

CHAPTER 7

FIELD ORIENTATION CONTROL OF A DOUBLY-FED SYNCHRONOUS RELUCTANCE MACHINE

7.1 Introduction

Doubly-fed reluctance machines having two stator windings (power and control windings) have received renewed attention in the last few years in adjustable-speed drives where efficiency optimization and energy conservation are desirable. In many low performance drive applications, the three-phase power windings are connected to the utility supply, while the rotor circuit is connected to either an inverter controlled ac or converter controlled dc sources. With controlled ac source connected to the control winding, the machine operates either in the synchronous, sub-synchronous or super-synchronous modes permitting large speed operation range. The feasibility of the doubly-fed reluctance machine with controlled ac power and control winding excitations for accepted field orientation-type performance have been demonstrated [73,74].

This chapter proposes a novel high-performance control of the doubly-fed synchronous reluctance in which the control winding is connected to a controlled current DC source. The power windings are connected to a voltage source inverter (VSI), which can be a current-controlled VSI or voltage-controlled VSI, to regulate the axis currents, voltages, and the frequency in the power windings. The drive system operates exactly like a DC machine possessing the same ease control. Two control schemes are investigated and the main focus are their operation characteristics in a wide speed range including the constant torque control below the base speed and constant output power above the base speed with maximum output torque.

In section 7.2, the field-orientation principle is introduced. It also gives the steady-state operation characteristics of the systems below and above the base speed. Two control schemes are described in section 7.3. Section 7.4 gives the design procedures of integral plus proportional (IP) controller, which presents mathematical algorithms to obtain the parameters of the IP controller with non-overshoot performance. The theoretical derivation is also included in this section. A novel input-output linearization technique and Butterworth method are set forth in Section 7.5, which is used in the design of the control scheme I. Sections 7.6 and 7.7 give the detailed description of both voltage-controlled and current-controlled VSI. In sections 7.8 and 7.9, the dynamical simulation results of two control systems are given and discussed. Finally, we draw conclusions in Section 7.10.

7.2 Field Orientation Principle

In general, an electric motor can be thought of as a controlled source of torque. Accurate control of the instantaneous torque produced by a motor is required in high-performance drive systems, e.g., those used for position control. The torque developed in the motor is a result of the interaction between current in the armature winding and the magnetic field produced in the field system of the motor. The field should be maintained at a certain optimal level, sufficiently high to yield a high torque per unit ampere, but not too high to result in excessive saturation of the magnetic circuit of the motor. With fixed field, the torque is proportional to the armature current.

Independent control of the field and armature currents is feasible in separately-excited dc motors where the current in the stator field winding determines the magnetic field of the motor, while the current in the rotor armature winding can be used as a direct means of torque control. The physical disposition of the brushes with respect to the stator field ensures optimal conditions for torque production under all conditions.

The Field Orientation Principle (FOP) defines conditions for decoupling the magnetic field control from the torque control. A field–oriented doubly-fed synchronous reluctance motor should emulate a separately-excited DC motor in two aspects:

(1) Both the magnetic field and the torque developed in the motor can be controlled independently.

(2) Optimal conditions for torque production, resulting in the maximum torque per unit ampere, occur in the motor both in the steady-state and in transient conditions of operation.

The power winding and control winding q-d equations of the doubly-fed synchronous reluctance machine in the rotor reference frame are

$$V_{qp} = R_p I_{qp} + p\lambda_{qp} + \omega_p \lambda_{dp} \tag{7.1}$$

$$V_{dp} = R_p I_{dp} + p\lambda_{dp} - \omega_p \lambda_{qp} \tag{7.2}$$

$$V_{qs}^{'} = R_s^{'} I_{qs}^{'} + p\lambda_{qs}^{'} \tag{7.3}$$

$$V_{ds}^{'} = R_s^{'} I_{ds}^{'} + p\lambda_{ds}^{'} \tag{7.4}$$

where

$$\lambda_{qp} = L_p I_{qp} + L_m I_{qs}^{'} \tag{7.5}$$

$$\lambda_{dp} = L_p I_{dp} + L_m I_{ds}^{'} \tag{7.6}$$

$$\lambda_{qs}^{'} = L_s^{'} I_{qs}^{'} + L_m I_{qp} \tag{7.7}$$

$$\lambda_{ds}^{'} = L_s^{'} I_{ds}^{'} + L_m I_{dp} \ . \tag{7.8}$$

Torque equation is expressed as

$$T_e = \left(\frac{3}{2}\right)(p_1 + q) L_m (I_{dp} I_{qs}^{'} - I_{qp} I_{ds}^{'}) \ . \tag{7.9}$$

The relationship of the rotor speed ω_r, load torque T_L and electrical torque T_e is

$$\frac{J}{P_r} p\omega_r = T_e - T_L \ . \tag{7.10}$$

J is the rotor inertia, and P_r is equivalent pole numbers of the rotor and equal to p_1+q.

If the control winding is connected as shown in Figure 7.1, the control winding currents I_{as}, I_{bs} , I_{cs}, and current source I_s have the relationships given in Equation (7 .11)

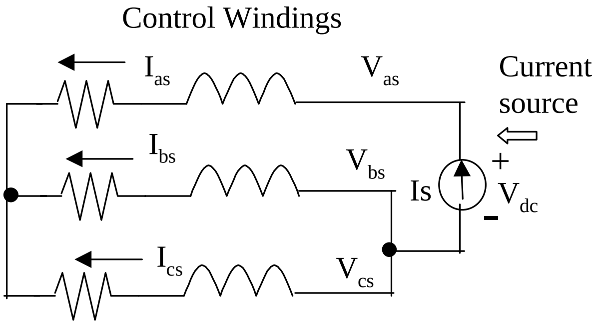

Figure 7.1. Control winding connection.

while the relationships among control winding voltages V_{as}, V_{bs}, V_{cs}, and V_{dc} are given in Equation (7.12):

$$\begin{aligned} &I_{as} = I_s, \quad I_{bs} = I_{cs} = -\frac{1}{2} I_s \\ &I_{as} + I_{bs} + I_{cs} = 0 \end{aligned} \tag{7.11}$$

$$\begin{aligned} &V_{bs} = V_{cs}, \quad V_{dc} = V_{as} - V_{bs} = V_{as} - V_{cs} \\ &V_{as} + V_{bs} + V_{cs} = 0\ . \end{aligned} \tag{7.12}$$

After performing abc-qd transformation as well as considering the turns-ratio, control winding q-d axis voltages and currents become

$$\begin{aligned} &V_{qs}^{'} = \frac{2}{3} V_{dc} \\ &V_{ds}^{'} = 0 \end{aligned} \tag{7.13}$$

and

$$\begin{aligned} &I_{ds}^{'} = 0 \\ &I_{qs}^{'} = I_s^{'}\ . \end{aligned} \tag{7.14}$$

Hence, the torque depends on the control winding q-axis current $I_{qs}^{'}$ and the power winding d-axis current I_{dp}. It is

$$T_e = \frac{3P_r}{2} L_m I_{dp} I_{qs}^{'} . \tag{7.15}$$

In field orientation control, $I_{qs}^{'}$ is used to control magnet flux similar to $L_{mq} I_{qs}^{'}$, while I_{dp} is used to control the torque.

We drive the motor in a wide speed range. From zero speed up to its base speed, the power winding voltage rises up to its maximum value at base speed and then limits to that value at higher speed. This speed range is called constant torque region. Maximum constant torque is achieved when the control winding dc current $I_{qs}^{'}$ is set at the rated value, with the d-axis power winding current I_{dp} set to the rated power winding current. At the same time the q-axis power winding current is set equal to zero. Above base speed, the power winding voltage is kept at rated value while airgap flux linkage need to be decreased to realize the constant power output. This goal is realized by regulating the power winding q-axis current I_{qp} and d-axis currents I_{dp} with the control winding current $I_{qs}^{'}$ set at the rated value. The output-power is constant above base speed, hence it is called constant-power or field-weakening region. To obtain maximum torque (and hence power) at any speed above base speed within the voltage and current rating, maximum torque field-weakening control strategy is used.

There are two operating modes above the base speed. The operating conditions for two modes are listed as follows [79-80]:

Mode I: current and voltage limited region:

$$V_{pm}^2 = V_{dp}^2 + V_{qp}^2 \tag{7.16}$$

$$I_{pm}^2 = I_{dp}^2 + I_{qp}^2 \tag{7.17}$$

where V_{pm} and I_{pm} are the voltage and current rated peak values, respectively. V_{dp} and V_{qp} are the q-d components of power winding voltage; I_{dp} and I_{qp} are the q-d components of power winding currents.

Mode II: Voltage-limited region:

$$V_{pm}^2 = V_{dp}^2 + V_{qp}^2 \tag{7.18}$$

$$I_{pm}^2 \geq I_{dp}^2 + I_{qp}^2 \tag{7.19}$$

Maximize T_e at each value of speed.

where T_e is electrical torque. V_{pm} and I_{pm} are the voltage and current rated peak values, respectively. V_{dp} and V_{qp} are the q-d components of power winding voltage; I_{dp} and I_{qp} are the q-d components of power winding currents.

Under the steady-state, the power winding q-d voltage equations are

$$V_{qp} = R_p I_{qp} + \omega_p L_p I_{dp} \tag{7.20}$$

$$V_{dp} = R_p I_{dp} - \omega_p L_p I_{qp} - L_m I_{qs}^{'} \ . \tag{7.21}$$

The peak value of power winding voltage V_{pm} is constant. It can be obtained from Equations (7.20) - (7.21) and expressed as

$$\begin{aligned} V_{pm}^2 &= V_{qp}^2 + V_{dp}^2 \\ &= \left(R_p I_{qp} + \omega_p L_p I_{dp}\right)^2 + \left(R_p I_{dp} - \omega_p L_p I_{qp} - L_m I_{qs}^{'}\right)^2 \end{aligned} \tag{7.22}$$

when the machine is running below the base speed, power winding q-axis current $I_{qp} = 0$ while the d-axis I_{dp} is set to be equal to the power winding peak rate current I_{pm}. At the same time, control winding current I'_{qs} is equal to the rated *dc* current I'_s (considering turns ratio). Hence, the base speed ω_{base} can be calculated using Equation (7.23), which is obtained from Equation (7.22):

$$\omega_{base} = -\frac{S_b}{2S_a} + \frac{\sqrt{S_b^2 - 4S_a S_c}}{2S_a} \tag{7.23}$$

where

$$S_a = L_p^2 I_{pm}^2 + L_m^2 I_s^{'2}$$

$$S_b = -2L_m R_p I_s^{'} I_{pm}$$

$$S_c = R_p^2 I_{pm}^2 - V_{pm}^2.$$

A simplified equation of ω_{base} is obtained by ignoring resistance R_p (R_p=0):

$$\omega_{base} = \frac{V_{pm}}{\sqrt{L_p^2 I_{pm}^2 + L_m^2 I_s^{'2}}}.$$

Mode I operation

By extending Equation (7.22) and using the current constraint condition (Equation (7.17)) in mode I, we can obtain

$$I_{dp} = \frac{T_{cc} I_{qp} - T_{aa}}{T_{bb}} \tag{7.24}$$

where

$$T_{aa} = V_{pm}^2 - (R_p^2 + \omega_p^2 L_m^2) I_{pm}^2 - \omega_p^2 L_m^2 I_s^{'2}$$

$$T_{bb} = 2\omega_p L_m R_p I_s^{'}$$

$$T_{cc} = 2\omega_p^2 L_m L_p I_s^{'}.$$

Substituting Equation (7.24) into Equation (7.17), the following equation is obtained:

$$(T_{cc}^2 + T_{bb}^2) \cdot I_{qp}^2 - 2T_{aa} T_{cc} \cdot I_{qp} + (T_{aa}^2 - T_{bb}^2 I_{pm}^2) = 0.$$

Its solution is

$$I_{qp} = -\frac{T_b}{2T_a} + \frac{\sqrt{T_b^2 - 4T_aT_c}}{2T_a} \tag{7.25}$$

where

$$T_a = T_{cc}^2 + T_{bb}^2$$

$$T_b = -2T_{aa}T_{cc}$$

$$T_c = T_{aa}^2 - T_{bb}^2 I_{pm}^2 .$$

Equations (7.24) and (7.25) are used to obtain the power winding q-axis and d-axis current I_{qp} and I_{dp} when the machine is operated in the Mode I region. The simplified equations of Equations (7.24) and (7.25) are obtained by ignoring the resistance R_p (R_p=0):

$$I_{qp} = -\frac{V_{pm}^2 - \omega_p^2 L_m^2 (I_{pm}^2 + I_s^{'2})}{2\omega_p^2 L_m L_p I_s^{'}}$$

$$I_{dp} = \frac{\sqrt{4\omega_p^4 L_m^2 L_p^2 I_s^{'2} I_{pm}^2 - [V_{pm}^2 - \omega_p^2 L_m^2 (I_{pm}^2 + I_s^{'2})]^2}}{2\omega_p^2 L_m L_p I_s^{'}} .$$

Torque is obtained by substituting the expression of I_{dp} into torque Equation (7.15).

Mode II operation

Substituting Equations (7.20-7.21) into the voltage constraint condition (Equation (7.18)) to yield

$$aa \cdot I_{dp}^2 + bb \cdot I_{dp} + cc = 0$$

where

$$aa = R_p^2 + \omega_p^2 L_p^2$$

$$bb = -2\omega_p^2 L_m R_p I_{qs}$$

$$cc = \omega_p^2 L_m^2 I_s^{'2} + (R_p^2 + \omega_p^2 L_p^2) I_{qp}^2 + 2\omega_p^2 L_m L_p I_s^{'} I_{qp} - V_{pm}^2.$$

Its solution is

$$I_{dp} = \frac{-bb + \sqrt{bb^2 - 4aa \cdot cc}}{2aa}$$

where I_{dp} is dependent on variable I_{qp}. I_{dp} can be expressed as a function of variable I_{qp} :

$$I_{dp} = f(I_{qp}) \quad .$$

Hence, from Equation (7-15), the torque equation can be expressed as

$$T_e = \frac{3P_r}{2} L_m I_s^{'} f(I_{qp}) \, .$$

To obtain the conditions of achieving maximum output torque, the torque equation is differentiated with respect to I_{qp} and then forced to zero, that is

$$\frac{dT_e}{dI_{qp}} = \frac{d}{dI_{qp}} (f(I_{qp})) = 0.$$

The solution of this equation is

$$I_{qp} = -\frac{\omega_p^2 L_m L_p I_s^{'}}{R_p^2 + \omega_p^2 L_p^2} \quad . \qquad (7.26)$$

Using equation (7.26) to replace variable I_{qp} in cc, I_{dp} is obtained and expressed as

$$I_{dp} = \frac{\omega_p L_m R_p I_s^{'} + V_{pm} \sqrt{L_p^2 \omega_p^2 + R_p^2}}{R_p^2 + \omega_p^2 L_p^2} \, . \qquad (7.27)$$

Hence, in mode II, if I_{dp} and I_{qp} are selected using Equations (7.26) and (7.27), not only the maximum torque is achieved, but also the voltage constraint condition is satisfied. The simplified equations of Equations (7.26) and (7.27) are obtained by ignoring the resistance R_p (R_p=0)

$$I_{qp} = -\frac{L_m}{L_p} I_s^{'}$$

$$I_{dp} = \frac{V_{pm}}{\omega_p L_p}.$$

By substituting the expression of I_{dp} into Equation (7.15), the torque is given as

$$T_e = \frac{3P_r}{2} \frac{L_m I_s^{'} V_{pm}}{\omega_p L_p} \ .$$

Boundary speed ω_{12}

At boundary speed point ω_{12} between Mode I and Mode II, the power winding q-axis and d-axis current I_{qp} and I_{dp} , calculated from Equations (7.26) and (7.27), also satisfy the current constraint condition in Mode I. By substituting Equations (7.26) and (7.27) into the current constraint Equation (7.17), the expression of the boundary speed point is obtained from

$$C_a^2 \omega_{12}^8 + 2C_a C_b \omega_{12}^6 + (C_b^2 - C_d^2 + 2C_a C_c)\omega_{12}^4 + (2C_b C_c - C_e^2)\omega_{12}^2 + C_c^2 = 0 \qquad (7.28)$$

where

$$C_a = I_{pm}^2 L_p^4 - L^2 L_p^2 I_s^{'2}; \quad C_b = 2R_p^2 L_p^2 I_{pm}^2 - L_m^2 R_p^2 I_s^{'2} - L_p^2 V_{pm}^2;$$

$$C_c = I_{pm}^2 R_p^4 - R_p^2 V_{pm}^2; \quad C_d = 2V_{pm} L_m R_p I_s^{'} L_p; \quad C_e = 2V_{pm} L_m R_p^2 I_s^{'}.$$

The simplified equation is obtained by ignoring the resistance R_p (R_p=0):

$$\omega_{12} = \frac{V_{pm}}{\sqrt{(L_p^2 I_{pm}^2 - L_m^2 I_s^{'2})}} \ .$$

The performance curves for wide speed range (below the base speed and above the base speed including Mode I and Mode II), shown in Figure (7.2), are computed using Equations (7.23) through (7.28). Three different control-winding currents are used to obtain these curves. Unit speed is equal to 377 *rad/s*. It is observed from Figure 7.2 (b) and 7.2(c) that Mode I region with constant rated current and constant rated voltage is narrow, however it increases when the current winding current increases, and so do the maximum speeds for this mode.

We can also see from other figures that, below the base speed, the d-axis power winding current is set to the constant rated values and the q-axis power winding current is equal to zero. Total power winding current and torque are held constant, but power

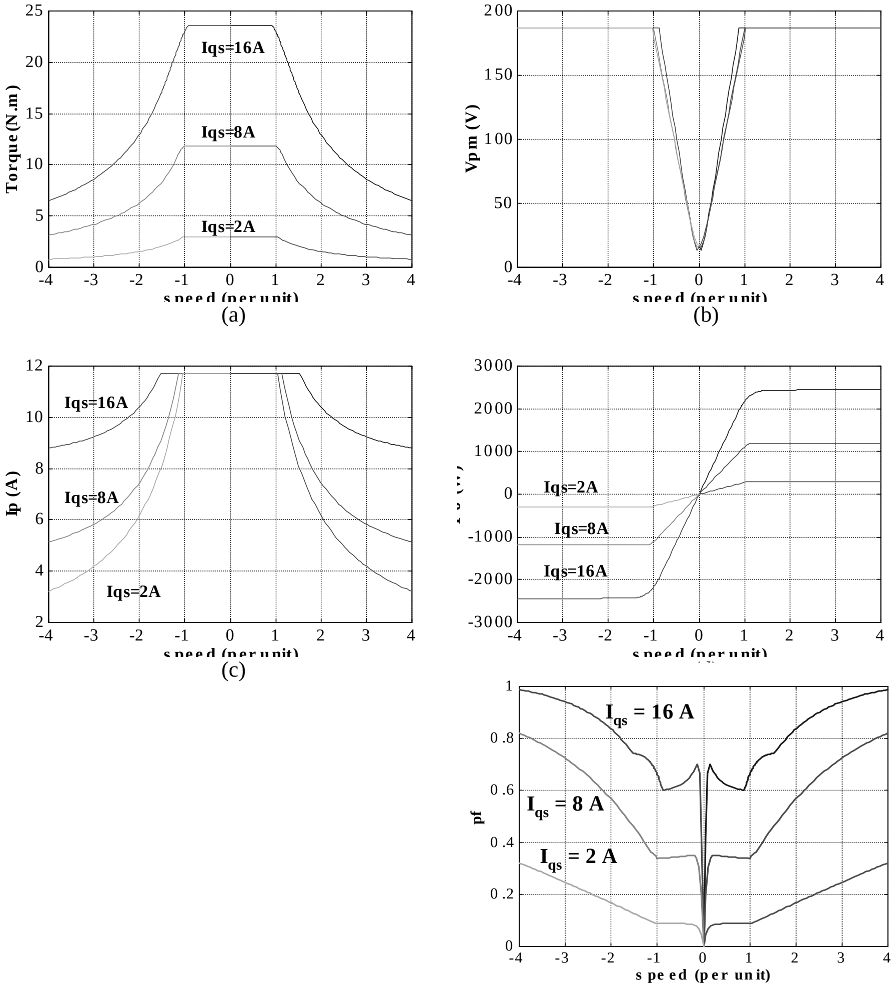

(a)

(b)

(c)

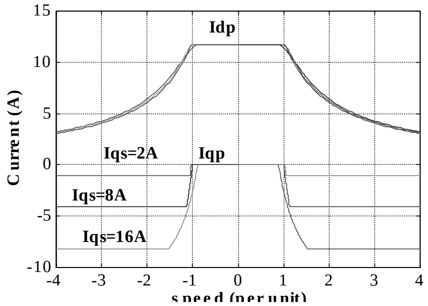

(e) (f)

Figure 7.2. Performance curves for extended speed range, maximum output torque operation. (a) Torque, (b) power winding phase voltage, (c) power winding current, (d) output power, (e) power winding q and d axis currents, (f) power factor.

winding voltage and output power increase with increasing value of rotor speed. The larger are the control winding currents, the larger the output torque; Above base speed, the d-axis power winding current I_{dp} decreases almost linearly with speed for a range, after which it tends to a constant value as the speed increases. The torque decreases almost linearly with speed, giving an almost constant output power characteristic. Figure 7.2(e) shows that there is a redistribution of the power winding axes currents with the winding current I'_{qs} set at its rated value above the base speed. The controllers need accurately reflect this redistributing characteristic in the command axis current values. In Figure 7.2(f), we can see that increasing rotor speed or control winding currents will increase the power factor of the motor control system.

7.3 Description of Two Control Schemes

Two control schemes, with current-controlled or voltage-controlled voltage source inverter, are investigated. Figure 7.3 gives the schematic diagram of the field-orientation control scheme I. The two inputs are the reference rotor speed and the power winding q-axis current, which is set to zero for constant torque operation and non-zero values for constant power operation. The three-phase power winding currents, measured and transformed to the rotor reference frame using the rotor angle measured with an encoder, are fed to a non-linear controller. The nonlinear controller generates reference q-d voltage components that are transformed into three-phase voltage reference for the VSI.

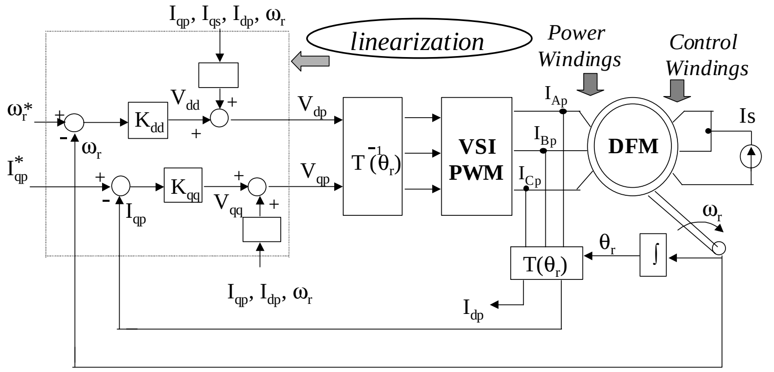

Figure 7.3. Control Scheme I: Field-orientation control of doubly fed synchronous reluctance machine with voltage-controlled voltage source inverter (VSI).

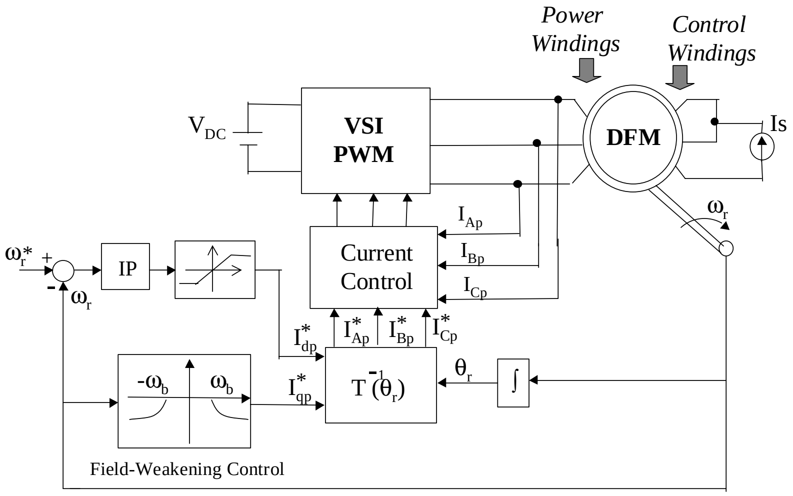

Figure 7.4. Control Scheme II: Field-orientation control of doubly-fed synchronous reluctance machine with current-controlled voltage source inverter (VSI).

The output of the VSI are used to drive the doubly-fed synchronous reluctance motor that has control winding connection shown in Figure 7.1.

Figure 7.4 gives the schematic diagram of the field-orientation control of doubly fed synchronous reluctance machine with current-controlled voltage source inverter. The three-phase power winding current are measured and used as a feedback signals for the current control of the VSI. The rotor angle is measured using an encoder and rotor speed is calculated using the integer. Below the base speed, field-weakening controller is switched off, and the reference q-axis current is set to zero. However, the reference q-axis current is non-zero values above the base speed. The field-weakening controller is switched on at this time. The speed error inputs to the IP controller that generates the reference d-axis current, its values limited in some range set by the saturation controller. The reference q-d currents are transformed to the reference three-phase power winding currents that compare with the three-phase feedback currents to obtain switching-time of the VSI's transistors. The output voltage of the VSI drives the doubly fed synchronous reluctance motor its control winding fed by a current source.

7.4 Design of the IP Controller

The Integral plus proportional (IP) controller is applied here because of its novel features [65]:

(1) IP controller can eliminates the current overshoot problem and has zero steady-state error. This is very useful for the protection of the electrical devices needing frequent stopping and starting.

(2) IP controller can also eliminate the speed and position overshoots for step changes without sacrificing the load torque response due to a load torque change.

The literature [66,67] presented a design procedure of IP controller that can be used for a three-order induction motor servo drive system. By using this design procedure, the parameters of the IP controller can be quantitatively decided and the control system can obtain no overshoot position response. We use the similar theoretical method to derive the design procedure for a second-order speed control system with non-overshoot speed response.

For a stable single-input single-output (SISO) nth order system expressed by

$$H(s) = \frac{b_o + b_1 S + b_2 S^2 + \ldots + b_{n-1} S^{n-1}}{a_o + a_1 S + a_2 S^2 + \ldots + S^n} = \sum_{i=1}^{n} \frac{h_i}{S + \mu_i} . \tag{7.29}$$

For a white noise input with variance σ_x^2, the variance E_o of the impulse response, or what is called the impulse energy of the output, can be determined to be [68]

$$E_o = \sum_{j=1}^{n} \sum_{i=1}^{n} \frac{h_i h_j}{\mu_i + \mu_j} \cong \sum_{i=1}^{n} \frac{h_i}{S + \mu_i} , \tag{7.30}$$

in which the impulse energy contribution corresponding to the eigenvalue μ_j is defined as [68]

$$e_j \cong \sum_{i=1}^{n} \frac{h_i h_j}{\mu_i + \mu_j} \tag{7.31}$$

For a stable linear system described by Equation (7.29), the variance Eo must be finite and positive, i.e., from Equation (7.30),

$$0 < (e_1 + e_2 + \ldots + e_n) < \infty . \tag{7.32}$$

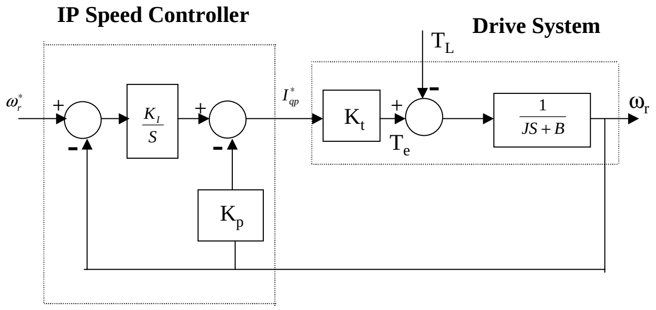

Figure 7.5. Block diagram of IP speed control system.

The speed control loop of the control scheme II is described by the block diagram Figure 7.5, where K_t is torque coefficient, and a and b can be expressed by the system viscous damping coefficient B and the inertia constant J. they are expressed as

$$K_t = \frac{3}{2}(p_1 + q)L_m I_{qs} \tag{7.33}$$

$$a = \frac{B}{J} \tag{7.34}$$

$$b = \frac{1}{J}. \tag{7.35}$$

The transfer function speed control loop can be found from Figure 7.5 as

$$\left.\frac{\omega_r(s)}{\omega_r^*(s)}\right|_{T_L=0} = \frac{K_I K_t b}{s^2 + (B + K_t K_p) b \cdot s + K_t K_I b}\ . \tag{7.36}$$

Second-order system in Figure 7.5 can also be expressed as

$$\left.\frac{\omega_r(s)}{\omega_r^*(s)}\right|_{T_L(s)=0} = \frac{h_1}{s+\mu_1} + \frac{h_2}{s+\mu_2}\ . \tag{7.37}$$

The relationship of coefficients between Equations (7.36) and (7.37) can be found as following:

$$h_1 + h_2 = 0 \tag{7.38}$$

$$\mu_1\mu_2 = h_1\mu_2 + h_2\mu_1 = K_I K_t B \tag{7.39}$$

$$\mu_1 + \mu_2 = (B + K_t K_p)b\,. \tag{7.40}$$

The unit-step response of transfer function is

$$y(t) = \frac{h_1}{\mu_1}\left(1 - e^{-\mu_1 t}\right) + \frac{h_2}{\mu_2}\left(1 - e^{-\mu_2 t}\right)\ . \tag{7.41}$$

For observing the overshoot, let $d(y(t))/dt = 0$ and $0<\mu_1<\mu_2$, then

$$\frac{dy(t)}{dt} = h_1 e^{-\mu_1 t} + h_2 e^{-\mu_2 t} = 0\ . \tag{7.42}$$

It is obvious that the overshoot of its step response will not occur if one of the following cases is satisfied:

(1) $h_1 > 0, h_2 > 0$;

(2) $h_1 < 0, h_2 < 0$;

(3) $h_1 > 0, h_2 < 0, h_1 > -h_2$;

(4) $h_1 < 0, h_2 > 0, -h_1 > h_2$.

When any one of these conditions are satisfied, Equation (7.42) is equal to zero only at $t = \infty$, hence overshoot will not occur.

For a second-order system, the expressions of μ_1 and μ_2 are obtained from Equation (7.31) as follows

$$e_1 = \frac{h_1^2}{2\mu_1} + \frac{h_1 h_2}{\mu_1 + \mu_2} \tag{7.43}$$

$$e_2 = \frac{h_2^2}{2\mu_2} + \frac{h_1 h_2}{\mu_1 + \mu_2} \quad . \tag{7.44}$$

By using the non-overshoot conditions in Equations (7.43) and (7.44), the conditions (1-4) are transferred into corresponding conditions listed as follows

(a) If $h_1 > 0$ and $h_2 > 0$, or $h_1 < 0, h_2 < 0$, then $e_1 > 0$ and $e_2 > 0$;

(b) If $h_1 > 0, h_2 < 0$ and $h_1 > -h_2$, or $h_1 < 0, h_2 > 0$ and $-h_1 > h_2$, then $e_1>0$, $e_2<0$ and $e_1+e_2>0$.

To match the general requirements for the speed drive, the following specifications are prescribed:

(i) The tracking steady-state error of speed is zero.

(ii) To avoid any overshoot in the command tracking response, the energy contributions of e_1 and e_2 corresponding to μ_1 and μ_2 are set according to the condition (a) and (b). For convenience of formulation, condition (b) is chosen. Accordingly, the relationships of e_1 and e_2 are set to $e_1 = K_1 e_2$ and $K_1<-1$.

(iii) The response time t_p is defined as the time for the unit-step response to increase from 0 to 90% of its final value.

Based on these prescribed specifications, and using the related equations, the following nonlinear equations are constructed:

$$f_1(\mu_1, \mu_2, h_1) = \frac{h_1}{\mu_1} - \frac{h_1}{\mu_2} - 1 = 0 \tag{7.45}$$

$$f_2(\mu_1, \mu_2, h_1) = e_1 - K_1 e_2 = \frac{h_1^2}{2\mu_1} - \frac{h_1^2(1-K_1)}{\mu_1 + \mu_2} - \frac{K_1 h_1^2}{2\mu_2} = 0 \tag{7.46}$$

$$f_3(\mu_1, \mu_2, h_1) = 0.9 - \left[\frac{h_1}{\mu_1}(1 - e^{-\mu_1 t_p}) - \frac{h_1}{\mu_2}(1 - e^{-\mu_2 t_p}) \right] = 0 \, . \tag{7.47}$$

To satisfy the condition of $0<\mu_1<\mu_2$, let $\mu_2 = \mu_1 + c^2$ and modified above nonlinear equations, we can obtain

$$f_1(\mu_1, c, h_1) = \frac{h_1}{\mu_1} - \frac{h_1}{\mu_1 + c^2} - 1 = 0 \tag{7.48}$$

$$f_2(\mu_1, c, h_1) = \frac{h_1^2}{2\mu_1} - \frac{h_1^2(1-K_1)}{\mu_1 + c^2} - \frac{K_1 h_1^2}{2\mu_1 + 2c^2} = 0 \tag{7.49}$$

$$f_3(\mu_1, c, h_1) = 0.9 - \left[\frac{h_1}{\mu_1}(1 - e^{-\mu_1 t_p}) - \frac{h_1}{\mu_1 + c^2}(1 - e^{-(\mu_1 + c^2)t_p}) \right] = 0 \tag{7.50}$$

where c is a finite positive constant. The unknown parameter h_1, μ_1, and c in Equations (7.48) through (7.50) can be solved using the Matlab program. Then the parameters of the controller K_p, K_I can be found from following Equations (7.51) through (7.53):

$$\mu_2 = \mu_1 + c^2 \tag{7.51}$$

$$K_I = \frac{\mu_1 \mu_2}{K_t b} \tag{7.52}$$

$$K_p = \frac{\left[\frac{(\mu_1 + \mu_2)}{b} - B) \right]}{K_t} . \tag{7.53}$$

The Matlab program using to obtain these parameters for non-overshoot performance is listed at Appendix 7C.

7.5 Nonlinear Controller Design

In the last few years, nonlinear control theory has been used in some electrical machine control systems [75-78]. The main reason of using nonlinear control techniques is to improve the existing control system and achieve high performance. Linear control methods rely on the key assumption of small range operation for the linear model to be valid. When the required operation range is larger, a linear controller is likely to perform very poorly or to be unstable, because the nonlinearities in the system cannot be properly compensated for. However, nonlinear controller may handle the nonlinearities in large range operation directly. The technological breakthroughs in digital signal processor (DSP) have made it possible to implement complex nonlinear control algorithms in the application of the electrical machine control.

In control scheme I, nonlinear controller is used to generate reference signals V_{dp} and V_{qp} for the voltage source inverter with space vector pulse width modulation technique. The principles of nonlinear control input-output linearization with decoupling are used to design the controllers [71,72,73]. The literature [73] has successfully used this control technique to control a doubly-fed reluctance machine with axially laminated anisotropic rotor and single-phase control windings fed by a dc source. The same control technique is used in control scheme I.

Finding a direct and simple relation between the system output and the control input constitutes the intuitive basis for the so-called input-output linearlization approach to nonlinear control design. Let us use an example to demonstrate this approach [72].

Consider a third-order system

$$\dot{x}_1 = \sin x_2 + (x_2 + 1)x_3$$

$$\dot{x}_2 = x_1^5 + x_3$$

$$\dot{x}_3 = x_1^2 + u$$

$$y = x_1 \ .$$

To generate a direct relationship between the output y and the input u, let us differentiate the output y

$$\dot{y} = \dot{x}_1 = \sin x_2 + (x_2 + 1)x_3 \ .$$

Since $\dot{y}$ is still not directly related to the input u, let us differentiate again. We now obtain

$$\ddot{y} = (x_2 + 1)u + f_1(x_1, x_2, x_3)$$

where

$$f_1(x_1, x_2, x_3) = (x_1^5 + x_3)(x_3 + \cos x_2) + (x_2 + 1)x_1^2 \, .$$

Now an explicit relationship between y and u has been found. If we choose the control input to be in the form

$$u = \frac{1}{x_2 + 1}(v - f_1)$$

where *v* is a new input to be determined, the nonlinearity above equation is canceled, and we obtain a simple linear doubly-integrator relationship between the output and the new input *v*,

$$\ddot{y} = v$$

The design of a controller for this doubly-integrator relation is simple, because of the availability of linear control techniques. For instance, let us define the error as

$$e = y(t) - y_d(t)$$

where $y_d(t)$ is desired output. Choosing the new input *v* as

$$v = \ddot{y}_d - k_1 e - k_2 \dot{e}$$

with k_1 and k_2 being positive constants, the error of the closed loop system is given by

$$\ddot{e} + k_2 \dot{e} + k_1 e = 0$$

which represents an exponentially stable error dynamics. If initially $e(0) = \dot{e}(0) = 0$, then $e(t) \equiv 0$, perfect control is achieved;otherwise, $e(t)$ converges to zero exponentially.

Therefore, the basic approach to design an input-output linearilized controller includes three steps:

(a) Repeatedly differentiate an output function until it is explicitly related to the input.

(b) Choose the input to cancel the nonlinearities and guarantee tracking convergence.

(c) Study the stability of the internal dynamics.

The input-output linearization and decoupling process ensures linear relationship between input and output variables with output-input pairs decoupled each other. The total number of differentiation for all the outputs is called the relative order, while the internal dynamics are comprised of n-r states (n is total number of the system dynamic states).

In the dynamic system described by Equations (7.1) through (7.10), the input variables are V_{dp} and V_{qp} are chosen as the input variables while ω_r and I_{qp} are chosen as output variables. From Equations (7.1) and (7.10), and using the condition $I_{ds} = 0$ because of the control windings connected with a DC current source, the following differential equations are obtained

$$\dot{I}_{qp} = \frac{1}{L_p} V_{qp} - \frac{R_p}{L_p} I_{qp} - \omega_r I_{dp} \tag{7.54}$$

$$\ddot{\omega}_r = \frac{Z}{L_p} V_{dp} + \left(-\frac{ZR_p}{L_p} \right) I_{dp} + Z\omega_r I_{qp} + \frac{Z\omega_r L_m I_{qs}^{'}}{L_p} \tag{7.55}$$

where $Z = \left(\frac{3P_r^2}{2J} \right) I_{qs} L_m$.

Equations (7.54) and (7.55) are combined as a matrix equation (7.56):

$$\begin{bmatrix} \ddot{\omega}_r \\ \dot{I}_{qp} \end{bmatrix} = \begin{bmatrix} \dfrac{Z}{L_p} & 0 \\ 0 & \dfrac{1}{L_p} \end{bmatrix} \begin{bmatrix} V_{dp} \\ V_{qp} \end{bmatrix} + \begin{bmatrix} -\dfrac{ZR_p}{L_p} I_{dp} + Z\omega_r I_{qp} + \dfrac{Z\omega_r L_m I'_{qs}}{L_p} \\ -\dfrac{R_p}{L_p} I_{qp} - \omega_r I_{dp} \end{bmatrix} . \tag{7.56}$$

This equation is linearized and decoupled and made to take the form of Equation (7.57) where Y_{dp} and Y_{qp} are new input variables.

$$\begin{bmatrix} \ddot{\omega}_r \\ \dot{I}_{qp} \end{bmatrix} = \begin{bmatrix} K_a & 0 \\ 0 & K_a \end{bmatrix} \begin{bmatrix} Y_{dp} \\ Y_{qp} \end{bmatrix} + \begin{bmatrix} F_1(t) & 0 \\ 0 & F_2(t) \end{bmatrix} \tag{7.57}$$

Equating Equations (7.57) and (7.56), input variables V_{qp} and V_{dp} are determined and given as

$$\begin{bmatrix} V_{dp} \\ V_{qp} \end{bmatrix} = \begin{bmatrix} \dfrac{L_p}{Z} K_a Y_{dp} + \dfrac{L_p}{Z} (F_1(t) - B_1(t)) \\ L_p K_1 Y_{qp} + L_p (F_2(t) - B_2(t)) \end{bmatrix} . \tag{7.58}$$

If Equation (7.58) are equated to the power winding q-d voltage Equations (7.1) and (7.2), Equations (7.59) and (7.60) are yielded

$$V_{dd} = L_p p I_{dp} = \frac{L_p}{Z} K_a Y_{dp} + \frac{L_p}{Z} F_1(t) \tag{7.59}$$

$$V_{qq} = L_p p I_{qp} = L_p K_a Y_{qp} + L_p F_1(t) \ . \tag{7.60}$$

Hence, Equation (7.58) is simplified as

$$\begin{bmatrix} V_{dp} \\ V_{qp} \end{bmatrix} = \begin{bmatrix} V_{dd} & -B_1(t) \\ V_{qq} & -B_2(t) \end{bmatrix} . \tag{7.61}$$

The quantities V_{dd} and V_{qq} are selected to be dependent on controlled and state variables to ensure that Equations (7.59) and (7.60) are linear and decoupled from each other.

Cascaded IP (integral-proportional) controller structure is adopted and shown in Figure 7.6. With expressions for V_{dd} and V_{qq} from Figure 7.6 and substituting Equation

(7.10) into Equations (7.59-7.60), the following transfer functions are obtained (with the disturbance load torque ignored):

$$\frac{I_{qp}}{I_{qp}^{*}} = \frac{K_q}{L_p S^2 + K_a S + K_q} \tag{7.62}$$

$$\frac{\omega_r}{\omega_r^{*}} = \frac{K_d K_c Z}{L_p S^3 + K_c S^2 + Z K_b K_c S + Z K_c K_d}. \tag{7.63}$$

The reference speed and reference q-axis power winding currents are ω_r^{*} and I_{qp}^{*}, respectively. The parameters transfer functions K_q, K_d and K_a-K_b are chosen to optimize the closed-loop eigenvalue locations using the Butterworth polynomial [71]. The Butterworth method locates the eigenvalues uniformly in the left-haft S-plane on a circle

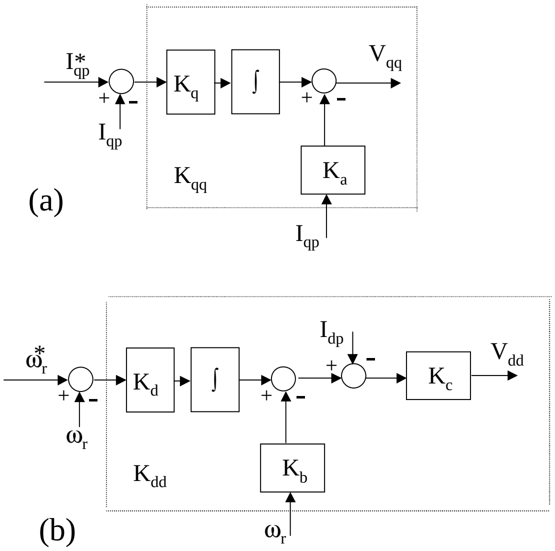

Figure 7.6. Integral proportinal linear and decouping controller structure. (a) Q-axis power winding current loop; (b) rotor speed loop.

of radius ω_o, with its center at the origin. The Butterworth polynomials for a transfer function with a second-order denominator is given as

$$S^2 + \sqrt{2}S\omega_o + \omega_o^2 = 0 \tag{7.64}$$

comparing Equations (7.60) and (7.58), we have

$$K_q = L_p\omega_o^2, K_a = \sqrt{2}\omega_o L_p \ . \tag{7.65}$$

For a transfer function with a third-order denominator, the Butterworth polynomial is

$$S^3 + 2\omega_o S^2 + 2\omega_o^2 S + \omega_o^3 = 0\,. \tag{7.66}$$

From Equations (7.66) and (7.63), the parameters of the speed control loop are given as

$$K_b = \frac{\omega_o}{Z}, K_c = 2\omega_o L_p, K_d = \frac{\omega_o^2}{2Z}\,. \tag{7.67}$$

To realize non-overshoot current response, the parameters of second-order current control loop described by Equation (7.62) can be computed using the same procedure described in section 7.3. However, we need to use the design procedure described in the references [66,67] to obtain the parameters of a third-order speed control loop with non-overshoot speed response.

The third-order speed control loop transfer function expressed in Equation (7.63), also can be transferred as

$$\frac{K_d K_c Z}{L_p S^3 + K_c S^2 + ZK_b K_c S + ZK_c K_d} = \frac{h_1}{s+\mu_1} + \frac{h_2}{s+\mu_2} + \frac{h_3}{s+\mu_3}$$

where

$$h_1 + h_2 + h_3 = 0$$

$$h_1(\mu_2+\mu_3) + h_2(\mu_1+\mu_3) + h_3(\mu_1+\mu_2) = 0$$

$$\frac{h_1}{\mu_1} + \frac{h_2}{\mu_2} + \frac{h_3}{\mu_3} = 1$$

$$\mu_1 + \mu_2 + \mu_3 = \frac{K_c}{L_p}$$

$$\mu_1\mu_2 + \mu_2\mu_3 + \mu_1\mu_3 = \frac{K_b K_c Z}{L_p}$$

$$\mu_1\mu_2\mu_3 = \frac{K_d K_c Z}{L_p}.$$

To obtain μ$_1$, μ$_2$ and μ$_3$ so that we can compute the parameters of non-overshoot speed response for this third-order speed control loop, the following nonlinear equations can be constructed:

$$f_1(\mu_1, \mu_2, \mu_3, h_2, h_3) = -(h_2 + h_3)(\mu_2 + \mu_3) + h_2(\mu_1 + \mu_3) + h_3(\mu_1 + \mu_2) = 0$$

$$f_2(\mu_1, \mu_2, \mu_3, h_2, h_3) = \frac{-(h_2 + h_3)}{\mu_1} + \frac{h_2}{\mu_2} + \frac{h_3}{\mu_3} - 1 = 0$$

$$f_3(\mu_1, \mu_2, \mu_3, h_2, h_3) = 0.9 - \{\frac{-(h_2 + h_3)}{\mu_1}[1 - e^{-\mu_1 t_{re}}] + \frac{h_2}{\mu_2}[1 - e^{-\mu_2 t_{re}}] + \frac{h_3}{\mu_3}[1 - e^{-\mu_3 t_{re}}]\} = 0$$

$$f_4(\mu_1, \mu_2, \mu_3, h_2, h_3) = e_2 - K_1 e_3 = 0$$

$$f_5(\mu_1, \mu_2, \mu_3, h_2, h_3) = e_1 - K_2(e_2 + e_3) = 0$$

$$e_2 = K_1 e_3 \qquad K_1 > 0$$

$$e_1 = K_2(e_2 + e_3) \qquad K_2 < -1$$

$$\mu_2 = \mu_1 + c_2^2$$

$$\mu_3 = \mu_1 + c_2^2 + c_3^2$$

where c_2^2 and c_3^2 are finite positive constants. The detailed derivation and its physical meaning for this nonlinear equation system are described in the reference [66,67].

After solving this nonlinear equation system, the parameters of the controllers can be computed using the expressions as follows:

$$K_c = L_p(\mu_1 + \mu_2 + \mu_3)$$

$$K_b = \frac{(\mu_1\mu_2 + \mu_2\mu_3 + \mu_1\mu_3)}{Z(\mu_1 + \mu_2 + \mu_3)}$$

$$K_d = \frac{\mu_1\mu_2\mu_3}{Z(\mu_1 + \mu_2 + \mu_3)}.$$

A Matlab program used to obtain these parameters is listed at Appendix 7D.

7.6 Voltage Source SPWM-Inverter

A voltage source inverter using space-vector pulse-wide modulation technique [47][69][70] is applied for the control scheme II. The performance of this inverter is simulated using Matlab/Simulink.

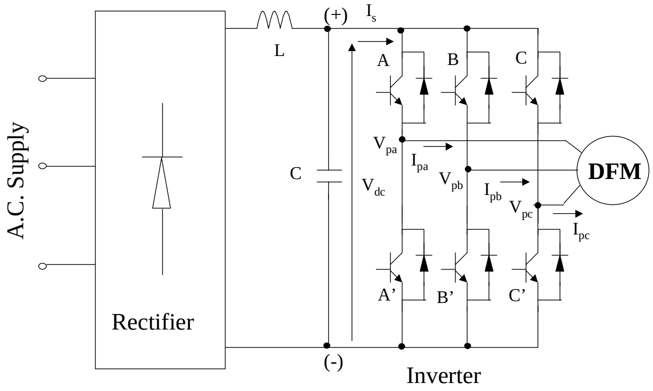

Figure 7.7. Circuit diagram of a three-phase VSI.

A diagram of the power circuit of the inverter is shown in Figure 7.7. The circuit has a bridge topology with three branches (phases), each consisting of two power switches and two freewheeling diodes. The inverter is supplied from an uncontrolled, diode-based rectifier, via a DC link that contains as LC filter in the inverted Γ configuration. In the circuit, the power switches in a given branch must never both be in the ON-state, since this would constitute a short circuit. On the other hand, if both the switches are in the OFF-state, then the potential of the corresponding output terminal is unknown to the control system of the inverter. Since only two combinations of states of the switches in each branch are allowed, a switching logic variable can be assigned to each phase of the inverter. In effect, only eight logic states are permitted for the whole power circuit. Defining the switching variables as

$$S_1 = \begin{cases} 0 \text{ if A is } OFF \text{ and A}' \text{ is } ON \\ 1 \text{ if A is } ON \text{ and A}' \text{ is } OFF \end{cases}$$

$$S_2 = \begin{cases} 0 \text{ if B is } OFF \text{ and B}' \text{ is } ON \\ 1 \text{ if B is } ON \text{ and B}' \text{ is } OFF \end{cases}$$

$$S_3 = \begin{cases} 0 \text{ if C is } OFF \text{ and C}' \text{ is } ON \\ 1 \text{ if C is } ON \text{ and C}' \text{ is } OFF \end{cases}$$

the instantaneous values of the line-to-line output voltages of the inverter are given by

$$V_{ab} = V_{dc}(S_1 - S_2) \tag{7.68}$$

$$V_{bc} = V_{dc}(S_2 - S_3) \tag{7.69}$$

$$V_{ca} = V_{dc}(S_3 - S_1) \tag*{(7.69)}$$

where Vdc is the DC supply voltage of the inverter.

In balanced three-phase systems, the line-to-neutral voltages can be calculated from the line-to-line voltages as

$$V_a = \frac{1}{3}(V_{ab} - V_{ca}) \tag{7.71}$$

$$V_b = \frac{1}{3}(V_{bc} - V_{ab}) \tag{7.72}$$

$$V_c = \frac{1}{3}(V_{ca} - V_{bc}) \tag{7.73}$$

hence, after substituting Equation (7.68-7.70) in Equation (7.71-7.73), the line-to-neutral voltages of the inverter are given by

$$V_a = \frac{V_{dc}}{3}(2S_1 - S_2 - S_3) \tag{7.74}$$

$$V_b = \frac{1}{3}(2S_2 - S_3 - S_1) \tag{7.75}$$

$$V_c = \frac{1}{3}(2S_3 - S_1 - S_2)\,. \tag{7.76}$$

By performing abc-qd transformation for Equation (7.74-7.75), we can obtain

$$V_{qd} = V_{dc}(S_1 - \frac{1}{2}S_2 - \frac{1}{2}S_3) + j(\frac{\sqrt{3}}{2}V_{dc})(S_2 - S_3)\,. \tag{7.77}$$

The output voltages can be represented as space vectors in the stator reference frame. Each vector corresponding to a given state of the inverter are listed in Table 7.1. The space vector diagram of line-to-neutral voltages of the VSI are shown in Figure 7.4. The relationship between the space vector and three phase voltages are expressed as

$$\vec{V} = V_a(t) + a \cdot V_b(t) + a^2 \cdot V_c(t) \tag{7.78}$$

where $a = e^{-j\frac{2\pi}{3}}$. $V_a(t)$, $V_b(t)$, and $V_c(t)$ are three phase output voltage:

$$V_a(t) = V_m \cos(\omega t + \phi) = \frac{V_m}{2}[e^{j(\omega t+\phi)} + e^{-j(\omega t+\phi)}] \qquad (7.79)$$

$$V_b(t) = V_m \cos(\omega t + \phi - \frac{2\pi}{3}) = \frac{V_m}{2}[e^{j(\omega t+\phi-\frac{2\pi}{3})} + e^{-j(\omega t+\phi-\frac{2\pi}{3})}] \qquad (7.80)$$

$$V_c(t) = V_m \cos(\omega t + \phi + \frac{2\pi}{3}) = \frac{V_m}{2}[e^{j(\omega t+\phi+\frac{2\pi}{3})} + e^{-j(\omega t+\phi+\frac{2\pi}{3})}]\ . \qquad (7.81)$$

ϕ is initial phase angle of the three phase voltages and V_m is the peak phase voltage. The magnitude of output voltage is adjustable if the modulation index *M*, *0#M#1*, is used and V_m is replaced by MV_m . Substituting Equations (7.79) through (7.81) into (7.78), we can obtain

Table 7.1. Inverter states and Spave Vector

S1, S2, S3	***i***	$\vec{\mathbf{V}}_i$
0, 0, 0	0	$\vec{V}_0 = 0$
0, 0, 1	1	$\vec{V}_1 = -\frac{V_{dc}}{2} - j\frac{\sqrt{3}}{2}V_{dc}$
0, 1, 0	2	$\vec{V}_1 = -\frac{V_{dc}}{2} + j\frac{\sqrt{3}}{2}V_{dc}$
0, 1, 1	3	$\vec{V}_3 = -V_{dc}$
1, 0, 0	4	$\vec{V}_4 = V_{dc}$
1, 0, 1	5	$\vec{V}_5 = \frac{V_{dc}}{2} - j\frac{\sqrt{3}}{2}V_{dc}$
1, 1, 0	6	$\vec{V}_6 = \frac{V_{dc}}{2} + j\frac{\sqrt{3}}{2}V_{dc}$
1, 1, 1	7	$\vec{V}_7 = 0$

$$\vec{V} = \frac{3}{2} M V_m e^{j\alpha}, \alpha = \omega t + \phi . \tag{7.82}$$

When α changes from 0 to 2π, $\vec{V}$ rotates one circle in Figure 7.8 and three phase output voltages finish one period. In Figure 7.8, we can see the non-zero base vectors divide the cycle into six, 60^o –wide sectors. The desired voltage vector, $\vec{V}^*$, located in a given sector, can be synthesized as a linear combination of the two adjacent base vectors, V_i and V_j , which are framing the sector, and either one of the two zero vectors, i.e..

$$\vec{V}^* = \frac{T_1}{T_s} V_i + \frac{T_2}{T_s} V_j + \frac{T_o}{T_s} V_z . \tag{7.83}$$

T_1 , T_2, and T_o are, respectively, the working time of state V_i , V_j, and V_o. V_z is either V_o or V_7. T_s is the switching interval of the power switching components. Assuming that space vector **V^*** locates in the sector as shown Figure 7.8, we can obtain the following equation

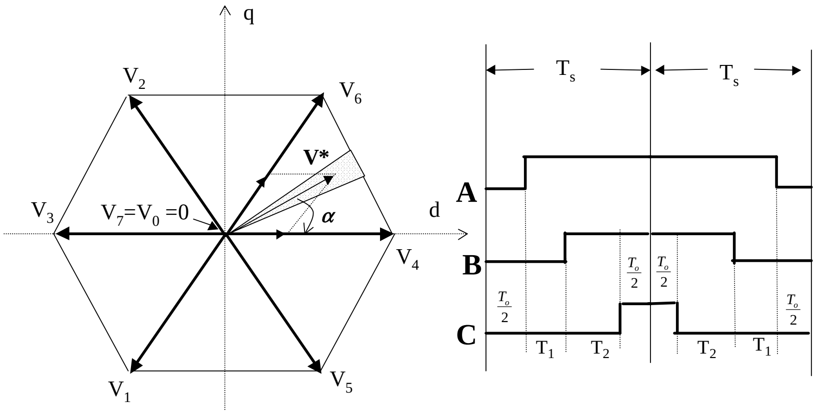

(a) (b)

Figure 7.8. Schematic of the space vector PWM. (a) Illustration of the space vector PWM strategy, (b) pulse patterns of symmetrical three-phase modulation.

by substituting $V_i = V_4$, $V_j = V_6$, and $V_z=V_7$, whose values are looked up in Table 7.1, into Equation (7.83):

$$V^* = V_{dc}(T_1 + \frac{1}{2}T_2) + (\frac{\sqrt{3}}{2}V_{dc}T_2)\cdot j\ .$$

This equation is equivalent to Equation (7.82), which can be extended as follows:

$$\vec{V} = \frac{\sqrt{3}}{2}MV_{dc}\cos\alpha + (\frac{\sqrt{3}}{2}MV_{dc}\sin\alpha)\cdot j\ .$$

Hence, by equating their real parts and imagnary parts, we can construct the equation system as follows:

$$T_s M\frac{\sqrt{3}}{2}\cos\alpha = T_1 + \frac{1}{2}T_2$$

$$T_s M\frac{\sqrt{3}}{2}\sin\alpha = \frac{\sqrt{3}}{2}T_2\ .$$

T_1 and T_2 can be easily obtained by solving this equation system and are expressed as

$$T_1 = T_s M\sin(60^o - \alpha)$$

$$T_2 = T_s M\sin\alpha\ .$$

When ***V**** locates in any sector, the general expression to calculate the state working time T_1, T_2 and T_0 are given as Equation (7.84):

$$\begin{aligned} T_1 &= T_s M\sin(60^o - \alpha') \\ T_2 &= T_s M\sin\alpha' \\ T_o &= T_s - T_a - T_b\ . \end{aligned} \tag{7.84}$$

If $0 \le \alpha \le 60^o, \alpha' = \alpha$;

If $60^o \le \alpha \le 360^o, \alpha' = \alpha - N\cdot 60^o$, N = 0,1,...,6 where V$_m$ is peak phase voltage and modulation index is expressed as $M = \frac{\sqrt{6}V_m}{V_{dc}}$.

If the over-modulation mode ($T_1 + T_2 > T_s$) occurs, the time duration should be scaled as Equations (7.85) and (7.86) to generate the best approximate of the desired voltage vector.

$$T_1^{'} = T_1 \cdot \frac{T_s}{T_1 + T_2}, \tag{7.85}$$

$$T_2^{'} = T_2 \cdot \frac{T_s}{T_1 + T_2}, \tag{7.86}$$

$$T_o^{'} = 0. \tag{7.87}$$

The symmetrical pulse patterns of zero-vector for one sampling period are illustrated in Figure 7.4(a). The state sequence corresponding to each sector is listed in Table 7.2.

Table 7.2. State Sequence of Each Sector

State sector	State Sequence
I.	|4-6-7|7-6-4|
II.	|6-2-0|0-2-6|
III.	|2-3-7|7-3-2|
IV.	|3-1-0|0-1-3|
V.	|1-5-7|7-5-1|
VI.	|5-4-0|0-4-5|

The time intervals T_1, T_2, and T_s are used to calculate the reference output voltages V_a^*, V_b^* and V_c^* of the VSI:

In Sector I:

$$T_1 V_{dc} = V_{ab}^* T_s; \;\; T_2 V_{dc} = V_{bc}^* T_s.$$

$$V_{ab}^* = \frac{T_1}{T_s} V_{dc}; \;\; V_{bc}^* = \frac{T_2}{T_s} V_{dc}; \;\; V_{ca}^* = -(V_{ab}^* + V_{bc}^*).$$

In Sector II:

$$T_1 V_{dc} = -V_{ca}^* T_s; \;\; T_2 V_{dc} = -V_{ab}^* T_s.$$

$$V_{ca}^* = -\frac{T_1}{T_s} V_{dc}; \;\; V_{ab}^* = -\frac{T_2}{T_s} V_{dc}; \;\; V_{ab}^* = -(V_{bc}^* + V_{ca}^*).$$

In Sector III:

$$T_1 V_{dc} = V_{bc}^* T_s; \;\; T_2 V_{dc} = V_{ca}^* T_s.$$

$$V_{bc}^* = \frac{T_1}{T_s} V_{dc}; \;\; V_{ca}^* = \frac{T_2}{T_s} V_{dc}; \;\; V_{ab}^* = -(V_{bc}^* + V_{ca}^*).$$

In Sector IV:

$$T_1 V_{dc} = -V_{ab}^* T_s; \;\; T_2 V_{dc} = -V_{bc}^* T_s.$$

$$V_{ab}^* = -\frac{T_1}{T_s} V_{dc}; \;\; V_{bc}^* = -\frac{T_2}{T_s} V_{dc}; \;\; V_{ca}^* = -(V_{ab}^* + V_{bc}^*).$$

In Sector V:

$$T_1 V_{dc} = V_{ca}^* T_s; \;\; T_2 V_{dc} = V_{ab}^* T_s.$$

$$V_{ca}^* = \frac{T_1}{T_s} V_{dc}; \;\; V_{ab}^* = \frac{T_2}{T_s} V_{dc}; \;\; V_{bc}^* = -(V_{ab}^* + V_{bc}^*).$$

In Sector VI:

$$T_1 V_{dc} = -V_{bc}^* T_s;\ \ T_2 V_{dc} = -V_{ca}^* T_s.$$

$$V_{bc}^* = -\frac{T_1}{T_s} V_{dc};\ \ V_{ca}^* = -\frac{T_2}{T_s} V_{dc};\ V_{ab}^* = -(V_{bc}^* + V_{ca}^*).$$

V_{ab}^*, V_{bc}^* and V_{ca}^* are line-to-line voltages and phase voltages V_a^*, V_b^* and V_c^* are given as

$$V_a^* = \frac{V_{ab}^* - V_{ca}^*}{3}$$

$$V_b^* = \frac{V_{bc}^* - V_{ab}^*}{3} \qquad (7.88)$$

$$V_c^* = \frac{V_{ca}^* - V_{bc}^*}{3}.$$

In Figure 7.3, the control signals V_{qp} and V_{dp} are used to computed the modulation M and initial phase angle ϕ, then the interval times T_1 and T_2 are obtained from Equation (7.84). Finally, Equation (7.88) are used to compute output phase voltages V_a^*, V_b^*, and V_c^* of the VSI. Figure 7.9 shows the simulation waveforms of power winding phase voltage and current whose frequency is equal to 60Hz with 5KHz switching frequency.

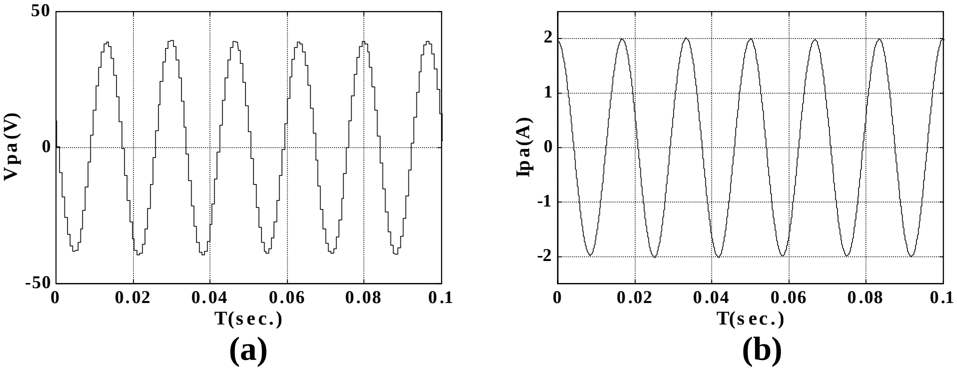

Figure 7.9. Simulation of the voltage-controlled PWM-VSI. (a) Power winding voltage waveform, (b) power winding current waveform.

7.7 Current Control in Voltage Source Inverters

A block diagram of a current-controlled VSI that is used in control scheme II is shown in Figure 7.10. The output currents, I_a,, I_b, and I_c, of the inverter are sensed and compared with the reference current signals, I_a^*, I_b^*, and I_c^*. Current error signals, ΔI_a, ΔI_b, and ΔI_c, are then applied to the hysteretic current controllers, which generate switching signals for the inverter switches.

The input-output characteristic of the phase-A hysteretic current controller is shown in Figure 7.10. The width of the hysteretic loop, denoted by h, represents the tolerance bandwidth for the controlled current. If the current error, ΔI_a, is greater than h/2, i.e., current I_a is unacceptably lower than the reference current, I_a^*, the corresponding line-to-neutral voltage, V_a, must be increased. This voltage is most strongly affected by the switching variable a, hence it is this variable that is regulated by the controller, and is set to a logic variable *1* (equivalently, "on" state of a power switch component) in the

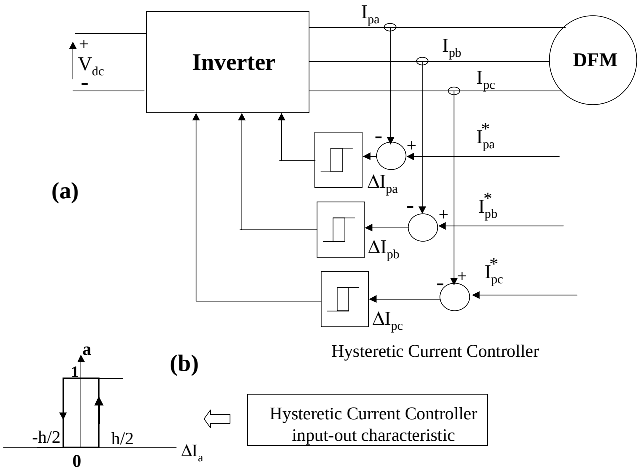

Figure 7.10. Block diagram of a current-controlled VSI.

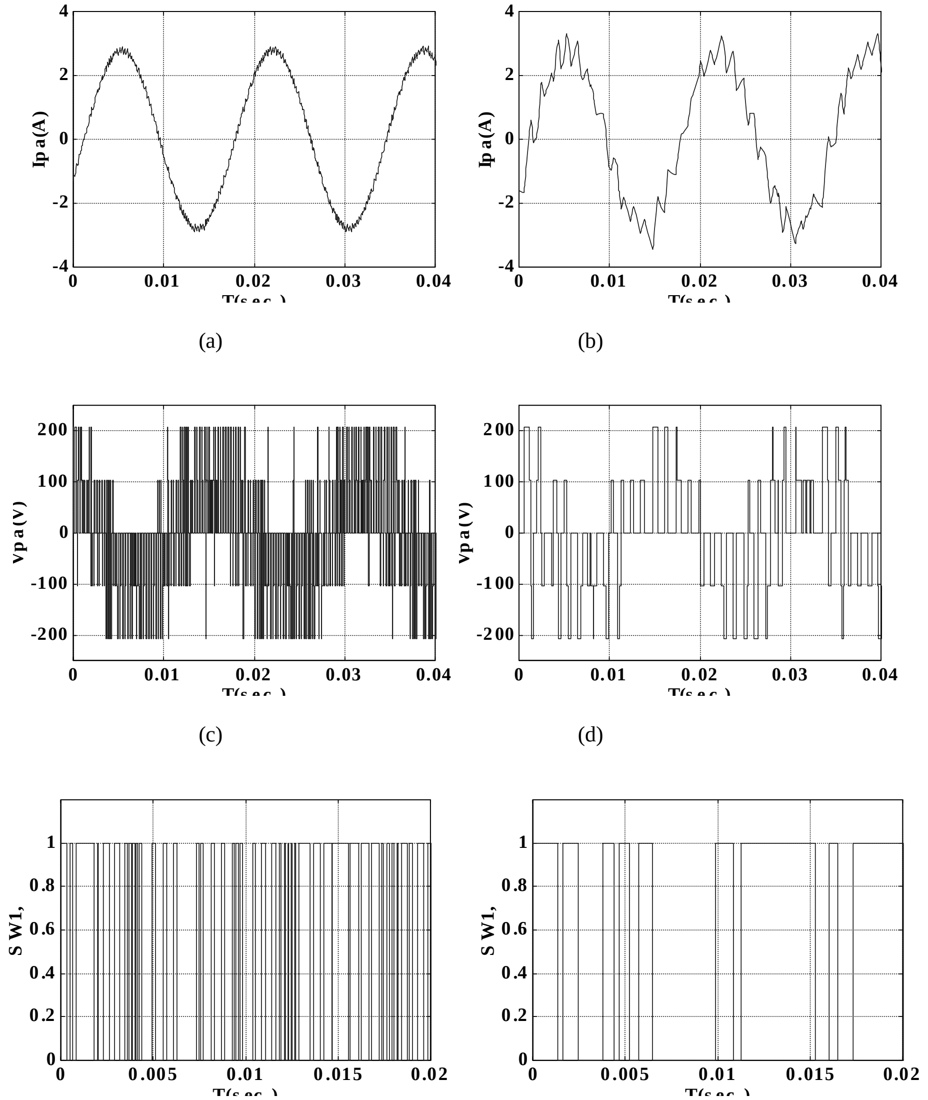

(a) (b)

(c) (d)

(e) (f)

Figure 7.11. Simulation of the current-controlled VSI. (a) Phase current with 2% tolerance bandwidth, (b) phase current with 10% tolerance bandwidth, (c) phase voltage with 2% tolerance, (d) phase voltage with 10% tolerance, (e) transistor switching signal (on = ‘1’, off = ‘0’) with 2% tolerance bandwidth, (f) transistor switching signal (on = ‘1’, off = ‘0’) with 10% tolerance bandwidth.

described situation. Conversely, an error less than $-h/2$ results in $a = 0$ (equivalently, “off” state of a power switch component) in order to decrease the voltage and current in question. No action is taken by the controller when current I_a stays within the tolerance band. The other two controllers operate in a similar manner.

The width, *h*, of the tolerance band affects the switching frequency of the inverter. The narrower the band, the more frequent switching takes place and the higher quality of the currents. This is illustrated in Figure 7.11, depicting simulation waveforms of power winding current and voltage for an inverter supplying the power windings of the machine at values of h equal to 10% in Figure 7.11(a) and 2% in Figure 7.11(b), of the amplitude of the reference current. Figure 7.11(c) and (d) show the transistor switching signals with 10% tolerance bandwidth and 2% tolerance bandwidth. It is obvious that the narrower the bandwidth, the higher the switching frequency of transistor.

7.8 Simulation Results Below the Base Speed

The simulations below illustrate the control performance of two control schemes presented in this chapter. The parameters of IP controller in control scheme II and nonlinear controller in control scheme I are listed in Appendix 7A.

The typical examples of constant torque application below the base speed are actuators and servo systems, which require maximum torque availability at all speeds to ensure maximum dynamic response. To investigate the performance of doubly-fed synchronous reluctance motor drive system below the base speed, the following simulation are used to demonstrate the dynamic response to step speed change and step torque change. The control winding current is chose as 8 A. The load torque is 4 N.m from 0 to 1.5 s and changes to 8 N.m from 1.5 s to 2.2 s.

Figure 7.12 illustrate the dynamic response of the motor drive for a step change of the reference speed from zero to the rated electrical base speed. Because we use non-overshoot design procedure to obtain the control parameters for two-order speed control loop (control scheme II) and for three-order speed control loop (control scheme I), there is no overshoot speed response in the simulation results, which can be seen in Figure 7.12(a). In Figures 7.12(b) to (d), we can see that, the torque and power winding d-axis current increase quickly to reach their maximum values, then they begin to decrease when the speed closes on the base speed, and at last the torque reaches an constant torque that is equal to 4 N.m load torque for this simulation example. When the speed reaches the base speed. The d-axis power winding current generating the corresponding torque also reachs its steady-state value. The q-axis current of the power winding aligns to the zero value so that the field orientation requirements are satisfied. The power winding q-axis and d-axis flux linkages, which are decided by q axis and d-axis current componenets, are illustrated in Figures 7.12(e) to (f).

The response to change load torque from 4 N.m to 8 N.m at t = 1.5 s is displayed in Figure 7.13. The step change of the load torque causes a speed dip as shown in Figure 7.13(a), but it recovers its value after a short transient because power winding d-axis current sharply increases to generate a bigger electrical torque against the change of load torque. During this process, power winding q-axis current has a little ripple around the zero value and aligns to zero value after a short transient. Figures 7.13(b) to (d) show this dynamic process. The dynamic response of the power winding q-axis and d-axis flux

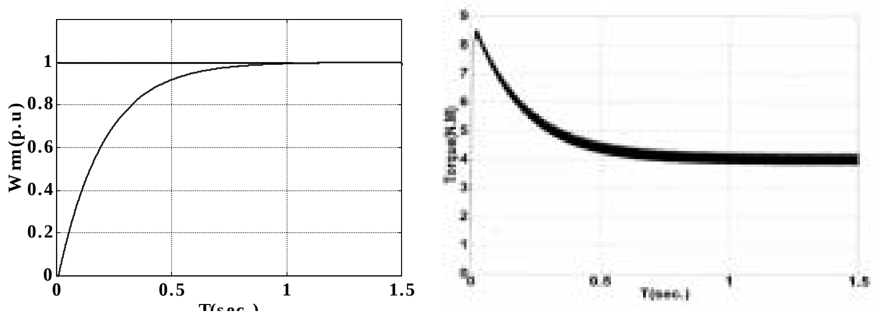

(a) (b)

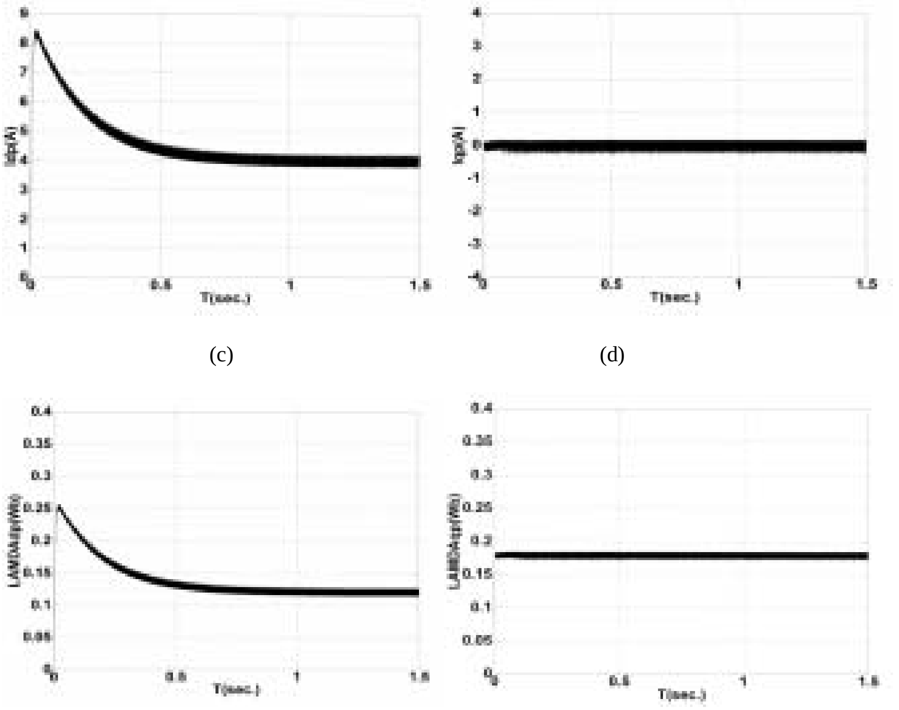

(c) (d)

(e) (f)

Figure 7.12. Dynamic response to a step-change of speed. (a) Reference and actual speed, (b) torque (c) power winding d-axis current, (d) power winding q-axis current, (e) power winding d-axis flux-linkage, (f) power winding q-axis flux-linkage.

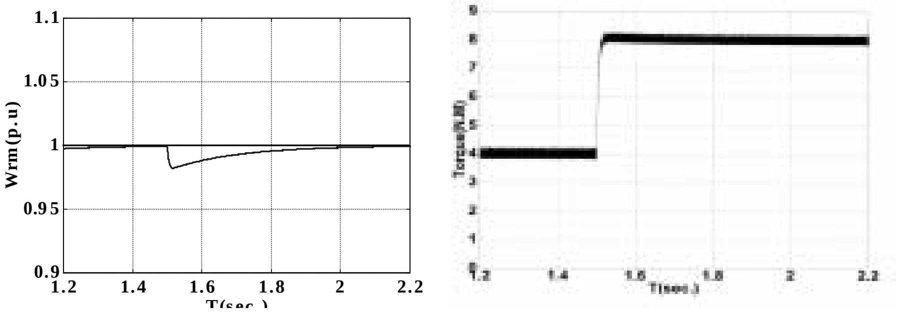

(a) (b)

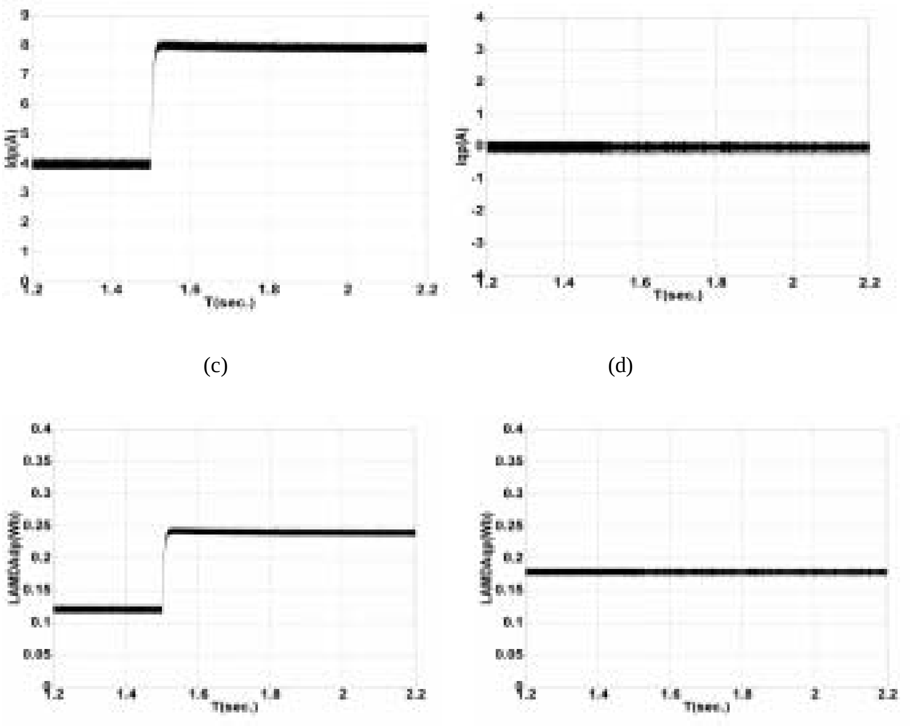

(c) (d)

(e) (f)

Figure 7.13. Response to change of load torque. (a) reference and actual speed, (b) torque (c) power winding d-axis current, (d) power winding q-axis current, (e) power winding d-axis flux-linkage, (f) power winding q-axis flux-linkage.

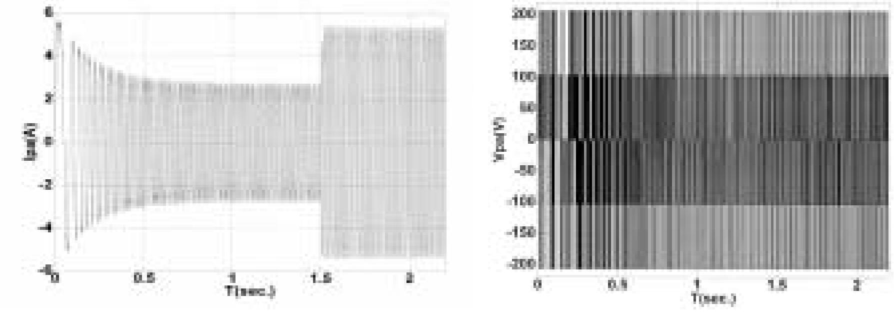

(a) (b)

Figure 7.14. Profiles of the phase current and voltage during the simulation process.

(a) Phase current, (b) phase voltage.

linkages are illustrated in Figure 7.13(e) to (f). They are affected by the change of the q-axis and d-axis current components.

The profiles of the power winding phase current and voltage are displayed in Figure 7.14. We can see, from 0 to 1.5 s, the voltage and current sharply increase and reach the steady-state values corresponding to a 4 N.m torque load. They increase at 1.5 s due to change load torque from 4 N.m to 8 N.m. Finally they reach new steady-state values corresponding to 8 N.m torque load.

7.9 Simulation Results Above the Base Speed

Some industrial and commercial applications require motors to operate over a wide speed range and rotating in both directions. A familiar example is the electric vehicle traction that requires high torque for low-speed acceleration and constant power (reduced torque) for high-speed cruising. To obtain constant power control above base speed, field-weakening techniques are used.

The following three cases demonstrate the dynamic process of a doubly-fed synchronous reluctance motor drive systems, which operate in a 2.5 times base speed range and rotate in two directions.

Case 1. We simulate the dynamic process of the control system with two-stage speed step-change: 2.5 times the base speed from 0 to 2.5 s and the base speed from 2.5 s to 4 s. The control winding current is chose as 8 A. A 4 N.m load torque is used from 0 to 1.5 s and then changes for 8 N.m from 1.5 s to 4 s.

Figure 7.15(a) shows the speed response to this two-stage speed step change command. The torque, d-axis and q-axis currents of the power windings are illustrated in Figures 7.15(b) and 7.15(c), where we can see that the torque and its control current, I_{dp}, sharply reach their maximum values which cause the speed to quickly increases. While the q-axis current, I_{qp}, is align to zero below the base speed and shapely changes to a negative constant value above base speed because of the field weakening control. Then the speed increase is slowed down with the decrease in torque and q-axis current. Finally the speed reach its command value, torque and current also reach their steady-state values. At t = 1.5 s, the load torque is changed from 4 N.m to 8 N.m, which causes the rotor speed a little dip but it is recovered quickly because the d-axis current I_{dp} and its corresponding torque quickly increase to new values to resist the change of speed.

At t = 2.5 s, the speed command proceeds to second stage by changing the speed command from 2.5 times the base speed to the base speed. The speed change causes the torque and torque control current, I_{dp}, sharply falling down to their minimum values, which farther causes the rotor speed to quickly decrease. When the speed closes on the speed command, the torque and d-axis current I_{dp} begin increase in inversely proportional to speed. The q-axis is still kept in some negative values before the speed falls down to the base speed and then change to the zero again.

The d-axis and q-axis flux linkages of power windings are shown in Figures 7.15(e) and 7.15(f), which are dependent on the d-q current components of power windings and control windings. Figure 7.16 gives the profile of phase current and voltage of power windings during the whole transient process. In Figure 7.16(a), we can clearly see that there are three transient stages in the whole transient process of phase current I_{pa}:

(1) From 0 to 1.5 s, speed command is equal to 2.5 times the base speed and load torque is set to 4 N.m.. Phase current I_{pa} of the power windings goes through its first transient stage. During this transient stage, transient current sharply increases to maximum value and then slowly decreases to a steady-state value. The frequency of the current increases step by step and then reaches 2.5 times the base frequency.

(2) From 1.5 s to 2.5 s, speed command is equal to 2.5 times the base speed but load torque is changed from 4 N.m to 8 N.m. Phase current I_{pa} of the power windings goes through its second transient stage. During this transient stage, the transient current quickly increases and reaches to a new steady-state value, which can generate a new electrical torque to balance the new load torque. The current frequency is kept constant.

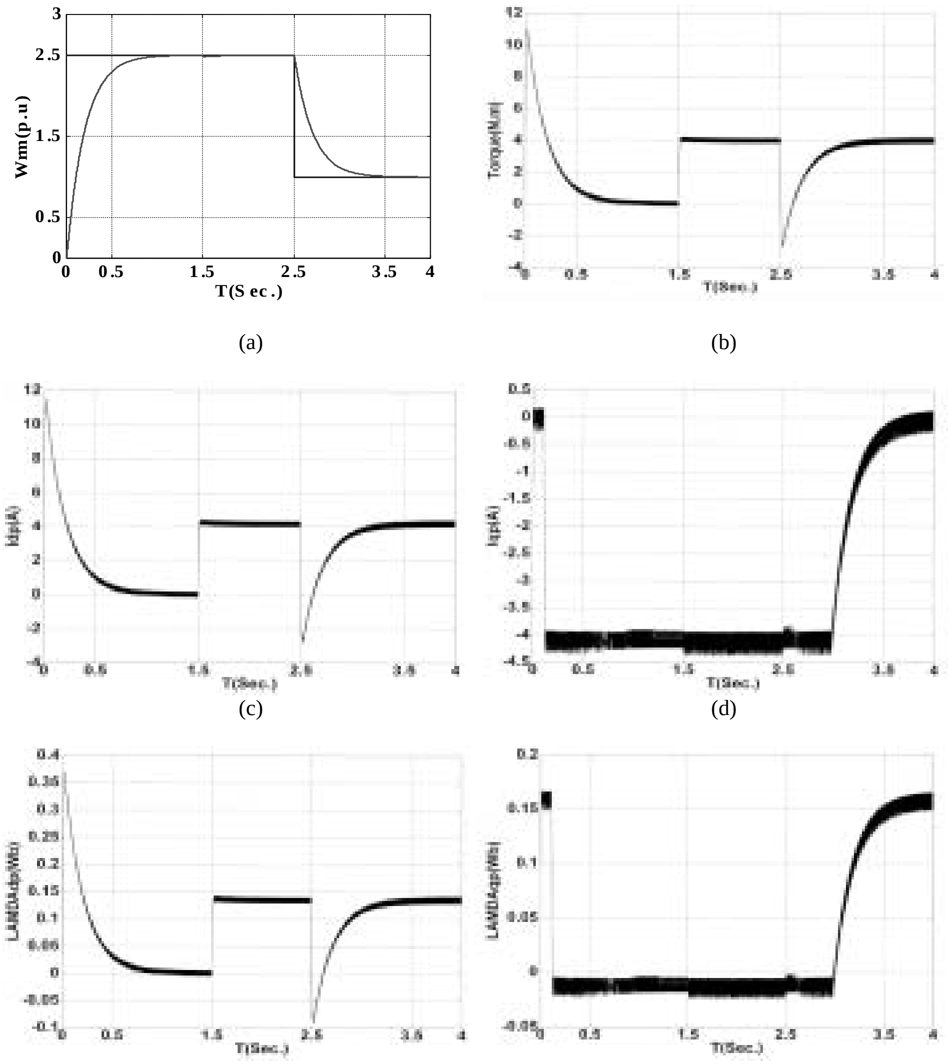

(a) (b) (c) (d) (e) (f)

Figure 7.15. Dynamic response to a wide speed range of 2.5 times base speed. (a) Reference and actual speed, (b) torque (c) power winding d-axis current, (d) power winding q-axis current, (e) power winding d-axis flux-linkage, (f) power winding q-axis flux-linkage.

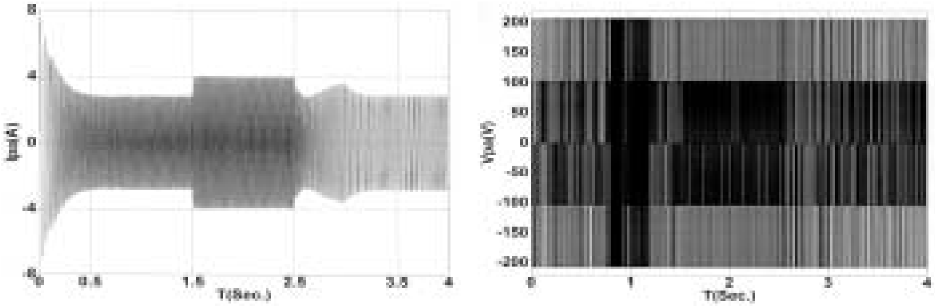

(a) (b)

Figure 7.16. Profiles of the power winding phase current and voltage during the simulation process. (a)Phase current, (b)phase voltage.

(3) From 2.5 s to 4 s, speed is changed from 2.5 times the base speed to 0.5 times the base speed and torque is kept at 8 N.m. Phase current I_{pa} of the power windings goes through its last stage. During this transient stage, the transient current increases to some value and then decreases and finally reaches to a new steady-state value. The current frequency decreases to the base current frequency.

Case 2. We simulate the dynamic process of the control system with trapezoid speed command. During the whole simulation process, a 4 N.m load torque is used and control winding current is chose as 8 A.

As shown in Figure 7.17(a), the command speed is seperated into six stages:

(1) The speed slopes up to twice the base speed from zero in first second.

(2) The speed is kept constant at twice the base speed for 1.5 seconds.

(3) The speed slopes down to 0.5 times the base speed from 2.5 s to 3.5 s.

(4) The speed is kept constant at 0.5 times base speed for 1 second.

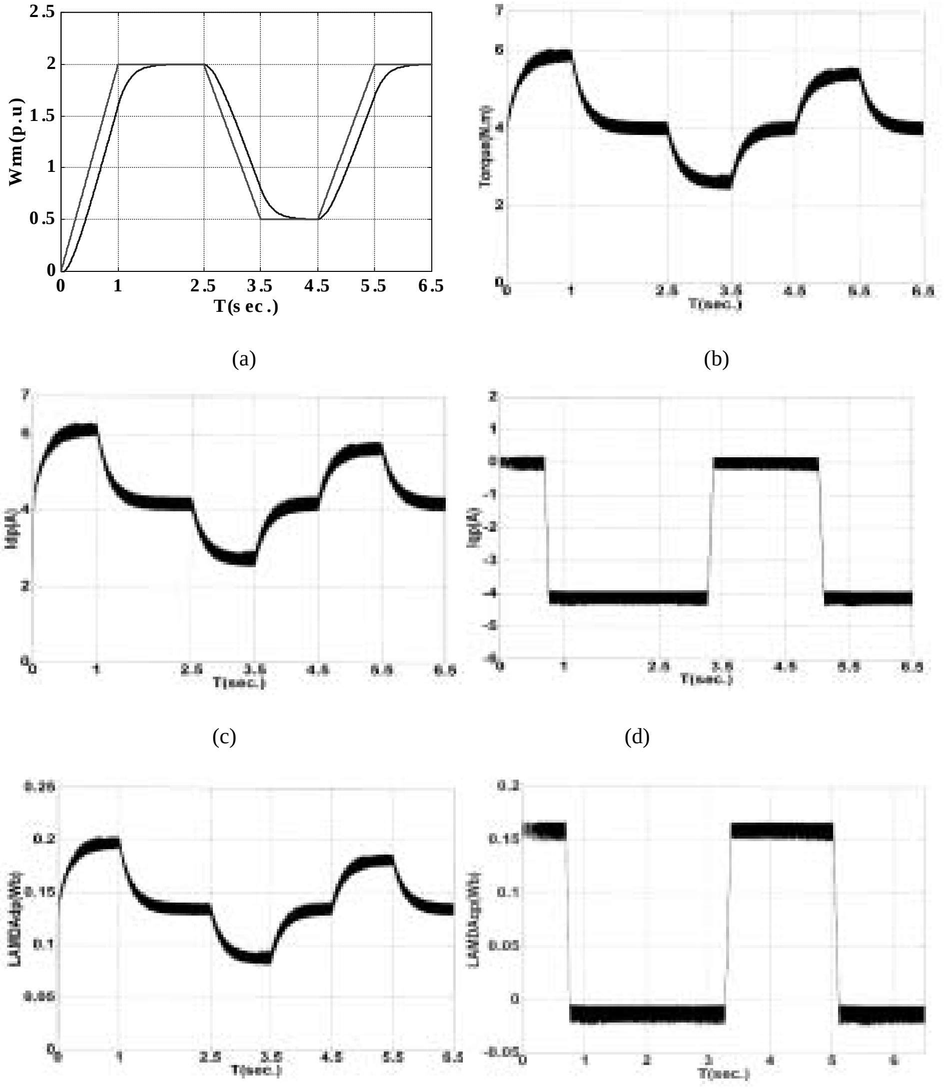

(a) (b)

(c) (d)

(e) (f)

Figure 7.17. Dynamic response to a trapezoid speed command. (a) Reference and actual speed, (b) torque (c) power winding d-axis current, (d) power winding q-axis current, (e) power winding d-axis flux-linkage, (f) power winding q-axis flux-linkage.

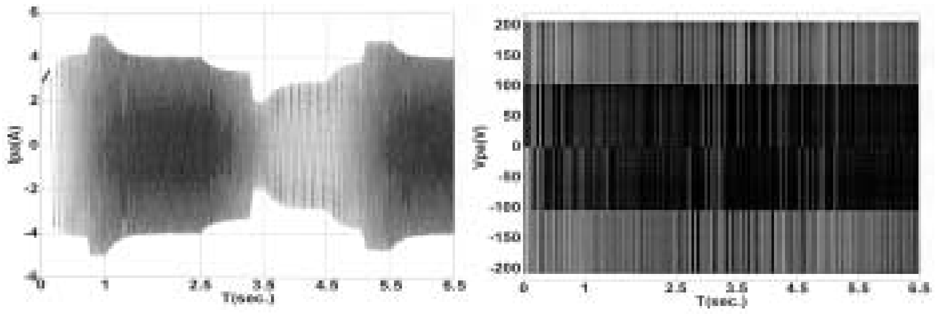

Figure 7.18. Profiles of the power winding phase current and voltage during the simulation process. (a) Phase current, (b) phase voltage.

(5) The speed slopes up to twice the base speed again in the time of 4.5 s to 5.5 s.

(6) The speed is kep constant at twice the base speed for 1.5 seconds.

The rotor speed follows the speed command very well and reaches the desired steady-state speeds: twice the base speed or 0.5 times the base speed.

Figures 7.17(b) and (c) illustrate the dynamic process of d-axis current of power windings. The up-slope speed causes the torque control current I_{dp} and its coresponding torque increament while the down-slope speed causes them decreament. When the speed reaches its stady-state values: 0.5 times the base speed and 2 times the base speed, I_{dp} and its corresponding torque also reach their teady-state values. Figure 7.17(d) displays the dynamic process of q-axis current of power windings, which is align to zero when speed is below base speed or becomes negative value when the speed is above the base speed.

Figures 7.18(e) and (f) illustrate the dynamic process of d-axis and q-axis flux linkages of power windings. Their profiles look similar to those of the d-axis and q-axis currents of the power windings because they are mainly dependent on theses currents.

The dynamic process of the phase current and voltage of the power windings is shown in Figures 7.19(a) and (b). we can clear see that there are six transient stages corresponding to the six-stage speed command.

Case 3. We simulate the dynamic process of the control system with a two-direction trapezoid speed command. During the whole simulation process, a 4 N.m load torque is used and control winding current is choosen as 8 A.

As shown in Figure 7.19(a), the speed command is seperated into six stages:

(1) The speed slopes up to twice the base speed from zero in first second.

(2) The speed is kept constant at twice the base speed for 1.5 s.

(3) The speed slopes down to negative twice the base speed from 2.5 s to 4.5 s.

(4) The speed is kept constant at negative twice the base speed for 1.5 seconds.

(5) The speed slopes up to twice the base speed in the time of 6 s to 8 s.

(6) The speed is kep constant at twice the base speed for 1.5 s.

The rotor speed follows this speed command very well either in clockwise direction or counter clockwise direction. The steady-state rotor speeds can also be obtained in both directions .

Figures 7.19(b) and (c) display the dynamic process of the torque control current I_{dp} and electrical torque. When the speed command is on its up-slope sides, I_{dp} and torque increase quickly and then keep at some values until the rotor speed closes its desired speed. At the monent of the rotor speed reaching its stedy-state values, I_{dp} and torque quickly decrease and hold at some values which generate an electrical torque to balance the load torque; When the speed command is on its down-slope sides, I_{dp} and

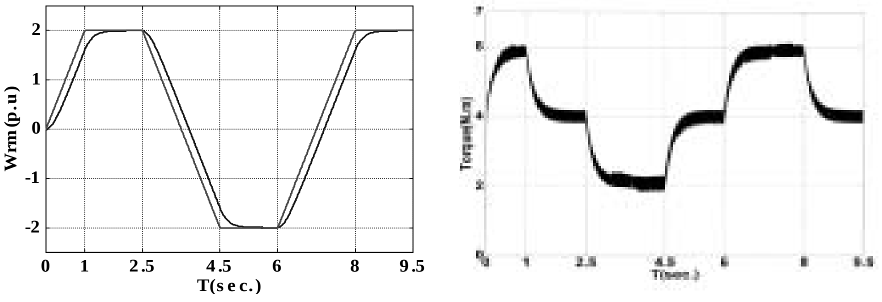

(a) (b)

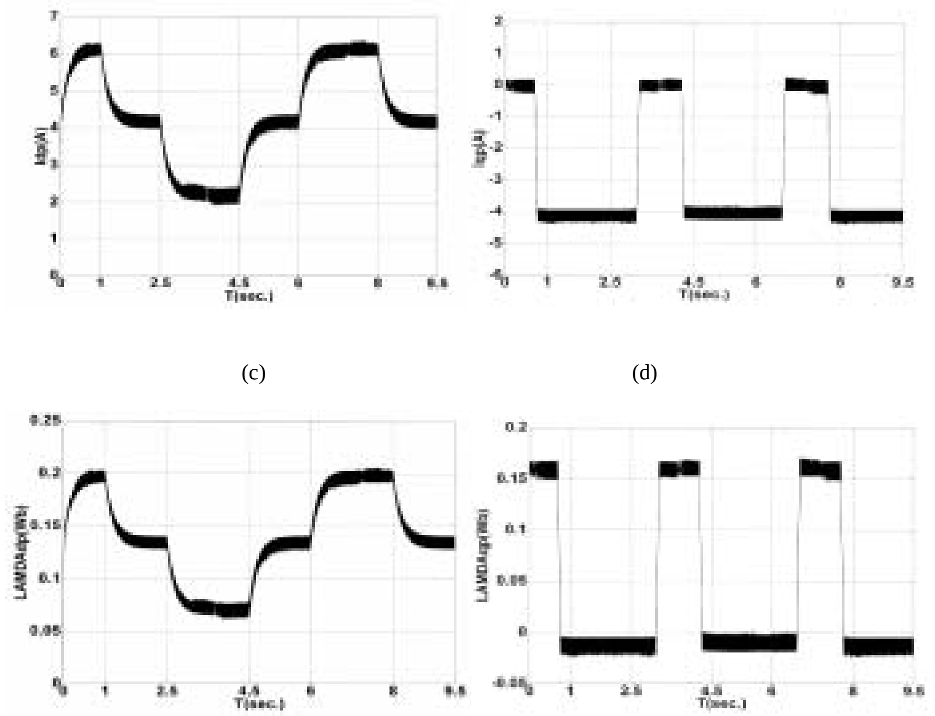

(c) (d)

(e) (f)

Figure 7.19. Dynamic response to a two-direction trapezoid speed command. (a) Reference and actual speed, (b) torque (c) power winding d-axis current, (d) power winding q-axis current, (e) power winding d-axis flux-linkage, (f) power winding q-axis flux-linkage.

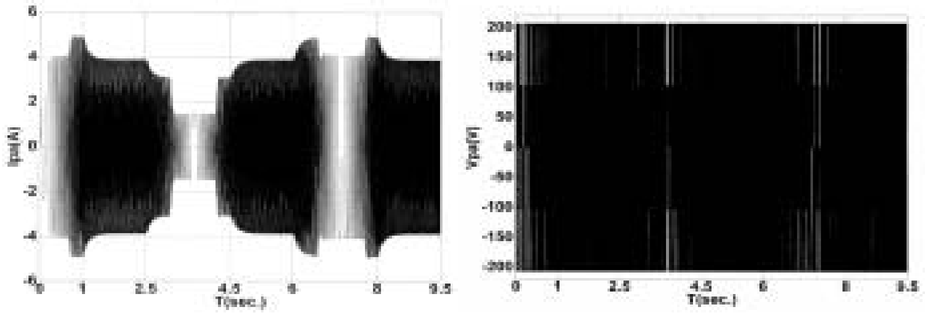

(a) (b)

Figure 7.20. Profiles of the power winding phase current and voltage during the simulation process. (a)Phase current, (b)phase voltage.

torque decrease quickly and then keep at some values so that the rotor speed quickly decreases and closes its desired speed. At the monent of the rotor speed reaches its steady-state values, I_{dp} and torque quickly increase and reach their steady-state values for balancing the load torque. By comparing three cases, this is noted that, if the trapezoid speed command is used, the change of the torque control current I_{dp} and torque are not as sharp as those of the step change speed command. Hence, using the trapezoid speed command is a good way to avoid the too big command current I_{dp}^*.

Figure 7.19(d) shows that q-axis current Iqp is align to zero below the base speed or is align to the negative values above the base speed because of the field weakening control.

The q-axis and d-axis flux linkages of the power windings are illustrated in Figures 7.19(e) and (f), they are dependent on the q-axis and d-axis currents of both the power windings and control windings.

Figure 7.20 illustrates the profiles of the phase current and voltage of the power windings during the whole dynamic process. It is observed from Figure 7.20(a) that there are six transient stages corresponding to the speed command.

Above simulation results have demonstrated the dynamic performance of control scheme II (using IP and hysteretic current control). The control scheme I (using linearization control) also has similar simulation results. Figures 7.21 and 7.22 give the evidence that the dynamic performance is the same as one of control scheme II in case 3.

A few factors cause transient difference between control scheme I and control scheme II in case 3:

(1) Two control schemes use different controller. One uses IP controller, the another uses linearization controller;

(2) In control scheme I, the voltage-controlled PWM-VSI is simulated using average voltage of switching period to replace true pulsating voltage, hence it is approximate simulation. However, the current-controlled PWM-VSI in control scheme II is simulated directly using true pulsating voltage. The simulation waveforms are shown in Figure 7.9 for voltage-

controlled PWM-VSI and Figure 7.11 for current-controlled PWM-VSI. Figure 7.20(b) shows the true phase-voltage waveform (pulsating voltage) while Figure 7.22(b) just shows the approximate phase-voltage waveform (average voltage of switching period).

(3) The higher switching frequency is used in control scheme II. 5 KHz switching frequency is used in current-controlled PWM-VSI while 2 KHz switching frequency is used in voltage-controlled PWM-VSI.

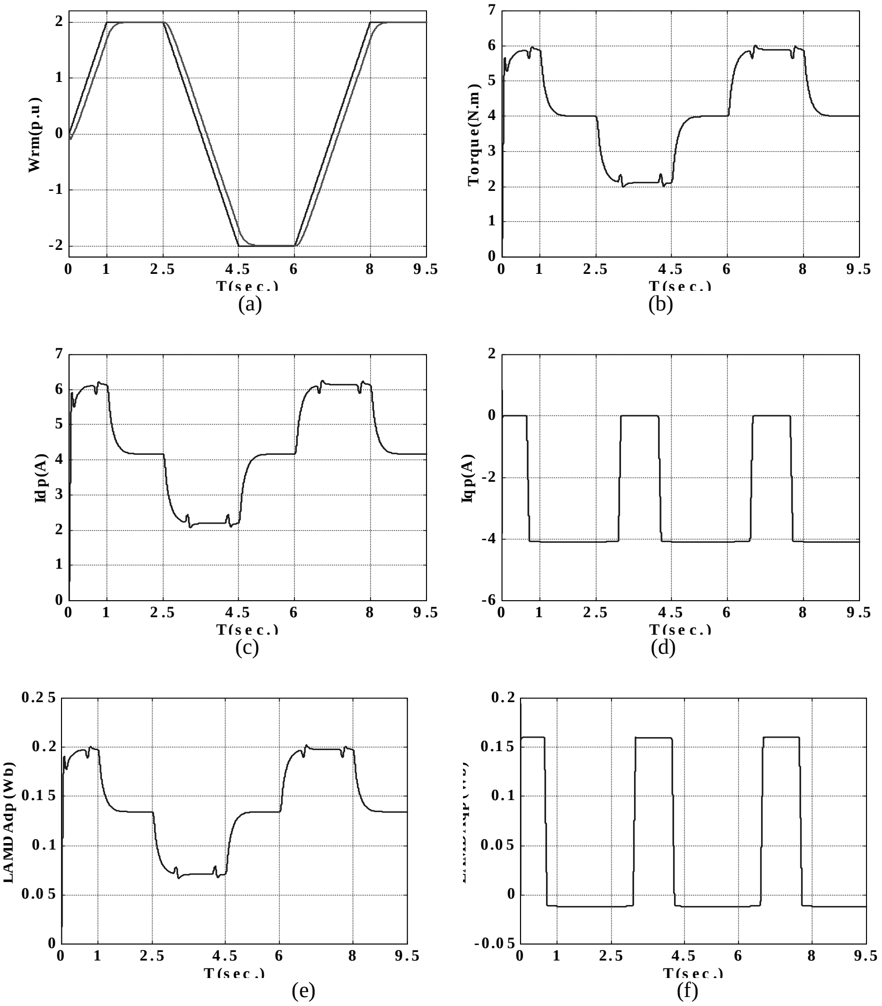

(a) (b)

(c) (d)

(e) (f)

Figure 7.21. Dynamic response to a two-direction trapezoid speed command for control scheme I. (a) Reference and actual speed, (b) torque (c) power winding d-axis current, (d) power winding q-axis current, (e) power winding d-axis flux-linkage, (f) power winding q-axis flux-linkage.

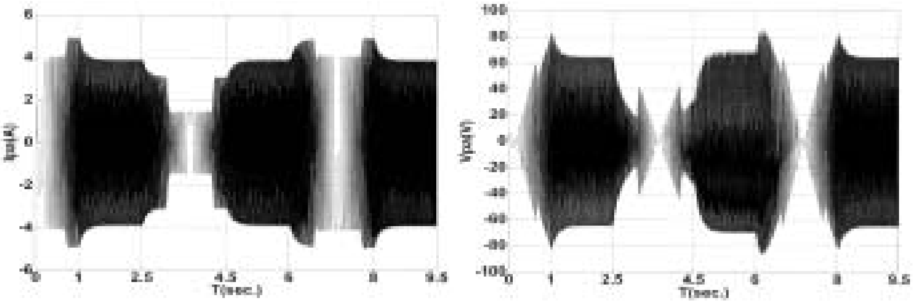

(a) (b)

Figure 7.22. Profiles of the power winding phase current and voltage during the simulation process for control scheme I. (a)Phase current, (b)phase voltage.

Although the dynamic responses of the control scheme II have more harmonic components, they should much close to the true results.

7.10 Conclusion

This chapter demonstrates the application of field orientation principle in a doubly-fed synchronous reluctance machine with dc control windings. The simulation results prove that this machine can be controlled like a separately excited dc motor.

The machine is controllable in a wide speed range including constant torque region and constant power region. The expressions to determine maximum torque and obtain field-weakening operation performance above base speed are given and satisfactorily used in the simulation. A design procedure and programs to quantitatively decide the IP parameters for a second-order speed loop are given, which can be used to obtain the performance of the non-overshoot speed response. The novel design methodology using input-output linearlization technique and Butterworth method are used for designing a nonlinear controller for the machine. The simulation results show that the prescribed control performance is achieved for IP controller and nonlinear controller.

Current-controlled PWM-VSI and voltage-controlled PWM-VSI, which are used

as a controllable source to supply the power winding of the machine, are described in details and their performance is successfully simulated using Matlab/Simulink.

Control scheme I with voltage-controlled PWM-VSI and control scheme II with current-controlled PWM-VSI are also simulated using Matlab/Simulink. They both demonstrate the similar performance. Their effectiveness shows that they are worth to be verified by the experiment.

CHAPTER 8

CONCLUSIONS AND SUGGESTION FOR FURTHER WORK

8.1 Conclusion

The research work on this dissertation has focused on modeling, simulation, and application of a doubly-fed reluctance machine.

A accurate mathematical model, which considers the core-loss of the machine, and its corresponding dynamic q-d equivalent circuits with series cores-loss resistance or shunt core-loss resistance are presented. The machine inherent parameters are obtained by using its steady-state equivalent circuits and experimental measurement. Based on this mathematical model, the mathematical models of a few generator systems were described. Some generator systems investigated in this dissertation include:

(a) Self-excited doubly-fed reluctance generator systems.

(b) Doubly-fed reluctance synchronous generator systems.

(c) Regulated DC power generation systems using doubly-fed synchronous reluctance machine.

Their dynamic performances were simulated using MATLAB/Simulink and ACSL program. The steady-state characteristics of these generator systems were obtained by simulation and experimental measurement. The potential applications of these generator systems had been revealed from the results of dynamic simulation and steady-state calculation.

The application of field-orientation principle in a doubly-fed synchronous reluctance machine with dc control windings was investigated. The simulation results prove that this machine can be controlled like a separated-excited dc motor in a wide speed range including constant torque control below the base speed and field weakening control above the base speed.

Two control schemes were investigated in the field orientation control system of doubly-fed synchronous reluctance machine. One had IP controller and current-controlled voltage-source inverter, and another had linearization controller and voltage-controlled PWM voltage-source inverter. The design procedures to obtain the parameters of controller were given.

The research work has made contribution in these areas:

(1) A dynamic model of doubly-fed reluctance machine considering the effects of core-loss and saturation was presented. It provided a more accurate model for the performance evaluation and the design of doubly fed reluctance machines. An approach to determine machine parameters from measurement was also provided.

(2) The performance characteristics of doubly-fed self-excited reluctance generator and doubly-fed synchronous reluctance generator as well as an innovative DC power generator scheme using doubly fed reluctance machine, were investigated and analysis were presented. These works revealed their potential applications.

(3) Two field orientation control schemes for a doubly-fed synchronous reluctance machine were investigated for high-performance operation both in the constant torque and constant power regions. The simulation results have provided valuable information for realization and application of the control systems.

8.2 Suggestion for Further Work

The research work revealed some inherent disadvantage of this experimental machine with simple salient laminated pole rotor structure. The disadvantages include:

(1) The inherent oscillatory instability of this class of reluctance machine when fed with variable-voltage, variable frequency source under open-loop control.

(2) Its core losses, saturation effect, and leakage inductances are relatively high.

To eliminate these inherent disadvantages, proper rotor structure and optimization designs are necessary. An axially laminated rotor structure will drastically reduce the effects of these disadvantages.

The simulation results have demonstrated that two field-orientation control schemes of doubly-fed synchronous reluctance machine are effective and robust. To verify the theory set forth and the effective of these two control schemes, experimental work will be necessary.

We hope that the proposed further research will improve the performance of this kind of machine and promote its applications in industry, military and power system given its low cost, high reliability and flexible control methods.

APPENDIX

Appendix 2A

The parameters of the experimental machine are:

Number of power winding pole pair, P = 1

Number of control winding pole pair, q = 3

Power winding per-phase resistance, Rp = 1.439 Ohms

Refered control winding per-phase resistance, Rs’ = 0.723 ohms

The ratio of the effective power winding to control winding turns, Np/Ns = 0.5.

Appendix 3A

$$L_{qqp} = \frac{3\mu_0 r\ell N_p^2 \pi\alpha}{2g_1} + \frac{3\mu_0 r\ell N_p^2}{4g_1 K_1 p} \sin\frac{K_1 p\pi\alpha}{2p_r} \{\cos 2(K_1 p\theta_{rm} - \theta_p)$$

$$\sum_{n=0}^{2p_r-1} \cos\frac{2K_1 p\pi n}{p_r} - \sin 2(K_1 p\theta_{rm} - \theta_p) \sum_{n=0}^{2p_r-1} \sin\frac{2K_1 p\pi n}{p_r}\} + \frac{3\mu_0 r\ell N_p^2 \pi\alpha}{2g_2} + \frac{3\mu_0 r\ell N_p^2}{8g_2 K_1 p}$$

$$\{\sin 2(K_1 p\theta_{rm} - \theta_p - \frac{K_1 p\pi\alpha}{2p_r}) \sum_{n=0}^{2p_r-1} \cos\frac{2K_1 p\pi(n+1)}{p_r} + \cos 2(K_1 p\theta_{rm} - \theta_p - \frac{K_1 p\pi\alpha}{2p_r})$$

$$\sum_{n=0}^{2p_r-1} \sin\frac{2K_1 p\pi(n+1)}{p_r} - \sin 2(K_1 p\theta_{rm} - \theta_p + \frac{K_1 p\pi\alpha}{2p_r}) \sum_{n=0}^{2p_r-1} \cos\frac{2K_1 p\pi n}{p_r}$$

$$- \cos 2(K_1 p\theta_{rm} - \theta_p + \frac{K_1 p\pi\alpha}{2p_r}) \sum_{n=0}^{2p_r-1} \sin\frac{2K_1 p\pi n}{p_r}\}.$$

$$L_{ddp} = \frac{3\mu_0 r\ell N_p^2 \pi\alpha}{2g_1} - \frac{3\mu_0 r\ell N_p^2}{4g_1 K_1 p}\sin\frac{K_1 p\pi\alpha}{2p_r}\{\cos 2(K_1 p\theta_{rm} - \theta_p)$$

$$\sum_{n=0}^{2p_r-1}\cos\frac{2K_1 p\pi n}{p_r} - \sin 2(K_1 p\theta_{rm} - \theta_p)\sum_{n=0}^{2p_r-1}\sin\frac{2K_1 p\pi n}{p_r}\} + \frac{3\mu_0 r\ell N_p^2 \pi\alpha}{2g_2} - \frac{3\mu_0 r\ell N_p^2}{8g_2 K_1 p}$$

$$\{\sin 2(K_1 p\theta_{rm} - \theta_p - \frac{K_1 p\pi\alpha}{2p_r})\sum_{n=0}^{2p_r-1}\cos\frac{2K_1 p\pi(n+1)}{p_r} + \cos 2(K_1 p\theta_{rm} - \theta_p - \frac{K_1 p\pi\alpha}{2p_r})$$

$$\sum_{n=0}^{2p_r-1}\sin\frac{2K_1 p\pi(n+1)}{p_r} - \sin 2(K_1 p\theta_{rm} - \theta_p + \frac{K_1 p\pi\alpha}{2p_r})\sum_{n=0}^{2p_r-1}\cos\frac{2K_1 p\pi n}{p_r}$$

$$- \cos 2(K_1 p\theta_{rm} - \theta_p + \frac{K_1 p\pi\alpha}{2p_r})\sum_{n=0}^{2p_r-1}\sin\frac{2K_1 p\pi n}{p_r}\}.$$

$$L_{qdp} = \frac{3\mu_0 r\ell N_p^2}{4g_1 K_1 p}\sin\frac{K_1 p\pi\alpha}{2p_r}\{\sin 2(\theta_p - K_1 p\theta_{rm})\sum_{n=0}^{2p_r-1}\cos\frac{2K_1 p\pi n}{p_r}$$

$$- \cos 2(\theta_p - K_1 p\theta_{rm})\sum_{n=0}^{2p_r-1}\sin\frac{2K_1 p\pi n}{p_r}\} + \frac{3\mu_0 r\ell N_p^2}{8g_2 K_1 p}$$

$$\{\cos 2(\theta_p - K_1 p\theta_{rm} + \frac{K_1 p\pi\alpha}{2p_r})\sum_{n=0}^{2p_r-1}\cos\frac{2K_1 p\pi(n+1)}{p_r} + \sin 2(\theta_p - K_1 p\theta_{rm} + \frac{K_1 p\pi\alpha}{2p_r})$$

$$\sum_{n=0}^{2p_r-1}\sin\frac{2K_1 p\pi(n+1)}{p_r} - \cos 2(\theta_p - K_1 p\theta_{rm} - \frac{K_1 p\pi\alpha}{2p_r})\sum_{n=0}^{2p_r-1}\cos\frac{2K_1 p\pi n}{p_r}$$

$$- \sin 2(\theta_p - K_1 p\theta_{rm} - \frac{K_1 p\pi\alpha}{2p_r})\sum_{n=0}^{2p_r-1}\sin\frac{2K_1 p\pi n}{p_r}\}.$$

.

$$L_{qqs} = \frac{3\mu_0 r\ell N_s^2\pi\alpha}{2g_1} + \frac{3\mu_0 r\ell N_s^2}{4g_1K_2q}\sin\frac{K_2q\pi\alpha}{2p_r}\{\cos 2(K_2q\theta_{rm} - \theta_s)$$

$$\sum_{n=0}^{2p_r-1}\cos\frac{2K_2q\pi n}{p_r} - \sin 2(K_2q\theta_{rm} - \theta_s)\sum_{n=0}^{2p_r-1}\sin\frac{2K_2q\pi n}{p_r}\} + \frac{3\mu_0 r\ell N_s^2\pi\alpha}{2g_2} + \frac{3\mu_0 r\ell N_s^2}{8g_2K_2q}$$

$$\{\sin 2(K_2q\theta_{rm} - \theta_s - \frac{K_2q\pi\alpha}{2p_r})\sum_{n=0}^{2p_r-1}\cos\frac{2K_2q\pi(n+1)}{p_r} + \cos 2(K_2q\theta_{rm} - \theta_s - \frac{K_2q\pi\alpha}{2p_r})$$

$$\sum_{n=0}^{2p_r-1}\sin\frac{2K_2q\pi(n+1)}{p_r} - \sin 2(K_2q\theta_{rm} - \theta_s + \frac{K_2q\pi\alpha}{2p_r})\sum_{n=0}^{2p_r-1}\cos\frac{2K_2q\pi n}{p_r}$$

$$-\cos 2(K_2q\theta_{rm} - \theta_s + \frac{K_2q\pi\alpha}{2p_r})\sum_{n=0}^{2p_r-1}\sin\frac{2K_2q\pi n}{p_r}\}.$$

$$L_{dds} = \frac{3\mu_0 r\ell N_s^2\pi\alpha}{2g_1} - \frac{3\mu_0 r\ell N_s^2}{4g_1K_2q}\sin\frac{K_2q\pi\alpha}{2p_r}\{\cos 2(K_2q\theta_{rm} - \theta_s)$$

$$\sum_{n=0}^{2p_r-1}\cos\frac{2K_2q\pi n}{p_r} - \sin 2(K_2q\theta_{rm} - \theta_s)\sum_{n=0}^{2p_r-1}\sin\frac{2K_2q\pi n}{p_r}\} + \frac{3\mu_0 r\ell N_s^2\pi\alpha}{2g_2} - \frac{3\mu_0 r\ell N_s^2}{8g_2K_2q}$$

$$\{\sin 2(K_2q\theta_{rm} - \theta_s - \frac{K_2q\pi\alpha}{2p_r})\sum_{n=0}^{2p_r-1}\cos\frac{2K_2q\pi(n+1)}{p_r} + \cos 2(K_2q\theta_{rm} - \theta_s - \frac{K_2q\pi\alpha}{2p_r})$$

$$\sum_{n=0}^{2p_r-1}\sin\frac{2K_2q\pi(n+1)}{p_r} - \sin 2(K_2q\theta_{rm} - \theta_s + \frac{K_2q\pi\alpha}{2p_r})\sum_{n=0}^{2p_r-1}\cos\frac{2K_2q\pi n}{p_r}$$

$$-\cos 2(K_2q\theta_{rm} - \theta_s + \frac{K_2q\pi\alpha}{2p_r})\sum_{n=0}^{2p_r-1}\sin\frac{2K_2q\pi n}{p_r}\}.$$

$$L_{qds} = L_{dqs} = \frac{3\mu_0 r\ell N_s^2}{4g_1K_2q}\sin\frac{K_2q\pi\alpha}{2p_r}\{\sin 2(\theta_s - K_2q\theta_{rm})\sum_{n=0}^{2p_r-1}\cos\frac{2K_2q\pi n}{p_r}$$

$$-\cos 2(\theta_s - K_2q\theta_{rm})\sum_{n=0}^{2p_r-1}\sin\frac{2K_2q\pi n}{p_r}\} + \frac{3\mu_0 r\ell N_s^2}{8g_2K_2q}$$

$$\{\cos 2(\theta_s - K_2q\theta_{rm} + \frac{K_2q\pi\alpha}{2p_r})\sum_{n=0}^{2p_r-1}\cos\frac{2K_2q\pi(n+1)}{p_r} + \sin 2(\theta_s - K_2q\theta_{rm} + \frac{K_2q\pi\alpha}{2p_r})$$

$$\sum_{n=0}^{2p_r-1}\sin\frac{2K_2q\pi(n+1)}{p_r} - \cos 2(\theta_s - K_2q\theta_{rm} - \frac{K_2q\pi\alpha}{2p_r})\sum_{n=0}^{2p_r-1}\cos\frac{2K_2q\pi n}{p_r}$$

$$-\sin 2(\theta_s - K_2q\theta_{rm} - \frac{K_2q\pi\alpha}{2p_r})\sum_{n=0}^{2p_r-1}\sin\frac{2K_2q\pi n}{p_r}\}.$$

.

$$L_{mqq} = \frac{3\mu_0 r\ell N_p N_s}{4g_1(K_1p + K_{2q})}\{-\sin[(\theta_p + \theta_s) - (K_1p + K_2q)\theta_{rm} - \frac{(K_1p + K_2q)\pi\alpha}{2p_r}]$$

$$\sum_{n=0}^{2p_r-1}\cos\frac{(K_1p + K_2q)\pi n}{p_r} + \cos[(\theta_p + \theta_s) - (K_1p + K_2q)\theta_{rm} - \frac{(K_1p + K_2q)\pi\alpha}{2p_r}]$$

$$\sum_{n=0}^{2p_r-1}\sin\frac{(K_1p + K_2q)\pi n}{p_r} + \sin[(\theta_p + \theta_s) - (K_1p + K_2q)\theta_{rm} + \frac{(K_1p + K_2q)\pi\alpha}{2p_r}]$$

$$\sum_{n=0}^{2p_r-1}\cos\frac{(K_1p + K_2q)\pi n}{p_r} - \cos[(\theta_p + \theta_s) - (K_1p + K_2q)\theta_{rm} + \frac{(K_1p + K_2q)\pi\alpha}{2p_r}]$$

$$\sum_{n=0}^{2p_r-1}\sin\frac{(K_1p + K_2q)\pi n}{p_r}\} + \frac{3\mu_0 r\ell N_p N_s}{4g_1(K_1p - K_{2q})}\{-\sin[(\theta_p - \theta_s) - (K_1p - K_2q)\theta_{rm}$$

$$-\frac{(K_1p - K_2q)\pi\alpha}{2p_r}]\sum_{n=0}^{2p_r-1}\cos\frac{(K_1p - K_2q)\pi n}{p_r} + \cos[(\theta_p - \theta_s) - (K_1p - K_2q)\theta_{rm}$$

$$-\frac{(K_1p - K_2q)\pi\alpha}{2p_r}]\sum_{n=0}^{2p_r-1}\sin\frac{(K_1p - K_2q)\pi n}{p_r} + \sin[(\theta_p - \theta_s) - (K_1p - K_2q)\theta_{rm}$$

$$-\frac{(K_1p - K_2q)\pi\alpha}{2p_r}]\sum_{n=0}^{2p_r-1}\cos\frac{(K_1p - K_2q)\pi n}{p_r} - \cos[(\theta_p - \theta_s) - (K_1p - K_2q)\theta_{rm}$$

$$-\frac{(K_1p - K_2q)\pi\alpha}{2p_r}]\sum_{n=0}^{2p_r-1}\sin\frac{(K_1p - K_2q)\pi n}{p_r}\}$$

$$+\frac{3\mu_0 r\ell N_p N_s}{4g_2(K_1p+K_{2q})}\{-\sin[(\theta_p+\theta_s)-(K_1p+K_2q)\theta_{rm}$$

$$+\frac{(K_1p+K_2q)\pi\alpha}{2p_r}]\sum_{n=0}^{2p_r-1}\cos\frac{(K_1p+K_2q)\pi(n+1)}{p_r}+\cos[(\theta_p+\theta_s)-(K_1p+K_2q)\theta_{rm}$$

$$+\frac{(K_1p+K_2q)\pi\alpha}{2p_r}]\sum_{n=0}^{2p_r-1}\sin\frac{(K_1p+K_2q)\pi(n+1)}{p_r}+\sin[(\theta_p+\theta_s)-(K_1p+K_2q)\theta_{rm}$$

$$-\frac{(K_1p+K_2q)\pi\alpha}{2p_r}]\sum_{n=0}^{2p_r-1}\cos\frac{(K_1p+K_2q)\pi n}{p_r}-\cos[(\theta_p+\theta_s)-(K_1p+K_2q)\theta_{rm}$$

$$-\frac{(K_1p+K_2q)\pi\alpha}{2p_r}\sum_{n=0}^{2p_r-1}\sin\frac{(K_1p+K_2q)\pi n}{p_r}\}+\frac{3\mu_0 r\ell N_p N_s}{4g_2(K_1p-K_{2q})}$$

$$\{-\sin[(\theta_p-\theta_s)-(K_1p-K_2q)\theta_{rm}+\frac{(K_1p-K_2q)\pi\alpha}{2p_r}]$$

$$\sum_{n=0}^{2p_r-1}\cos\frac{(K_1p-K_2q)\pi(n+1)}{p_r}+\cos[(\theta_p-\theta_s)-(K_1p-K_2q)\theta_{rm}+\frac{(K_1p-K_2q)\pi\alpha}{2p_r}]$$

$$\sum_{n=0}^{2p_r-1}\sin\frac{(K_1p-K_2q)\pi(n+1)}{p_r}+\sin[(\theta_p-\theta_s)-(K_1p-K_2q)\theta_{rm}-\frac{(K_1p-K_2q)\pi\alpha}{2p_r}]$$

$$\sum_{n=0}^{2p_r-1}\cos\frac{(K_1p-K_2q)\pi n}{p_r}-\cos[(\theta_p-\theta_s)-(K_1p-K_2q)\theta_{rm}-\frac{(K_1p-K_2q)\pi\alpha}{2p_r}$$

$$\sum_{n=0}^{2p_r-1}\sin\frac{(K_1p-K_2q)\pi n}{p_r}\}$$

$$
\begin{aligned}
&L_{mdd}=-\frac{3\mu_0 r\ell N_p N_s}{4g_1(K_1p+K_{2q})}\{-\sin[(\theta_p+\theta_s)-(K_1p+K_2q)\theta_{rm}-\frac{(K_1p+K_2q)\pi\alpha}{2p_r}]\\
&\sum_{n=0}^{2p_r-1}\cos\frac{(K_1p+K_2q)\pi n}{p_r}+\cos[(\theta_p+\theta_s)-(K_1p+K_2q)\theta_{rm}-\frac{(K_1p+K_2q)\pi\alpha}{2p_r}]\\
&\sum_{n=0}^{2p_r-1}\sin\frac{(K_1p+K_2q)\pi n}{p_r}+\sin[(\theta_p+\theta_s)-(K_1p+K_2q)\theta_{rm}+\frac{(K_1p+K_2q)\pi\alpha}{2p_r}]\\
&\sum_{n=0}^{2p_r-1}\cos\frac{(K_1p+K_2q)\pi n}{p_r}-\cos[(\theta_p+\theta_s)-(K_1p+K_2q)\theta_{rm}+\frac{(K_1p+K_2q)\pi\alpha}{2p_r}]\\
&\sum_{n=0}^{2p_r-1}\sin\frac{(K_1p+K_2q)\pi n}{p_r}\}+\frac{3\mu_0 r\ell N_p N_s}{4g_1(K_1p-K_{2q})}\{-\sin[(\theta_p-\theta_s)-(K_1p-K_2q)\theta_{rm}\\
&-\frac{(K_1p-K_2q)\pi\alpha}{2p_r}]\sum_{n=0}^{2p_r-1}\cos\frac{(K_1p-K_2q)\pi n}{p_r}+\cos[(\theta_p-\theta_s)-(K_1p-K_2q)\theta_{rm}\\
&-\frac{(K_1p-K_2q)\pi\alpha}{2p_r}]\sum_{n=0}^{2p_r-1}\sin\frac{(K_1p-K_2q)\pi n}{p_r}+\sin[(\theta_p-\theta_s)-(K_1p-K_2q)\theta_{rm}\\
&-\frac{(K_1p-K_2q)\pi\alpha}{2p_r}]\sum_{n=0}^{2p_r-1}\cos\frac{(K_1p-K_2q)\pi n}{p_r}-\cos[(\theta_p-\theta_s)-(K_1p-K_2q)\theta_{rm}\\
&-\frac{(K_1p-K_2q)\pi\alpha}{2p_r}]\sum_{n=0}^{2p_r-1}\sin\frac{(K_1p-K_2q)\pi n}{p_r}\}
\end{aligned}
$$

$$-\frac{3\mu_0 r\ell N_p N_s}{4g_2(K_1p+K_{2q})}\{-\sin[(\theta_p+\theta_s)-(K_1p+K_2q)\theta_{rm}$$

$$+\frac{(K_1p+K_2q)\pi\alpha}{2p_r}]\sum_{n=0}^{2p_r-1}\cos\frac{(K_1p+K_2q)\pi(n+1)}{p_r}+\cos[(\theta_p+\theta_s)-(K_1p+K_2q)\theta_{rm}$$

$$+\frac{(K_1p+K_2q)\pi\alpha}{2p_r}]\sum_{n=0}^{2p_r-1}\sin\frac{(K_1p+K_2q)\pi(n+1)}{p_r}+\sin[(\theta_p+\theta_s)-(K_1p+K_2q)\theta_{rm}$$

$$-\frac{(K_1p+K_2q)\pi\alpha}{2p_r}]\sum_{n=0}^{2p_r-1}\cos\frac{(K_1p+K_2q)\pi n}{p_r}-\cos[(\theta_p+\theta_s)-(K_1p+K_2q)\theta_{rm}$$

$$-\frac{(K_1p+K_2q)\pi\alpha}{2p_r}\sum_{n=0}^{2p_r-1}\sin\frac{(K_1p+K_2q)\pi n}{p_r}\}+\frac{3\mu_0 r\ell N_p N_s}{4g_2(K_1p-K_{2q})}$$

$$\{-\sin[(\theta_p-\theta_s)-(K_1p-K_2q)\theta_{rm}+\frac{(K_1p-K_2q)\pi\alpha}{2p_r}]$$

$$\sum_{n=0}^{2p_r-1}\cos\frac{(K_1p-K_2q)\pi(n+1)}{p_r}+\cos[(\theta_p-\theta_s)-(K_1p-K_2q)\theta_{rm}+\frac{(K_1p-K_2q)\pi\alpha}{2p_r}]$$

$$\sum_{n=0}^{2p_r-1}\sin\frac{(K_1p-K_2q)\pi(n+1)}{p_r}+\sin[(\theta_p-\theta_s)-(K_1p-K_2q)\theta_{rm}-\frac{(K_1p-K_2q)\pi\alpha}{2p_r}]$$

$$\sum_{n=0}^{2p_r-1}\cos\frac{(K_1p-K_2q)\pi n}{p_r}-\cos[(\theta_p-\theta_s)-(K_1p-K_2q)\theta_{rm}-\frac{(K_1p-K_2q)\pi\alpha}{2p_r}$$

$$\sum_{n=0}^{2p_r-1}\sin\frac{(K_1p-K_2q)\pi n}{p_r}\}$$

Appendix 3B

$$L'_{ddp} = \frac{d}{d\theta_{rm}}(L_{ddp}) = -\frac{3\mu_0 r\ell N_p^2}{2g_1}\sin\frac{K_1 p\pi\alpha}{2p_r}\{-\sin 2(K_1 p\theta_{rm} - \theta_p)$$

$$\sum_{n=0}^{2p_r-1}\cos\frac{2K_1 p\pi n}{p_r} - \cos 2(K_1 p\theta_{rm} - \theta_p)\sum_{n=0}^{2p_r-1}\sin\frac{2K_1 p\pi n}{p_r}\} - \frac{3\mu_0 r\ell N_p^2}{4g_2}$$

$$\{\cos 2(K_1 p\theta_{rm} - \theta_p - \frac{K_1 p\pi\alpha}{2p_r})\sum_{n=0}^{2p_r-1}\cos\frac{2K_1 p\pi(n+1)}{p_r} - \sin 2(K_1 p\theta_{rm} - \theta_p - \frac{K_1 p\pi\alpha}{2p_r})$$

$$\sum_{n=0}^{2p_r-1}\sin\frac{2K_1 p\pi(n+1)}{p_r} - \cos 2(K_1 p\theta_{rm} - \theta_p + \frac{K_1 p\pi\alpha}{2p_r})\sum_{n=0}^{2p_r-1}\cos\frac{2K_1 p\pi n}{p_r}$$

$$+\sin 2(K_1 p\theta_{rm} - \theta_p + \frac{K_1 p\pi\alpha}{2p_r})\sum_{n=0}^{2p_r-1}\sin\frac{2K_1 p\pi n}{p_r}\}.$$

$$L'_{qqp} = \frac{d}{d\theta_{rm}}(L_{dp}) = \frac{3\mu_0 r\ell N_p^2}{2g_1}\sin\frac{K_1 p\pi\alpha}{2p_r}\{-\sin 2(K_1 p\theta_{rm} - \theta_p)$$

$$\sum_{n=0}^{2p_r-1}\cos\frac{2K_1 p\pi n}{p_r} - \cos 2(K_1 p\theta_{rm} - \theta_p)\sum_{n=0}^{2p_r-1}\sin\frac{2K_1 p\pi n}{p_r}\} + \frac{3\mu_0 r\ell N_p^2}{4g_2}$$

$$\{\cos 2(K_1 p\theta_{rm} - \theta_p - \frac{K_1 p\pi\alpha}{2p_r})\sum_{n=0}^{2p_r-1}\cos\frac{2K_1 p\pi(n+1)}{p_r} - \sin 2(K_1 p\theta_{rm} - \theta_p - \frac{K_1 p\pi\alpha}{2p_r})$$

$$\sum_{n=0}^{2p_r-1}\sin\frac{2K_1 p\pi(n+1)}{p_r} - \cos 2(K_1 p\theta_{rm} - \theta_p + \frac{K_1 p\pi\alpha}{2p_r})\sum_{n=0}^{2p_r-1}\cos\frac{2K_1 p\pi n}{p_r}$$

$$+\sin 2(K_1 p\theta_{rm} - \theta_p + \frac{K_1 p\pi\alpha}{2p_r})\sum_{n=0}^{2p_r-1}\sin\frac{2K_1 p\pi n}{p_r}\}.$$

$$L'_{dds} = \frac{d}{d\theta_{rm}}(L_{dds}) = -\frac{3\mu_0 r\ell N_s^2}{2g_1}\sin\frac{K_2 q\pi\alpha}{2p_r}\{-\sin 2(K_2 q\theta_{rm} - \theta_s)$$

$$\sum_{n=0}^{2p_r-1}\cos\frac{2K_2 q\pi n}{p_r} - \cos 2(K_2 q\theta_{rm} - \theta_q)\sum_{n=0}^{2p_r-1}\sin\frac{2K_2 q\pi n}{p_r}\} - \frac{3\mu_0 r\ell N_s^2}{4g_2}$$

$$\{\cos 2(K_2 q\theta_{rm} - \theta_s - \frac{K_2 q\pi\alpha}{2p_r})\sum_{n=0}^{2p_r-1}\cos\frac{2K_2 q\pi(n+1)}{p_r} - \sin 2(K_2 q\theta_{rm} - \theta_s - \frac{K_2 q\pi\alpha}{2p_r})$$

$$\sum_{n=0}^{2p_r-1}\sin\frac{2K_2 q\pi(n+1)}{p_r} - \cos 2(K_2 q\theta_{rm} - \theta_s + \frac{K_2 q\pi\alpha}{2p_r})\sum_{n=0}^{2p_r-1}\cos\frac{2K_2 q\pi n}{p_r}$$

$$+\sin 2(K_2 q\theta_{rm} - \theta_s + \frac{K_2 q\pi\alpha}{2p_r})\sum_{n=0}^{2p_r-1}\sin\frac{2K_2 q\pi n}{p_r}\}.$$

$$L'_{qqs} = \frac{d}{d\theta_{rm}}(L_{qqs}) = \frac{3\mu_0 r\ell N_s^2}{2g_1}\sin\frac{K_2 q\pi\alpha}{2p_r}\{-\sin 2(K_2 q\theta_{rm} - \theta_s)$$

$$\sum_{n=0}^{2p_r-1}\cos\frac{2K_2 q\pi n}{p_r} - \cos 2(K_2 q\theta_{rm} - \theta_q)\sum_{n=0}^{2p_r-1}\sin\frac{2K_2 q\pi n}{p_r}\} + \frac{3\mu_0 r\ell N_s^2}{4g_2}$$

$$\{\cos 2(K_2 q\theta_{rm} - \theta_s - \frac{K_2 q\pi\alpha}{2p_r})\sum_{n=0}^{2p_r-1}\cos\frac{2K_2 q\pi(n+1)}{p_r} - \sin 2(K_2 q\theta_{rm} - \theta_s - \frac{K_2 q\pi\alpha}{2p_r})$$

$$\sum_{n=0}^{2p_r-1}\sin\frac{2K_2 q\pi(n+1)}{p_r} - \cos 2(K_2 q\theta_{rm} - \theta_s + \frac{K_2 q\pi\alpha}{2p_r})\sum_{n=0}^{2p_r-1}\cos\frac{2K_2 q\pi n}{p_r}$$

$$+\sin 2(K_2 q\theta_{rm} - \theta_s + \frac{K_2 q\pi\alpha}{2p_r})\sum_{n=0}^{2p_r-1}\sin\frac{2K_2 q\pi n}{p_r}\}.$$

$$L'_{dqp} = \frac{d}{d\theta_{rm}}(L_{dqp}) = -\frac{3\mu_0 r\ell N_p^2}{2g_1}\sin\frac{K_1p\pi\alpha}{2p_r}\{-\cos 2(K_1p\theta_{rm} - \theta_p)$$

$$\sum_{n=0}^{2p_r-1}\cos\frac{2K_1p\pi n}{p_r} - \sin 2(K_1p\theta_{rm} - \theta_p)\sum_{n=0}^{2p_r-1}\sin\frac{2K_1p\pi n}{p_r}\} - \frac{3\mu_0 r\ell N_p^2\pi\alpha}{4g_2}$$

$$\{-\sin 2(K_1p\theta_{rm} - \theta_p - \frac{K_1p\pi\alpha}{2p_r})\sum_{n=0}^{2p_r-1}\cos\frac{2K_1p\pi(n+1)}{p_r} + \cos 2(K_1p\theta_{rm} - \theta_p - \frac{K_1p\pi\alpha}{2p_r})$$

$$\sum_{n=0}^{2p_r-1}\sin\frac{2K_1p\pi(n+1)}{p_r} + \sin 2(K_1p\theta_{rm} - \theta_p + \frac{K_1p\pi\alpha}{2p_r})\sum_{n=0}^{2p_r-1}\cos\frac{2K_1p\pi n}{p_r}$$

$$-\cos 2(K_1p\theta_{rm} - \theta_p + \frac{K_1p\pi\alpha}{2p_r})\sum_{n=0}^{2p_r-1}\sin\frac{2K_1p\pi n}{p_r}\}.$$

$$L'_{mqq} = \frac{3\mu_0 r\ell N_p N_s}{4g_1}\{\cos[(\theta_p + \theta_s) - (K_1p + K_2q)\theta_{rm} - \frac{(K_1p + K_2q)\pi\alpha}{2p_r}]$$

$$\sum_{n=0}^{2p_r-1}\cos\frac{(K_1p + K_2q)\pi n}{p_r} + \sin[(\theta_p + \theta_s) - (K_1p + K_2q)\theta_{rm} - \frac{(K_1p + K_2q)\pi\alpha}{2p_r}]$$

$$\sum_{n=0}^{2p_r-1}\sin\frac{(K_1p + K_2q)\pi n}{p_r} - \cos[(\theta_p + \theta_s) - (K_1p + K_2q)\theta_{rm} + \frac{(K_1p + K_2q)\pi\alpha}{2p_r}]$$

$$\sum_{n=0}^{2p_r-1}\cos\frac{(K_1p + K_2q)\pi n}{p_r} - \sin[(\theta_p + \theta_s) - (K_1p + K_2q)\theta_{rm} + \frac{(K_1p + K_2q)\pi\alpha}{2p_r}]$$

$$\sum_{n=0}^{2p_r-1}\sin\frac{(K_1p + K_2q)\pi n}{p_r}\} + \frac{3\mu_0 r\ell N_p N_s}{4g_1}\{\cos[(\theta_p - \theta_s) - (K_1p - K_2q)\theta_{rm}$$

$$- \frac{(K_1p - K_2q)\pi\alpha}{2p_r}]\sum_{n=0}^{2p_r-1}\cos\frac{(K_1p - K_2q)\pi n}{p_r} + \sin[(\theta_p - \theta_s) - (K_1p - K_2q)\theta_{rm}$$

$$- \frac{(K_1p - K_2q)\pi\alpha}{2p_r}]\sum_{n=0}^{2p_r-1}\sin\frac{(K_1p - K_2q)\pi n}{p_r} - \cos[(\theta_p - \theta_s) - (K_1p - K_2q)\theta_{rm}$$

$$- \frac{(K_1p - K_2q)\pi\alpha}{2p_r}]\sum_{n=0}^{2p_r-1}\cos\frac{(K_1p - K_2q)\pi n}{p_r} - \sin[(\theta_p - \theta_s) - (K_1p - K_2q)\theta_{rm}$$

$$- \frac{(K_1p - K_2q)\pi\alpha}{2p_r}]\sum_{n=0}^{2p_r-1}\sin\frac{(K_1p - K_2q)\pi n}{p_r}\}$$

$$+\frac{3\mu_0 r\ell N_p N_s}{4g_2}\{\cos[(\theta_p+\theta_s)-(K_1p+K_2q)\theta_{rm}+\frac{(K_1p+K_2q)\pi\alpha}{2p_r}]$$

$$\sum_{n=0}^{2p_r-1}\cos\frac{(K_1p+K_2q)\pi(n+1)}{p_r}-\sin[(\theta_p+\theta_s)-(K_1p+K_2q)\theta_{rm}+\frac{(K_1p+K_2q)\pi\alpha}{2p_r}]$$

$$\sum_{n=0}^{2p_r-1}\sin\frac{(K_1p+K_2q)\pi(n+1)}{p_r}-\cos[(\theta_p+\theta_s)-(K_1p+K_2q)\theta_{rm}-\frac{(K_1p+K_2q)\pi\alpha}{2p_r}]$$

$$\sum_{n=0}^{2p_r-1}\cos\frac{(K_1p+K_2q)\pi n}{p_r}-\sin[(\theta_p+\theta_s)-(K_1p+K_2q)\theta_{rm}-\frac{(K_1p+K_2q)\pi\alpha}{2p_r}]$$

$$\sum_{n=0}^{2p_r-1}\sin\frac{(K_1p+K_2q)\pi n}{p_r}\}+\frac{3\mu_0 r\ell N_p N_s}{4g_2}\{\cos[(\theta_p-\theta_s)-(K_1p-K_2q)\theta_{rm}$$

$$+\frac{(K_1p-K_2q)\pi\alpha}{2p_r}]\sum_{n=0}^{2p_r-1}\cos\frac{(K_1p-K_2q)\pi(n+1)}{p_r}+\sin[(\theta_p-\theta_s)-(K_1p-K_2q)\theta_{rm}$$

$$+\frac{(K_1p-K_2q)\pi\alpha}{2p_r}]\sum_{n=0}^{2p_r-1}\sin\frac{(K_1p-K_2q)\pi(n+1)}{p_r}-\cos[(\theta_p-\theta_s)-(K_1p-K_2q)\theta_{rm}$$

$$-\frac{(K_1p-K_2q)\pi\alpha}{2p_r}]\sum_{n=0}^{2p_r-1}\cos\frac{(K_1p-K_2q)\pi n}{p_r}-\sin[(\theta_p-\theta_s)-(K_1p-K_2q)\theta_{rm}$$

$$-\frac{(K_1p-K_2q)\pi\alpha}{2p_r}]\sum_{n=0}^{2p_r-1}\sin\frac{(K_1p-K_2q)\pi n}{p_r}\}$$

$$L'_{mdd} = \frac{3\mu_0 r\ell N_p N_s}{4g_1}\{-\cos[(\theta_p + \theta_s) - (K_1p + K_2q)\theta_{rm} - \frac{(K_1p + K_2q)\pi\alpha}{2p_r}]$$

$$\sum_{n=0}^{2p_r-1}\cos\frac{(K_1p + K_2q)\pi n}{p_r} - \sin[(\theta_p + \theta_s) - (K_1p + K_2q)\theta_{rm} - \frac{(K_1p + K_2q)\pi\alpha}{2p_r}]$$

$$\sum_{n=0}^{2p_r-1}\sin\frac{(K_1p + K_2q)\pi n}{p_r} + \cos[(\theta_p + \theta_s) - (K_1p + K_2q)\theta_{rm} + \frac{(K_1p + K_2q)\pi\alpha}{2p_r}]$$

$$\sum_{n=0}^{2p_r-1}\cos\frac{(K_1p + K_2q)\pi n}{p_r} + \sin[(\theta_p + \theta_s) - (K_1p + K_2q)\theta_{rm} + \frac{(K_1p + K_2q)\pi\alpha}{2p_r}]$$

$$\sum_{n=0}^{2p_r-1}\sin\frac{(K_1p + K_2q)\pi n}{p_r}\} + \frac{3\mu_0 r\ell N_p N_s}{4g_1}\{\cos[(\theta_p - \theta_s) - (K_1p - K_2q)\theta_{rm}$$

$$- \frac{(K_1p - K_2q)\pi\alpha}{2p_r}]\sum_{n=0}^{2p_r-1}\cos\frac{(K_1p - K_2q)\pi n}{p_r} + \sin[(\theta_p - \theta_s) - (K_1p - K_2q)\theta_{rm}$$

$$- \frac{(K_1p - K_2q)\pi\alpha}{2p_r}]\sum_{n=0}^{2p_r-1}\sin\frac{(K_1p - K_2q)\pi n}{p_r} - \cos[(\theta_p - \theta_s) - (K_1p - K_2q)\theta_{rm}$$

$$- \frac{(K_1p - K_2q)\pi\alpha}{2p_r}]\sum_{n=0}^{2p_r-1}\cos\frac{(K_1p - K_2q)\pi n}{p_r} - \sin[(\theta_p - \theta_s) - (K_1p - K_2q)\theta_{rm}$$

$$- \frac{(K_1p - K_2q)\pi\alpha}{2p_r}]\sum_{n=0}^{2p_r-1}\sin\frac{(K_1p - K_2q)\pi n}{p_r}\}$$

$$+\frac{3\mu_0 r\ell N_p N_s}{4g_2}\{-\cos[(\theta_p+\theta_s)-(K_1p+K_2q)\theta_{rm}+\frac{(K_1p+K_2q)\pi\alpha}{2p_r}]$$

$$\sum_{n=0}^{2p_r-1}\cos\frac{(K_1p+K_2q)\pi(n+1)}{p_r}-\sin[(\theta_p+\theta_s)-(K_1p+K_2q)\theta_{rm}+\frac{(K_1p+K_2q)\pi\alpha}{2p_r}]$$

$$\sum_{n=0}^{2p_r-1}\sin\frac{(K_1p+K_2q)\pi(n+1)}{p_r}-\cos[(\theta_p+\theta_s)-(K_1p+K_2q)\theta_{rm}-\frac{(K_1p+K_2q)\pi\alpha}{2p_r}]$$

$$\sum_{n=0}^{2p_r-1}\cos\frac{(K_1p+K_2q)\pi n}{p_r}-\sin[(\theta_p+\theta_s)-(K_1p+K_2q)\theta_{rm}-\frac{(K_1p+K_2q)\pi\alpha}{2p_r}]$$

$$\sum_{n=0}^{2p_r-1}\sin\frac{(K_1p+K_2q)\pi n}{p_r}\}+\frac{3\mu_0 r\ell N_p N_s}{4g_2}\{\cos[(\theta_p-\theta_s)-(K_1p-K_2q)\theta_{rm}$$

$$+\frac{(K_1p-K_2q)\pi\alpha}{2p_r}]\sum_{n=0}^{2p_r-1}\cos\frac{(K_1p-K_2q)\pi(n+1)}{p_r}+\sin[(\theta_p-\theta_s)-(K_1p-K_2q)\theta_{rm}$$

$$+\frac{(K_1p-K_2q)\pi\alpha}{2p_r}]\sum_{n=0}^{2p_r-1}\sin\frac{(K_1p-K_2q)\pi(n+1)}{p_r}-\cos[(\theta_p-\theta_s)-(K_1p-K_2q)\theta_{rm}$$

$$-\frac{(K_1p-K_2q)\pi\alpha}{2p_r}]\sum_{n=0}^{2p_r-1}\cos\frac{(K_1p-K_2q)\pi n}{p_r}-\sin[(\theta_p-\theta_s)-(K_1p-K_2q)\theta_{rm}$$

$$-\frac{(K_1p-K_2q)\pi\alpha}{2p_r}]\sum_{n=0}^{2p_r-1}\sin\frac{(K_1p-K_2q)\pi n}{p_r}\}$$

Appendix 4A

$$
\begin{aligned}
\Delta_R = {} & B_{s1}(-\omega_p\omega_s L_o C_q B_{ss2} - R_o B_{s2}) + T_{s1}(R_o(T_{s2} + \omega_s^2 C_q) + \omega_p\omega_s L_o C_q T_{ss2}) \\
& + (1-\omega_p^2 C_p L_o)(-B_{s2}B_{ss1} + \omega_q^2 C_q T_{ss1} + T_{s2}T_{ss1} - \omega_p\omega_s C_q T_{ss2}) \\
& + \omega_p C_p R_o(-\omega_s C_q B_{ss2} B_{ss1} + \omega_q^2 C_2 \omega_p + T_{s2}\omega_p + \omega_q C_q T_{ss1} T_{ss2})
\end{aligned}
$$

$$
\begin{aligned}
\Delta_I = {} & B_1(-\omega_2 C_q B_{ss2} R_o + \omega_p L_o B_{s2}) + T_{s1}(R_o\omega_s C_2 T_{ss2} - \omega_p L_o(T_{s2} + \omega_s^2 C_q)) \\
& + (1-\omega_p^2 C_p L_o)(-\omega_s C_q B_{ss2} B_{ss1} + \omega_s^2 C_q \omega_p + T_{s2}\omega_p + \omega_s C_2 T_{ss2} T_{ss1}) \\
& - \omega_p C_p R_o(-B_{s2}B_{ss1} + \omega_s^2 C_q T_{ss1} + T_{s2}T_{ss1} - \omega_s\omega_p C_q T_{ss2}
\end{aligned}
$$

$$aa = -C_p C_q L_o (T_{ss1} + T_{ss2})$$

$$ba = C_p L_o (2T_{ss1} + T_{ss2}) C_q \omega_r$$

$$
\begin{aligned}
ca = {} & L_o C_q (B_{s1}B_{ss2} - T_{s1}T_{ss2}) + C_q(T_{ss1} + T_{ss2}) \\
& - C_p L_o((T_{ss1}T_{s2} - B_{ss1}B_{s2}) + C_q \omega_r^2 T_{ss1}
\end{aligned}
$$

$$da = L_o C_q \omega_r (T_{s1}T_{ss2} - B_{s1}B_{ss2}) - (2T_{ss1} + T_{ss2}) C_2 \omega_r$$

$$ea = (T_{ss1}T_{s2} - B_{ss1}B_{s2}) + C_q \omega_r^2 T_{ss1}$$

$$fa = C_p C_q$$

$$ga = -2 C_p C_q \omega_r$$

$$ha = C_p C_q (B_{ss2}B_{ss1} - T_{ss1}T_{ss2}) + (T_{s1}C_q + T_{s2}C_p) + C_p C_q \omega_r^2$$

$$ia = \omega_r C_p C_{q(} (T_{ss1}T_{ss2} - B_{ss1}B_{ss2}) - 2T_{s1} C_q \omega_r$$

$$ja = (T_{s1}T_{s2} - B_{s1}B_{s2}) + T_{s1} C_q \omega_r^2$$

$$la = -C_p C_q (T_{ss1} + T_{ss2})$$

$$ma = 2 C_p C_q T_{ss1} \omega_r + C_p C_q T_{ss2} \omega_r$$

$$na = C_q(B_{s1}B_{ss2} - T_{s1}T_{ss2}) + C_p(B_{ss1}B_{s2} - T_{ss1}T_{s2}) - C_pC_qT_{ss1}\omega_r^2$$

$$qa = C_q\omega_r(T_{s1}T_{ss2} - B_{s1}B_{ss2})$$

$$sa = -C_pC_qL_o$$

$$ta = 2C_pC_qL_o\omega_r$$

$$ua = -L_oT_{s1}C_q + C_q - C_pC_qL_o(B_{ss2}B_{ss1} - T_{ss2}T_{ss1}) - L_oT_{s2}C_p - C_pC_qL_o\omega_r^2$$

$$va = 2L_oT_{s1}C_q\omega_r - 2C_q\omega_r + C_pC_qL_o\omega_r(B_{ss2}B_{ss1} - T_{ss2}T_{ss1})$$

$$xa = L_o(B_{s1}B_{s2} - T_{s1}T_{s2}) - L_oT_{s1}C_q\omega_r^2 + C_q(B_{ss2}B_{ss1} - T_{ss2}T_{ss1}) + C_q\omega_r^2 + T_{s2}$$

$$ya = -C_q\omega_r(B_{ss2}B_{ss1} - T_{ss2}T_{ss1})$$

$$C_1 = -f_as_a$$

$$C_2 = -(f_at_a + g_as_a)$$

$$C_3 = a_al_a - f_au_a - g_at_a - h_as_a$$

$$C_4 = a_am_a + b_al_a - f_av_a - g_au_a - h_at_a - i_as_a$$

$$C_5 = a_an_a + b_am_a + c_al_a - f_ax_a - g_av_a - h_au_a - i_at_a - j_as_a$$

$$C_6 = a_ao_a + b_an_a + c_am_a + d_al_a - f_ay_a - g_ax_a - h_av_a - i_au_a - j_at_a$$

$$C_7 = b_ao_a + c_an_a + d_am_a + e_al_a - g_ay_a - h_ax_a - i_av_a - j_au_a$$

$$C_8 = C_aO_a + d_an_a + e_am_a - h_ay_a - i_ax_a - j_av_a$$

$$C_9 = d_ao_a + e_an_a - i_ay_a - j_ax_a$$

$$C_{10} = e_ao_a - j_ay_a$$

Appendix 4B

Matlab Program

```
%Double-fed generator steady-state analysis.
%Power winding denoted by “1” and control winding denoted by “2”.
c2=90.e-6;rr1=1.4392;rr2=2.8933;lo=0.00015;
for num=1:1:3
if num==1;c1=168.e-6;wr=377*2*45/60;
ktt=0.185;
%ktt=0.2;
end;
if num==2;c1=168.e-6;wr=377*2*50/60;
ktt=0.207;
%ktt=0.244;
end;
if num==3;c1=168.e-6;wr=377*2*55/60;
ktt=0.215;
%ktt=0.27;
end;
for x=1:1:41;
lamx=(x-1)*ktt/40;
```

```
lamm=lamx;
lam(num,x)=lamx;
rm2=7.24*lamm^2-4.25*lamm+1.58;
ls2=-0.55*lamm^2+0.09*lamm+0.0385;
lm=-0.44*lamm^2+0.085*lamm+0.0373;
rm1=-4.05*lamm^2-1.47*lamm+1.217;
ls1=-0.36*lamm^2+0.09*lamm+0.0385;
r1=rr1+rm1;
r2=rr2+rm2;
lls2=ls2-lm;
lls1=ls1-lm;
e=1/((1/lm+1/lls1+1/lls2)*lls1);
f=1/((1/lm+1/lls1+1/lls2)*lls2);
ts1=-ls2/(ls1*ls2-lm^2);bs1=lm/(ls1*ls2-lm^2);
ts2=-ls1/(ls1*ls2-lm^2);bs2=lm/(ls1*ls2-lm^2);
tss1=-r1*ls2/(ls1*ls2-lm^2);bss1=r1*lm/(ls1*ls2-lm^2);
tss2=-r2*ls1/(ls1*ls2-lm^2);bss2=r2*lm/(ls1*ls2-lm^2);

aa=-c1*c2*lo*(tss1+tss2);
ba=c1*lo*(2*tss1+tss2)*c2*wr;
ca=lo*c2*(bs1*bss2-ts1*tss2)+c2*(tss1+tss2)-c1*lo*((tss1*ts2-
bss1*bs2)+c2*wr^2*tss1);
da=lo*c2*wr*(ts1*tss2-bs1*bss2)-(2*tss1+tss2)*c2*wr;
```

```
ea=(tss1*ts2-bss1*bs2)+c2*wr^2*tss1;

fa=c1*c2;
ga=-2*c1*c2*wr;
ha=c1*c2*(bss2*bss1-tss2*tss1)+ts1*c2+ts2*c1+c1*c2*wr^2;
ia=wr*c1*c2*(tss1*tss2-bss1*bss2)-2*ts1*c2*wr;
ja=(ts1*ts2-bs1*bs2)+ts1*c2*wr^2;

la=-c1*c2*(tss1+tss2);
ma=2*c1*c2*tss1*wr+c1*c2*tss2*wr;
na=c2*(bs1*bss2-ts1*tss2)+c1*(bss1*bs2-tss1*ts2)-c1*c2*tss1*wr^2;
oa=c2*wr*(ts1*tss2-bs1*bss2);

sa=-c1*c2*lo;
ta=2*c1*c2*lo*wr;
ua=-lo*ts1*c2-lo*ts2*c1+c2-c1*c2*lo*(bss2*bss1-tss2*tss1)-c1*c2*lo*wr^2;
va=2*lo*ts1*c2*wr-2*c2*wr+c1*c2*lo*wr*(bss2*bss1-tss2*tss1);
xa=lo*(bs1*bs2-ts1*ts2)-lo*ts1*c2*wr^2+c2*(bss2*bss1-tss2*tss1)+c2*wr^2+ts2;
ya=-c2*wr*(bss2*bss1-tss2*tss1);
aw1=-fa*sa;
bw1=-fa*ta-ga*sa;
cw1=aa*la-fa*ua-ga*ta-ha*sa;
dw1=aa*ma+ba*la-fa*va-ga*ua-ha*ta-ia*sa;
```

```
ew1=(aa*na+ba*ma+ca*la-fa*xa-ga*va-ha*ua-ia*ta-ja*sa);
fw1=(aa*oa+ba*na+ca*ma+da*la-fa*ya-ga*xa-ha*va-ia*ua-ja*ta);
gw1=(ba*oa+ca*na+da*ma+ea*la-ga*ya-ha*xa-ia*va-ja*ua);
hw1=(ca*oa+da*na+ea*ma-ha*ya-ia*xa-ja*va);
iw1=(da*oa+ea*na-ia*ya-ja*xa);
jw1=(ea*oa-ja*ya);
cw=[aw1 bw1 cw1 dw1 ew1 fw1 gw1 hw1 iw1 jw1];
w1=roots(cw);
for mm=1:1:9;
if imag(w1(mm))==0,test1=1;else test1=0;end;
if real(w1(mm))>1,test2=1;else test2=0;end;
if real(w1(mm))<wr,test3=1;else test3=0;end;
kw=test1*test2*test3*mm;
if kw>0,km=kw;
end;
end;
ww1(num,x)=w1(km);
ww2(num,x)=wr-ww1(num,x);
ro(num,x)=-
(sa*ww1(num,x)^5+ta*ww1(num,x)^4+ua*ww1(num,x)^3+va*ww1(num,x)^2+xa*ww1
(num,x)+ya)/(la*ww1(num,x)^3+ma*ww1(num,x)^2+na*ww1(num,x)+oa);
ao=ts1*(ro(num,x)-ww1(num,x)*lo*j)/(1-ww1(num,x)^2*c1*lo-
ww1(num,x)*c1*ro(num,x)*j);
```

```
bo=bs1*(ro(num,x)-ww1(num,x)*lo*j)/(1-ww1(num,x)^2*c1*lo-ww1(num,x)*c1*ro(num,x)*j);
k11=bss2-bs2/(-ww2(num,x)*c2*j);k12=-ww2(num,x)*j+tss2-ts2/(-ww2(num,x)*c2*j);
lamqds1=(k12*lamx)/(e*k12-f*k11);
lamqds2=-(k11*lamx)/(e*k12-f*k11);
k21=ao+ww1(num,x)*j+tss1;k22=bo+bss1;
lamqdss1=(k22*lamx)/(e*k22-f*k21);
lamqdss2=-(k21*lamx)/(e*k22-f*k21);
vqds1(num,x)=ao*lamqds1+bo*lamqds2;
vp(num,x)=sqrt(real(vqds1(num,x))^2+imag(vqds1(num,x))^2);
iqds1(num,x)=-ts1*lamqds1-bs1*lamqds2;
ip(num,x)=sqrt(real(iqds1(num,x))^2+imag(iqds1(num,x))^2);
vqds2(num,x)=-(ts2*lamqds2+bs2*lamqds1)/(ww2(num,x)*c2*j);
iqds2(num,x)=-ts2*lamqds2-bs2*lamqds1;
vs(num,x)=sqrt(real(vqds2(num,x))^2+imag(vqds2(num,x))^2);
is(num,x)=sqrt(real(iqds2(num,x))^2+imag(iqds2(num,x))^2);
iqdo(num,x)=vqds1(num,x)/(ro(num,x)-ww1(num,x)*lo*j);
io(num,x)=sqrt(real(iqdo(num,x))^2+imag(iqdo(num,x))^2);
po(num,x)=3*io(num,x)^2*ro(num,x)/2.0;
rro(num,x)=1.0/ro(num,x);
f2(num,x)=ww2(num,x)/(2.0*pi);
f1(num,x)=ww1(num,x)/(2.0*pi);
end;
```

```
end;

end;
```

Appendix 4C

ACSL PROGRAM

Double-Fed Generator Starting Transient Dynamic Simulation

```
.............................CONSTANT PHASE=2.094395,R11=1.4392,R22=0.7233,RO=16

           CONSTANT C1=168.E-6,C2=360.E-6,LO=0.00015,RD1=2.6568

          CONSTANT RD2=2.3022,LSD1=0.0373,LSD2=0.0385,LMD=0.0164

           CONSTANT MQSIC1=5.e-5,MDSIC1=5.e-5,MQSIC2=5.e-5

           CONSTANT MDSIC2=3.e-2,VQIC1=5.e-5,VDIC1=5.e-5

           CONSTANT IQIC=1.e-4,IDIC=1.e-5,WEIC=0.0

           CONSTANT VQIC2=5.e-5,VDIC2=2.0,THIC=0.0,NRIC=0.0

          CONSTANT PI=3.1412,WRR=377.0, RO2=16.0, RO1=16.0

           CONSTANT TSTOP=0.8,NSTOP=0.8

           CINTERVAL CINT=1.E-4

           MAXTERVAL MAXT=5.E-4


INITIAL

           RQ1=RD1

           RQ2=RD2

           LSQ1=0.0373
```

```
          LSQ2=0.0385
          LMQ=0.0164
         LLSD1=(LSD1-LMD)
          LLSD2=(LSD2-LMD)
          LLSQ1=(LSQ1-LMQ)
          LLSQ2=(LSQ2-LMQ)
          LMMQ=1.0/(1.0/LMQ+1.0/LLSQ1+1.0/LLSQ2)
         GUNC1=1.0/C1
          GUNC2=1.0/C2
END

DYNAMIC
DERIVATIVE
          WR=WRR*2.0*55/60
          THETAR=INTEG((W1-WR),NRIC)
          THETER=INTEG((W1),THIC)
          RO=RSW((T.LT.1.0),RO1,RO2)
          LAMQS1=INTEG((VQS1+TSSQ1*LAMQS-
          W1*LAMDS1+BSSQ1*LAMQS2),MQSIC1)
          LAMDS1=INTEG((VDS1+TSSD1*LAMDS1+W1*LAMQS1+BSSD1*LAMDS
          2),MDSIC1)

          LAMQS2=INTEG((VQS2+TSSQ2*LAMQS2-(W1-
          WR)*LAMDS2+BSSQ2*LAMQS1),MQSIC2)
```

```
LAMDS2=INTEG((VDS2+TSSD2*LAMDS2+(W1-WR)*LAMQS2+BSSD2*LAMDS1),MDSIC2)
VQ=GUNC1*TSQ1*LAMQS1+BSQ1*GUNC1*LAMQS2-W1*VDS1-GUNC1*IQO
VQS1=INTEG(VQ,VQIC1)
VD=GUNC1*TSD1*LAMDS1+BSD1*GUNC1*LAMDS2+W1*VQS1-GUNC1*IDO
VDS1=INTEG(VD,VDIC1)
VQS2=INTEG((GUNC2*TSQ2*LAMQS2+BSQ2*GUNC2*LAMQS1-(W1-WR)*VDS2),VQIC2)
VDS2=INTEG((GUNC2*TSD2*LAMDS2+BSD2*GUNC2*LAMDS1+(W1-WR)*VQS2),VDIC2)
 IQO=INTEG((VQS1/LO-RO*IQO/LO-W1*IDO),IQIC)
 IDO=INTEG((VDS1/LO-RO*IDO/LO+W1*IQO),IDIC)
 IQS1=-(TSQ1*LAMQS1+BSQ1*LAMQS2)
 IDS1=-(TSD1*LAMDS1+BSD1*LAMDS2)
 IQS2=-(TSQ2*LAMQS2+BSQ2*LAMQS1)
IDS2=-(TSD2*LAMDS2+BSD2*LAMDS1)
VAS1=(VQS1*COS(THETER)+VDS1*SIN(THETER))*SQRT(2.0/3.0)
VBS1=(VQS1*COS(THETER-PHASE)+VDS1*SIN(THETER-PHASE))*SQRT(2.0/3.0)
VCS1=(VQS1*COS(THETER+PHASE)+VDS1*SIN(THETER+PHASE))*SQRT(2.0/3.0)
```

```
VAS2=(VQS2*COS(THETAR)+VDS2*SIN(THETAR))*SQRT(2.0/3.0)*2.0
VBS2=(VQS2*COS(THETAR+PHASE)+VDS2*SIN(THETAR+PHASE))*SQR
T(2.0/3.0)
VCS2=(VQS2*COS(THETAR-PHASE)+VDS2*SIN(THETAR-
PHASE))*SQRT(2.0/3.0)
VS1=SQRT(VQS1**2+VDS1**2)
VS2=SQRT(VQS2**2+VDS2**2)
IAS1=(IQS1*COS(THETER)+IDS1*SIN(THETER))*SQRT(2.0/3.0)
IBS1=(IQS1*COS(THETER-PHASE)+IDS1*SIN(THETER-
PHASE))*SQRT(2.0/3.0)
ICS1=(IQS1*COS(THETER+PHASE)+IDS1*SIN(THETER+PHASE))*SQRT(2
.0/3.0)
Ipa=ias1
Vpa=vas1
IAS2=(IQS2*COS(THETAR)+IDS2*SIN(THETAR))*SQRT(2.0/3.0)/2.0
IBS2=(IQS2*COS(THETAR+PHASE)+IDS2*SIN(THETAR+PHASE))*SQRT(
2.0/3.0)
ICS2=(IQS2*COS(THETAR-PHASE)+IDS2*SIN(THETAR-
PHASE))*SQRT(2.0/3.0)

WA=VDS1*LLSD2+VDS2*LLSD1-LLSD1*WR*LAMQS2
WB=LAMDS1*(TSSD1*LLSD2+BSSD2*LLSD1-LLSD2**2*BSSD1/LLSD1-
LLSD2*TSSD2)
```

```
    W1=-(WA+WB)/(LLSD2*LAMQS1+LLSD1*LAMQS2)
    w2=wr-w1
    f1=w1/(2.0*pi)
    f2=w2/(2.0*pi)
    TSSQ1=-RQ1*LSQ2/(LSQ1*LSQ2-LMQ**2.0)
    BSSQ1=RQ2*LMQ/(LSQ1*LSQ2-LMQ**2.0)
    TSSD1=-RD1*LSD2/(LSD1*LSD2-LMD**2.0)
    BSSD1=RD1*LMD/(LSD1*LSD2-LMD**2.0)
    TSSQ2=-RQ2*LSQ1/(LSQ1*LSQ2-LMQ**2.0)
    BSSQ2=RQ2*LMQ/(LSQ1*LSQ2-LMQ**2.0)
    TSSD2=-RD2*LSD1/(LSD1*LSD2-LMD**2.0)
    BSSD2=RD2*LMD/(LSD1*LSD2-LMD**2.0)
    TSQ1=-LSQ2/(LSQ1*LSQ2-LMQ**2.0)
    BSQ1=LMQ/(LSQ1*LSQ2-LMQ**2.0)
    TSD1=-LSD2/(LSD1*LSD2-LMD**2.0)
    BSD1=LMD/(LSD1*LSD2-LMD**2.0)

    TSQ2=-LSQ1/(LSQ1*LSQ2-LMQ**2.0)
    BSQ2=LMQ/(LSQ1*LSQ2-LMQ**2.0)
    TSD2=-LSD1/(LSD1*LSD2-LMD**2.0)
    BSD2=LMD/(LSD1*LSD2-LMD**2.0)
PROCEDURAL
    LAMQM=LMMQ*(LAMQS1/LLSQ1+LAMQS2/LLSQ2)
```

```
          LAMM=ABS(LAMQM)

          RME1=-4.05*LAMM**2.0-1.47*LAMM+1.217

          RME2=7.24*LAMM**2.0-4.25*LAMM+1.58

          LME=-0.44*LAMM**2.0+0.0851*LAMM+0.0164

          LSE1=-0.36*LAMM**2.0+0.0906*LAMM+0.0373

.......................................................LSE2=-0.55*LAMM**2.0+0.09*LAMM+0.0385


         RM1=RSW((LAMM.GE.0.2),0.7608,RME1)

          RM2=RSW((LAMM.GE.0.2),0.7408,RME2)

          LSQ1=RSW((LAMM.GE.0.2),0.041,LSE1)

          LSQ2=RSW((LAMM.GE.0.2),0.0345,LSE2)

          LMQ=RSW((LAMM.GE.0.2),0.01577,LME)

          RQ1=R11+RM1

          RQ2=R22+RM2

          LLSQ1=(LSQ1-LMQ)

          LLSQ2=(LSQ2-LMQ)

          LMMQ=1.0/(1.0/LMQ+1.0/LLSQ1+1.0/LLSQ2)

END

END

          TERMT(T.GE.TSTOP)

END

END
```

Appendix 5A

Control Winding Mathematical Model of doubly-fed synchronous reluctance machine with dc control winding excitation.

$$V_{as} = R_s I_{as} + p\lambda_{as}$$

$$= R_s I_{as} + p[L_{aa} I_{as} + L_{ab} I_{bs} + L_{ac} I_{cs} + L_{aA} I_{Ap} + L_{aB} I_{Bp} + I_{aC} I_{Cp}]$$

$$= R_s I_{as} + p\{(\frac{3}{2} L_{m12} + L_{ls}) I_{as} + L_{m12} \cos[(p_1 + q)\theta_{rm}] I_{As}$$

$$+ \cos[(p_1 + q)\theta_{rm} - \frac{2\pi}{3}] I_{Bs} + \cos[(p_1 + q)\theta_{rm} + \frac{2\pi}{3}] I_{Cs}\}$$

$$= R_s I_{as} + p\{L_s I_{as} + L_{m12}[I_{Ap} \cos\theta_r + I_{Bp} \cos(\theta_r - \beta) + I_{cp} \cos(\theta_r + \beta)\}$$

$$= R_s I_{as} + p\{L_s I_{as} + L_{m12}[\mathrm{Re}(e^{j\theta_r}) R(I_{qdp} e^{j\theta_p}) + \mathrm{Re}(e^{j(\theta_r - \beta)}) \mathrm{Re}(I_{qdp} e^{j(\theta_p - \beta)})$$

$$+ \mathrm{Re}(e^{j(\theta_r + \beta)}) \mathrm{Re}(I_{qdp} e^{j(\theta_p + \beta)})]\}$$

$$= R_s I_{as} + p\{L_s I_{as} + \frac{1}{2} L_{m12} (\mathrm{Re}[I_{qdp} e^{j(\theta_r + \theta_p)}] + \mathrm{Re}[I_p e^{j(\theta_r + \theta_p)} e^{-j2\beta}]$$

$$+ \mathrm{Re}[I_{qdp} e^{j(\theta_r + \theta_p)} e^{j2\beta}] + 3\,\mathrm{Re}[I^*_{qdp} e^{j(\theta_r - \theta_p)}]\}$$

$$= R_s I_{as} + p\{L_s I_{as} + \frac{3}{2} L_{m12}\, \mathrm{Re}[I^*_{qdp} e^{j(\theta_r - \theta_p)}]\}$$

Replacing the V_{as}, I_{as} with the equation (5.17) and (5.18) gives

$$\mathrm{Re}[V_{qds}] = R_s\,\mathrm{Re}[I_{qds}] + p\{L_s\,\mathrm{Re}[I_{qds}] + \frac{3}{2}L_{m12}\,\mathrm{Re}[I_{qdp}^{*}e^{j(\theta_r-\theta_p)}]\}$$

$$= \mathrm{Re}[R_s I_{qds} + p\{L_s I_{qds} + \frac{3}{2}L_{m12} I_{qdp}^{*}e^{j(\theta_r-\theta_p)}\}]$$

Removing the ‘Re’ operator on both sides of the equation obtains the q-d complex-form equation of the power winding

$$V_{qds} = R_s I_{qds} + p\{L_s I_{qds} + \frac{3}{2}L_{m12} I_{qdp}^{*}e^{j(\theta_r-\theta_p)}\}.$$

Appendix 5B

Power Winding Mathematical Model of doubly-fed synchronous reluctance machine with dc control winding excitation.

$$V_{Ap} = R_p I_{Ap} + p\lambda_{Ap}$$

$$= R_p I_{Ap} + p[L_{AA}I_{Ap} + L_{AB}I_{Bp} + L_{AC}I_{Cp} + L_{Aa}I_{as} + L_{Ab}I_{bs} + L_{Ac}I_{cs}]$$

$$= (R_p I_{Ap} + L_p pI_{Ap}) + L_{m12}\,p\{\cos[(p_1+q)\theta_{rm}]I_{as} + \cos[(p_1+q)\theta_{rm} - \beta]I_{bs}$$

$$+ \cos[(p_1+q)\theta_{rm} + \beta]I_{cs}\}$$

$$= (R_p I_{Ap} + L_p pI_{Ap}) + L_{m12}\,p\{\mathrm{Re}(e^{j\theta_x})I_{as} + \mathrm{Re}(e^{j\theta_x}e^{-j\beta})I_{bs} + \mathrm{Re}(e^{j\theta_x}e^{j\beta})I_{cs}\}$$

Replacing V_{ap}, I_{ap}, I_{as}, I_{bs} and I_{cs} with the equations (5.10), (5.11), (5.17) and (5.18) gives

$$\mathrm{Re}[V_{qdp}e^{j\theta_p}] = (R_p + L_p p)\mathrm{Re}[I_{qdp}e^{j\theta_p}] + L_{m12}p\{\mathrm{Re}[e^{j\theta_r}]\mathrm{Re}[I_{qds}]$$

$$+\mathrm{Re}[e^{j(\theta_r-\beta)}]\mathrm{Re}[I_{qds}e^{-j\beta}] + \mathrm{Re}[e^{j(\theta_r+\beta)}]\mathrm{Re}[I_{qds}e^{j\beta}]\}$$

$$= (R_p + L_p p)\mathrm{Re}[I_{qdp}e^{j\theta_p}] + \frac{1}{2}L_{m12}p\{\mathrm{Re}[I_{qds}e^{j\theta_r}] + \mathrm{Re}[I_{qds}e^{j\theta_r}e^{-j2\beta}]$$

$$+\mathrm{Re}[I_{qds}e^{j\theta_r}e^{j2\beta}] + 3\mathrm{Re}[I_{qds}^{*}e^{j(\theta_r-\theta_p)}e^{j\theta_p}]\}$$

$$= \mathrm{Re}[(R_p + L_p p)I_{qdp}e^{j\theta_p}] + \frac{1}{2}L_{m12}p\{\mathrm{Re}[I_{qds}e^{j\theta_r}(1+e^{-j2\beta}+e^{j2\beta})]$$

$$+3\mathrm{Re}[I_{qds}^{*}e^{j(\theta_r-\theta_p)}e^{j\theta_p}]\}$$

$$= \mathrm{Re}[R_pI_{qdp}e^{j\theta_p} + (j\omega_pL_p + L_p p)I_{qdp}e^{j\theta_p}]$$

$$+\frac{3}{2}L_{m12}\,\mathrm{Re}[(j\omega_p + p)I_{qds}^{*}e^{j(\theta_r-\theta_p)}e^{j\theta_p}]$$

Removing the ‘Re’ operator from two sides of the equation obtains

$$I_{qdp}e^{j\theta_p} = R_pI_{qdp}e^{j\theta_p} + (j\omega_pL_p + L_p p)I_{qdp}e^{j\theta_p} + \frac{3}{2}L_{m12}(j\omega_p + p)I_{qds}^{*}e^{j(\theta_r-\theta_p)}e^{j\theta_p}$$

The q-d complex-form equation is obtained by dividing ‘ $e^{j\theta_p}$ ’ from both sides of the equation.

$$I_{qdp} = R_pI_{qdp} + j\omega_p[L_pI_{qdp} + \frac{3}{2}L_{m12}I_{qds}^{*}e^{j(\theta_r-\theta_p)}] + p[L_pI_{qdp} + \frac{3}{2}L_{m12}I_{qds}^{*}e^{j(\theta_r-\theta_p)}].$$

Appendix 5C

Torque equation of doubly-fed synchronous reluctance machine with dc control winding excitation.

$$T_e = [I_{Ap} \quad I_{Bp} \quad I_{Cp}] \frac{d}{d\theta_{rm}} \begin{bmatrix} L_{Aa} & L_{Ab} & L_{Ac} \\ L_{Ba} & L_{Bb} & L_{Bc} \\ L_{Ca} & L_{Cb} & L_{Cc} \end{bmatrix} \begin{bmatrix} I_{as} \\ I_{bs} \\ I_{cs} \end{bmatrix}$$

$$\begin{bmatrix} L_{Aa} & L_{Ab} & L_{Ac} \\ L_{Ba} & L_{Bb} & L_{Bc} \\ L_{Ca} & L_{Cb} & L_{Cc} \end{bmatrix} = L_{m12} \begin{bmatrix} \cos[(p_1+q)\theta_{rm}] & \cos[(p_1+q)\theta_{rm} - \frac{2\pi}{3}] & \cos[(p_1+q)\theta_{rm} + \frac{2\pi}{3}] \\ \cos[(p_1+q)\theta_{rm} - \frac{2\pi}{3}] & \cos[(p_1+q)\theta_{rm} + \frac{2\pi}{3}] & \cos[(p_1+q)\theta_{rm}] \\ \cos[(p_1+q)\theta_{rm} + \frac{2\pi}{3}] & \cos[(p_1+q)\theta_{rm}] & \cos[(p_1+q)\theta_{rm} - \frac{2\pi}{3}] \end{bmatrix}$$

$$= L_{m12} \begin{bmatrix} \mathrm{Re}[e^{j\theta_r}] & \mathrm{Re}[e^{j(\theta_r-\beta)}] & \mathrm{Re}[e^{j(\theta_r+\beta)}] \\ \mathrm{Re}[e^{j(\theta_r-\beta)}] & \mathrm{Re}[e^{j(\theta_r+\beta)}] & \mathrm{Re}[e^{j\theta_r}] \\ \mathrm{Re}[e^{j(\theta_r+\beta)}] & \mathrm{Re}[e^{j\theta_r}] & \mathrm{Re}[e^{j(\theta_r-\beta)}] \end{bmatrix}$$

$$\frac{d}{d\theta_{rm}} \begin{bmatrix} L_{Aa} & L_{Ab} & L_{Ac} \\ L_{Ba} & L_{Bb} & L_{Bc} \\ L_{Ca} & L_{Cb} & L_{Cc} \end{bmatrix}$$

$$= (p_1+q)L_{m12} \begin{bmatrix} \mathrm{Re}[je^{j\theta_r}] & \mathrm{Re}[je^{j(\theta_r-\beta)}] & \mathrm{Re}[je^{j(\theta_r+\beta)}] \\ \mathrm{Re}[je^{j(\theta_r-\beta)}] & \mathrm{Re}[je^{j(\theta_r+\beta)}] & \mathrm{Re}[je^{j\theta_r}] \\ \mathrm{Re}[je^{j(\theta_r+\beta)}] & \mathrm{Re}[je^{j\theta_r}] & \mathrm{Re}[je^{j(\theta_r-\beta)}] \end{bmatrix}$$

$$\left[I_{Ap} \quad I_{Bp} \quad I_{Cp}\right] = \left[\mathrm{Re}[I_{qdp}e^{j\theta_p}] \quad \mathrm{Re}[I_{qdp}e^{j(\theta_p-\beta)}] \quad \mathrm{Re}[I_{qdp}e^{j(\theta_p+\beta)}]\right]$$

$$\left[I_{Ap} \quad I_{Bp} \quad I_{Cp}\right] \frac{d}{d\theta_{rm}} \begin{bmatrix} L_{Aa} & L_{Ab} & L_{Ac} \\ L_{Ba} & L_{Bb} & L_{Bc} \\ L_{Ca} & L_{Cb} & L_{Cc} \end{bmatrix} = (p_1+q)L_{m12} \begin{bmatrix} AA \\ BB \\ CC \end{bmatrix}$$

Where

$$AA = \mathrm{Re}[I_{qdp}e^{j\theta_p}]\mathrm{Re}[je^{j\theta_r}] + \mathrm{Re}[I_{qdp}e^{j(\theta_p-\beta)}]\mathrm{Re}[je^{j(\theta_r-\beta)}] + \mathrm{Re}[I_{qdp}e^{j(\theta_p+\beta)}]\mathrm{Re}[je^{j(\theta_r+\beta)}]$$

$$= \frac{1}{2}\{\mathrm{Re}[jI_{qdp}e^{j(\theta_p+\theta_r)}] + \mathrm{Re}[jI_{qdp}e^{j(\theta_p+\theta_r)}e^{-j2\beta}] + \mathrm{Re}[jI_{qdp}e^{j(\theta_p+\theta_r)}e^{j2\beta}] + 3\mathrm{Re}[jI_{qdp}^{*}e^{j(\theta_r-\theta_p)}]\}$$

$$= \frac{3}{2}\mathrm{Re}[jI_{qdp}^{*}e^{j(\theta_r-\theta_p)}]$$

$$BB = \mathrm{Re}[I_{qdp}e^{j\theta_p}]\mathrm{Re}[je^{j(\theta_r-\beta)}] + \mathrm{Re}[I_{qdp}e^{j(\theta_p-\beta)}]\mathrm{Re}[je^{j(\theta_r+\beta)}] + \mathrm{Re}[I_{qdp}e^{j(\theta_p+\beta)}]\mathrm{Re}[je^{j\theta_r}]$$

$$= \frac{1}{2}\{\mathrm{Re}[jI_{qdp}e^{j(\theta_p+\theta_r)}e^{-j\beta}] + \mathrm{Re}[jI_{qdp}e^{j(\theta_p+\theta_r)}] + \mathrm{Re}[jI_{p}e^{j(\theta_p+\theta_r)}e^{j\beta}] + 3\mathrm{Re}[jI_{qdp}^{*}e^{j(\theta_r-\theta_p)}e^{-j\beta}]\}$$

$$= \frac{3}{2}\mathrm{Re}[jI_{qdp}^{*}e^{j(\theta_r-\theta_p)}e^{-j\beta}]$$

$$CC = \mathrm{Re}[I_{qdp}e^{j\theta_p}]\mathrm{Re}[je^{j(\theta_r+\beta)}] + \mathrm{Re}[I_{qdp}e^{j(\theta_p-\beta)}]\mathrm{Re}[je^{j\theta_r}] + \mathrm{Re}[I_{qdp}e^{j(\theta_p+\beta)}]\mathrm{Re}[je^{j(\theta_r-\beta)}]$$

$$= \frac{1}{2}\{\mathrm{Re}[jI_{qdp}e^{j(\theta_p+\theta_r)}e^{j\beta}] + \mathrm{Re}[jI_{qdp}e^{j(\theta_p+\theta_r)}e^{-j\beta}] + \mathrm{Re}[jI_{p}e^{j(\theta_p+\theta_r)}] + 3\mathrm{Re}[jI_{qdp}^{*}e^{j(\theta_r-\theta_p)}e^{j\beta}]\}$$

$$= \frac{3}{2}\mathrm{Re}[jI_{qdp}^{*}e^{j(\theta_r-\theta_p)}e^{j\beta}]$$

$$\begin{bmatrix} I_{Ap} & I_{Bp} & I_{Cp} \end{bmatrix}\frac{d}{d\theta_{rm}}\begin{bmatrix} L_{Aa} & L_{Ab} & L_{Ac} \\ L_{Ba} & L_{Bb} & L_{Bc} \\ L_{Ca} & L_{Cb} & L_{Cc} \end{bmatrix}\begin{bmatrix} I_{as} \\ I_{bs} \\ I_{cs} \end{bmatrix}$$

$$= (p_1+q)L_{m12}\begin{bmatrix} \frac{3}{2}\mathrm{Re}[jI_{qdp}^{*}e^{j(\theta_r-\theta_p)}] \\ \frac{3}{2}\mathrm{Re}[jI_{qdp}^{*}e^{j(\theta_r-\theta_p)}e^{-j\beta}] \\ \frac{3}{2}\mathrm{Re}[jI_{qdp}^{*}e^{j(\theta_r-\theta_p)}e^{j\beta}] \end{bmatrix}^{T}\begin{bmatrix} \mathrm{Re}[I_{qds}] \\ \mathrm{Re}[I_{qds}e^{j\beta}] \\ \mathrm{Re}[I_{qds}e^{-j\beta}] \end{bmatrix}$$

$$= \frac{3}{2}(p_1+q)L_{m12}\{\mathrm{Re}[jI_{qdp}^{*}e^{j(\theta_r-\theta_p)}]\mathrm{Re}[I_{qds}] + \mathrm{Re}[jI_{qdp}^{*}e^{j(\theta_r-\theta_p)}e^{-j\beta}]\mathrm{Re}[I_{qds}e^{j\beta}]$$

$$+\mathrm{Re}[jI_{qdp}^{*}e^{j(\theta_r-\theta_p)}e^{j\beta}]\mathrm{Re}[I_{qds}e^{-j\beta}]\}$$

$$= \frac{3}{2}(p_1+q)L_{m12}(\frac{1}{2})\{3\mathrm{Re}[jI_{qdp}^{*}e^{j(\theta_r-\theta_p)}I_{qds}] + \mathrm{Re}[jI_{qdp}^{*}e^{j(\theta_r-\theta_p)}I_{qds}^{*}(1+e^{-j2\beta}+e^{j2\beta})]$$

$$= \frac{3}{2}(p_1+q)(\frac{3}{2}L_{m12})\mathrm{Re}[jI_{qdp}^{*}e^{j(\theta_r-\theta_p)}I_{qds}]$$

The final form of torque equation is

$$T_e = \frac{3}{2}(p_1+q)L_m\,\mathrm{Re}[jI_{qdp}^{*}I_{qds}e^{j(\theta_r-\theta_p)}]$$

Where, $L_m = \frac{2}{3}L_{m12}$.

Appendix 6A

The parameters of the lead acid battery [61]

Battery capacitance C_{bp} = 54,000 F

Discharging resistance R_{b1} = 0.001Ω

Discharging capacitance C_{b1} = 1.0F

Self-charging Resistance R_{bp} = 10,000 Ohms

Open circuit battery voltage = 24 V

Connecting resistance R_{bt} = 0.05Ω

Internal resistance Rbs = 0.002Ω

Appendix 7A

```
%Program to obtain the electrical characteristics of DF machine
%for a wide speed range including above base speed and below speed range.
%rate value calculation:
clear all
basetime=4;
for mm=1:1:3
%Ojo's machine parameters
%vpm=187;rp=0.7;wp=377;lp=0.043;lm=0.0385;ipm=9.3477;pr=8;
%Wu's machine parameters
 vpm=187;rp=1.4;wp=377;lp=0.041;lm=0.021;ipm=11.7107;pr=4;
   if mm==1;iqs=16;end
   if mm==2;iqs=8;end
   if mm==3;iqs=2;end
 %calculate the peak rate current.
 %ipm=(wp*lm*rp*iqs)/(rp^2+wp^2*lp^2)+sqrt((wp*lm*iqs*rp)^2...
 %-(rp^2+wp^2*lp^2)*((wp*lm*iqs)^2-vpm^2))/(rp^2+wp^2*lp^2)
 %iss(mm)=ipm
 %vpm=sqrt((rp^2+wp^2*lp^2)*ipm^2+wp^2*lm^2*iqs^2-2*wp*lm*rp*iqs*idp)
 %ipm=(wp*lm*rp*iqs)/(rp^2+wp^2*lp^2)+sqrt((wp*lm*iqs*rp)^2...
 %-(rp^2+wp^2*lp^2)*((wp*lm*iqs)^2-vpm^2))/(rp^2+wp^2*lp^2)
 %calculate the base speed.
 ssa=lp^2*ipm^2+lm^2*iqs^2;ssb=-2*lm*rp*iqs*ipm;ssc=rp^2*ipm^2-vpm^2;
```

```
 wbb(mm)=-ssb/(2*ssa)+sqrt(ssb^2-4*ssa*ssc)/(2*ssa)

 %approximated equation to calculate the base speed by chossing rp=0;

 awbb(mm)=vpm/sqrt(lp^2*ipm^2+lm^2*iqs^2)

%boundary point between Mode I and Mode II

la=ipm^2*lp^4-lm^2*lp^2*iqs^2;

lb=2*rp^2*lp^2*ipm^2-lm^2*rp^2*iqs^2-lp^2*vpm^2;

lc=ipm^2*rp^4-rp^2*vpm^2;

ld=2*vpm*lm*rp*iqs*lp;

le=2*vpm*lm*rp^2*iqs;

kk1=la^2;

kk2=2*la*lb;

kk3=lb^2-ld^2+2*la*lc;

kk4=2*lb*lc-le^2;

kk5=lc^2;

mwm=[kk1 kk2 kk3 kk4 kk5];

wn=roots(mwm);

awnn=sqrt(wn);

w12(mm)=max(awnn)

wee=w12(mm);

nwee=w12(mm);

if wee>=basetime*377; wee=basetime*377; nwee=basetime*377; end;

%approximated equation to calculate the boundary speed by choosing rp=0;

aw12(mm)=vpm/sqrt(lp^2*ipm^2-lm^2*iqs^2)
```

```
%below the base speed

for nn=1:1:21;

   wbe(mm,nn)=wbb(mm)*(nn-1)/20;

   wp=wbe(mm,nn);

   iidp(mm,nn)=ipm;

   iiqp(mm,nn)=0;

   tor(mm,nn)=1.5*4*iqs*iidp(mm,nn)*lm;

   po(mm,nn)=tor(mm,nn)*wbe(mm,nn)/4;

   iip(mm,nn)=sqrt(iidp(mm,nn)^2+iiqp(mm,nn)^2);

   vpo(mm,nn)=sqrt((rp^2+wp^2*lp^2)*iip(mm,nn)^2+wp^2*lm^2*iqs^2...

      +2*wp^2*lm*lp*iqs*iiqp(mm,nn)-2*wp*lm*rp*iqs*iidp(mm,nn));

end

for nn=1:1:21;

   nwbe(mm,nn)=-wbb(mm)*(nn-1)/20;

   wp=abs(nwbe(mm,nn));

   niidp(mm,nn)=ipm;

   niiqp(mm,nn)=0;

   ntor(mm,nn)=1.5*4*iqs*niidp(mm,nn)*lm;

   npo(mm,nn)=ntor(mm,nn)*nwbe(mm,nn)/4;

   niip(mm,nn)=sqrt(niidp(mm,nn)^2+niiqp(mm,nn)^2);

   nvpo(mm,nn)=sqrt((rp^2+wp^2*lp^2)*niip(mm,nn)^2+wp^2*lm^2*iqs^2...

      +2*wp^2*lm*lp*iqs*niiqp(mm,nn)-2*wp*lm*rp*iqs*niidp(mm,nn));

end
```

```
%above the base speed

%Mode I

for nn=22:1:72;

   wbe(mm,nn)=wbb(mm)+(wee-wbb(mm))*(nn-21)/51;

   wp=wbe(mm,nn);

   s1=10e-4*(vpm^2-(rp^2+wp^2*lp^2)*ipm^2-wp^2*lm^2*iqs^2);

   s2=10e-4*(2*wp*lm*rp*iqs);s3=10e-4*(2*wp^2*lm*lp*iqs);

   ta=s2^2+s3^2;tb=2*s1*s2;tc=s1^2-s3^2*ipm^2;

   iidp(mm,nn)=-tb/(2*ta)+sqrt(tb^2-4*ta*tc)/(2*ta);

   iiqp(mm,nn)=(s1+s2*iidp(mm,nn))/s3;

   tor(mm,nn)=1.5*4*iqs*iidp(mm,nn)*lm;

   po(mm,nn)=tor(mm,nn)*wbe(mm,nn)/4;

   iip(mm,nn)=sqrt(iidp(mm,nn)^2+iiqp(mm,nn)^2);

   vpo(mm,nn)=sqrt((rp^2+wp^2*lp^2)*iip(mm,nn)^2+wp^2*lm^2*iqs^2...

      +2*wp^2*lm*lp*iqs*iiqp(mm,nn)-2*wp*lm*rp*iqs*iidp(mm,nn));

end

for nn=22:1:72;

   nwbe(mm,nn)=-wbb(mm)+(-nwee+wbb(mm))*(nn-21)/51;

   wp=abs(nwbe(mm,nn));

   s1=10e-4*(vpm^2-(rp^2+wp^2*lp^2)*ipm^2-wp^2*lm^2*iqs^2);

   s2=10e-4*(2*wp*lm*rp*iqs);s3=10e-4*(2*wp^2*lm*lp*iqs);

   ta=s2^2+s3^2;tb=2*s1*s2;tc=s1^2-s3^2*ipm^2;

   niidp(mm,nn)=-tb/(2*ta)+sqrt(tb^2-4*ta*tc)/(2*ta);
```

```
   niiqp(mm,nn)=(s1+s2*iidp(mm,nn))/s3;

   ntor(mm,nn)=1.5*4*iqs*niidp(mm,nn)*lm;

   npo(mm,nn)=ntor(mm,nn)*nwbe(mm,nn)/4;

   niip(mm,nn)=sqrt(niidp(mm,nn)^2+niiqp(mm,nn)^2);

   nvpo(mm,nn)=sqrt((rp^2+wp^2*lp^2)*niip(mm,nn)^2+wp^2*lm^2*iqs^2...

      +2*wp^2*lm*lp*iqs*niiqp(mm,nn)-2*wp*lm*rp*iqs*niidp(mm,nn));

end

%mode II

for nn=73:1:123;

   wbe(mm,nn)=wee+(basetime*377-wee)*(nn-73)/50;

    wp=wbe(mm,nn);

    iiqp(mm,nn)=-wp^2*lm*lp*iqs/(rp^2+wp^2*lp^2);

    iidp(mm,nn)=(wp*lm*rp*iqs+vpm*sqrt(lp^2*wp^2+rp^2))/(rp^2+wp^2*lp^2);

    tor(mm,nn)=1.5*4*iqs*iidp(mm,nn)*lm;

    po(mm,nn)=tor(mm,nn)*wbe(mm,nn)/4;

    iip(mm,nn)=sqrt(iidp(mm,nn)^2+iiqp(mm,nn)^2);

    vpo(mm,nn)=sqrt((rp^2+wp^2*lp^2)*iip(mm,nn)^2+wp^2*lm^2*iqs^2...

       +2*wp^2*lm*lp*iqs*iiqp(mm,nn)-2*wp*lm*rp*iqs*iidp(mm,nn));

 end;

 for nn=73:1:123;

    nwbe(mm,nn)=-nwee+(-basetime*377+nwee)*(nn-73)/50;

    wp=abs(nwbe(mm,nn));

    niiqp(mm,nn)=-wp^2*lm*lp*iqs/(rp^2+wp^2*lp^2);
```

```
    niidp(mm,nn)=(wp*lm*rp*iqs+vpm*sqrt(lp^2*wp^2+rp^2))/(rp^2+wp^2*lp^2);
    ntor(mm,nn)=1.5*4*iqs*niidp(mm,nn)*lm;
    npo(mm,nn)=ntor(mm,nn)*nwbe(mm,nn)/4;
    niip(mm,nn)=sqrt(niidp(mm,nn)^2+niiqp(mm,nn)^2);
    nvpo(mm,nn)=sqrt((rp^2+wp^2*lp^2)*niip(mm,nn)^2+wp^2*lm^2*iqs^2...
      +2*wp^2*lm*lp*iqs*niiqp(mm,nn)-2*wp*lm*rp*iqs*niidp(mm,nn));
end;
end
```

Appendix 7B

Control Scheme I:

K_a =35.54

K_b = 0.1042

K_c = 2.4019

K_q =15791

K_d = 0.6955

J = 0.0025 Kg-m^2

B = 0.0.

Control Scheme II:

$K_I = 2.871$

$K_p = 0.58$

$J = 0.0025$ Kg-m^2

$B = 0.0.$

Appendix 7C

```
%Program used to calculate the IP parameters for two-order speed loop.
%aao/(s^2+aa1*s+aa2)
%main program--KIP2.m and subprogram---KIP.m
clear all
%parameters
global u1 c1 h1 tre k1;
pr=4;lm=0.02;iqs=8;tre=0.4;k1=-2;lp=0.041;
J=0.0025;b=1/J;B=0.0; kt=(3/2)*pr*lm*iqs;
uo=5;co=1;ho=1
ss=fsolve('KIP',[uo co ho]')
u1=ss(1)
c1=ss(2)
h1=ss(3)
u2=u1+c1^2
ki=u1*u2/(kt*b)
kp=((u1+u2)/b-B)/kt
```

```
end;

%Subprogram Kip2.m
function q=KIP(p)
global u1 c1 h1 tre k1;
u1=p(1);c1=p(2);h1=p(3);
q=zeros(3,1);
%coefficiences parameter
q(1)=h1/u1-h1/(u1+c1^2)-1;
q(2)=h1^2/(2*u1)-h1^2*(1-k1)/(2*u1+c1^2)-k1*h1^2/(2*u1+2*c1^2);
q(3)=0.9-((h1/u1)*(1-exp(-u1*tre))-(h1/(u1+c1^2))*(1-exp(-(u1+c1^2)*tre)));
end;
```

Appendix 7D

```
%program used to calculate the IP parameters for three-order speed loop.
%aao/(S^3+aa2*S^2+aa1*S+aao)
%main program--KIP3.m and subprogram---KIPP.m
clear all
%parameters
global u1 c2 c3 h2 h3 tre k1 k2;
k1=1.2;k2=-2;tre=0.4;
uo1=20;co2=2;co3=2;ho2=0.3;ho3=3;
```

```
ss=fsolve('KIPP',[uo1 co2 co3 ho2 ho3]')
u1=ss(1)
c2=ss(2)
c3=ss(3)
h2=ss(4)
h3=ss(5)
u2=u1+c2^2;
u3=u1+c2^2+c3^2;
aa2=u1+u2+u3;
aa1=u1*u2+u2*u3+u3*u1;
aao=u1*u2*u3;
%Dr.Ojo controller
pr=4;lm=0.02;lp=0.04;iqs=10;j=0.0025;
z=(3*pr^2*lm*iqs)/(4*j);
k3=lp*aa2
kd=lp*aao/(z*k3)
k2=lp*aa1/(z*k3)
end;
%Subprogram of Kip3.m
function q=KIPP(p)
global u1 c2 c3 h2 h3 tre k1 k2;
u1=p(1);c2=p(2);c3=p(3);h2=p(4); h3=p(5);
q=zeros(5,1);
%coefficiences parameter
```

```
q(1)=-(h2+h3)*((u1+c2^2)+(u1+c2^2+c3^2))+h2*(u1+(u1+c2^2+c3^2))...
   +h3*(u1+(u1+c2^2));
q(2)=-(h2+h3)/u1+h2/(u1+c2^2)+h3/(u1+c2^2+c3^2)-1;
q(3)=0.9-(-(h2+h3)*(1-exp(-u1*tre))/u1...
   +h2*(1-exp(-(u1+c2^2)*tre))/(u1+c2^2)...
   +h3*(1-exp(-(u1+c2^2+c3^2)*tre))/(u1+c2^2+c3^2));
q(4)=(-(h2+h3)*h2/(u1+(u1+c2^2))+h2^2/(2*(u1+c2^2))...
   +h2*h3/((u1+c2^2)+(u1+c2^2+c3^2)))...
   -k1*(-(h2+h3)*h3/(u1+(u1+c2^2+c3^2))...
   +h2*h3/((u1+c2^2)+(u1+c2^2+c3^2))+h3^2/(2*(u1+c2^2+c3^2)));
q(5)=((h2+h3)^2/(2*u1)-(h2+h3)*h2/(u1+(u1+c2^2))...
   -(h2+h3)*h3/((u1+c2^2+c3^2)+u1))...
   -k2*((-(h2+h3)*h2/(u1+(u1+c2^2))...
   +h2^2/(2*(u1+c2^2))+h2*h3/((u1+c2^2)+(u1+c2^2+c3^2)))...
   +(-(h2+h3)*h3/(u1+(u1+c2^2+c3^2))+h2*h3/((u1+c2^2)+(u1+c2^2+c3^2))...
   +h3^2/(2*(u1+c2^2+c3^2))));
end;
```

REFERENCES

1. L. J. Hunt, "A new type of induction motor," J. IEE (Lond.), 1907, 38, pp. 648-677

2. F. Creedy, "Some developments in multi-speed cascade induction motors," J. IEE (Lond.), 1921, 59, pp. 511-537.

3. G. H. Rawcliffe, "Induction motors: old and new," Proc. Roy. Soc. (Lond.), 1970, 117, (7), pp. 1277-1290

4. A. R. W. Broadway, L. Burbridge, "Self-cascaded machine: a low-speed motor or high-frequency brushless alternator," Proc. IEE, vol.117, Juy 1970, pp. 1277-1290.

5. A. R. W. Broadway, "Cageless induction motor," Proc. IEE, vol. 118, 1971, pp. 1593-1600.

6. A. R. W. Broadway, "Brushless stator-controlled synchronous-induction machine," Proc. IEE, vol. 120, August 1973, pp. 860-866.

7. A. R. W. Broadway and G. Thomas, "Brushless cascade alternator," Proc. IEE, vol. 121,1974, pp. 1529-1535.

8. A. Kusko and B. C. Somuah, "Speed control of a single frame cascade induction motor with slip power pump back," IEEE Trans. on Industry Application, 1978, Vol.14, (2), pp. 97-105.

9. F. Shibata and K. Taka "speed control system for brushless cascade induction motors in control range of slips S1>1 and S2>1," IEEE Trans. on Energy Conversion, 1987, Vol.2, (2), pp.246-263.

10. C. D. Cook and B. H. Smith, "Effects of machine parameter values on dynamic response and stability regions of doubly-fed cascade induction machines," Proc. IEE. Electr. Power Appl. 1983, 130, (2), pp. 137-142.

11. C. D. Cook and B. H. Smith, "Stability and stabilization of doubly-fed single-frame cascade induction machines," Proc. IEE, 1979, 126, (11), pp. 1168-1174.

12. A. K. Wallace, R. Spee and H. K. Lauw, "The potential of brushless doubly-fed machines for adjustable speed," IEEE Industry Applications Society, pulp and paper industries annual conference, Seattle, 1990, pp. 45-50.

13. A. K. Wallace and R. Spee, "Research development and application studies for brushless doubly-fed machines," Seminarios International De Motors Electricos E acionamentos Regulares, Sao Paulo, Brazil, 1991, pp. 41-60.

14. C. J. Heyne and A. M. El-Antably, "Reluctance and doubly-excited reluctance motors," Final report, Oak Ridge National Laboratories, Report ORNL/SUB/81-95013/1.

15. A. K. Wallace, R. Spee and H. K. Lauw, "Dynamic modeling of brushless doubly-fed mahines," IEEE Industry Applications Society Annual Meeting, 1989, pp. 329-334.

16. R. Spee, A. K. Wallace and H. K. Lauw, "Performance simulation of bruless doubly-fed adjustable speed drives," IEEE Industry Applications Society Annual Meeting, 1989, pp. 738-743.

17. P. Rochelle, R. Spee and A. K. Wallace, "The effect of stator winding configuration on the performance of brushless doubly-fed machines in adjustable speed drives," IEEE Industry Applications Society Annual Meeting, 1990, pp. 331-337.

18. A. K. Wallace, R. Spee and P. Rochelle, "Rotor modelling and development for brushless doubly-fed machines," International Conference on Electrical Machine, ICEM'90, Boston, 1990, pp. 54-59.

19. R. Li, A. K. Wallace and R. Spee, "Dynamic simulation of brushless doubly-fed machines," IEEE Trans. on Energy Conversion, 1991, Vol.6, (3), pp. 445-452.

20. R. Li, A. K. Wallace and R. Spee, "Two axis model development of cage-rotor brushless doubly-fed machines," IEEE Trans. on Energy Conversion, 1991, Vol.6, (3), pp. 453-460.

21. M. S. Boger, A. K. Wallace, R. Spee, R. Li, "Investigation of appropriate pole number combinations for brushless doubly-fed machines applied to pump drives," IEEE Trans. on Industry Application, 1996, Vol.32 (1), pp. 189-194.

22. S. Williamson and A. C. Ferreira, "Generalised theory of the brushless doubly-fed machine. Part 2: Model verification and performance," IEE Proc., Electr. Power Appl., 1997, 144, (2), pp. 123-129.

23. S. Williamson and A. C. Ferreira, "Generalised theory of the brushless doubly-fed machine. Part 1: Analysis," IEE Proc., Electr. Power Appl., 1997, 144, (2), pp. 111-121.

24. A. C. Ferreira and S. Williamson, "Iron loss and saturation in brushless doubly-fed machines," IEEE Industry Applications Society Annual Meeting, New Orlean, 1997, pp. 97-103.

25. F. Liang, L. Xu and T. A. Lipo, "d-q analysis of a variable speed doubly-AC excited reluctance motor," Electric Machine and Power System, Vol.19, pp. 125-138, 1991.

26. L. Xu, F. Liang and T. A. Lipo, "Transient Model of a doubly-excited reluctance motor," IEEE Trans. on Energy Conversion, Vol.6, No.1, pp. 126-132, March 1991.

27. O. Ojo and Z. Wu, "Modeling of the doubly-fed reluctance machines using harmonic balance technique and Manley-Rowe power frequency relationship," IEEE Industry Applications Society Annual Meeting, 1996, pp. 794-800.

28. Novotny, D. W. and T. A. Lipo, *Vector Control and Dynamics of AC drives*, Oxford University Press. 1996.

29. Y. Liao and C. Sun, "A low cost, robust position sensorless control scheme for doubly-fed reluctance motor drives," IEEE Industry Application Society Annual Meeting, 1993, pp.437-444.

30. Y. Liao and C. Sun, "A novel position sensorless control scheme for doubly fed reluctance motor drives," IEEE Trans. on Industry Application, Vol.30, No5, Sep./Oct., 1994, pp. 1210-1218.

31. L. Xu, L. Zhen and E. H. Kim, "Field orientation control of a doubly excited brushless reluctance machine," IEEE Industry Application Society Annual Meeting, 1996, pp.319-325.

32. R. Li, R. Spee, A. K. Wallace and G. C. Alexander, "Synchronous drive performance of brushless doubly-fed motors," IEEE Trans. on Industry Application, Vol.30, No.4, July/August, 1994.

33. R. Li, A. K. Wallace and R. Spee,:"Determination of converter control algorithms for brushless doubly-fed induction motor drive using Floquet and Lyapunov techniques," IEEE Trans. on Power Electronics, Vol.10, No.1, January, 1995.

34. P. G. Holmes, and N. A. Elsonbaty, "Cyclonvertor-excited divided-winding doubly-fed machine as wind-power convertor," IEE Proc., Electr. Power Appl., March 1984, vol.131, pp.61-69.

35. Y. Tang, L. Xu, "Stator field oriented control of doubly-excited induction machine in wind power generating system," 35th Midwest Symposium on Circuits and System", Wachington, DC, August 9-12, 1992.

36. L. Xu and Y. Tang, "A novel wind-power generating system using field orientation controlled doubly-excited brushless reluctance machine," IEEE Industry Application Society Annual Meeting, 1992, pp.408-413.

37. S. G. Jeong, and M. H. Park, "Steady state analysis of a stand alone wound rotor induction generator excited by a PWM inverter," IEEE Industry Application Society Annual Meeting, 1987, pp. 790-797.

38. R. Pene, J. C. Clare and G. M. Asher, "A doubly fed induction generator using back-to-back PWM converters supplying an isolated load from a variable speed wind turbine," IEE Proc.-Electr. Power Appl., Vol. 143, No.5, September 1996, pp. 380-387.

39. O. Ojo and Z. Wu, "Synchronous operation of a dual-winding reluctance generator," to be published in the IEEE Trans. on Energy Conversion.

40. O. Ojo and Z. Wu, "Performance characteristics of dual-winding reluctance generators," IEE Proceeding. -Electr. Power Appl. November 1997, Vol. 144, Issue 6, pp. 461-468.

41. O. Ojo and Z. Wu, "Regulated DC power generation using mixed-pole synchronous reluctance machines," IEEE Industry Application Society Annual Meeting, 1997, pp. 263-270.

42. S. Williamson and M. S. Boger, "Impact of inter-bar currents on the performance of brushless doubly-fed motor," IEEE Industry Applications Society Annual Meeting, New Orlean, 1997, pp. 188-195.

43. L. Xu, Y. Tang and L. Ye, "Comparison study of rotor structures of doubly excited brushless reluctance machine by finite element analysis," IEEE Trans. on Energy Conversion, Vol.9, No.1, March 1994, pp. 165-171.

44. L. Xu and F. Wang, "Comparative study of magnetic coupling for a doubly fed brushless machine with reluctance and cage rotors," IEEE Industry Application Annual Meeting, New Orlean, 1997, pp. 326-331.

45. S. Williamson, "Power factor improvement in cage-rotor induction motors," IEE Proc., Electr. Power Appl., 1983, 130, (2), pp. 121-129.

46. S. Williamson and E. R. Laithwaite, "Generalized harmonic analysis for the steady-state performance of sinusoidally-excited cage induction motors," IEE Proc., Electr. Power Appl., 1985, 132, (3), pp. 157-163.

47. W. V. D. B Heinz and B, H-C. Skudelny, "Analysis and realization of a pulsewidth modulator based on voltage space vectors," IEEE Trans. on Industry Application, vol. 24, No. 1, January/February, 1988, pp. 142-148.

48. N. L. Schmitz and D. W. Novotny, *Introductory Electromechanics*, (book), Ronald Press, New York, 1965.

49. T. A. Lipo, *Analysis of synchronous Machines*, (Lecture Notes), University of Wisconsin-Madison, 1987.

50. E. Spooner and A. C. Williamson, "Mixed pole windings and some applications," IEE Proceedings, Part B, vol.137, No.2, March 1992, pp.89-97.

51. L. Ye, "Design, Analysis and Performance Test of a Doubly Fed Reluctance Machine," (Master thesis), The Ohio State University, 1994.

52. L. Xu, "Design and Evaluation of a reluctance machine drive system," Ph.D. dissertation, University of Wisconsin-Madison, 1990.

53. S. J. Chapman, *Electric Machinery Fundamentals*, (book), McGraw-Hill, 1985.

54. B. S. Gury and H. R. Hiziroglu, *Electric Machinery and Transformers*, (book), Harcourt Bruce Jovanovich, Publishers, 1988.

55. G. J. Retter, *Matrix and Space-Phasor Theory of Electrical Machines*, (book), Akademiai Kiads, Budepest, 1987.

56. A. Nayfeh and B. Balachandran, *Applied Nonlinear Dynamics*, (book), John Wiley and Sons, Inc., New York, 1995.

57. J. M. Manley and H. E. Rowe, "Some properties of nonlinear elements, part 1: general energy relations," Proceedings of the IRE, vol.44, pp.904-913, 1956.

58. R. H. Pantell, "General power relationship for positive and negative non-linear resistive elements," Proceedings of the IRE, vol.46, no.12, pp.1910-1913, 1958.

59. P. Penfield, *Frequency-Power Formulas*, (book), MIT press, 1960.

60. A. P. Russell and I. E. D. Pickup, "An analysis of the induction motor, part 3-power/frequency relationships," IEE Proceedings, vol.129, no.5, pp.243-247, September 1982.

61. Z. M. Salameh, M. A. Casacca and W. A. Lynch, "A mathematical model of a lead-acid batteries," IEEE Trans. on Energy Conversion, vol.7, no.1, pp. 93-98, 1998.

62. O. Ojo, J. Cox and Z. Wu, "DC power generation using interior permanent-magnet machines," IEEE Trans. On Energy Conversion, vol.12, no.4, pp.351-356, December 1997.

63. E. Van. Dijk, H. J. N. Spruijt, D. O'Sullivan and J. B. Klassens, "PWM-switch modeling of DC-DC converters," IEEE Trans. on Power Electronics, vol.10, no.6, pp.659-665, November 1995.

64. Vatche Vorperian, "Simplified analysis of PWM converters using model of PWM switch part II: Discontinuous conduction mode," IEEE Trans. On Aerospace and electronics, vol.26, no.3, pp.497-505, May 1990.

65. P. K. Nandam and P. C. Sen, "Analog and digital speed control of DC drives using proportional-integral and integral-proportional control techniques," IEEE Trans. on Industrial Electronics, vol.34, no.2, pp.227-233, May 1997.

66. C. M. Liaw, F. J. Lin and Y. S. Kung, "Design and implementation of a high performance induction motor servo drive," IEEE Proceedings-B, vol. 140, no. 4, pp.241-248, July 1993.

67. F. J. Lin, "A digital signal processor based robust integral-proportional controller for an induction motor servo drive," Electric Power Systems Research vol.37, pp.129-136, 1996.

68. M. Ouyang, C. M. Liaw, and C. T. Pan, "Model reduction by power decomposion and frequency response matching," IEEE Trans. on Automatic Control, vol.32, no.1, pp.59-62, January 1987.

69. A. M. Trzynadlowski, *The Field Orientation Principle in Control of Induction Motors*, (book), Kluwer Academic Publishers.

70. D. C. Lee, S. K. Sal and M. H. Park, "High performance current regulator for a field-orientation controlled induction motor drive," IEEE Trans. on Inductry Applications, vol.30, no.5, pp.1247-1257, September/October, 1994.

71. B. Friedland, *Control System Design, an Introduction to State-Space Methods*, (book), McGraw-Hill, New York, 1986.

72. J. Slotine and W. Li, *Applied Nonlinear Control*, (book), Prentice Hall, New York, 1991.

73. O. Ojo, "Field orientation control of a doubly-fed synchronous reluctance machine," Conference Record of the 29th Annual IEEE PESC conference, pp.1276-1282, 1998.

74. L. Xu, L. Zhen and E. Kim, "Field orientation control of a doubly-excited brushless reluctance machine," IEEE Trans. on Industry Applications, vol. 34, no. 1, pp. 148-155, January/ February 1998.

75. D. Grenier, L. A. Dessaint, O. Akhrif, Y. Bonnassieux, and B. L. Pioufle, “Experimental nonlinear torque control of a permanent-magnet synchronous motor using saliency,” IEEE Trans. On Industry Electronics, vol.44, no. 5, pp. 680-686, Oct., 1997.

76. T.-G. Park and K. –S. Lee, “SMC-based adaptive input-output linearising control of induction motors,” IEE Proceedings Control Theory Application, vol. 145, no. 1, pp. 55-61, January 1998.

77. M. Tarbouchi and H. Le-Huy, “High-performance control by input-output linearlization technique of an induction motor,” IEEE Industry Application Annual Meeting, New York, 1996, pp. 373-378.

78. M. Bodson, J. N. Chiasson, R. T. Novotnak and R. B. Rekowski, “High-performance nonlinear feedback control of a permanent magnet stepper motor,” IEEE Trans. On Control Systems Technology, vol. 1, no. 1, pp.5-13, March 1993.

79. W.L. Soong and T.J.E. Miller, “Field-weakening performance of brushless synchronous AC motor drives,” IEE Proc.-Electr. Power Appl., Vol. 141, No. 6, pp. 331-340,November 1994.

80. B. J. Chalmers, L. M. Musaba and D. F. Gosden, “Variable-frequency synchronous motor drives for electric vehicles,” IEEE Trans. On Industry Applications, Vol. 32, N0. 4, pp. 896-903, July/August, 1996.

81. John Cox, *Analysis of an Interior Permanent Magnet Machine Operating in Generator Mode*, Master Thesis, Tennessee Technological University, 1996.

82. O. Ojo and O. Omozusi, “Modeling and analysis of an interior perfornent-magnet DC-DC converter generator system,” IEEE Power Electronics Specialists Conference Record, pp. 929-935, June, 1997.